LHCb Vertex Locator Upgrade Development and Rare b-quark Decays in LHCb

Thesis submitted in accordance with the requirements of the
University of Liverpool for the degree of Doctor of Philosophy
by

Vinícius Franco Lima

Supervisors: Dr. David Hutchcroft
Prof. Gianluigi Casse

Oliver Lodge Laboratory
Department of Physics
University of Liverpool

July 2019

Longe do estéril turbilhão da rua,
Beneditino escreve! No aconchego
Do claustro, na paciência e no sossego,
Trabalha e teima, e lima , e sofre, e sua!

Mas que na forma se disfarce o emprego
Do esforço: e trama viva se construa
De tal modo, que a imagem fique nua
Rica mas sóbria, como um templo grego

Não se mostre na fábrica o suplício
Do mestre. E natural, o efeito agrade
Sem lembrar os andaimes do edifício:

Porque a Beleza, gêmea da Verdade
Arte pura, inimiga do artifício,
É a força e a graça na simplicidade.
-Olavo Bilac

Aos meus irmãos, Caio Victor e Mariana

Abstract

LHCb Vertex Locator Upgrade Development and Rare b-quark Decays in LHCb

This work describes contributions and results obtained within the scope of the LHCb collaboration. Analysis of two decays of b hadrons using the LHCb detector are discussed: $\Lambda_b^0 \rightarrow pKJ/\psi(\mu\mu)$ and its use to probe lepton universality and the very rare $B^+ \rightarrow a_1^+(1260)(\pi\pi\pi)\mu\mu$ and its feasibility in LHCb. The development and testing of the LHCb Vertex Locator(VELO) upgrade pixel sensors and readout chips is presented, with a discussion of the challenges and solutions of a silicon detector operating at 5.1 mm from the LHC interaction region. There is an extensive discussion on the testing of different silicon sensor designs both before and after irradiation up to a fluence of $8 \times 10^{15}\,1\,\text{MeV}\,\text{n}_{eq}\,\text{cm}^{-2}$. Results obtained in the laboratory and in a testbeam environment are shown, proving the chosen solution, a planar n-on-p, 200 µm thick, 450 µm guard-ring sensor design meets LHCb's requirements. The testing methods for sensors and readout chips for the module production are presented together with a new method to bias hybrid pixel assemblies under vacuum before wire-bonding. This work was part of the campaign to deliver the VELO upgrade detector for a 2020 installation and physics operation in the LHC in 2021.

Declaration of Authorship

This thesis is the result of my own work, except where a specific reference to the work of others is made. This thesis has not been submitted for any other qualification to this or any other university.

Vinícius Franco Lima

Acknowledgements

It is incredibly hard to summarise all of the people that I have to thank for helping me throughout my PhD. I'll let my non-britishness shine in this section, please bear with me.

The Liverpool LHCb group who guided me through the PhD and helped me go wherever I wanted to go. Thanks to Tara Shears, Stephen Farry and Themis Bowcock for the support and advice. Karol Hennessy for being the coolest. Gianluigi Casse which was always supportive and offered good advice. David Hutchcroft, supervised me through good and bad and was always on my side. He always had a wise point of view that helped my sometimes hectic focus, I'm enormously grateful.

The Liverpool HEP group at large for all the support. Specially Tony Smith and the people at the workshop, that were always helpful when I was assembling the lab setup in the clean room. Also, all the students, specially in my year: Adam, Lauren, Tab and Heather.

I also have to thank the Liverpool LHCb group and STFC for giving me resources to go on a LTA at CERN, working directly with the people involved in the VELO project and analysis. This was an amazing opportunity and I will remember fondly of the intense work and freedom that I experienced there.

The LHCb VELO group was fundamental on all of my hardware work, but I guess more importantly, an amazing group of people to work with. Paula Collins, that chose to give me responsibilities that I wasn't sure I could take, I hope it paid off. Kazu, a constant friend and supervisor, who I have just too much to thank for any amount of space. Jan Buytaert, that discussed and helped me test the biasing through the ASIC idea. Raphael Dumps, who overworked himself to help me save the idea of the vacuum jig from what it looked like scrap to an actual solution for the VELO production. Martin van Beuzekom that still receives emails from me about some intricacy of the Timepix/Velopix and is always interested and helpful. Victor Coco, who endured a lot of me blabbing about IV

curves and helped me with results in this thesis.

The SPS testbeam crew, that was forged in radiation and coffee. Again, Kazu and Martin for always being there, and seemingly never sleeping. Heinrich for all the support. Elena, Tim and Emma, I'm very glad we were all in the same team, you are a group of amazing physicists and are all going to go do great things. "Beam is on/ Beam is on-on/ Beam is - ON".

Of course I have to mention Vieux-Bureau, the headquarters of my CERN adventures way before I even lived there. Benedetta and Miguel, my incredible friends and housemates, always ready for talking nonsense as well as talking serious (but mostly nonsense). I will miss the impromptu Reculet runs, parties and board games. As the third and final Brazilian in Vieux-Bureau, I'm very happy we could say goodbye to the house with a bang.

The University of Liverpool Karate Club was largely responsible for keeping my sanity though four years of PhD by subjecting me to intense pain and joy. I'm very proud of having been part of this amazing group. Ebba and Naomi, whom I will never forgive for making me listen to Simple Plan. Tashia for being such a good friend. The Maccies who took me in after I came back and helped me eat all of the food.

The maths lot, that randomly took me in on the first month and here we are. Sam, Stephen, Kathryn that were there for pubs, barbecues, bingos and everything in between. Louis and Sophie, which are dear friends and also let me drop on their place quite a few times. Michael, if you are reading this, you should be thanking me for putting up with you. In any case, thanks for listening to all the drama, reading a specially badly written chapter of this document and giving me *playful distractions* during my PhD such as placing joists, being cold and breaking up concrete.

Essa tese não teria sido escrita sem o esforço monumental dos meus pais e da minha família. As saudades de estar longe dos meus país é uma dor terrível, silenciosa e constante. Se me sinto assim, me resta imaginar o que meus pais sentiram. O crédito, de fato, é mais deles do que meu. Especialmente minha mãe, Rita, quem eu amo demais e sei que sofreu com a distância. Meu pai, Ulysses que sempre me incentivou a dar o meu melhor. Meus irmãos Caio Victor e Mariana, de quem eu morro de orgulho.

Os meus amigos brasileiros direto da UFRJ para o CERN, que me ajudaram tanto com física quanto com a vida: Bruno, Oscar, Ana Bárbara, Mateus e Carol. Ana Bárbara, que já

me aguentava falando pelos cotovelos desde aquele sofrido ônibus saindo do Fundão → Nova América às 8 da noite e agora me atura até na Europa.

Ao CNPq, através do programa Ciências sem Fronteiras, que financiou o meu doutorado durante quatro anos. Não foge à mim a realidade do Brasil e a responsabilidade da educação e da ciência em garantir a qualidade de vida de um povo que por vezes é tão sofrido.

Last but not least, thanks to Liverpool itself. This city took very good care of me, and it will always be in my heart.

Contents

Abstract v

Declaration of Authorship vii

Acknowledgements ix

Contents xvi

List of Figures xxii

1 Introduction 1

2 The LHCb Experiment 5

2.1 Physics Goals . . . 5

2.2 The Large Hadron Collider . . . 5

2.2.1 A Note on Luminosity . . . 6

2.3 LHCb Detector Description . . . 10

2.3.1 Magnet . . . 11

2.3.2 Tracking Detectors . . . 12

2.3.3 Particle Identification . . . 18

2.3.4 DAQ and Trigger . . . 22

2.3.5 Offline Analysis . . . 25

2.4 LHCb Upgrade . . . 26

2.4.1 Upstream Tracker (UT) . . . 28

2.4.2 SciFi Tracker . . . 29

2.4.3 RICH . . . 31

2.4.4 Calorimeter and Muon Systems . . . 32
2.4.5 Trigger and DAQ . . . 32

3 The Standard Model 35
3.1 Introduction to Standard Model . . . 35
3.1.1 Anatomy of the Standard Model . . . 36
3.1.2 Flavour and the CKM Matrix . . . 43
3.1.3 Standard Model Shortcomings . . . 44
3.2 Lepton Universality . . . 46
3.2.1 Effective Field Theory Interpretation . . . 48

4 Rare b-quark Decays 51
4.1 R_{pK} Measurement . . . 51
4.1.1 Candidate Selection . . . 55
4.1.2 PDF Determination . . . 56
4.2 Evaluation of the $B^+ \to a_1^+(1260)(\pi^+\pi^-\pi^+)\mu^+\mu^-$ . . . 66
4.2.1 Generation and Reconstruction Efficiencies . . . 66
4.2.2 Offline Selection . . . 67
4.2.3 Estimation on the Yield . . . 69

5 Silicon Sensors 73
5.1 Interaction of Particles with Matter . . . 73
5.1.1 Energy Deposition . . . 74
5.1.2 Scattering in Materials . . . 76
5.2 Silicon Sensors in High Energy Physics . . . 76
5.2.1 Silicon and the pn-Junction . . . 77
5.2.2 Breakdown Mechanisms . . . 83
5.2.3 Signal Formation . . . 85
5.2.4 Silicon Hybrid Pixel Detectors . . . 86
5.3 Radiation Damage Effects . . . 87
5.3.1 Leakage Current Increase . . . 91
5.3.2 Charge Collection Loss . . . 92
5.3.3 Effective Doping Concentration . . . 92
5.3.4 Double Junction . . . 93

5.3.5 Charge Multiplication 96

6 VELO Upgrade **99**
6.1 Physics Impact and Requirements 99
6.2 Mechanics 103
6.3 Cooling 107
6.3.1 Microchannel Cooling 107
6.4 The VeloPix 109
6.4.1 Signal, Thresholds and Timestamps 111
6.5 Readout Electronics and DAQ 115
6.6 Sensors 117
6.6.1 Sensor Designs 117
6.7 Sensor Studies using the Timepix3 Telescope 120
6.7.1 n-on-n Edge Noise Analysis 121
6.7.2 Interchip Efficiency 126

7 High Voltage Tolerance **131**
7.1 Testing Setups 132
7.2 Non-Irradiated Sensors 134
7.3 Irradiated Sensors 140
7.4 Parylene and Irradiation 142
7.5 Breakdown Voltage Temperature Dependence 145
7.5.1 Temperature and Calibration 146
7.5.2 Testing for Thermal Runaway 147
7.5.3 Effective Band Gap Energy 151
7.5.4 Breakdown Temperature Behaviour 155

8 Bias-through-ASIC Method **161**
8.1 Tile Probe Card Setup 161
8.2 Bias-through-ASIC Method 164
8.3 Vacuum Hood 169
8.4 Conclusion 169

9 Conclusion and Outlook **173**

A HOP Variable Implementation **179**

A.0.1 Implemented Algorithm 182

A.0.2 Results and Comparison 182

B Irradiation Campaign **185**

References **191**

List of Figures

2.1 The CERN accelerator complex . . . 7
2.2 The LHC ring . . . 8
2.3 Luminosity seen by LHCb during Run I . . . 9
2.4 The LHCb Experiment . . . 10
2.5 Production of $b\bar{b}$ quark pairs at the LHC . . . 11
2.6 LHCb's magnet . . . 12
2.7 LHCb magnetic field profile . . . 13
2.8 Cross sections of the VELO silicon sensors . . . 14
2.9 Trend of the current on the VELO sensors as function of time . . . 15
2.10 Impact parameter resolution as function of track momentum . . . 16
2.11 LHCb Tracker Turicensis . . . 16
2.12 LHCb gaseous outer tracker stations . . . 17
2.13 Hybrid photon detector for the RICH . . . 19
2.14 Cherenkov angle as a function of momentum for different particles . . . 20
2.15 Example of $K^{\pm}$ identification efficiency . . . 20
2.16 LHCb muon stations . . . 21
2.17 Organisation of the different trigger strategies for Run I and II . . . 23
2.18 Original LHCb full trigger scheme . . . 23
2.19 Online alignment update of the VELO using data from HLT1 . . . 25
2.20 Trigger yield as a function of luminosity . . . 27
2.21 LHCb Experiment after upgrades . . . 28
2.22 Upstream tracker design . . . 29
2.23 Scintillating fibre tracker mat end . . . 29
2.24 SciFi tracker stations . . . 30

2.25 Example of two RICH upgrade cells . . . 31
2.26 New DAQ scheme in the upgrade . . . 33

3.1 Scattering between two particles into two particles . . . 36
3.2 Example of Bhabha scattering betweeen e^- and e^+ . . . 36
3.3 Fermions and bosons in the standard model . . . 37
3.4 Electroweak currents mediated by electroweak bosons . . . 39
3.5 Proton-proton interaction at the LHC . . . 42
3.6 Lowest order flavour changing neutral currents in the SM . . . 47
3.7 Compiled measurements of R_K and R_{K^*} . . . 48
3.8 Compiled measurements of R_D and R_{D^*} . . . 49

4.1 Feynman diagram depicting the resonant J/ψ decay channel . . . 52
4.2 Sketch of production ratio of di-muon pairs in the q^2 range of b quark decays . . . 53
4.3 Comparison between Λ_b^0 mass distributions . . . 54
4.4 BDT classifier output and performance . . . 56
4.5 Comparison between different PDFs for the Λ_b^0 signal using a MC simulation 59
4.6 Example of Λ_b^0 candidates in data under different mass hypothesis . . . 60
4.7 Keys PDF estimation for the B_s^0 decays reconstructed as Λ_b^0 . . . 61
4.8 Keys PDF estimation for the B^0 decays reconstructed as Λ_b^0 . . . 62
4.9 Keys PDF estimation for the Λ_b^0 candidates with swapped hadrons. . . . 63
4.10 Fits for the PDF B^0 and B_s^0 components found in data using the correct mass hypothesis. . . . 63
4.11 Data Fit for the Λ_b^0 mass spectrum . . . 64
4.12 Example Fits for Run I data for muons and electrons. . . . 65
4.13 Example of variables for particle identification of π tracks . . . 68
4.14 Example of variables with high discriminatory power used as input for the BDT . . . 70

5.1 Energy loss of a relativistic charged particle as function of $\beta\gamma$ . . . 75
5.2 Angular scattering angle distribution . . . 77
5.3 Silicon lattice structure . . . 78
5.4 Electronic band structure in an intrinsic silicon lattice . . . 79

5.5 Setup of a p-n junction . . . 81
5.6 Capacitance behaviour of p-n junctions . . . 82
5.7 Band gap scheme in a heavily reverse biased p-n junction . . . 84
5.8 Scheme of a Hybrid Pixel Detector assembly . . . 86
5.9 Scheme showing the edge region of a sensor . . . 87
5.10 Simulation of the vacancies generated in a silicon bulk . . . 88
5.11 Example of common defects introduced in the crystalline structure by irradiation . . . 89
5.12 Radiation damage cross section as a function of incident particle energy . 90
5.13 Effect of annealing on the effective dopant concentration . . . 91
5.14 Example of the effective depletion voltage as a function of fluence . . . 94
5.15 Velocity of charges generated in a silicon bulk illuminated by a laser at different depths . . . 95
5.16 Different models for the junction configuration of irradiated sensors . . 96
5.17 Edge TCT scan of an irradiated sensor . . . 96
5.18 Comparison between the observed total charge collected and leakage current 97

6.1 Example of ambiguity from a combination of hits in strip readout . . . 100
6.2 Depiction of relevant points for impact parameter measurement . . . 101
6.3 Impact parameter resolution as a function of $1/p_T$ . . . 102
6.4 Expected VELO radiation flux per fb^{-1} . . . 102
6.5 Positions of all 26 VELO Upgrade stations and the 52 modules . . . 103
6.6 Module Full Assembly . . . 104
6.7 Module Mechanical Assembly . . . 105
6.8 VELO nominal module position with respect to the RF foil . . . 106
6.9 Full VELO design . . . 106
6.10 Microchannel design . . . 108
6.11 Thermal simulation of the substrate temperature . . . 109
6.12 VeloPix readout ASIC floor plan . . . 110
6.13 Analog pre-amplifier scheme present in each pixel . . . 111
6.14 Steps taken during the equalisation of a single pixel . . . 112
6.15 Structure of the VeloPix output packet . . . 113
6.16 Evolution of the base threshold level of 32 individual pixels . . . 114

6.17 Difference in ASIC only noise level observed pixel by pixel when compared to the noise level before irradiation . . . 114
6.18 Structure of the DAQ chain in the VELO Upgrade . . . 116
6.19 MiniDAQ data output packet after data processing . . . 116
6.20 Underside of a triple tile bump-bonded to VeloPix ASICs . . . 118
6.21 Scheme showing the area with elongated pixels in the sensors . . . 118
6.22 Underside of a HPK sensor with UBM in place . . . 119
6.23 Photograph of the Testbeam setup at CERN . . . 120
6.24 Charge Collection Efficiency measurements done using upgrade sensor prototypes . . . 122
6.25 Charge Collection Efficiency measurements for irradiated sensors . . . 122
6.26 Example of edge noise seen in irradiated n-on-n sensors . . . 123
6.27 Time distribution of hits in the edge and elsewhere . . . 124
6.28 Effect of the IKrum setting on a n-on-n sensor . . . 125
6.29 Time over Threshold measurements in the edge Region for two irradiated sensors . . . 125
6.30 Schematic of the n-on-n guard-ring scheme . . . 126
6.31 Irradiated n-on-p sensor measurements at different bias voltages and IKrum values . . . 127
6.32 Hitmap for a long run with the beam positioned over the interchip region 128
6.33 Efficiency for the T1 assembly as a function of the column number . . . 129
6.34 Intrapixel efficiency for the T1 assembly . . . 130

7.1 Photograph of the laboratory setup assembled at Liverpool . . . 133
7.2 Cooling block inside the vacuum chamber at CERN . . . 134
7.3 Current Density as a function of bias voltage for n-on-p HPK design . . . 135
7.4 Current Density as a function of bias voltage for Micron n-on-p and n-on-n designs . . . 136
7.5 Current Density as a function of bias voltage for a single and a triple HPK n-on-p assembly . . . 136
7.6 HPK sensors with guard-ring size of 450 µm IV scans . . . 138
7.7 IV curves for n-on-p Micron sensors, singles and triples, with a 450 µm guard-ring . . . 138

7.8 IV curves for n-on-n Micron sensors, with 450 µm guard-ring 139
7.9 IV curves for the first batch of thinned tiple assemblies 139
7.10 IV curves for sensors irradiated at IRRAD 141
7.11 IV curves for sensors non-uniformly irradiated at KIT 141
7.12 IV curves for sensors uniformly irradiated at JSI, IST and KIT 142
7.13 Microscope image detailing damage due to spark 143
7.14 Microscope images of proton irradiated sensors parylene damage 144
7.15 Microscope images of neutron irradiated sensors 144
7.16 IV curves for proton irradiated sensors at KIT 146
7.17 Temperature calibration curve 147
7.18 Leakage Current and temperature of assembly S22 as function of bias voltage 148
7.19 Power in KIT proton irradiated sensor due to leakage current for various temperatures 148
7.20 Leakage current of assembly T26 in a vacuum tank while ASICs are turned on 149
7.21 Image taken with an infrared camera through the IR window in the Liverpool vacuum tank 150
7.22 Fit example for IV curve of irradiated sensor at −35 °C 152
7.23 Fit of the saturation current as a function of temperature 153
7.24 Leakage current scaling with temperature at different voltages for a neutron irradiated n-on-p sensor 153
7.25 E_{eff} measurements as a function of bias voltage 154
7.26 Fitted IV curves taken with T25 at different temperatures 155
7.27 IV curves of triple assemblies irradiated with protons at Birmingham and IRRAD 156
7.28 Breakdown Voltage of proton irradiated sensors as a function of temperature 157
7.29 Comparison of Leakage current as a function of voltage for different irradiation fluences 159
7.30 Trend of the κ parameter for nine different sensors with four different irradiation profiles 160

8.1 Image showing the wirebond connections on a VeloPix ASIC 162

8.2 Output of the white-light interferometry for surveying flatness of the surface in which the ASICs will be placed . . . 163
8.3 Image displaying the reference mark on each mechanical tile . . . 164
8.4 Difference in nominal positions and measured pad positions on the probe station . . . 165
8.5 Scheme of the orientation of p and n-type implants in both the VELO Upgrade Sensors and the VeloPix and the equivalent diode circuit . . . 166
8.6 Images of needles being positioned on a VeloPix hybrid in order to test the connections between sensor and ASIC backside . . . 167
8.7 Voltage measured across the p-bulk and n-well on the VeloPix . . . 168
8.8 Voltage measured across the p-bulk ground contact and the VeloPix backside 168
8.9 Comparison between the regular method of biasing a sensor (through readout pad) and the through the ASIC backside . . . 169
8.10 Pictures with details of the vacuum hood . . . 170
8.11 IV measurements taken with the vacuum hood . . . 170

A.1 Example of resonance peaks reconstructed in LHCb . . . 179
A.2 Different bremsstrahlung emissions in LHCb . . . 180
A.3 HOP variable schematic . . . 181
A.4 Comparison between the software implemented in LHCb and reference HOP variable . . . 183
A.5 Comparison between the software implemented in LHCb and reference HOP mass . . . 184

B.1 KIT non-uniform irradiation profile for triple (left) and single (right) assemblies. . . . 186
B.2 Birmingham non-uniform irradiation profile for triple assemblies . . . 188
B.3 IRRAD fluence profile for full fluence samples . . . 189

1 Introduction

Modern day particle physics is dominated by one particular effective field theory, called the Standard Model (SM), that has proved itself remarkably good in describing nature at the smallest scales humans have probed so far. This theory, although very successful, fails to explain basic features of the observed universe, such as the lack of antimatter or the lack of a good explanation for dark matter.

To test the SM to the limit of what is technologically feasible, physicists built an accelerator that can reach high energy collisions at a very high rate. In order to achieve the necessary energy, this accelerator, called the Large Hadron Collider (LHC), had to be built with a circumference of 27 km. Perhaps more important than the energy, the LHC, on its quest to detect remarkably rare events, was built to be the brightest collider ever, with collisions happening every 25 ns.

Around the accelerator ring there are four points in which the beams collide and in each one experiments were built. These experiments surround the area around the collision points with detectors. The detectors save information of particles passing through them so that physicists can reconstruct what happened in a particular collision. Each experiment employs its own strategy, choosing a specific detector design to reconstruct these collisions.

The biggest physics result so far coming from the LHC was the discovery of the Higgs boson by the CMS [1] and ATLAS [2] experiments in 2012. With this discovery, the last particle predicted by the SM was found, and the goal was set to find evidence of events produced in the LHC that the SM cannot predict.

The LHCb Experiment specialises in precisely measuring properties of particle decays generated in LHC collisions. Such measurements can shed light on several aspects of particle physics, amongst them the existence of beyond standard model physics at a higher energy scale. LHCb can do this by accurately measuring decay rates, which give information on the probabilities of a certain decay to occur. The probabilities of a certain decay

can depend on physics of higher energy scales than the scales directly accessible by the LHC through the effect of loop corrections. So, by probing the decays of certain particles, such as b quarks, one can investigate the existence of beyond standard model physics.

The detectors employed to do this measurements are very customised. The requirements on precision, timing, radiation hardness and efficiency mean that one cannot just buy a standard solution. The development of new detectors is a big effort made by all LHC experiments to achieve the best possible physics that technology permits. In the case of LHCb, after running for 10 years with its original detectors, the collaboration is preparing a detector upgrade. This change in detectors will allow the experiment to operate with many more simultaneous collisions, ultimately improving the statistics used in LHCb measurements.

In particular LHCb has a very special vertex detector called VELO. It is composed of silicon tracking sensors that get very close to the nominal interaction region of the LHC. This detector is used to find the position of the original interaction vertex between two protons and the vertex at which particles generated by the initial collision decay. This information is fundamental to differentiate b mesons from other particles, which is very important for the physics goals of LHCb. A large part of this document is focused on the upgrade of the VELO. This upgrade will ensure the VELO performance at the higher rates of simultaneous collisions that will be used in the upgrade.

This thesis is divided in nine chapters, including Introduction and a final Summary. On **Chapter 2** there is a detailed description of the LHCb Experiment, how it is designed, the performance of its sub-detectors and the trigger and offline reconstruction structure. The upgrade of the experiment is also discussed, with the reasons for the upgrade and its main changes.

Chapter 3 is a short review of the Standard Model, its main features and shortcomings. The more recent measurements , specially the anomalies on the lepton universality measurements are also discussed. This is followed by **Chapter 4**, that goes into detail on the measurement of R_{pk} and the strategies to select and fit the control mode $\Lambda_b^0 \to pKJ/\psi(\mu\mu)$. This Chapter also includes a discussion on the decay $B^+ \to a_1(1260)^+(\pi\pi\pi)\mu\mu$, where I estimate the yields for the decay involving the $a_1(1260)^+$ are estimated for the present LHCb dataset.

Chapter 5 changes gears, as the discussion shifts to Silicon detectors and how they are used for precise tracking in high-energy physics experiments. The particularities of the

silicon structure and how the radiation damage affects the properties of these detectors on a macroscopic level are also discussed. In **Chapter 6** the upgraded Vertex Locator for LHCb is described in detail, along with my direct contributions. These contributions include the measurements of threshold drift of the ASIC under irradiation, the nature of the n-on-n edge noise on irradiated sensors and the cluster finding efficiency of irradiated sensors in the interchip region.

The measurement of the high voltage tolerance of the prototype sensors for the VELO upgrade can be found in **Chapter 7**. In it, there is a summary of the main findings of the testing campaign before and after irradiation which were used as input for the final decision on the sensor design to be used in the detector. The careful measurements and analysis of all the IV curves taken during the sensor R&D were my direct contribution. These results were an important input to the final sensor decision during the sensor Production Readiness Review (PRR). Special attention is dedicated to the temperature and irradiation dependancy of the breakdown in irradiated sensors. The temperature dependant breakdown is an effect I noticed, which needed to be understood as it could affect the operation of the VELO at end of its lifetime.

Finally, **Chapter 8** describes the new method developed to test the current versus voltage behaviour of production grade sensors for the VELO. This method was used to build a testing setup, that is used both to qualify the bump-bonding of ASIC and sensor assemblies as well as test the high voltage tolerance of sensors up to 1000 V. My involvement on this jig was fundamental, as I came up with the basic design, using the bias-through-ASIC idea, and oversaw the construction of it. Without it, the testing of sensors up to 1000 V after bump-bonding and before module construction would not be possible. As time of writing this 273 sensor tiles for the production of the VELO have been tested with this setup.

Additionally there are two Appendices that add more detail to the work contained in the thesis. **Appendix B** details the irradiation procedures used on the sensors to test their performance at end of life irradiation levels. **Appendix A** discusses the implementation of a variable useful for improving electron final state reconstruction.

Alas, all good things must end, and so does this thesis. **Chapter 9** refers back to the main developments of this document and puts it in the context of the next steps for the work developed here.

2 The LHCb Experiment

The LHCb Experiment is one of the four major experiments at the Large Hadron Collider (LHC). It exploits the very forward b hadron production at the LHC in order to measure decay vertices very precisely. In this chapter the LHC accelerator is briefly introduced and the current LHCb experiment and its future upgraded detectors are described.

2.1 Physics Goals

The LHCb is an experiment built to study heavy flavour physics at the LHC. It focuses primarily on the measurements of the CP-violation parameters in the quark sector and rare decays involving hadrons containing b and c quarks.

Very rare decays, such as $B_s \rightarrow \mu^+\mu^-$, are extremely sensitive to loop corrections from new massive particles that Beyond Standard Model (BSM) physics might introduce. Hence, precision measurements performed at LHCb can probe mass scales higher than the ones achieved by direct production at LHC energies.

LHCb also focuses on measuring production processes at high η/small angles[1] close to the beam (LHCb covers the $2 < \eta < 5$ region), generating complementary results to the ones obtained by ATLAS and CMS, both only covering the central η region.

2.2 The Large Hadron Collider

The LHC [3] was built to produce pp collisions at centre-of-mass energy of 14 TeV. It was built in the tunnel that originally hosted the Large Electron Positron Collider (LEP),

[1] η is called pseudorapidity and defined by -ln[tan(θ/2)] where θ is the angle with respect to the beam axis.

a 26.7 km long ring, with a depth between 45 m to 170 m, close to Geneva, Switzerland.

Figure 2.1 depicts the accelerator complex used at CERN. By being built on the same ring as LEP, the LHC could profit from all the injection facilities that were also used for LEP. The beam acceleration starts with the linear accelerator (Linac2, to be replaced by Linac4 in 2020). The Linac2 feeds 50 MeV protons into the Proton Synchrotron Booster, a stack of 4 superimposed synchrotron rings that will further accelerate the protons to 1.4 GeV before injecting them in the PS [4]. The Proton Synchrotron was originally installed in 1959 as CERN's flagship accelerator, but continues in operation today being an injection step for experiments conducted at CERN. From the PS the beam is injected with an energy of 26 GeV into the Super Proton Synchrotron (SPS). The SPS is a 7-km ring that began operation in 1976 and is where the W and Z bosons were discovered by the UA1 and UA2 experiments.The SPS accelerates the stored protons to 450 GeV before injection into the the LHC.

The LHC tunnel is composed of 8 straight sections and 8 arcs (Figure 2.2 includes a depiction of the geographical position of the accelerator and experiments in the proximity of Geneva). Due to the two counter-rotating beams having the same charge, it is necessary to keep them in separated rings that are only combined in the beam-crossing regions. The high field necessary to keep the protons in orbit is obtained using superconducting magnets, operating at temperatures as low as 1.9 K [3]. On the LHC straight sections there are instrumentation areas, for beam monitoring and caverns in which experiments are located. There are four major experiments in the LHC: ALICE, ATLAS, CMS and LHCb. ALICE is installed in point 2 and is a dedicated experiment for ion-ion collisions, usually taken near the end of the year stop. ATLAS and CMS are positioned in points 1 and 5 respectively and are the general purpose detectors, looking into finding deviations from SM predictions as well as clear evidence of beyond the standard model physics using all the luminosity that LHC can deliver.

2.2.1 A Note on Luminosity

Luminosity is a measure of how intense accelerator collisions are. Given a physics process cross-section, the number of events generated at the collision point is a simple function

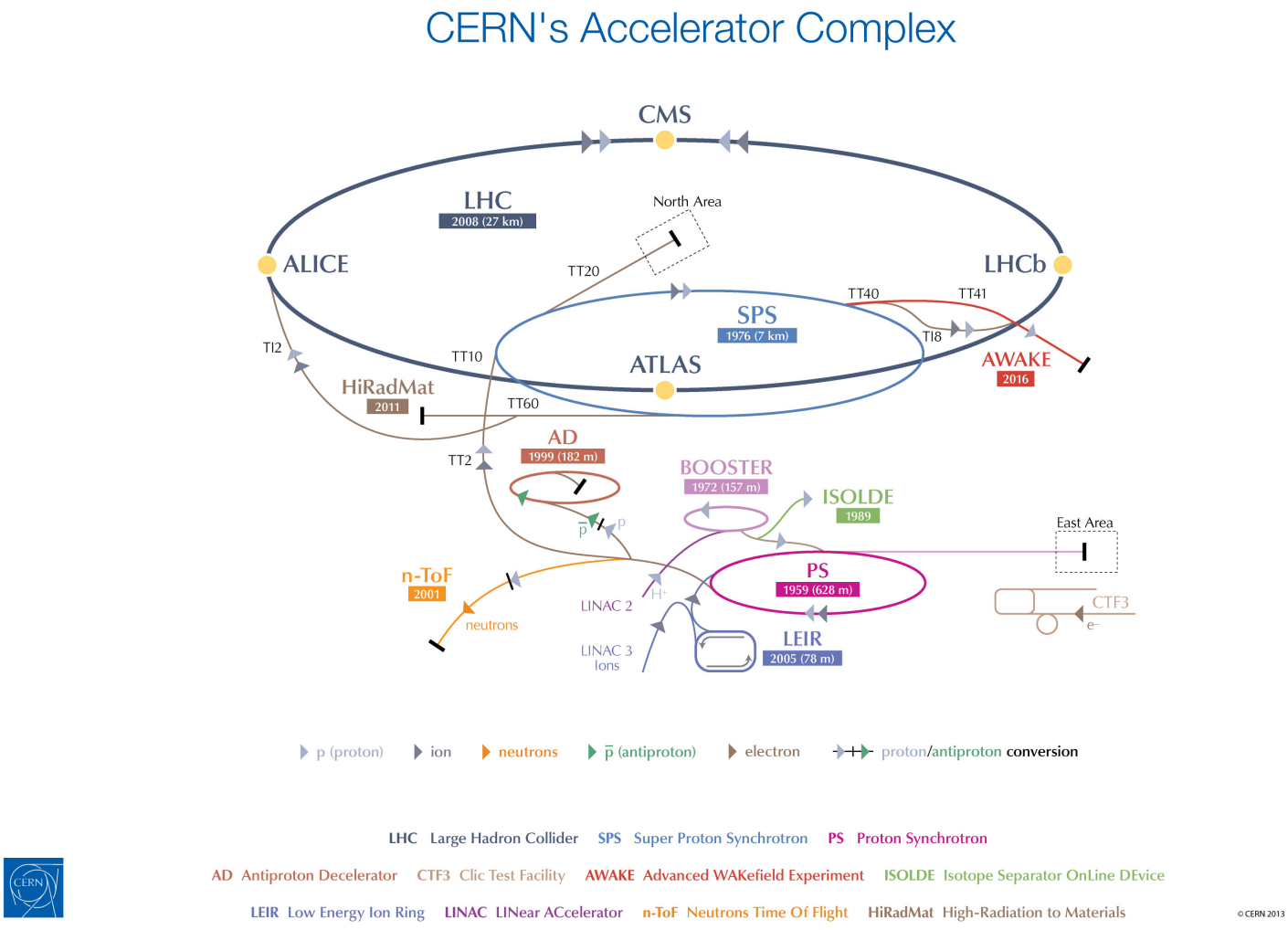

Figure 2.1: The CERN accelerator complex [5].

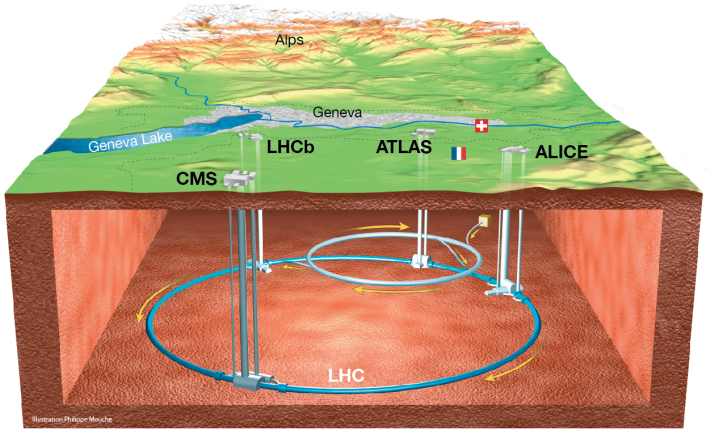

Figure 2.2: The LHC ring under the border between France and Switzerland, near Geneva [6].

of the time-integrated luminosity and the cross-section of that process:

$$N_{events} = L\sigma_{event}, \tag{2.1}$$

It is important to notice that all the physical variables of a given process between two particles are completely contained in the cross-section. The instantaneous luminosity, contains information about the beams and their crossing and it is given by:

$$\mathcal{L} = \frac{N_b^2 n_b f_{rev} \gamma_r}{4\pi\epsilon_n \beta^*} F \tag{2.2}$$

where N_b is the number of particles in a bunch, n_b the number of bunches, f_{rev} the revolution frequency, γ_r the Lorentz factor, ϵ_n the normalised transverse beam emittance, β^* the beta-star function and F is the geometric reduction factor due to a crossing angle between bunches, which is maximal when bunches are colliding head on [3]. β^* is the value of the transverse size of the beam at the interaction point while the beam emittance is a measure of the size of the phase space of particles in the beam.

Equation 2.1 refers to a total generated number of events, which is usually not what the data taken comprises of. It is up to the physicists to determine all the factors from data taking that might influence the total number of events detected in an experiment

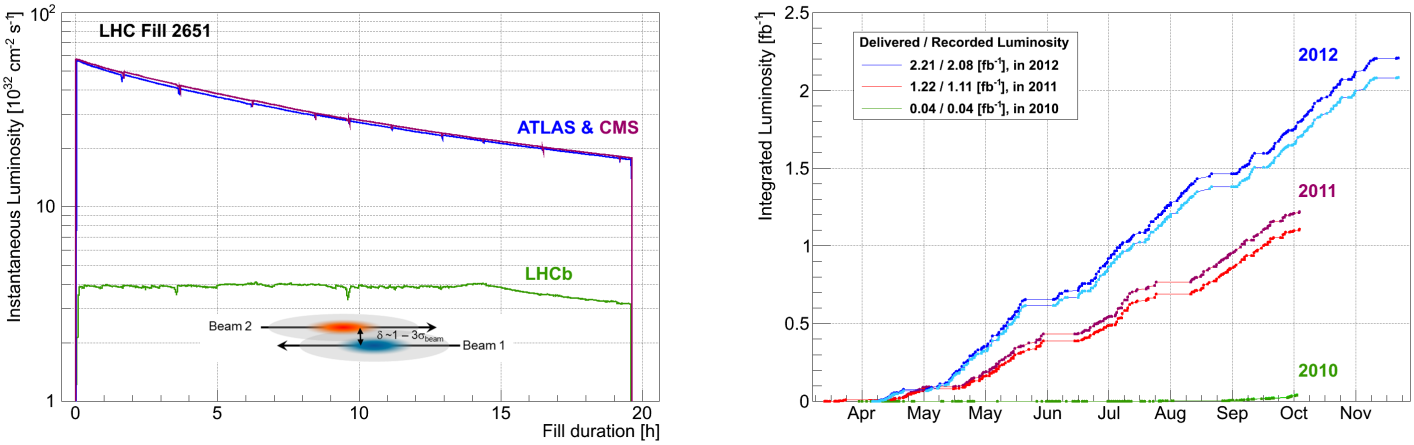

Figure 2.3: Examples of luminosity at LHCb during Run I.The plot on the left illustrates how the instantaneous luminosity is controlled in LHCb by steering the beams closer together as the time progresses. The plot on the right shows the accumulation of data (integrated luminosity) as a function of time [7].

such as acceptance, trigger and detector reconstruction. For the studies done at LHCb, for example, higher than designed instantaneous luminosities might increase occupancies in the tracker, leading to loss of momentum resolution which will impact the number of events available for a given physics analysis. Figure 2.3 shows the luminosity delivered to LHCb is controlled to be constant throughout the fill until the beam dump, and the increase in integrated luminosity over the course of the Run I data taking period [8].

Several measurements depend on the precise determination of the luminosity delivered at LHCb, and this is done through two techniques: Beam-Gas Imaging (BGI) and van der Meer Scans (vdM). Both of these methods are used to determine the density of each beam in the transverse plane with respect to the beam movement. This information can be used in combination with the beam current to estimate the number of interactions between the two beams. The BGI method consists of reconstructing particles generated by beam-gas interactions to image the density of the beam. The vdM scan uses a steering of one beam with respect to the other to scan the intensity of collisions, with this scan one can estimate the position and distribution of the combined distributions of both beams.

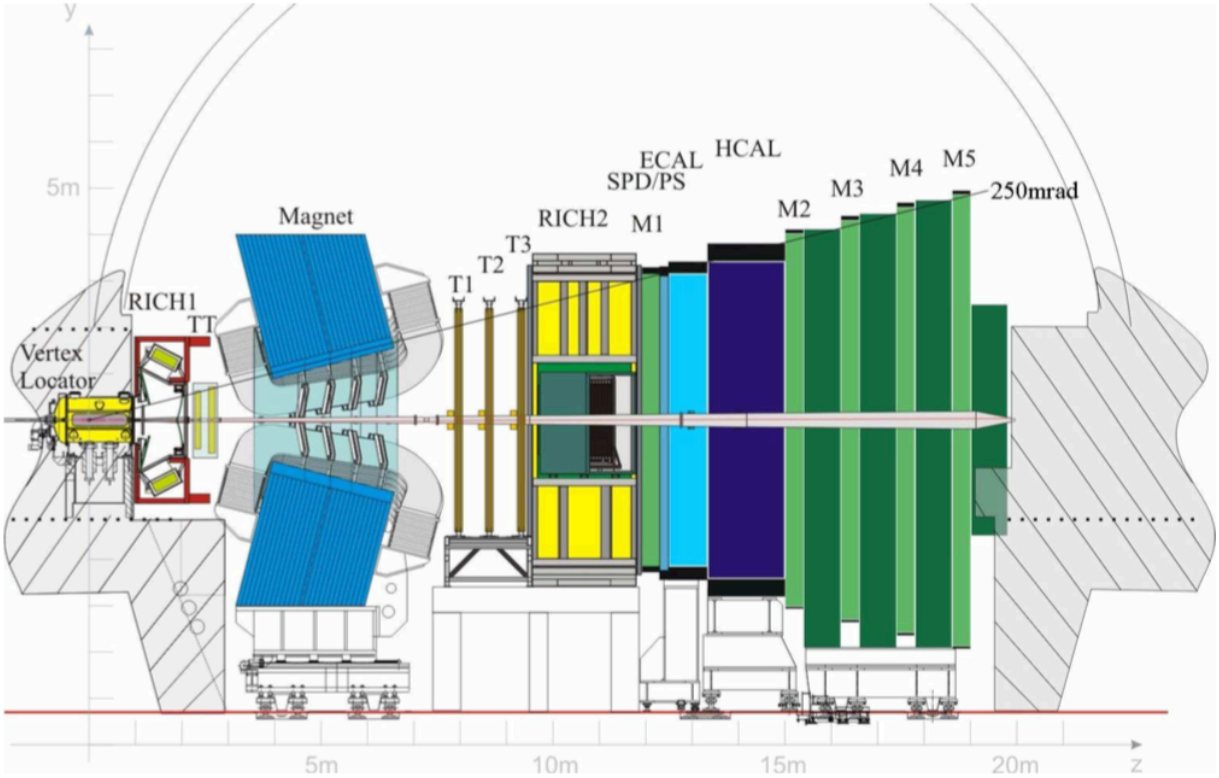

Figure 2.4: View of the LHCb Experiment [9]

2.3 LHCb Detector Description

The LHCb experiment (Figure 2.4) was carefully designed to take advantage of the unique conditions that the LHC provides for the study of b and c quarks. The choice of building a forward single-arm spectrometer was motivated by the angular distribution of the generated $b\bar{b}$ pairs that concentrates in the forward or backward cone (Fig. 2.5), being heavily boosted by the initial momentum from the parton-parton pair that interacts at the collision region. In order to correctly identify the decays and their kinematical properties, LHCb needs an excellent vertex determination, tracking, momentum resolution and particle identification. In the following section these systems will be described.

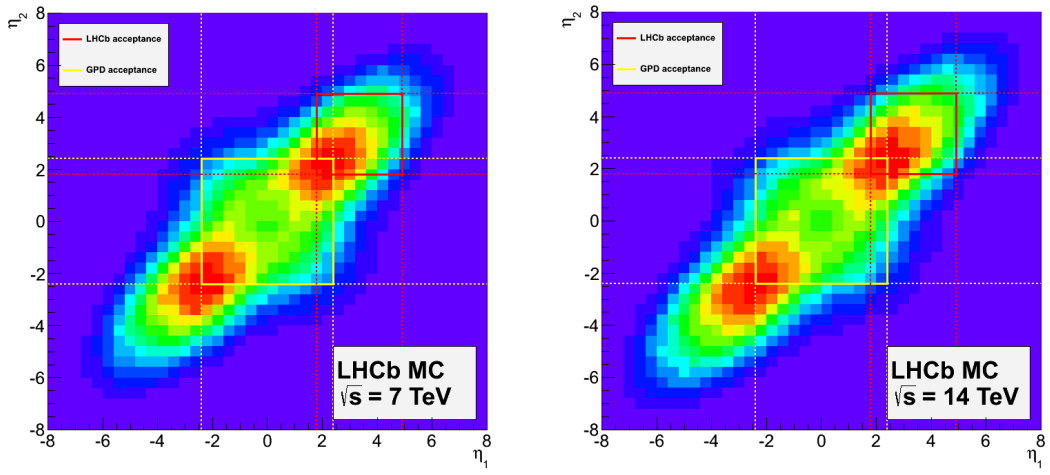

Figure 2.5: Production of $b\bar{b}$ quark pairs at LHC at 7 TeV (left) and 14 TeV (right) as a function of the rapidity of each quark [10]. The rapidity regions enclosed by the yellow boxes are covered by ATLAS and CMS, while the red box details the LHCb geometric acceptance.

2.3.1 Magnet

The detector has a single dipole magnet in order to measure the momentum of charged particles. In Figure 2.6 we can see the magnet itself, composed of two identical saddle-shaped coils designed to match the acceptance of the experiment. The coils are made out of pure Al-99.7 with a 25 mm diameter central channel for water cooling. The yoke forms a window frame, holding both of the coils, and it is composed of 100 mm thick laminated low carbon steel with a total weight of 1500 tons.

The experiment's momentum resolution depends on the knowledge of the magnetic field seen by a particle throughout its path. Therefore, a careful procedure for the mapping of the magnetic field had to be performed. The measurement apparatus was a grid of cards, each one with 3 orthogonal hall probes, globally aligned to the experiment's reference point. In Figure 2.7 we have the shape of the magnetic field as a function of the direction along the beam pipe (from the VELO to the Muon Stations), the overall precision of the field map is quoted to be $4 \times 10^{-4} \delta \mathrm{B/B}$, and magnitude is 4 T m. LHCb is capable of taking data with the magnetic field in two polarities (positive and negative values of Fig. 2.7). The data samples are split approximately equally between polarities and this variation is used

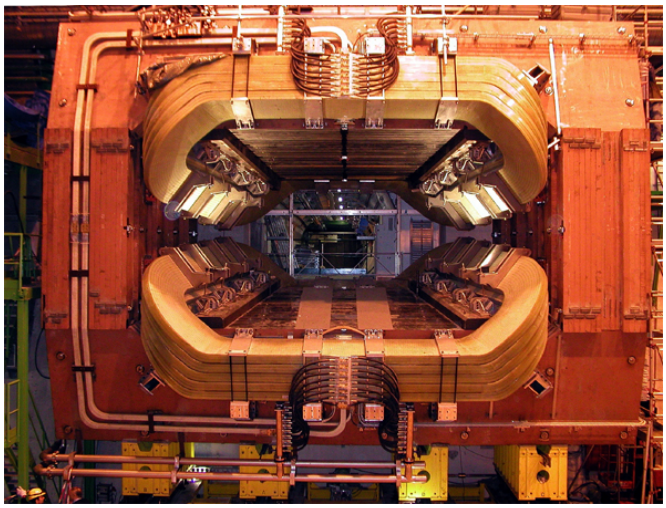

Figure 2.6: Picture of the LHCb magnet after its installation. [11].

to cross-check systematic reconstruction effects.

2.3.2 Tracking Detectors

The detectors responsible for the trajectory reconstruction in LHCb measure charged particles that are long lived enough to traverse most of LHCb, namely: $p^{\pm}$, $\mu^{\pm}$, $\pi^{\pm}$, $e^{\pm}$ and $K^{\pm}$. Given the presence of the 4 T m magnet it is also possible to determine the momentum of each of these particles and hence completely reconstruct their kinematical properties.

The LHCb tracking is composed of the vertex locator (VELO), the Tracker Turicensis (TT), and the tracking stations T1, T2 and T3. They use a combination of silicon detectors and straw-tubes, and will be described in the following sections.

The Vertex Locator (VELO)

The VELO is responsible for precisely determining the positions of the Primary Vertex (PV), the point of interaction between two partons. It is also responsible for determining the point of decay of short lived particles created in the primary interaction.

The VELO is composed by 42 silicon modules positioned along the beam axis (z), with each module having silicon microstrip n-on-n sensors on both of its sides providing

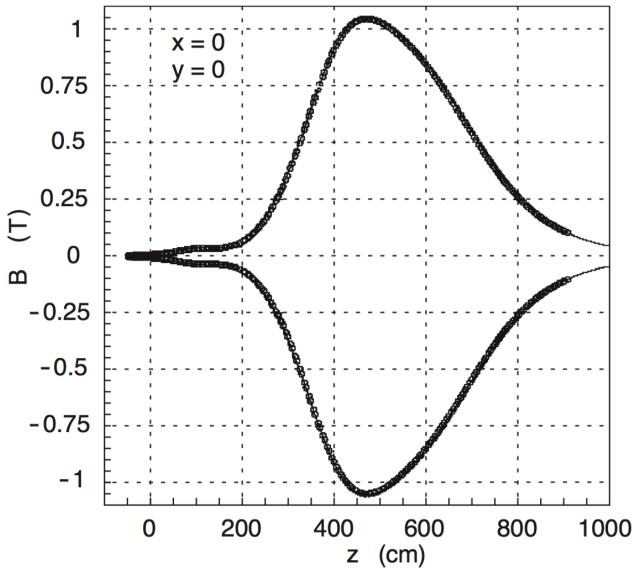

Figure 2.7: Magnetic field profile as a function of the z axis (direction along the beam pipe). [9]

R and ϕ coordinate measurements (Figure 2.8). The detector surrounds LHCb interaction region. During injection, the LHC beam aperture overlaps with the position the VELO needs to be for physics data acquisition and hence the necessity for the modules on both sides to be mounted in a support that can be moved out of position during beam injection.

The proximity of the microstrip sensors to the beam exposes the silicon sensors to a intense radiation flux. This motivated the choice of n-on-n sensors with p-spray deposits to isolate the n-strips developed to be radiation tolerant. The R-sensors have linearly variable pitch between strips of 38 µm at the smallest radius and 101.6 µm at the outer radius of 41.9 mm. The ϕ sensors are divided into inner and outer regions with different pitches in order to cope with high occupancies, with the inner region pitch is 78.3 µm while the outer region has a pitch 39.3 µm. Both R and ϕ sensors have thickness of 300 µm. Both sensors and readout electronics are cooled using an evaporative CO_2 system. The coolant evaporates at -28ºC at the base of module, resulting in a sensor temperature of $-7 \pm 2\,^{\circ}C$ in the region closes to the beam. In Figure 2.9 it is possible to observe the evolution of the sensors' leakage current as a function of time, scaling with the radiation flux. The Impact Parameter (IP) is the distance of closest approach between a reconstructed trajectory and a reconstructed primary vertex. The IP is a very important variable in differentiating B

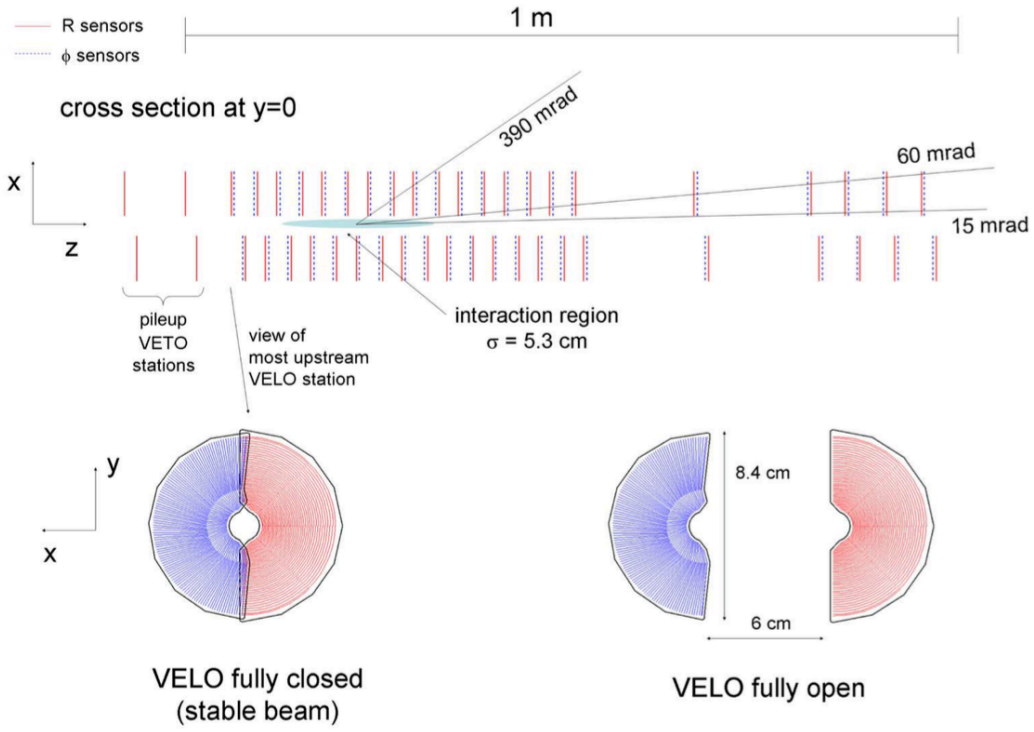

Figure 2.8: Cross sections of the VELO silicon sensors in their nominal positions. Blue stripes are ϕ sensors and red striped are R measuring sensors. The nominal beam position is at the origin in the xy plane. [9]

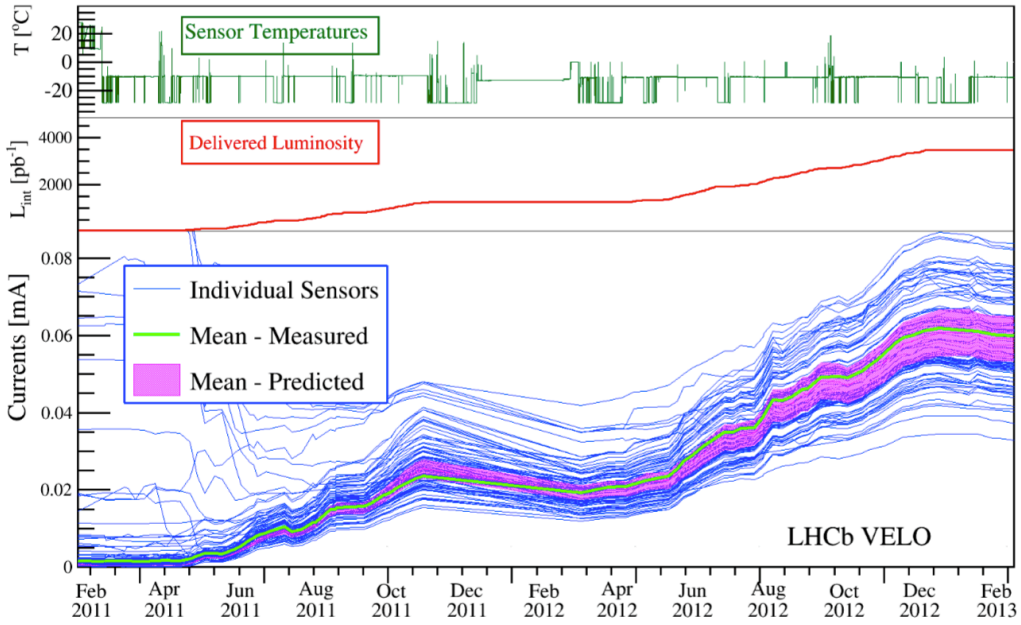

Figure 2.9: The bottom plot shows the current of each VELO sensor versus time, with the luminosity and temperature history on mid and top plots respectively [12].

decays from other particles produced in the PV, and the measured IP resolution is of the order of 13 µm (Figure 2.10).

Silicon Tracker

The Silicon tracker is a common project that comprises the Tracker Turicensis (TT), positioned between RICH1 and the Magnet, and the Inner Tracker (IT) which is the inner region of the tracking stations (T1, T2 and T3 in Figure 2.4). Each ST station is composed of four planes ($x-u-v-x$) where x denotes a vertical plane orientation, u and v denote a -5º and +5º deviation from the vertical plane respectively, as can be seen on Figure 2.11. The planes are composed of p-on-n silicon sensors that are 500μm thick with a strip pitch of 183μm on the TT station and 320/410μm thick with a pitch of 198μm for the IT stations. Silicon sensor technology is used in order to cope with the hit occupancy (that reaches levels of $5 \times 10^{-2} cm^{-2}$ per event in the innermost regions of the TT and $1.5 \times 10^{-2} cm^{-2}$ on the IT) while maintaining a small material budget, as LHCb momentum resolution is dominated by multiple scattering.

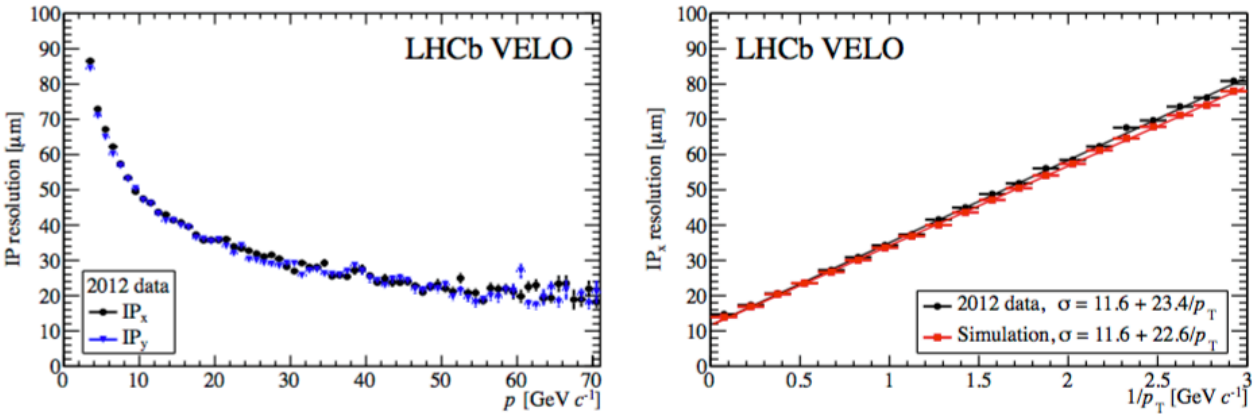

Figure 2.10: On the left we have $\sigma(\mathrm{IP}_x)$ and $\sigma(\mathrm{IP}_y)$ as a function of the track momentum and on the right we have a comparison between 2012 data and simulation for $\sigma(\mathrm{IP}_x)$ as a function of $1/\mathrm{p}_T$ [12].

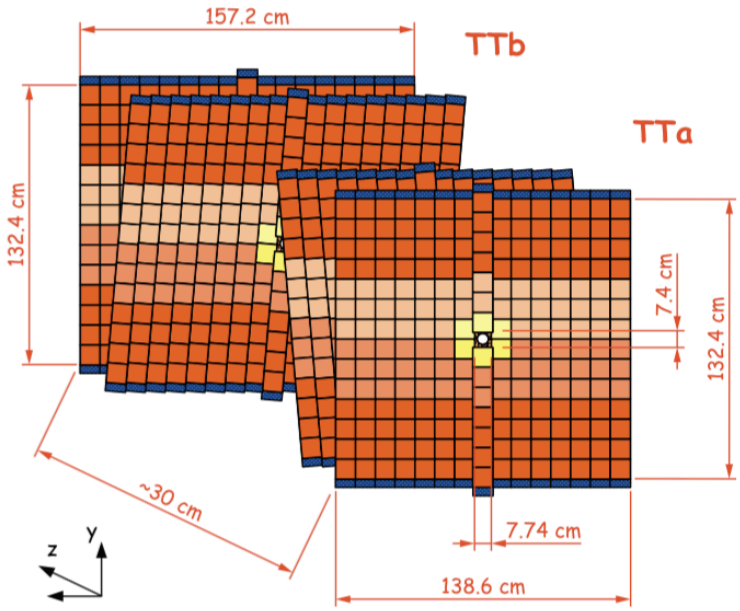

Figure 2.11: LHCbTT station, each plane is separated by 30cm from one another [13].

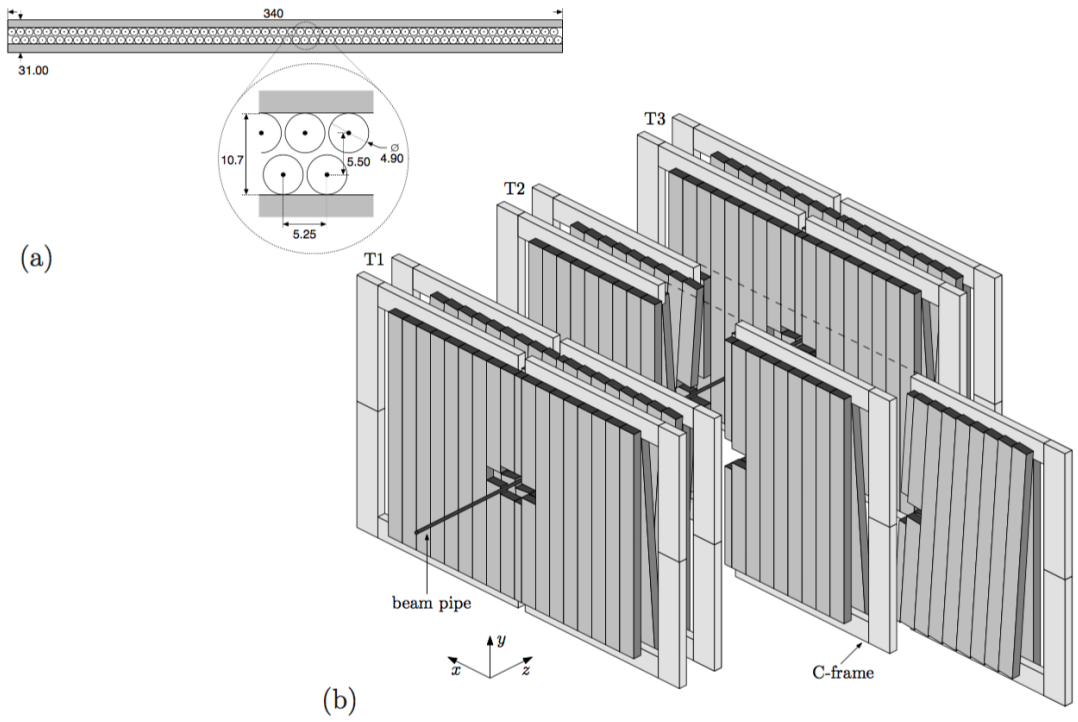

Figure 2.12: OT stations: the details of contruction of one measuring plane (a) and the assembly of each station around the beam pipe at LHCb [9].

Outer Tracker (OT)

The OT is a set of drift-time detectors placed in the tracking stations T1, T2 and T3. It covers the outer region of the tracking system, complementing the IT to cover the whole LHCb acceptance. Following the same orientation the Silicon Tracker planes, each OT station is composed of 4 modules oriented in the aforementioned $x-u-v-x$ directions (Figure 2.12). Each module is composed of two stacked layers of straw tubes filled with a gas mixture of 70% Argon and 30% CO_2 with the anode wire set to +1550V, achieving a drift time of less than 50 ns and a spatial resolution of 200 µm.

Threshold	C_4F_{10}	CF_4
p [GeV/c]	17.72	29.64
K [GeV/c]	9.31	15.58
π [GeV/c]	2.62	4.39

Table 2.1: List of RICH1 and RICH2 radiators and their specific momentum thresholds.

2.3.3 Particle Identification

Ring Imaging Cherenkov (RICH)

The main tool in LHCb for tagging the flavour of hadrons is the combination of two RICH detectors that are designed to provide particle identification capabilities over a large momentum range (2-100GeV/c). Figure 2.4 shows the two RICH detectors: RICH1, positioned immediately after the VELO, and RICH2, located between the last tracking station (T3) and the first muon station (M1). Both of them work by having a gas radiator (C_4F_{10} and CF_4 for RICH 1 and 2, respectively) that the charged particles traverse whilst emitting Cherenkov radiation.

Cherenkov radiation is emitted if a charged particle moves through a medium at a velocity higher than light's phase velocity. A mathematically thorough derivation of this phenomena is done in [14]. The angle (θ_c) of the radiation emitted with respect to the direction of motion of the particle depends directly on the particle's velocity:

$$\cos\theta_c = \frac{1}{n\beta} \tag{2.3}$$

From this equation the threshold for Cherenkov light becomes apparent considering that:

$$n = \frac{c}{v_{\text{medium}}}; \beta = \frac{v_{\text{particle}}}{c} \tag{2.4}$$

and that $\cos\theta_c$ cannot assume values bigger than one. The threshold for each material is important because it sets a minimum momentum for which particles will cause Cherenkov emission at all. Table 2.1 details the threshold for p, K and π on each radiator.

Once emitted, this radiation is reflected by mirrors leading the Cherenkov light to a set of hybrid photon detectors (HPD) outside of LHCb's acceptance. The HPD (Figure 2.13) has a photocathode that emits electrons when excited by the Cherenkov light which

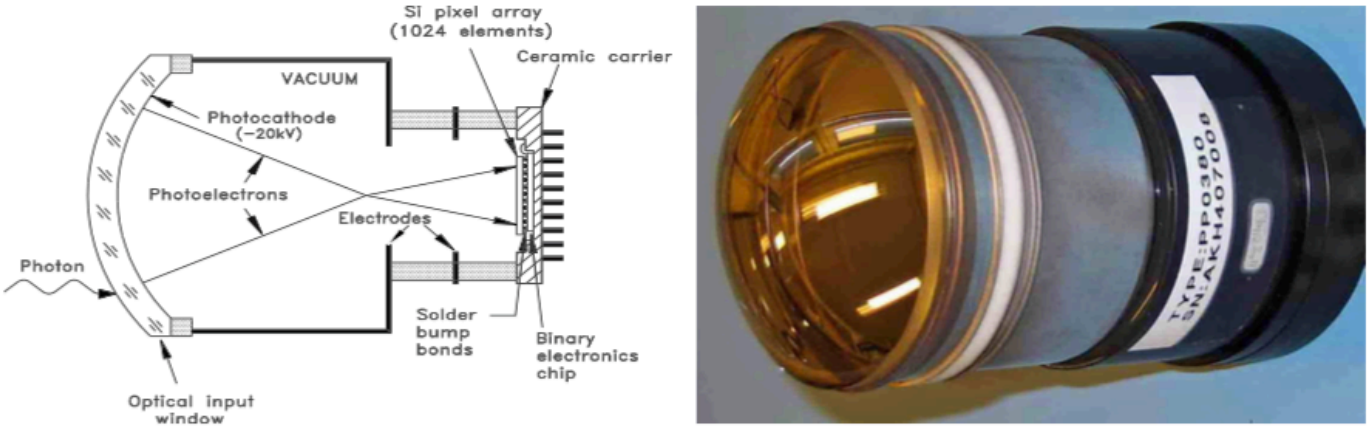

Figure 2.13: Schematic (left) and a photograph (right) of a pixel HPD [9].

then get accelerated by a potential of about 20kV inside the HPD towards a segmented silicon detector that allows to identify where the photon hit the HPD photocathode.

In order to test which particle hypothesis fits best with the measured Cherenkov radiation, LHCb builds a likelihood estimator for each particle species. Using the tracker information, this estimator considers both momentum and the expected path inside the RICH system, to calculate the expected number of photons for a given mass hypothesis around the trajectory of the charged particle. From this we get a likelihood of a given hypothesis for each track. This information will be later combined with other PID systems in order to obtain a global likelihood for each mass hypothesis. The plot in Figure 2.14 shows how well we can identify the angle of a given particle in the C_4F_{10} momentum range. For a physics analysis the difference in the log of likelihoods between two mass hypothesis is used. Figure 2.15 shows an example of Kaon efficiency and K-π misidentification; the overall log-likelihood Kaon efficiency is 95% with a π misID rate of 10%.

Muon Stations

The detectors positioned the farthest from the interaction point are the Muon Stations (M1, M2, M3, M4 and M5 in Figure 2.4). They are responsible for identifying muons. Due to their high mass (105 MeV/c^2), lack of strong interaction and long lifetime (2.2×10^{-6}s) muons travel much farther in matter than any other charged particle. Covering a total area

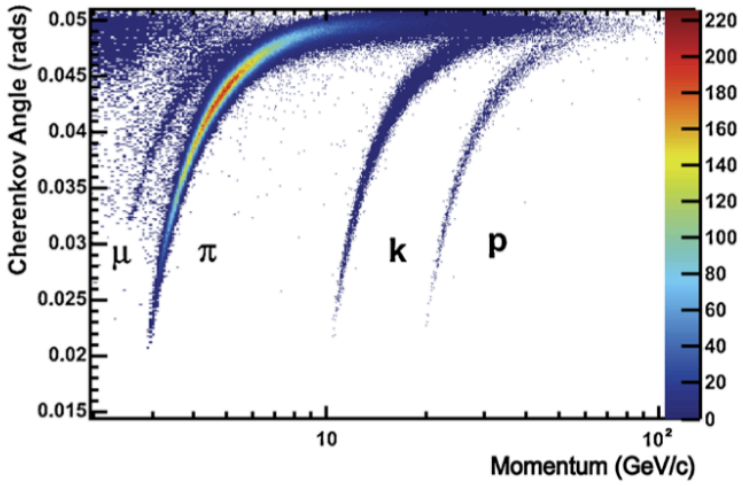

Figure 2.14: Cherenkov angle measurements as a function of momentum for different tracks. Although the RICH is mostly used for hadron identification, it is possible to see a clear muon curve at very low momentum [15].

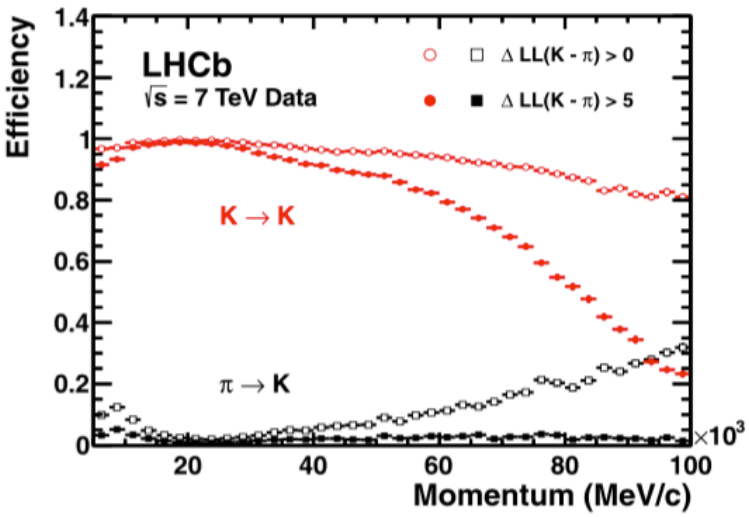

Figure 2.15: Kaon identification efficiency (red) and K-π misidentification (black) [15].

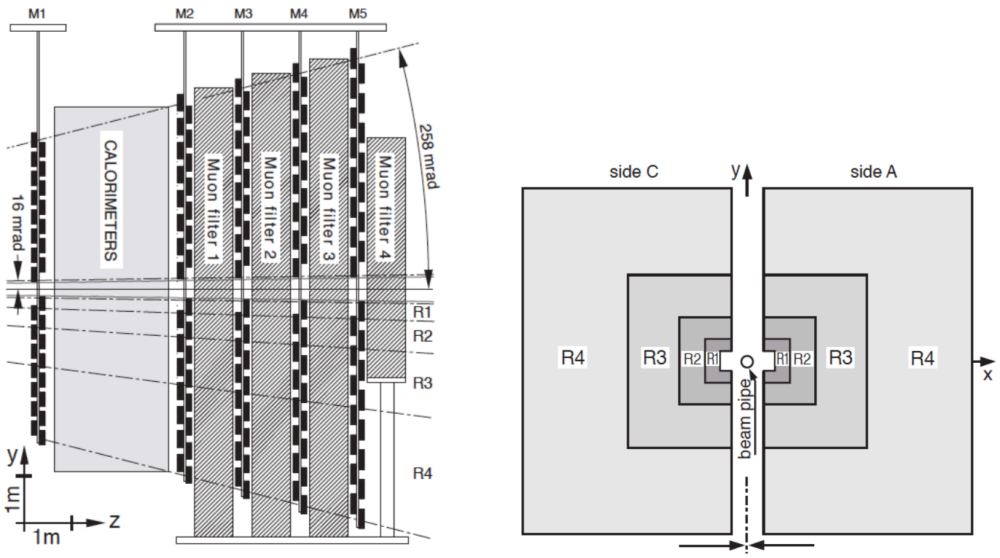

Figure 2.16: View of the Muon stations and Muon region division [16].

of approximately 435m^2 there are four different stations after the calorimeters interleaved with 80cm thick iron absorbers that help stopping any shower remnants coming from hadrons in the HCAL. Each station is divided in 4 regions (Figure 2.16); from R4 to R1 the readout channel density increases to optimise their occupancy. The detectors are multi-wire proportional chambers using a gas composition of $Ar/CO_2/CF_4$(40:55:5), except in the innermost region of M1 which is built with Gas Electron Multipliers (GEM) due to the higher particle flux closer to the beam pipe. The Muon Stations are readout at 40MHz, giving input to the L0 Trigger (Section 2.3.4) to select high transverse momentum muons, and are also used for further muon identification offline.

The muon system has provides muon identification to the offline analysis by constructing a Log Likelihood based on the track momentum and how many hits were detected in the muon stations and how close they are to the extrapolated track position in the muon system. The efficiency of the muon identification is quoted to be above 98% on average with pion and kaon misidentification below 1% [17].

Calorimeters

The LHCb calorimeter is responsible, together with the Muon System for providing information for the hardware trigger level. It is also responsible for measuring neutral particles

energy and contributing for particle identification [9].

The calorimeter is composed of four parts: scintillating-pad detector (SPD), pre-shower detector (PS), electromagnetic calorimeter (ECAL) and hadronic calorimeter (HCAL).The pre-shower is a thin scintillator layer that is used for separation between photons and electrons. Both the ECAL and HCAL aim at completely containing electromagnetic and hadronic showers in order to more precisely measure the total shower energy. The ECAL has total of $25X_0$ while the HCAL has a total of $5.6\lambda_0$. All calorimeters use the same technology: scintillation light transmitted through wavelength-shifting fibres to photomultiplier tubes. They are both sampling calorimeters interleaving the scintillation material with iron absorbers. The measured energy resolution of the ECAL as measured in a test beam is $\sigma_E/E = 8\%/\sqrt{E} \oplus 0.8\%$ while the HCAL energy resolution $\sigma_E/E = (69 \pm 5)\%/\sqrt{E} \oplus (9 \pm 2)\%$, both resolutions using E measured in GeV [9].

2.3.4 DAQ and Trigger

The LHCb trigger is responsible for quickly deciding whether or not to keep the data readout by the detectors. Given the 40MHz bunch crossing rate, the trigger decision has to be taken quickly, to reject uninteresting events while having a high efficiency for the signal.

The first trigger level (L0) is completely implemented in hardware, through the use of FPGAs[2]. The L0 uses information from the Calorimeters and Muon Stations to decide to trigger one event or not. It is divided in lines (hadron, muon, di-muon, electron) with specific selections and bandwidth limits (see Figure 2.17). A decision from L0 to trigger an event will cause all other detectors to output the data of that particular bunch crossing. Ultimately, the L0 has to reduce the rate from 40MHz to 1.1MHz, which is the maximum output rate of the front-end ASICs used in VELO and the ST [18].

After L0, all detectors are readout and their data pushed into the Event Filter Farm (EFF), a CPU farm that runs both HLT1 and HLT2 C++ applications. The High Level Trigger scheme has changed over the course of the years, showcasing the flexibility allowed by using a software trigger.

[2]Field Programmable Gate Array

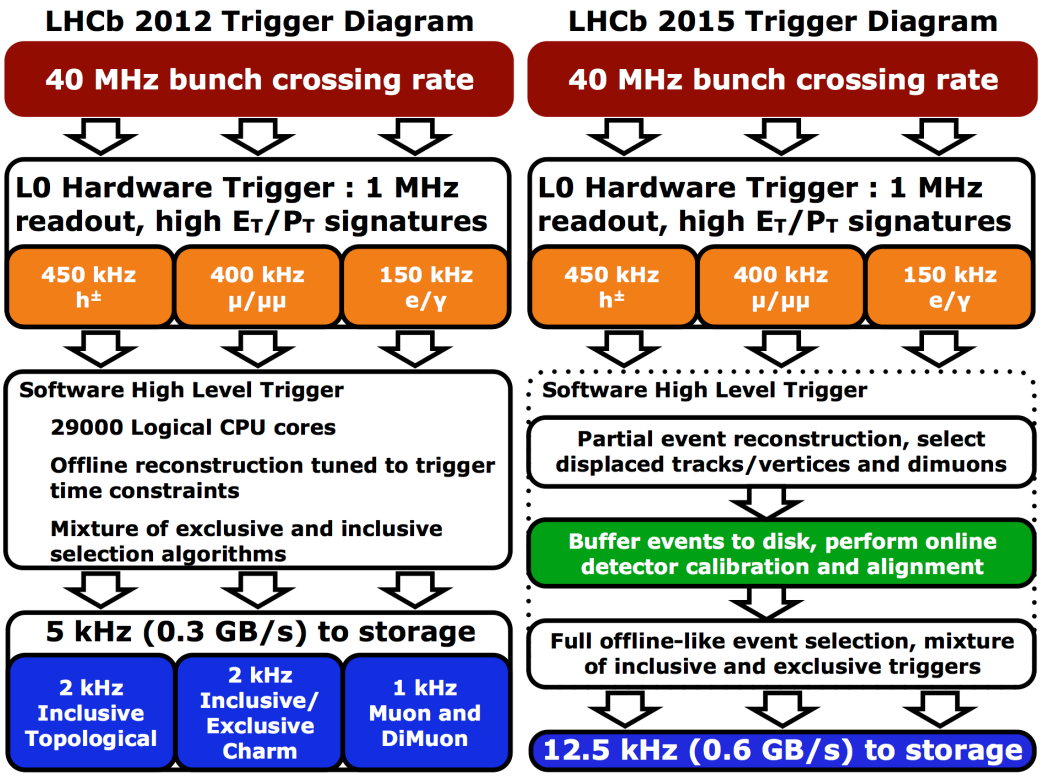

Figure 2.17: Different trigger strategies for Run I (left) and Run II (right) [19].

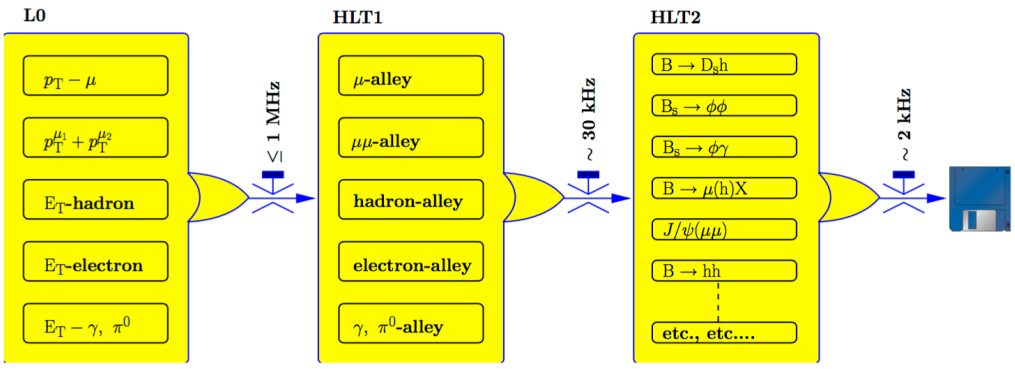

Figure 2.18: The original LHCb trigger scheme (HLT rates are outdated). Events that pass one of trigger stage will be evaluated by related lines on the next trigger stage [9].

HLT Run I

HLT1 in Run I used a simplified version of tracking in order to quickly identify interesting tracks that could trigger the event. Figure 2.18 shows how events are pushed down "alleys" based on the previous trigger stage. As an example the L0-μ trigger will cause HLT to look for high p_t muon tracks, and trigger on those if confirmed. The main purpose of HLT1 is to reduce the rate coming from L0 enough so that HLT2 has time to use more sophisticated reconstruction to select events.

In 2012 a fraction of the events that passed the L0 trigger had their raw information written to a disk buffer rather than being forwarded to the HLT. The advantage of this scheme is that as long as the buffer is not completely full, one can operate the L0 with lower thresholds, recuperating some efficiency that would be lost in the L0. This was possible since the EFF is idle during the periods in which the LHC is not in stable beams (70% of the time).

Coming from the HLT1 into HLT2, algorithms will use the whole tracking system to perform the track reconstruction with PID information in order to apply physics motivated selections to the events.

HLT Run II

Important changes were implemented for Run II in LHCb. The EFF increased in size from 29000 CPUs to 52000 CPUs, allowing for a higher output of events (Figure 2.17). The increased computational power and experience with buffering events to disk allowed for the change in architecture of the HLT1 and HLT2.

During Run II all of the events coming from L0 get passed on to HLT1 application instances and, thanks to code optimisations, tracks with a p_t as low as 500 MeV/c can be reconstructed. If an event passes the trigger, it gets written to the data storage in the EFF. A small part of the data selected by HLT1 then is used for calibration and alignment of detectors, a process that takes a few minutes. Any misalignment on the tracker would impact the momentum resolution degrading the quality of reconstruction in the HLT2. If necessary, the new obtained alignment constants are updated and used by HLT2, which will perform offline-quality reconstruction on all the events saved in the EFF (Figure 2.19). Because of the operation cycle of the LHC, the EFF is running during physics data taking with all resources dedicated to HLT1 and buffering events to disk, while periods with

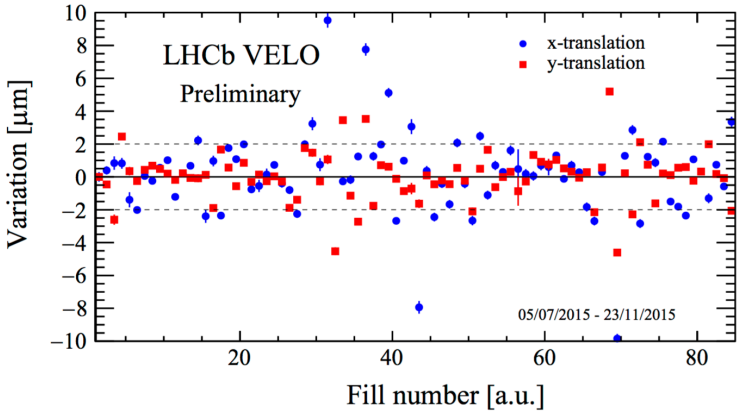

Figure 2.19: Example of the online VELO alignment using HLT1 selected data. When online alignment results are within 2 μm from initial values they are not updated. [20].

no data being taken the EFF is still fully active running the HLT2 on the events saved by HLT1. HLT2 will reconstruct all tracks, and assign particle ID when possible, then physics selections are applied to select inclusive and exclusive decays.

The quality of reconstruction in the HLT2 level during Run II allows LHCb to implement the so called "Turbo" lines that output a few trigger lines straight to analysis-ready data, without the need for any further reconstruction [21]. Turbo lines also save space by discarding the raw data from sub-detectors, keeping only information relevant for the reconstructed decay.

2.3.5 Offline Analysis

Once the event coming from the detector passed the trigger, it is saved for further reprocessing. Both in Run I and II, the data will be reconstructed using the appropriate alignment and calibrations. The reconstruction, which consists in retrieving all recorded hits in a detector, doing the pattern recognition to identify trajectories, finding primary vertices of interaction and assigning PID likelihood, is performed by the C++ application Brunel.

Brunel is executed centrally by the LHCb experiment, and the reconstructed objects are saved in a DST (Data Summary Tape) file. From the DST files a central "stripping" selection is done. The DaVinci application has the Brunel output as input and applies

selections based on requirements of the analysis working groups. This step is a central pre-selection on LHCb recorded data, saving both time and disk space so that not every individual analysis has to run through the entire LHCb dataset. Usually stripping selections are aimed at a general group of analyses involving similar decays (such as $b \to sll$), and from them data can be easily reconstructed to specific analysis task.

From the stripping, data gets divided into separate files, called streams, that group similar stripping lines such as "CHARM" or "LEPTON". Some of the data output by DaVinci uses the μDST format, that discards all raw event information, keeping only the reconstructed tracks selected by the stripping and optionally VELO-only tracks that allow for re-fitting of the PV; this data format is optimised for very high rate events in which maximising number of recorded events is more important than the possibility of keeping the possibility to run reconstruction of those events on the offline analysis. The files from stripping get copied over to different sites on the GRID and are available for access by users.

From then on, users can run the DaVinci application, configuring it such that the correct cuts, trigger requirements and mass hypothesis are applied. The output of DaVinci will usually be a ROOT Tuple containing relevant variables for the reconstructed event (chosen by the user).

2.4 LHCb Upgrade

By the end of 2018, LHCb is expected to have an integrated luminosity of 8 fb^{-1}. However, continuing to take data at this rates into Run III brings diminishing returns to reducing uncertainties on physics results. An increase in luminosity from the present $4 \times 10^{32}\text{cm}^{-2}\text{s}^{-1}$ to $20 \times 10^{32}\text{cm}^{-2}\text{s}^{-1}$ would allow LHCb to gather enough data to match theory uncertainties on many channels by the end of Run III. The LHC would be capable of delivering a higher instantaneous luminosity to LHCb without any changes on the accelerator, but as mentioned in Section 2.3.4, the current LHCb trigger scheme is limited to 1 MHz L0 output. Because the maximum readout rate is set, in order to increase the number of signal events selected, more strict L0 cuts can be used. For hadronic trigger lines, the discriminating power of L0 cuts saturates such that the required increase in thresholds results in less signal efficiency. This saturation of the trigger as a function of luminosity can be observeed in Fig. 2.20, where is also possible to notice that the μ decays do not suffer the

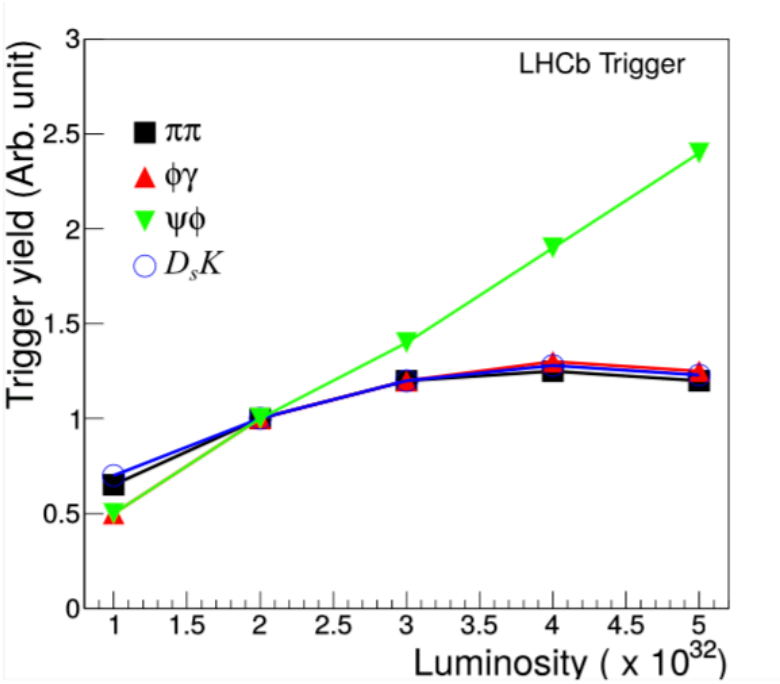

Figure 2.20: Trigger yield normalised to Run I values as a function of Luminosity in the current LHCb [22].

same effect. That is due to the good signal-background discriminating power of the muon chambers, allowing for highly efficient muon triggers even in a high pile-up[3] environment.

Therefore, in order to operate LHCb at a higher pile-up, it is necessary to change the trigger in such a way that we can maintain signal efficiency while rejecting more background events.

As described in Section 2.3.4, the current L0 only uses general information from the VELO pile-up modules, Calorimeters and Muon System. The proposal for the LHCb Upgrade is to completely remove the L0 requirements, and read all the detectors at 40Mhz. This means that all the information from the detector is pushed to the EFF which will be able to do a simplified reconstruction allowing the first trigger stage to use information such as impact parameter and track χ^2.

However, such readout wouldn't be possible with original TELL1 boards or the readout ASICs that do not operate at a 40 MHz readout rate, such as the Beetle. That is the reason for changing many of LHCb readouts in the Upgrade. In fact, the detectors that

[3]Pile-Up is defined in LHCb as the mean number of visible pp interactions per bunch crossing

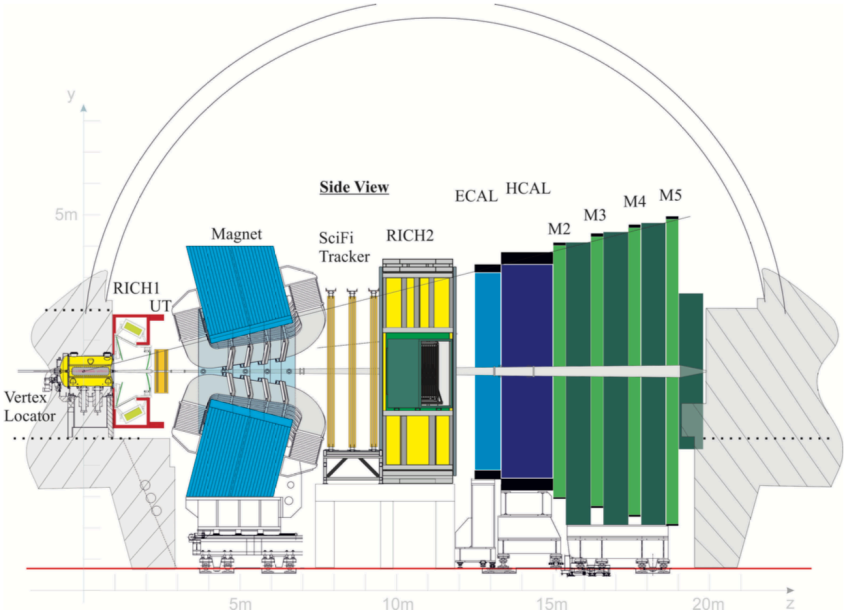

Figure 2.21: View of the LHCb Experiment after the Upgrade [22].

are already used as input for the L0 trigger (readout every 25 ns) will not have major interventions (Figure 2.21). To improve the pattern recognition in the increased pile-up environment, the newly installed detectors will also have a higher granularity (number of channels per area), especially in the regions closest to the beam-pipe.

An overview of the new detector designs for the LHCb Upgrade follows, excluding the VELO Upgrade that will be throughly described in Chapter 6.

2.4.1 Upstream Tracker (UT)

The UT will be placed downstream of RICH1, in the location where now the TT is located. It is responsible for identifying decays that happen outside of the VELO such as $K_s \rightarrow \pi^+\pi^-$ and considerably improves the LHCb's momentum resolution.

The UT will be composed of 4 different silicon sensor types (Figure 2.22), including one that has a beam pipe cut out, to maximise acceptance at very low angles (close to the beam pipe).

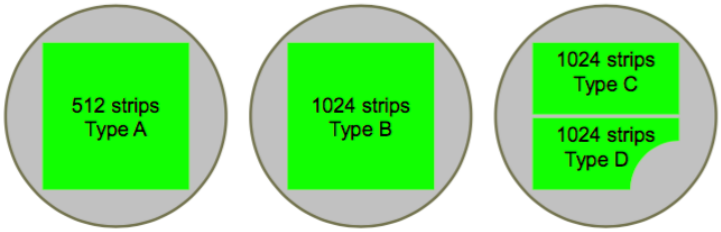

Figure 2.22: The four different types of sensors used for the UT tracker. Type A sensors are p-on-n, all the other sensors are n-on-p. [23].

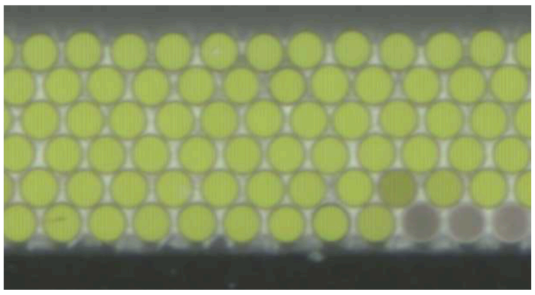

Figure 2.23: A Fibre Mat end, showing the 6 layers of fibres stacked and glued [23].

2.4.2 SciFi Tracker

The SciFi Tracker is the chosen replacement for the tracking stations T1, T2 and T3 on the current LHCb detector. The SciFi will have 3 stations, each composed of 4 detection planes organised in a x-u-v-x orientation where u and v are oriented $\pm 5°$ with respect to the vertical x axis (Figure 2.24). The measuring planes are divided in 12 modules, a module being a collection of 8 fibre mats each containing 6 stacked layers of 250 µm scintillating fibre bonded to each other using epoxy (Fig. 2.23). In total 11 000 km of scintillating fibres will be used in the SciFi.

The scintillation light generated inside each fibre is detected by Silicon Photomultipliers (SiPMs) that are located either at top or bottom of each fibre mat, depending on the mat location. Each mat has 4 SiPM for light detection, each with 128 individual readout channels. The SiPMs are kept in a cold box, at $-40°$C, to reduce the dark count rate. Signals coming from the SiPMs are readout directly by the PACIFIC ASIC [24].

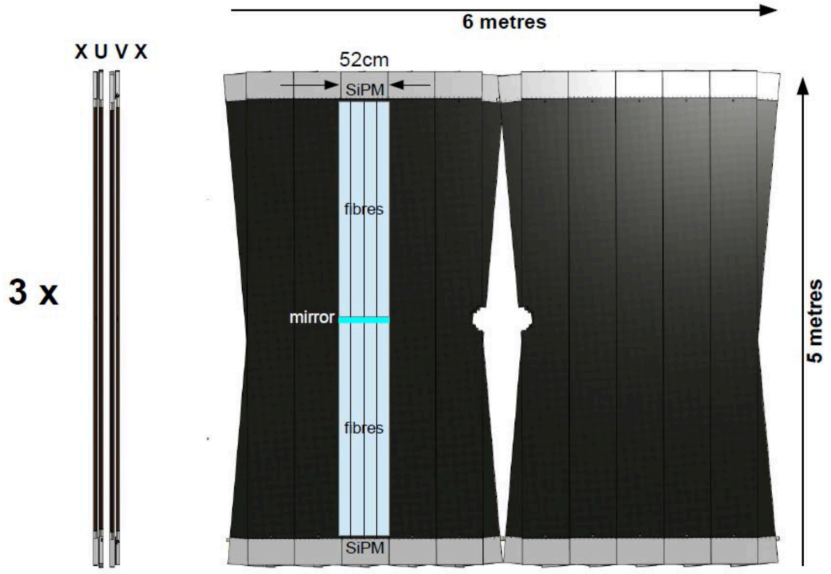

Figure 2.24: View of one SciFi tracking station in the Upgrade. [23]. Each one of the stations is composed of 4 planes following the x-u-v-x angles mentioned previously. Each measuring plane is composed of 12 modules, 6 being readout by SiPMs at the top and 6 at the bottom. Each module is composed of several layers of fibres closely stacked together.

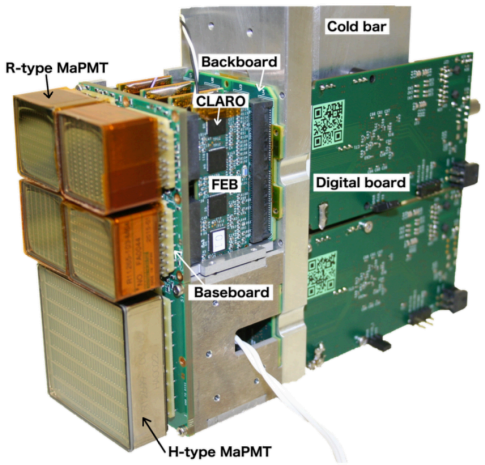

Figure 2.25: Example of two RICH Upgrade cells. [26].

2.4.3 RICH

The most important change in both RICH1 and RICH2 designs is the substitution of the current HPDs, for commercial multianode photomultipliers (MaPMTs). RICH1 will also have a modified optical design in order to cope with the large hit occupancy in the central detector region. The change will move the focal length of the spherical mirror, increasing it by 40%. The PMTs position will also be moved accordingly.

Two different models of MaPMTs, produced by Hamamatsu[4], will be used: the "R-type cell" is a 64 channel (8x8 pixel) MaPMT, with a surface area of 25×25 mm and the "H-type cell", with the same number of channels but an area of 50×50 mm. In both cases each channel is connected to the CLARO ASIC, responsible for pulse shaping and signal-to-threshold discrimination, set on a channel to channel basis. The H-type cells are going to be utilised in RICH2 low occupancy regions as a way of decreasing complexity and cost [25]. Figure 2.25 shows two different types of a RICH cells, together with a cold bar that brings the cooling to the readout ASICs.

[4]http://www.hamamatsu.com/us/en/index.html

2.4.4 Calorimeter and Muon Systems

The LHCb Calorimeters are expected to be able to operate at the increased instantaneous luminosity without any modifications to the calorimeter cells. The PMTs used to readout the scintillation light will have their gain reduced in order to maintain the anode current and a longer operational lifetime. This gain change will be compensated by the new front-end electronics.

Similar to the Calorimeter system, the operation of the Muon System will not require changes on the detector elements. In fact the most striking difference is the removal of the M1 station from LHCb. Due to increased occupancy in the upgrade, the occupancy in M! would just be too high, rendering it of little use to track reconstruction. Additionally, there will extra shielding added HCAL and M2, increasing the protection in the muon station M2 from remnants of HCAL showers that were not fully contained. Extra shielding will also be added after M5, protecting that station from scattering that happens in accelerator parts behind LHCb.

2.4.5 Trigger and DAQ

As previously mentioned, LHCb will have a trigger completely implemented in software. This means coping with at 40MHz bunch crossing rate, with an average Pile-up of 7.6 [27]. All detector front-end electronics will be connected to custom data acquisition boards, MiniDAQ, designed using Aria10[5] FPGAs. These DAQ boards will be responsible for receiving data from the front-end readout and packaging it in the GBT protocol, and sending it via optical fibre to the event building farm. Different software will be loaded in the MiniDAQ, allowing it for configuration, slow-control and timing to be sent to the detector electronics (SOL40), or the data readout (TELL40).

The data from the TELL40 comes in the form of multi-event packets (MEPs) containing several different hits from a single MiniDAQ board. This information is sent to the event builder PCs (Figure 2.26). These PCs unpack the incoming MEPs from the experiment and pair all the hits that came from the same bunch crossing, forming one event. This information is used to perform clustering and performing basic tracking that will be used for a Low Level Trigger (LLT).

[5]https://www.altera.com/products/fpga/arria-series/arria-10/support.html

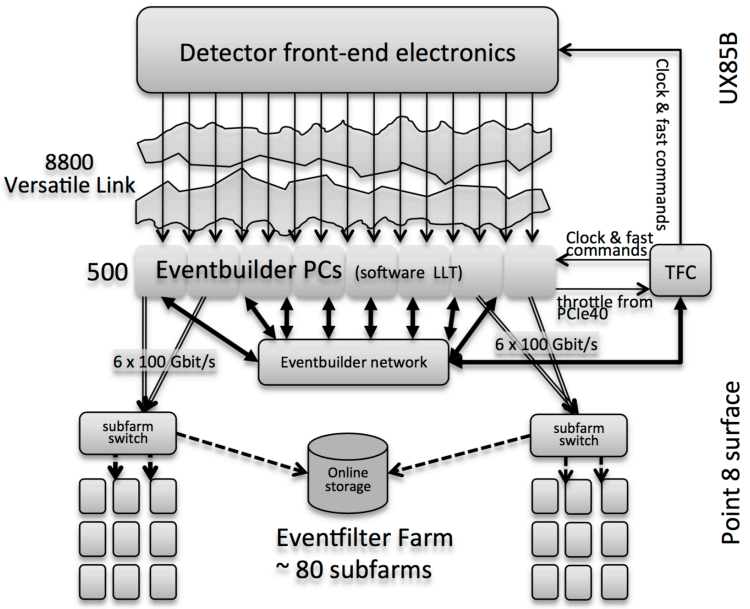

Figure 2.26: Scheme of the DAQ for the LHCb Upgrade [27].

It is important to note that the step of correctly unpacking, sorting, clustering and tracking online at an average rate of 30 MHz[6] is a big computational challenge. Considering the estimated average event size of 100 kB, the aggregated expected bandwidth is 32 Tbit/s arriving at the 500 event builder PCs.

From the LLT the events that pass the trigger will be forwarded to the Event Filter Farm, which will apply a trigger procedure mirroring the Calibration- HLT2 routine used during the Run II LHCb trigger.

[6]Maximum visible bunch crossing rate at LHCb in upgrade conditions.

3 The Standard Model

In this Chapter we will briefly discuss the theoretical background of the Standard Model (SM) of particle physics, and the motivation behind the physics analysis described in Chapter 4. This chapter will stay clear from a historical review into the development of the SM, but expose the groundworks of what is contained in the model and what are the challenges with respect to cosmological observables.

3.1 Introduction to Standard Model

The SM is formed by the conjunction of the Glashow-Salam-Weinberg Model of Electroweak interactions with the quantum theory for strong interactions. It deals with the particles observed when physicists probe the nature of matter at very high energies when compared to the temperature of the present day universe. But it also is capable of producing incredibly precise predictions for fundamental quantities in nature such as the measurement of the electron′s anomalous magnetic dipole moment, g_e [28].

This model is built to represent the particle interactions observed in nature. One can obtain predictions for physical phenomena by calculating the probability of a given initial state to final state transition. As physicists, we are mostly interested in calculating the probability of a scattering process in which initial states interact somehow and output final states (Fig. 3.1).

Quantum Field Theory is a tool that allows us to calculate, given an interaction, what is the probability of an initial state $|i, i'\rangle$ to scatter into a final state $\langle k, k'|$. This calculations often are done through the expansion of a path integral into a power series. As it turns out, each term in this power series can be visualised as a particular interaction process. These terms are drawn as Feynman diagrams (Fig. 3.2). The diagrams help construct the ampli-

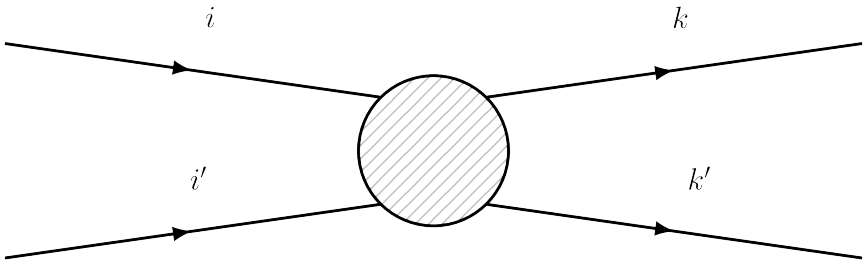

Figure 3.1: Two initial free particle states, i and i', approach each other and interact in the shaded region from which two other states k and k' emerge.

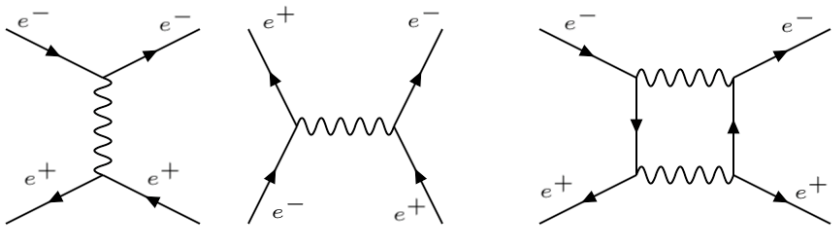

Figure 3.2: Example of the Electrodynamic diagrams involved in Bhabha scattering between an electron and a positron. The two diagrams in the left are 'tree level', of the lowest order, while the one on the right is an example of a higher order diagram.

tude calculation, associating terms in the equations for incoming and outgoing fermions and bosons (currents), vertices terms (interactions) and propagators for any internal lines. A higher number of internal vertices in the diagrams represents higher order corrections to the amplitude. It is worth pointing out that Feynman diagrams are not depictions of interactions, but rather a tool to calculate individual amplitudes. The resulting complex amplitudes then have to be summed and squared[1] in order to obtain a physical answer.

3.1.1 Anatomy of the Standard Model

The SM describes the interactions between the fermions fields, through a set of 3 interactions. The strong interaction occurs between quarks and is mediated by gluons. The weak interaction involves any left-handed particles and is mediated by the $W^{\pm}$ and Z^0 bosons. Finally, electromagnetism is mediated by photons and it occurs between any particles that possess electric charge. The last piece of the SM is the Higgs boson, discovered in 2012,

[1] Like in quantum mechanics, effects of interference come from this step.

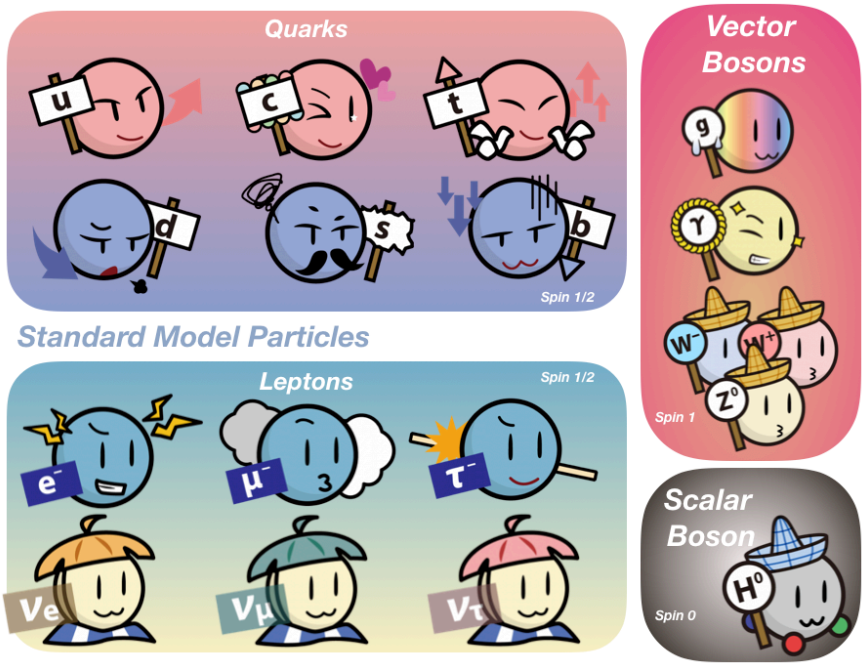

Figure 3.3: Fermions and Bosons that are part of the Standard Model.The four vector bosons are gauge bosons responsible for interactions between fermionic fields. Each vertical line of quarks and fermions composes one generation. The Higgs boson is the only scalar, responsible for generating mass of all other particles. Particle design by [29].

which is responsible for assigning mass to all non-massless particles[2](Fig. 3.3).

Let us take a step back and discuss the central idea behind the construction of this model: Symmetries. The most fundamental symmetry the Standard Model is the Poincaré group. This includes translational, rotational and Lorentz boosts as a symmetry of the system, after all no physical phenomena should be dependent on any of these parameters. It follows from Noether's theorem that for every continuous symmetry there will be a quantity conserved over time. So the symmetries associated with the Poincaré group lead immediately to the conservation of momentum, angular momentum and energy.

The same idea of a symmetry inducing a conserved quantity can be applied to the interactions themselves. A gauge symmetry is the freedom to choose any gauge parameter for your Lagrangian and not change the physics that comes out of it. As an example, we can require that the behaviour of fermions do not change upon the multiplication by a

[2]As far as the SM is concerned, neutrinos are massless and the theoretical framework through which they acquire mass is not well known yet.

local phase [30]:

$$U(x)\psi(x) = \psi'(x) = e^{i\phi(x)}\psi(x), \tag{3.1}$$

where $\psi(x)$ are spinor fields and $\phi(x)$ is an arbitrary function of x. If we try to write a Dirac equation Lagrangian that respects invariance under this transformation an alteration of the simple derivative ∂_μ is necessary. The new derivative, D_μ, is defined by:

$$D_\mu = \partial_\mu - ieA_\mu, \tag{3.2}$$

where A_μ, is a vector field and transforms as $U(x)A_\mu = A_\mu + \frac{1}{e}\partial_\mu\phi(x)$. By requiring only that the free field Lagrangian is invariant under local gauge transformation U(x), we obtain a Lagrangian:

$$\mathcal{L} = \bar{\psi}(i\gamma^\mu\partial_\mu - m)\psi + e\bar{\psi}\gamma^\mu\psi A_\mu, \tag{3.3}$$

which includes the γ^μ, known as the Dirac matrices, that are used to appropriately handle Lorentz boosts in a spinor field. The vector field A_μ, introduced previously, couples with the spinor field ψ exactly like the electromagnetic vector potential. This coupling has a constant e, purposely named after the electrical charge. It is a remarkable result that requiring the physics to not be affected by an arbitrary local phase choice implies the existence of a gauge field that is of the same form as the electromagnetic field. This machinery is thoroughly exploited in the SM and extended models to produce interactions between particles.

Electroweak Interactions

The Electroweak interactions follow the symmetry $SU(2)_L \times U(1)_Y$[3], that is spontaneously broken on the energy scale we live in. This broken symmetry gives rise to the electromagnetic interaction mediated by the photon. Also from the broken symmetry the weak interaction emerges, mediated by the massive $W^\pm$ and Z^0 bosons.

Quantum Electromagnetism (QED) deals with the interaction between charged particles through the exchange of photons, which are spin-1 massless bosons. We have already

[3]Y is the weak hypercharge. Y satisfies $Q = I_3 + \frac{1}{2}Y$, where Q is the electrical charge and I_3 the third component of the weak isospin

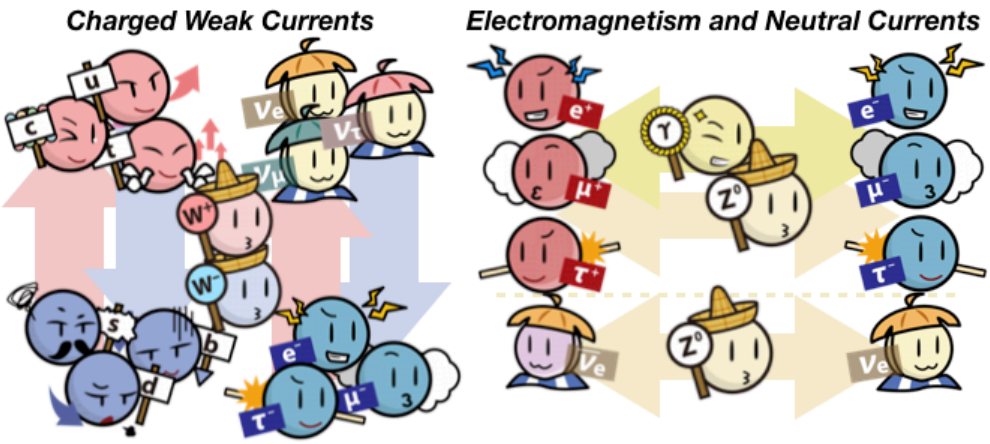

Figure 3.4: The two types of electroweak currents and how the fermions that participate in electroweak interactions are connected by them. The $W^{\pm}$ and Z^0 also connect to one another, but these interactions are not discussed here. Particle designs by [29].

discussed the U(1) gauge symmetry embedded in QED. The electromagnetic current is of the form:

$$e\bar{\psi}\gamma^{\mu}\psi, \tag{3.4}$$

One can see that this current is completely vectorial, it couples the same with electrons of both chiralities (e_L, e_R), for exemple. This requires a singlet copy of each right handed fermion to be added to the SM:

$$e_R, \mu_R, \tau_R, u_R, d_R, c_R, s_R, t_R, b_R \tag{3.5}$$

with the clear exclusion of the neutrinos, as they are neutral and do not couple to photons at all.

For the weak interactions the situation is dramatically different since it maximally breaks parity symmetry, as it does not interact with right handed particles at all. The charged weak currents connect weak isospin left-handed doublets:

$$\begin{pmatrix} \nu_l \\ l \end{pmatrix}_L, \begin{pmatrix} q_u \\ q_d \end{pmatrix}_L, \tag{3.6}$$

where l and ν_l are a lepton and its corresponding neutrino and q_u, q_d are up and down-

charged quarks for all three generations of fermions. So left-handed fermions are assigned $\pm\frac{1}{2}$ values of weak isospin third component (I_3), while for right-handed fermions $I_3 = 0$. One can write the charged weak current between two quarks as:

$$\frac{g}{2\sqrt{2}}\left(\bar{u}_i\gamma^\mu(1-\gamma^5)V_{ij}d_j\right), \tag{3.7}$$

where g is the weak coupling constant, u and d are the quark spinors and V_{ij} is the CKM matrix element (to be discussed later). By adding the term[4] $(1-\gamma^5)$ we guarantee that only the left handed component of the spinors contribute. By imposing the SU(2) symmetry to weak interactions we have an extra neutral boson W^3 that cannot be interpreted as a photon as it only acts on left handed particles. The addition of an extra B field that respects a U(1) weak hypercharge symmetry allows for a basis rotation between the B and W^3 into the Z^0 and the photon fields:

$$\begin{pmatrix} A_\mu \\ Z^0_\mu \end{pmatrix} = \begin{pmatrix} \cos\theta_W & \sin\theta_W \\ -\sin\theta_W & \cos\theta_W \end{pmatrix} \begin{pmatrix} B^\mu \\ W^{3\mu} \end{pmatrix}, \tag{3.8}$$

where θ_W is called the Weinberg angle, defined by $\sin\theta_W = \mathrm{e/g}$. The Z^0 allows for construction of neutral weak currents in the SM, as an example, the electron neutral current:

$$\frac{1}{2}(\bar{u}_e\gamma^\mu(g_V^e - g_A^e\gamma^5)u_e), \tag{3.9}$$

where g_V and g_A are the vector and axial-vector couplings, respectively. The axial-vector coupling is defined by the I_3 component of weak isospin (in the case of an electron g_A^e= -1/2) while the vector coupling is given by $I_3 - 2Qsin^2\theta_W$ (in the case of an electron, $g_V^e = 0.9442$) while the vector component originates in the B field associated with $\mathrm{U}(1)_Y$ symmetry.

To build gauge invariance in the Electroweak sector, there cannot be any mass terms to the fermions or gauge bosons. However, it is a fact that the $W^\pm$ and Z^0 bosons and all charged fermions are massive. The solution for this problem is to dynamically generate the mass terms by the way of interaction with an additional scalar field. The Higgs field is a scalar field used to spontaneously break the $\mathrm{SU}(2)_L\times\mathrm{U}(1)_Y$ electroweak symmetry, which directly generates mass for bosons and allows for Yukawa interactions to generate mass

[4] $(1\pm\gamma^5)$ is a matrix that is used to extract the right and left handed chiral components of a spinor, respectively.

terms for the fermions.

Strong Interactions

Quantum Chromodynamics (QCD) is what describes how protons and neutrons can form bound states, how quarks interact with each other. It governs the dynamics at very hot/dense states of matter such as the very early universe. QCD gains its name from the unique charge associated with this interaction, dubbed "colour". In QCD there are three different colours (R,G,B)[5], originally postulated as a way of making anti-symmetric wave-functions of mesons composed of the same flavour [30]. In the SM only quarks and gluons possess colour, so no other elementary particles interact through the strong force.

The defining feature of QCD is that it is a non-abelian gauge field with an $SU(3)_C$ symmetry, meaning that there are in fact 8 gauge bosons(gluons) that take part in the interaction, being colour charged as well. This feature causes the coupling constant α_s to diverge at low momentum transfers and tend to zero as the momentum transfers increase. The result of this behaviour is two fold: quark-gluon states are always confined in colourless states of colour-anticolour or R+G+B, and that perturbative methods are not suited to make predictions at the lower energy scales ($\approx 10^2$ MeV). The colourless states are called hadrons in general, or mesons/baryons depending on wether they are composed of two or three valence[6] quarks.

Considerable effort goes into dealing with QCD calculations in order to obtain good Monte-Carlo simulations for the behaviour of parton-parton collisions at the LHC. The protons in the collider have a complex structure, and at the energies involved, the gluons play a very important role. Most collisions will produce highly inelastic scatters between two partons, while the rest of each proton will most likely have a small momentum transfer interaction with the other proton debris.

The main interaction, or hard process (HP in Fig. 3.5) is a high Q^2 scatter, where Q^2 is the momentum squared transfer between two objects. This process happens on a time scale much shorter than the times involved on the gluon exchanges inside the proton. As a result the hard-scattered parton is kicked out before the momentum transfer can be distributed amongst other partons, breaking the proton structure. This process leaves soft

[5] And its respective anti-colours $\bar{R}, \bar{G}, \bar{B}$.

[6] Valence here stands for quarks that continue to exist for a long time within the hadron as opposed to quarks coming from excitations of the QCD vacuum.

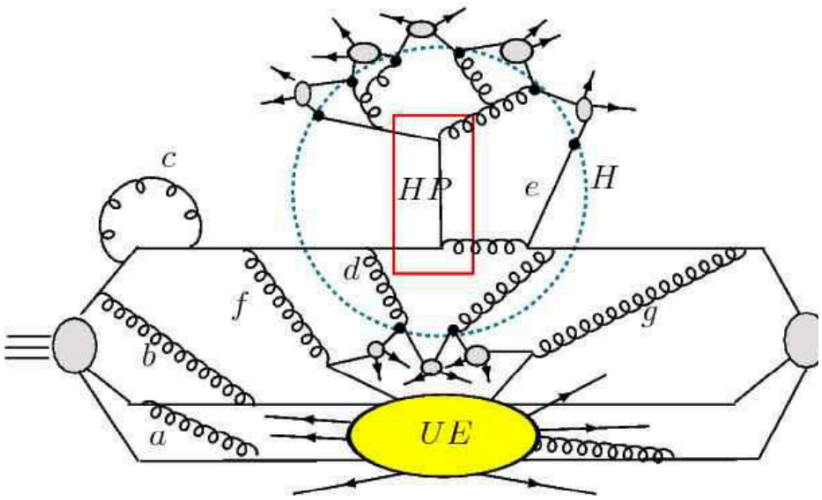

Figure 3.5: Scheme of proton-proton interaction at the LHC. Most collisions only have one pair of partons interacting with a high centre-of-mass energy, the hard process (HP). Simultaneously the other constituents of the original protons will go through soft interactions, generating a distribution of partonic showers, the underlying event (UE), adding complexity to the overall collision [31].

gluons in the proton disconnected, which adds extra products to the interaction. The high Q^2 partons start to irradiate through QCD and Electroweak processes. This irradiation will continue until the energy scale of partons allow for hadronisation (H circle in Fig. 3.5) to take place, when all partons generated are combined in colourless singlets.

The cross-section of a process from a proton-proton collision as a function of a hadronical observable X can be written as [31]:

$$\frac{d\sigma}{dX} = \sum_{j,k} \int_{\hat{X}} f_j(x_1, Q_i) f_k(x_2, Q_i) \frac{d\hat{\sigma}_{jk}(Q_i, Q_f)}{d\hat{X}} F(\hat{X} \to X; Q_i, Q_f), \tag{3.10}$$

where j and k are all the parton types on both protons, $f_j(x_1, Q_i)$ is the parton distribution function (PDF) that contains number density of a parton with momentum fraction x probed with a momentum Q. The term $\frac{d\hat{\sigma}_{jk}(Q_i,Q_f)}{d\hat{X}}$ is the differential cross-section of the $\hat{X}$ partoninc kinematical variable, F is the probability that given a parton state $\hat{X}$ leads to a hadron observable X and finally, Q_i and Q_f define scales of hard perturbative processes dominate over initial and final state evolutions.

The simulation of collisions in LHCb is done using a tuned version [32] of PYTHIA [33], that handles the simulation of the initial partonic collision starting from the PDF of both protons. It evolves the scattering process while keeping track of the correlations between quark and gluon colours, up to the hadronisation scale in which the final state quarks are bundled in hadrons. For LHCb, after the hadronisation step the generated particles are handed over to another software called EVTGEN that handles the hadronic decays [34].

3.1.2 Flavour and the CKM Matrix

Flavour is the name given to the fermionic numbers describing their electroweak family, such as strangeness for strange quarks. One of the most fundamental processes in the SM is the decay of particles. Every fermion in the SM will ultimately decay into a combination of the first generation fermions, and these decays are governed primarily by the weak interactions. This is different from production processes, which are often produced through QCD interactions in the LHC, for example.

The mechanism through which we can have transitions between generations through the weak force was first developed by Cabibbo to explain strange particles and their decays. This phenomenon could be implemented by introducing a basis rotation from the mass states to the weak states:

$$|d'\rangle = \cos\theta_c|d\rangle + \sin\theta_c|s\rangle, \tag{3.11}$$

where θ_c is the Cabibbo angle, which quantifies how much the weak eigenstate d' is mixed in the mass eigenstates d and s.

In the SM, we deal with the different mass and flavour eigenstates of all quarks by using a mixing matrix, the Cabibbo-Kobayashi-Maskawa (CKM) matrix. This matrix is used directly into the basic vertex of charged weak currents as the V_{xy} term:

$$W^{\pm} = i\frac{g_2}{2\sqrt{2}}\gamma_\mu(1-\gamma_5)V_{xy}^{(*)}, \tag{3.12}$$

This term is what allows transitions to different generations through charged weak currents.

The matrix transformation from the mass eigenstates to the weak eigenstates is written as:

$$\begin{bmatrix} d' \\ s' \\ b' \end{bmatrix} = \begin{bmatrix} V_{ud} & V_{us} & V_{ub} \\ V_{cd} & V_{cs} & V_{cb} \\ V_{td} & V_{ts} & V_{tb} \end{bmatrix} \begin{bmatrix} d \\ s \\ b \end{bmatrix}, \tag{3.13}$$

Requiring that the weak currents are conserved amounts to requiring that the CKM matrix is unitary: $V_{CKM}^{\dagger} V_{CKM} = 1$. As a result, the matrix has only 3 free parameters and one complex phase. This complex phase is the mechanism for producing CP-violation effects in the SM. Several groups work on combining results from different experimental probes in order to find the best fit for the V_{ij} elements of the matrix. At this point the magnitudes of the matrix elements are known to good precision [35]:

$$V_{CKM} = \begin{bmatrix} 0.97446 \pm 0.00010 & 0.22452 \pm 0.00044 & 0.00365 \pm 0.00012 \\ 0.22438 \pm 0.00044 & 0.97359^{+0.00010}_{-0.00011} & 0.04214 \pm 0.00076 \\ 0.00896^{+0.00024}_{-0.00023} & 0.04133 \pm 0.00074 & 0.999105 \pm 0.000032 \end{bmatrix}, \tag{3.14}$$

as one can see, the matrix is clearly non-diagonal, meaning that we do observe mixing between all quark families. Although non-diagonal, the mixing is deeply hierarchical, and transitions from the first to the third generations are very suppressed. In fact one can identify the reason for the long lifetime of b quarks just by observing the order of magnitude of the V_{ub} and V_{cb} elements, which are absolutely tiny when compared to transition elements from the second to the first generation.

3.1.3 Standard Model Shortcomings

For all of its success, the SM as far as we know, fails to explain several features of the observed universe. Its most glaring omissions are: the lack of an explanation for the matter-antimatter imbalance in the universe, the lack of a good candidate to account for the cold dark matter density observed and no good source for the cosmological constant or dark energy.

A matter-antimatter imbalance can be produced by the CP violation mechanism present

in the SM. However, we know from CMB[7] measurements that the observed number asymmetry in the universe is of the order of:

$$\frac{n_B}{n_\gamma} \approx 10^{-9}, \tag{3.15}$$

here n_B and n_γ are the baryon and photon number density, respectively. An estimate of how much imbalance is produced in the SM with the current parameters is obtained by dimensional analysis of the Jarlskog invariant[8] at the Electroweak phase transition temperature yields an estimate of 10^{-20} for the SM asymmetry, clearly many orders of magnitude away from the observed in cosmology [36].

The cosmological standard model for a big-bang origin of the universe is called ΛCDM. The naming comes from the two terms added to Einstein field equations in order to fit the observations of our universe. Λ stands for the cosmological constant, a volumetric energy density associated with the vacuum, also known as dark energy. The CDM part stands for Cold Dark Matter, referring to the needed extra matter to match the observed universe evolution.

Evidence for the presence of some kind of dark matter is abundant. We know of its existence not only as a feature from the CMB spectrum, but also from gravitational lensing and galactic formation [37]. The best fit for the CMB spectrum has CDM accounting for the observed ≈26% energy density of Universe [38], with regular matter having ≈5% of the total energy density. This CDM has to be neutral, as we do not see it in the electromagnetic spectrum, and composed of massive particles so they allow for normal matter to cluster in its gravity and form the large scale structures we observe today.

Even though we have this large abundance of dark matter in the universe, the SM has no particle that would fit as a good candidate for dark matter, the closest match being the neutrino. Unfortunately neutrinos are too light and relativistic during the early phases of the universe, yielding the wrong structures during structure formation. Limits on the lower band of dark matter candidates are around $m_{DM} > 2\,\text{keV}$ [39].

The presence of Dark Energy is established by computing the Einstein Field equations for the observed universe supposing isotropy and homogeneity. The free parameter Λ, the cosmological constant, is a free parameter in General Relativity and there is no reason why

[7] Cosmic Microwave Background
[8] A measure of the total CP violation present in the CKM matrix

it should assume any one value. The issue with the presence of dark energy is the size of the contribution. If we use the Standard Model quantum vacuum as a source of energy density, the answer is many many times the observed value of the cosmological constant. The current understanding is that both General Relativity and the SM leave some aspect of physics behind, and thus can't properly predict the dark energy density [40].

As we finish this section on the Standard Model, it is important to reiterate how incredibly successful the SM is. Not only the SM was capable of reproducing experimental measurements with great accuracy, it also had great predictive power, foreseeing the discovery of the third generation of fermions, the W and Z bosons, and the Higgs boson. Nonetheless there is a disparity between experimental observations of our universe and predictions of the SM. This is the main motivation for looking at new effects not predicted within the SM.

3.2 Lepton Universality

Due to the nature of neutral currents in the Standard Model, Flavour Changing Neutral Currents (FCNC) processes are forbidden at tree level. This means that transitions such a $b \to d$,$b \to s$, $b \to sl^+l^-$, $b \to s\gamma$ only happen due to contribution from loop diagrams. As an example of the size of FCNC contribution in the SM, the decay of the B_s^0 meson into two μ is predicted by the SM to have a branching ratio of $(3.23 \pm 0.27) \times 10^{-9}$ [41].

The loop contributions open space for Beyond Standard Model (BSM) physics components to affect the observed decays, even if we are at an energy scale much lower than the one necessary for direct production of new BSM particles. There is interest in measuring such rare processes because any deviation from the standard model opens a window into what the physics at higher energy scales can be.

LHCb uses several decays of B mesons in order to constrain the possible BSM contributions to these decays. This is done by measuring predicted decay rates and angular distributions and comparing results to the expected from the SM. We will be mostly interested in $b \to sl^+l^-$ transitions, for which the lowest possible order diagrams can be found in Figure 3.6. From LEP measurements we know that both Z^0 and $W^\pm$ bosons have the same branching ratios for all three charged leptons, which is also the assumption in the SM [42].

There are significant challenges in measuring and doing SM predictions for cross-

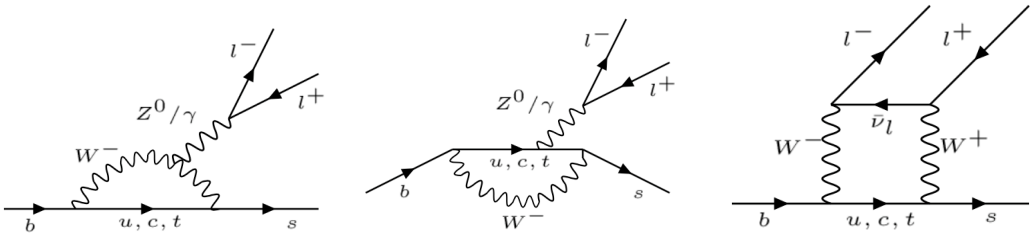

Figure 3.6: Lowest possible order diagrams for the FCNC $b \to sl^+l^-$ transition in the Standard Model.

sections of such decays with the precision necessary to test the SM. Testing the Lepton Universality (LU) of a particular decay is a way to compare observables with SM predictions that are both theoretically and experimentally 'clean' [43]. The measurement of LU is done through the measurement of a ratio of the same decay through two different lepton flavours. In this ratio the effects of the particular hadronic part of the decay are factored out. If a BSM component couples differently according to the lepton generation, it would be clearly seen in the ratio measurement. Specifically, the LU test is the ratio of branching fractions integrated over the momentum transfer of the lepton pair (q^2):

$$R_H = \frac{\int_{q^2_{min}}^{q^2_{max}} \mathcal{B}(B \to H\mu^+\mu^-)dq^2}{\int_{q^2_{min}}^{q^2_{max}} \mathcal{B}(B \to He^+e^-)dq^2}, \tag{3.16}$$

where H is the hadronic part of the B-hadron decay, q^2_{min} and q^2_{max} are the limits of the di-lepton spectrum used. This measurement is done using muons and electrons as they are much easier to reconstruct in the detectors and also much closer in mass. The ratio of any R_H measurement involving $b \to sl^+l^-$ is expected to be $1 \pm \mathcal{O}(10^{-3})$, where the uncertainty comes from the difference in available phase space between electrons and muons [43].

LHCb, BaBar and Belle have performed measurements of R_K and R_{K^*}, the most recent results displayed in Figure 3.7. In LHCb the most appropriate q^2 intervals for this measurement are $1.0 < q^2 < 6.0\,\mathrm{GeV}^2/\mathrm{c}^4$ for R_K and $0.045 < q^2 < 1.1\,\mathrm{GeV}^2/\mathrm{c}^4$, $1.1 < q^2 < 6.0\,\mathrm{GeV}^2/\mathrm{c}^4$ for R_{K^*}. The LHCb results show a depressed number of muon decays when compared to the electrons. Although the deviation from the SM is not enough to claim an absolute mismatch between experiment and data, the pull on both

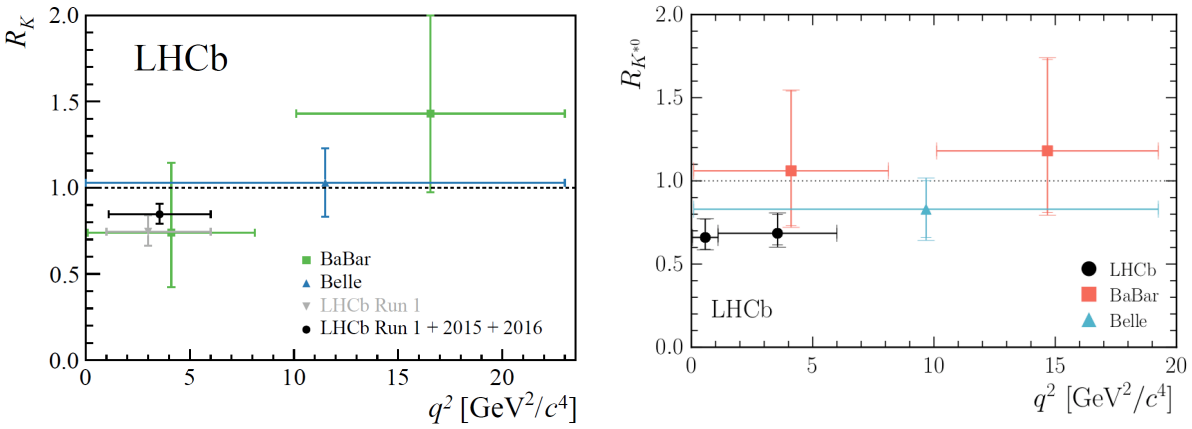

Figure 3.7: Compiled measurements of R_K and R_{K*} for LHCb, BaBar and Belle [44] [45].

channels points towards a consistent picture of some BSM component.

Presently, there are other flavour anomalies or apparent deviations from the . As an example, R(D) and R(D*) ratios which are measured ratios between semileptonic decays of D and D* mesons into μ or τ leptons. The ratio expected from SM predictions is off the experimental measurements by approximately 3.8σ (Figure 3.8 shows a comparison between SM and heavy flavour experiments) [42].

3.2.1 Effective Field Theory Interpretation

The LHCb experiment uses the decays of particles as a laboratory for probing physics processes. The energy scale (μ) involved in these decays are much lower than the scale of electroweak bosons, $\mu \ll M_W$. On this scale one can approximate a process by using an effective weak Hamiltonian, with interactions between currents governed by operators, much the same way Fermi's original weak interaction theory. This way we can integrate out the degrees of freedom of the electroweak bosons in the standard model, and any additional interaction terms of BSM models in to a series of coefficients that effectively reproduce the couplings of the higher energy scale module on a lower scale:

$$\mathcal{H}_{eff} = \frac{G_F}{\sqrt{2}} \frac{e}{16\pi^2} V_{tb} V_{ts}^* \left[\sum_i (C_i(\mu) O_i + C_i' O_i') + h.c. \right], \tag{3.17}$$

where the coefficients C_i are called Wilson coefficients, and contain all the information

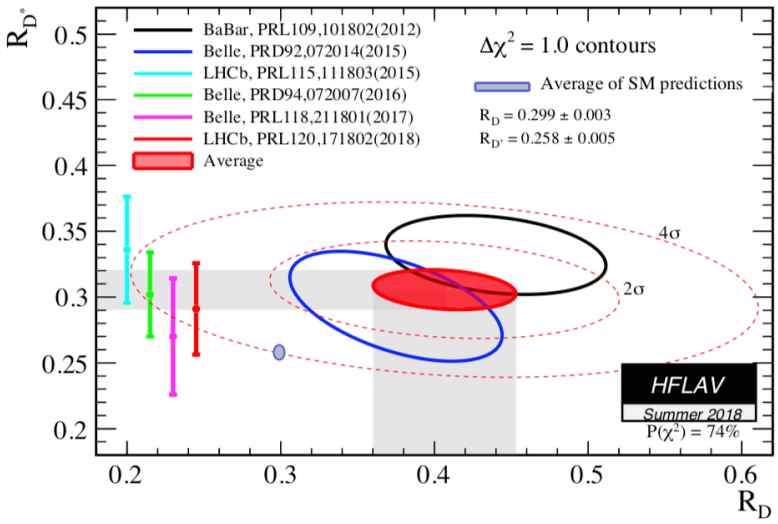

Figure 3.8: Compiled measurements of R_D and R_{D^*} for LHCb, BaBar and Belle [42].

about higher scale effects, O_i are the operators governing interaction between currents. We included the CKM elements for a $b \to s$ transition as this is transition discussed previously, but could easily be changed to a $b \to d$ process.

Of all the coefficients that can be considered in the effective Hamiltonian the electroweak FCNC transitions, such as $b \to sll$ (Figure 3.6), are mostly mediated by three operators [46]:

$$\begin{aligned} O_7 &= m_b(\bar{s}\sigma_{\mu\nu}(1+\gamma_5)bF^{\mu\nu}), & O_{7'} &= m_b(\bar{s}\sigma_{\mu\nu}(1-\gamma_5)bF^{\mu\nu}), \\ O_9 &= e(\bar{s}\gamma_\mu(1-\gamma_5)b)(\bar{l}\gamma^\mu l), & O_{9'} &= e(\bar{s}\gamma_\mu(1+\gamma_5)b)(\bar{l}\gamma^\mu l), \\ O_{10} &= e(\bar{s}\gamma_\mu(1-\gamma_5)b)(\bar{l}\gamma^\mu\gamma_5 l), & O_{10'} &= e(\bar{s}\gamma_\mu(1+\gamma_5)b)(\bar{l}\gamma^\mu\gamma_5 l), \end{aligned} \tag{3.18}$$

where m_b is the running bottom quark mass, l stands for e, μ, τ and the operators O and O' correspond to different chiralities on the $b \to s$ currents. In particular O_7 is responsible for modelling electromagnetic interactions such a $b \to s(d)\gamma$. Both O_9 and O_{10} are semileptonic currents (O_{10} has an extra chirality term added to the leptons w.r.t. O_9).

Discussions regarding measurements of angular distributions or lepton universality measurements often use the effective Hamiltonian machinery as a way of comparing high

energy models to effects seen in B-hadron decays. This approach becomes a framework for the combination of several different results in terms of the measurement of the Wilson coefficients, in which each experimental inputs can be probed on whether they form a consistent physics signature.

4 | Rare b-quark Decays

In this Chapter two b-quark decays through flavour changing neutral currents will be discussed: the measurement of Lepton Universality using the decay $\Lambda_b^0 \to pKl^+l^-$ and the feasibility study of observation of the $B^+ \to a^+(\pi^+\pi^-\pi^+)\mu^+\mu^-$ decay in LHCb data.

4.1 R_{pK} Measurement

As discussed in Chapter 3, one can probe differences between lepton flavours in the $b \to sl^+l^-$ transition by measuring the ratio of branching fractions with different leptons. Indication of different ratios between different leptons are in direct opposition to SM predictions, and indicate the presence of new physics at a higher energy scale. Anomalies observed by LHCb do not possess significance for claiming a new physics effect (they are around 2.6σ), but observing the same effect in different independent decays will improve the combined sensitivity.

This type of measurement has been performed in B meson decays associated with $K^{\pm}$ and $K^*(892)$ hadrons. In the case of the analysis presented here, the hadronic system chosen to perform this measurement is the Λ_b^0 baryon. If undergoing a $b \to sl^+l^-$ transition the most likely final state contains hadronic particles p and K and so the ratio between lepton flavours for this decay is dubbed R_{pK}:

$$R_{pK} = \frac{\mathcal{B}(\Lambda_b \to pK\ \mu^+\mu^-)}{\mathcal{B}(\Lambda_b \to pK\ e^+e^-)}. \tag{4.1}$$

However, measuring the branching ratios of both the μ and e modes involves measuring the absolute efficiency of reconstruction of these tracks, which is very challenging. Alternatively, one can measure R_{pK} as a double ratio using the $\Lambda_b \to pK\ J/\psi(l^+l^-)$

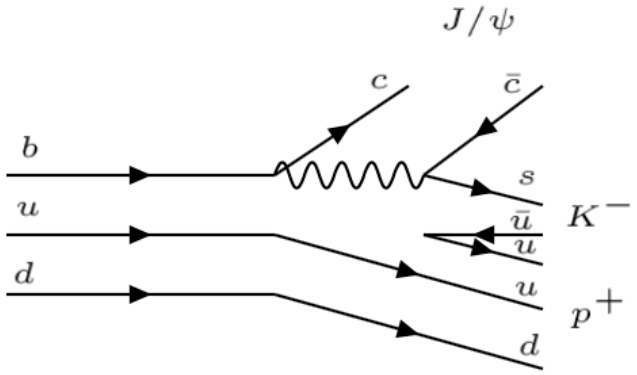

Figure 4.1: Diagram of the Λ_b^0 decay in the pKJ/ψ mode.

mode as a normalisation channels on each of the lepton flavours:

$$\text{Ratio}_\mu = \frac{\mathcal{B}(\Lambda_b \to pK\ \mu^+\mu^-)}{\mathcal{B}(\Lambda_b \to pK\ J/\psi(\mu^+\mu^-))}, \tag{4.2}$$

$$\text{Ratio}_e = \frac{\mathcal{B}(\Lambda_b \to pK\ e^+e^-)}{\mathcal{B}(\Lambda_b \to pK\ J/\psi(e^+e^-))}. \tag{4.3}$$

By using the double ratio, all efficiencies involved in reconstructing μ and e tracks are factored out. The efficiencies left to consider in this ratio method are reconstruction (including acceptance), trigger and selection efficiencies that can be extracted from simulations. The final R_{pK} measurement is done by taking the ratio:

$$R_{pK}^{-1} = \frac{\text{Ratio}_e}{\text{Ratio}_\mu}. \tag{4.4}$$

This method works because the J/ψ decay ratio between the $\mu^+\mu^-$ and e^+e^- modes is very close to 1[1] [35]. The J/ψ decays are much more common than the non-resonant $b \to sl^+l^-$ transition due to the tree level decay depicted in Figure 4.1. The key difference between the two processes is that the J/ψ channel shows up as a very sharp q^2 resonance[2](Figure 4.2). A selection of the J/ψ mode can be made by only accepting decays with a lepton pair mass close to the nominal J/ψ mass (2900 MeV/c^2<m$_{J/\psi}$ <3200 MeV/c^2).

The electron channels have an additional difficulty as the momentum resolution for

[1] A small sub percent level difference arises from the different available phase space
[2] q^2 stands for the the lepton pair invariant mass squared in this case.

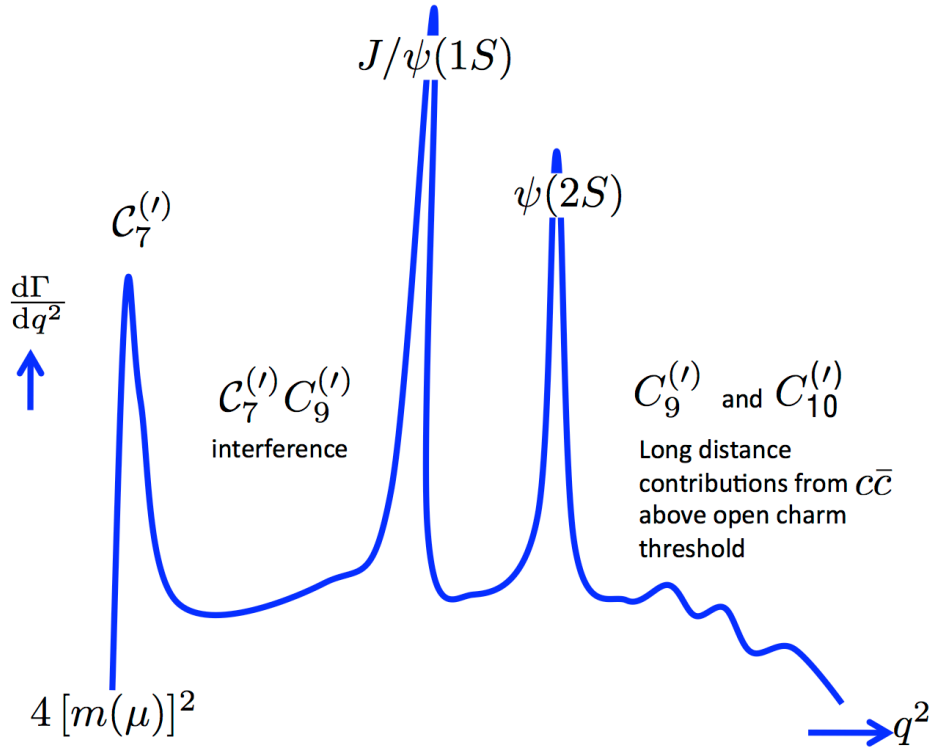

Figure 4.2: A sketch of the production cross-section of the $b \to s\mu^+\mu^-$ as a function of the q^2 of the lepton pair. It starts at the di-muon mass threshold, which equates to $4m_\mu^2$ in the q^2 axis. The rare modes of interest are located in the region before the J/ψ q^2 production region [47].

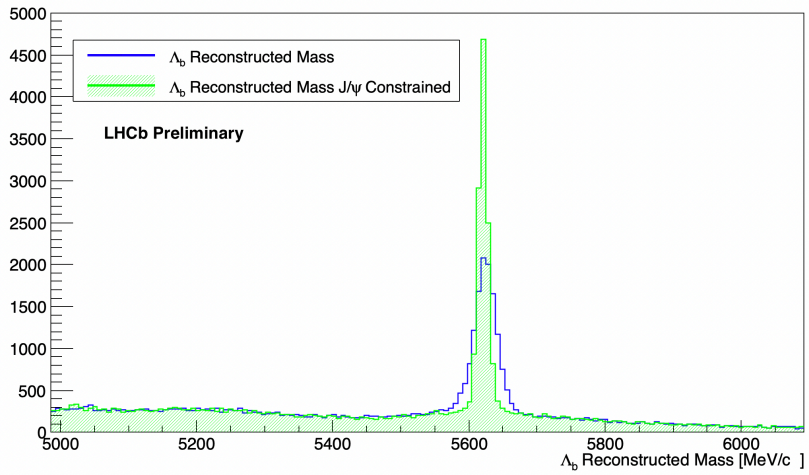

Figure 4.3: Comparison between mass distributions of Λ_b^0 candidates with and without using the J/ψ vertex mass constraint with a subset of Run I data.

electrons tracks suffers from scattering leading to broader mass peaks. This can make the modelling of the mass spectrum more complicated as the mass windows considered have to be larger and partially reconstructed background becomes an important component of the radiative tail. To help reduce this contribution, an implementation of the so-called HOP variable was introduced in the LHCb software. This variable exploits LHCb's excellent vertex reconstruction to recover information about the original electron momentum lost to bremsstrahlung, which helps differentiate it from partially reconstructed background . More details about the variable and the implementation of it can be found in Appendix A, which describes and contextualises the contents of the internal LHCb note [48].

It is important to note the vertex constraints used during reconstruction for the J/ψ decay channel. One can use a kinematical constraint (in this case the J/ψ mass) to fit the four momenta of a particular decay vertex which largely improves the mass resolution [49]. For obvious reasons this constraint will not be applied to the non resonant mode (lower mass than the window mentioned previously), but for the J/ψ mode this vertex fitting can be very useful for a better distinction between signal and background components. Figure 4.3 exemplifies the difference in mass spectra with or without the J/ψ mass constraint. Throughout the next sections the invariant mass displayed will be the constrained variant.

BDT input variables
Λ_b^0 Vertex χ^2
$\log_{10}(\Lambda_b^0$ IP $\chi^2)$
$\log_{10}$(1-Λ_b^0 DIRA)
$\Lambda_b^0\, p_T$
$\log_{10}(\mu$ IP $\chi^2 \times \mu$ IP $\chi^2)$
$\log_{10}(p$ IP $\chi^2 \times K$ IP $\chi^2)$
$\Lambda^*\, p_T$ - ($\mathrm{p}_{p_T} + K_{p_T}$)

Table 4.1: List of input variables for BDT classifier. Vertex χ^2 stands for the quality of reconstruction of the Λ_b vertex, IP is the impact parameter, DIRA stands for the cosine of the angle between momentum and direction of flight and Xp_T is the transverse momentum of particle X.

4.1.1 Candidate Selection

Candidate selection is the process through which the particles reconstructed in LHCb are combined and chosen to match a particular interesting decay. The strategy for selecting candidates is to impose basic requirements on each of the daughter particles, trying to exclude fake tracks and mis-reconstructed events. Then, a BDT[3] multivariate classifier is trained using a Monte-Carlo(MC) $\Lambda_b^0 \to J/\psi(\mu^+\mu^-)pK$ sample as signal and a high mass selection (5820 MeV/c^2< $\mathrm{m}_{\Lambda_b^0}$ <5970 MeV/c^2) of data as background. The so called Signal MC sample is a dataset in which each simulated proton-proton collision is guaranteed to contain at least one signal decay within the LHCb acceptance. The BDT classifier is trained using only the kinematical variables, a list of which can be found in Table 4.1. These variables have been optimised so that they vary smoothly which improves the training performance. This BDT was optimised with minimising the number of variable inputs, as it facilitates the training and testing procedures. Although the final selection will use a BDT with higher number of variables, this selection has good enough performance to be used as a starting point to determine the signal and background PDFs.

In Figure 4.4 one can see an example of the output of the BDT classifier and the efficiency versus rejection power for a test MC sample (different dataset from the one used in training). This BDT main effect is to suppress the combinatorial background and the estimated efficiency using MC sample for the selection is $\epsilon_{BDT} = 89.2\% \pm 0.4\%$,

[3]Boosted Decision Tree

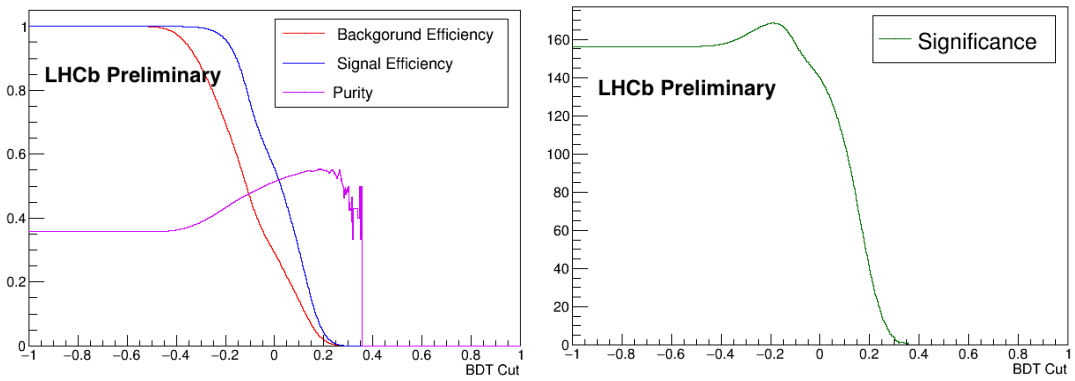

Figure 4.4: BDT Classifier output efficiencies, background rejection and significance ($S/\sqrt{S+B}$). Number of signal is extracted from a MC sample and the background is extracted from a high mass sideband window on the data. Background sample is weighted to the same luminosity. The optimal BDT selection was chosen to be the maximum of the significance distribution.

which is a satisfactory performance for a minimal selection.

After BDT selection, particle identification (PID) selection criteria are applied to the sample. These criteria use variables dubbed `PID ProbNN`, which are generated centrally by LHCb offline reconstruction. These variables use information from the PID detectors, particle's momentum, transverse momentum (p_t) and χ^2/nDoF as well as global information of the event such as number of hits in the preshower and position of the track in the detector ($\eta\,\phi$) to infer the likelihood of a reconstructed track to match a mass hypothesis by means of a neural network. Table 4.2 summarises all the cuts done in the PID variables. There are also additional criteria, as minimum momentum and p_T cuts and acceptance requirements to make sure the tracks traverse the calorimeters in case of the hadrons and the muon stations in the case of the muons.

After selection, the resulting mass spectrum will be composed of signal candidates and other contributions that can be modelled independently. The mass models for each of the components will be discussed in the next section.

4.1.2 PDF Determination

An important analysis task is the correct evaluation of the number of signal events for each channel. In order to correctly estimate this number it is necessary to compose a

	PID Cuts
p	MC12TuneV3_ProbNNp>0.2 MC12TuneV3_ProbNNK<0.8 MC12TuneV3_ProbNNπ<0.7
K	MC12TuneV3_ProbNNp<0.8 MC12TuneV3_ProbNNK>0.2
μ	MC12TuneV3_ProbNNμ>0.1

Table 4.2: List of particle identification selection criteria for the final state particles of the Λ_b^0.

probability density function (PDF) that correctly describes both the signal distribution and the contribution from several different background sources.

The choice of the PDF modelling was done using a set of MC samples generated using the LHCb framework described in Chapter 2. Specific background contributions were simulated by generating MC samples in a similar way, but using known background channels. Each of the individual contributions for the mass distribution needs to be modelled to have a good knowledge of the final yield of signal events. In the next two subsections the steps to decide the PDFs for each contribution will be described.

Λ_b Signal PDF

Using MC truth-matched candidates from the $\Lambda_b^0 \to J/\psi(\mu^+\mu^-)pK$ MC sample that passed the selection described in the precious section one can estimate the signal probability density function (PDF) model for the mass distribution. From the a few tentative PDF options, the four better performing PDF models were considered to be used in the resonant fit. These include a combination of Crystal Ball functions, Voigtian, Gaussians and the Ipatia distribution.

A Crystal Ball function can be used in order to correctly model the radiative tail in the low mass region of the invariant mass distribution of the Λ_b due to final state photon emission. This function is defined as a gaussian peak and a exponential decay:

$$f(x) = \begin{cases} N \cdot \exp(-\frac{(x-x_0)^2}{2\sigma^2}), & \text{for } \frac{x-\bar{x}}{\sigma} > -\alpha \\ N \cdot A \cdot (B - \frac{x-\bar{x}}{\sigma})^{-n}, & \text{for } \frac{x-\bar{x}}{\sigma} \leq -\alpha \end{cases} \tag{4.5}$$

chosen with parameters A and B in terms of α and n such that the function and its deriva-

PDF	χ^2/NDF	NDF	Yield [#Events]
Crystal Ball + Breit Wigner	1.92	7	57782 $\pm$ 661
Crystal Ball + Voigtian	1.98	8	57768 $\pm$ 240
Crystal Ball + Double Gaussian	16.92	9	56603 $\pm$1777
Ipatia $\circledast$ Gaussian	0.86	9	57713 $\pm$ 240

Table 4.3: Goodness of fit comparing the four different PDFs. The Crystal Ball + Double Gaussian can be excluded as possible PDF for extracting signal number. The yield in this case should be compared to the 57715 events present in the sample inside the fit range, matching very well the fit yields.

tive transition continuously from the gaussian peak to the polynomial tail [50]. The Ipatia function is a generalised PDF used to correctly model high statistics mass distributions and is better described in [51]. We use this function convolved with a Gaussian. The Breit-Wigner is a common peak shaped distribution:

$$f(x, x_0, \gamma, N) = N \cdot \left(\frac{\gamma^2}{(x - x_0)^2 + \gamma^2} \right) \tag{4.6}$$

while the Voigtian is a name used to refer to a Breit-Wigner convolved with a Gaussian.

Figure 4.5 contains a comparison between the PDF models discussed fitting a MC Signal sample. The PDF models are compared qualitatively by examining the pull distribution, defined on each bin plotted by:

$$\text{Pull} = \frac{N_{\text{data}} - N_{\text{PDF}}}{\sigma_{\text{data}}}. \tag{4.7}$$

Each component of a particular PDF is constrained to have the same mean as the other components. The PDF model using only a sum of Gaussian curves does not correspond to the distribution found in the data (magenta curve and points). The options using a Voigtian and Breit-Wigner curves perform better but do not show the constant pull distribution seen in the Ipatia fit. This is the reason why Ipatia was chosen to match the Λ_b^0 peak. In Table 4.3 we have the χ^2/NDF for all four fits, that allow us to measure the goodness of each fit and the yield of each fit which should be compared to the number of events in the distribution. The parameter values obtained in this MC fit are to be used later on the data fit.

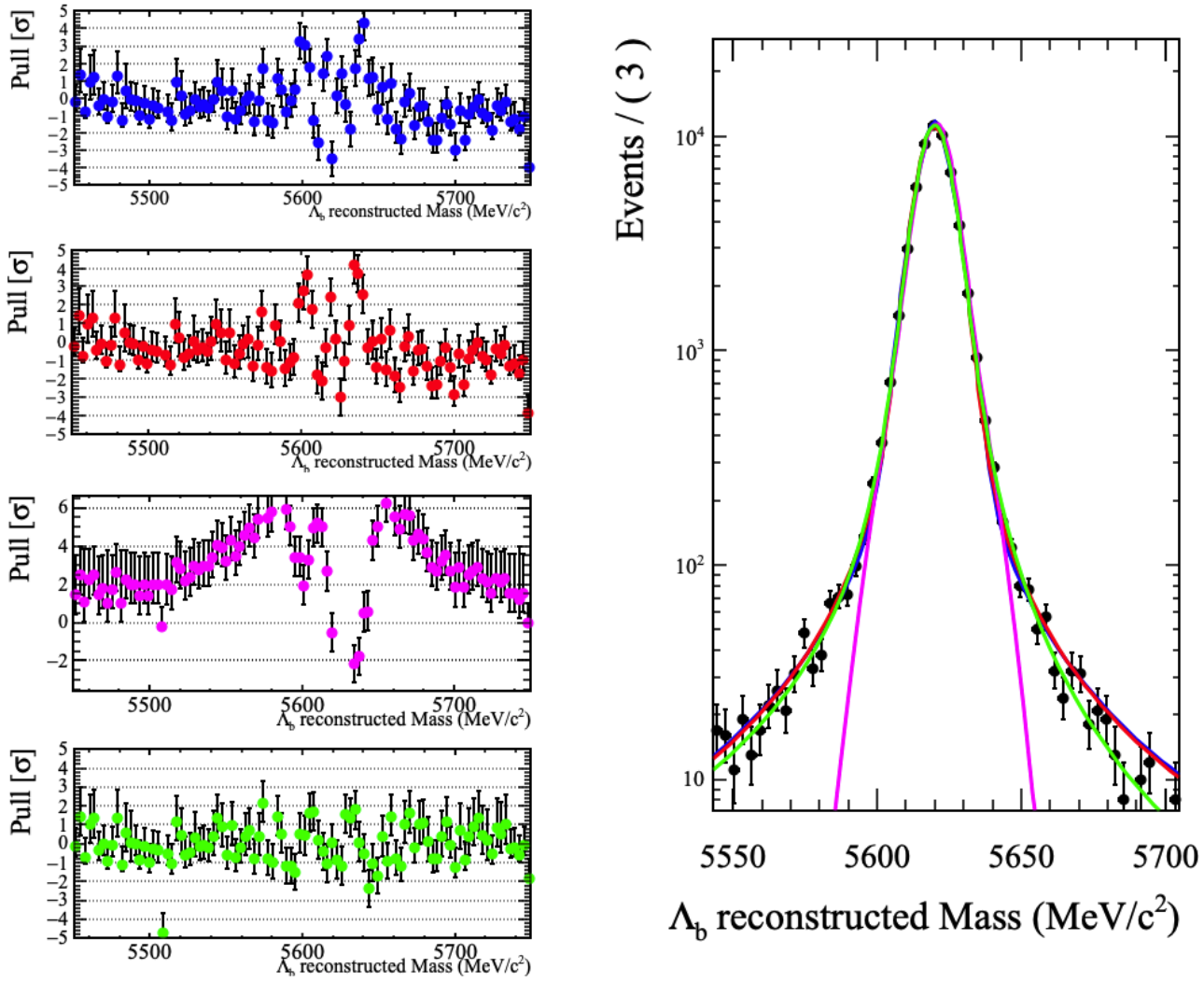

Figure 4.5: Fits with different PDFs. The PDFs are: Crystal Ball + Breit-Wigner (Blue), Crystal Ball + Voigtian(Red), Crystal Ball + Double Gaussian(Pink) and Ipatia convolved with a Gaussian(Green). On the left we have the pull distribution[4] of each fit with respect to the data distribution. It is clear that a gaussian line shape does not match well the distribution, and the Voigtian and Breit-Wigner curves having a large variance at the peak. The Ipatia function provides the best fit overall.

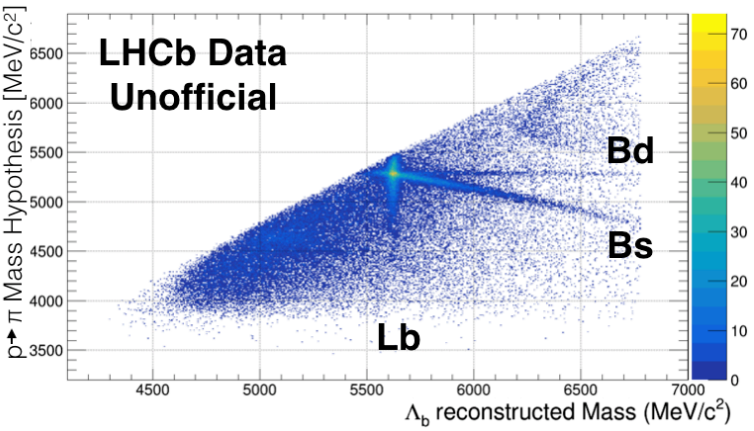

Figure 4.6: Λ_b^0 candidates in a small subset of LHCb 2012 data, plotted as a function of the reconstructed Λ_b^0 mass and the mass of the final state upon substitution of the final state proton for the pion mass hypothesis. There were kinematical and lepton ID selections applied to this sample. It is possible to identify the distinct contributions from B^0 and B_s^0 decays.

B Meson Decays Contributions

According to measurements from LHCb [52], the ratio of production between Λ_b^0 and B^0 mesons, $\frac{f_{\Lambda_b}}{f_d}$, varies as a function of p_{T} between 0.7 and 0.2. This means that B^0 mesons are produced more often than Λ_b^0 baryons, becoming a relevant source of background events due to the their masses being similar. In particular, two decays have a significant contribution to our selected events: $B^0 \to K^*(892)(K\pi)J/\psi$ and $B_s^0 \to \phi(K^+K^-)J/\psi$.

Using kinematical selections and particle identification on the muon tracks one can easily observe the contribution of the B^0 and B_s^0 decays to the reconstructed Λ_b^0 candidates. In Figure 4.6 all the candidates in a subset of LHCb data are shown on two axis: the reconstructed Λ_b^0 mass and the mass of the same candidate, but assuming a π mass instead of a proton mass in the final state. If the candidates were coming only from Λ_b^0 decays, there should be only a peak on the x-axis and a broad distribution along the y-axis. What can be seen is that there is a resonant contribution on along the y-axis, indicating that the π mass hypothesis is the correct one for these decays. For the B_s^0 decays none of the two hypothesis is the correct one and so the peak appears as a diagonal, as the K is in between the π and p.

As the B_s^0 contribution comes mostly through the sharp $\phi(1020)$ resonance it is possi-

ble to apply a veto to it by requiring the reconstructed mass when substituting the proton mass by the K mass is not within a 12 MeV window from the $\phi(1020)$ mass. Still, some candidates do pass the combination of selection and the ϕ mass veto; the mass distribution of these candidates is modelled by using the Keys PDF kernel estimation [53]. This estimator uses data to construct a PDF by summing a sequence of Gaussians for each entry. In Figure 4.7 it is possible to observe the PDF extracted from simulated B_s^0 decays that passed the selection.

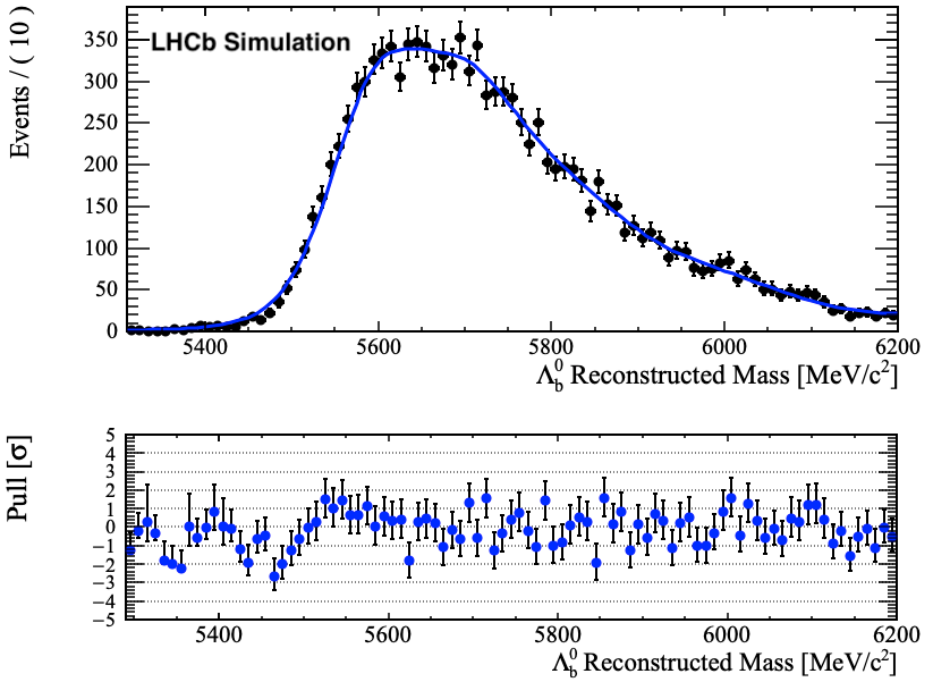

Figure 4.7: Distribution (blue line) obtained by using Keys PDF estimation on a $B_s^0 \to \phi(1020)(KK)J/\psi(\mu\mu)$ Monte-Carlo sample of events reconstructed as if they were Λ_b^0 decays.

The B_0 decay is more challenging as the $K^*(892)$ resonance is not as sharp, meaning that a simple mass veto has a larger impact on the signal efficiency and thus is not used. In the same way it was done for the B_s^0, the distribution for the B_0 decays is obtained by applying the kinematical and PID selection criteria on a MC sample of the $B^0 \to K^*(892)(K\pi)J/\psi$ decay reconstructed as $\Lambda_b^0 \to pKJ/\psi$ and use the kernel estimation on the reconstructed mass distribution. Figure 4.8 shows an example of the PDF obtained using this method.

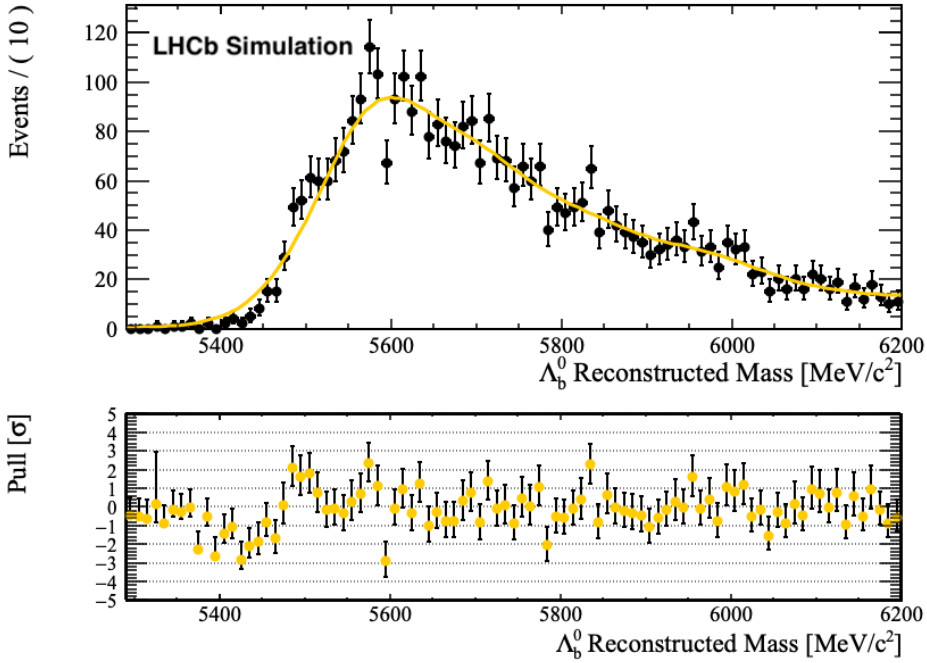

Figure 4.8: Distribution (orange line) obtained by using Keys PDF estimation on a $B^0 \to K^*(892)(K\pi)J/\psi(\mu\mu)$ Monte-Carlo sample of events reconstructed as if they were Λ_b^0 decays.

The last relevant contribution to the muon channel is the mis-ID swap between p-K in the final state. The PID selection removes most of the candidates that have had their hadron IDs swapped, however a small number still should be accounted for. This swapped ID events is modelled by using MC events to obtain a mass distribution used to extract a Keys PDF. This contribution is expected to be very small in the final fit. Figure 4.9 shows the PDF for the $p - K$ swap.

Given that both the contributions of the B^0 and B_s^0 mesons appear very close to each other in the mass range, the yields of the two components are very correlated. To maintain a stable fit, the ratio between the two decays is extracted from the selected data. This is done by applying a veto on a 30 MeV/c^2 window around the nominal Λ_b^0 mass and around the other mass hypothesis (i.e. veto around the B_s mass in the $p \to K$ hypothesis when looking at B^0 and vice-versa). Then, using the appropriate mass hypothesis, one can perform a simple fit using a crystal ball and exponential background model to extract the yields in the B^0 and B_s^0 decay channels. Figure 4.10 contains both of these fits performed in half the 2012 data sample, which is used to obtain the yields of each decay. Using these

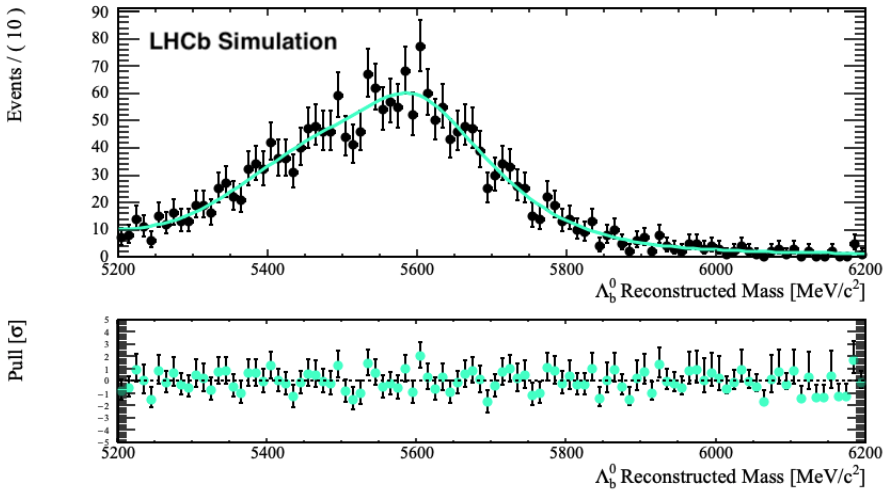

Figure 4.9: Distribution (teal line) obtained by using Keys PDF estimation on the p-K swapped events in a Monte-Carlo sample of events.

yields one can constrain the contributions from B^0 and B_s^0 channels in the final data Λ_b^0 fit.

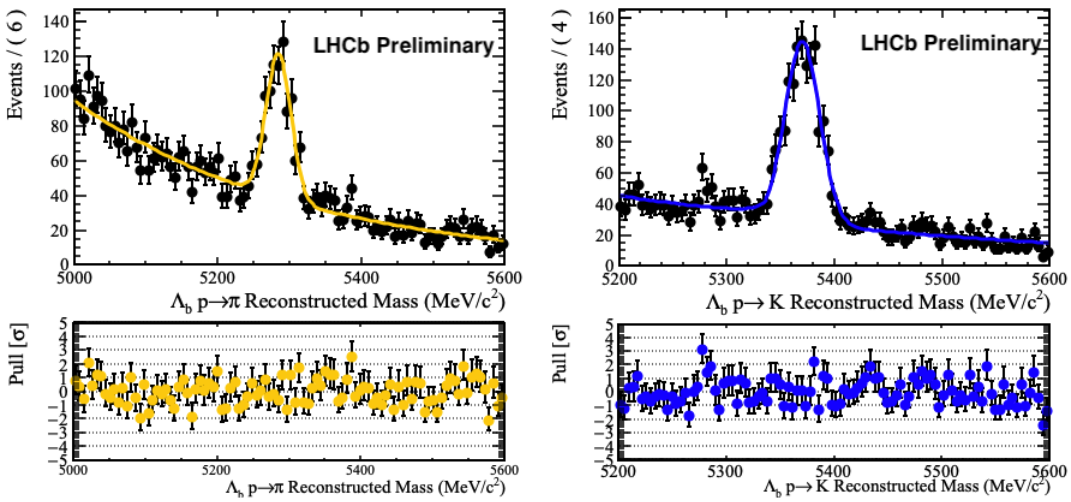

Figure 4.10: Fitted Run I data distributions of B^0(left) and B_s^0(right) decays that passed the selection in their respective correct mass hypothesis. The signal is modelled by a simple Crystal-Ball shape while the background is modelled by an exponential. It was The yields in these fits are used to constrain the yields of $N(B_s^0)$ and $N(B^0)$ in the final Λ_b^0 fit.

Data Fit

Finally, one can add all the contributions to the signal peak in order to obtain a final fit from which is possible to extract a yield for the number of $\Lambda_b^0 \to pKJ/\psi(\mu\mu)$ decays observed in LHCb. An additional exponential background distribution is added to account for candidates coming from random combinations of tracks that were not removed by the selection criteria. Figure 4.11 is the fit using all the candidates for 2012 data sample, where a total of 21890 ± 174 signal events were observed. One can notice that the exponential background is very flat, which is very hard to avoid in this arrangement since there is not a simple way of getting a pure combinatorial sample to model it. It is also relevant to note that the Ipatia function, although fitting for the peak shape well, is sensitive and the minimiser has difficulties with convergence, for this reason the function for modelling the signal contribution was later changed to a double-sided crystal ball, which is a crystal ball that allows for exponential tails on both sides of the peak. This fitting procedure is used in the final analysis to obtain the yields on the control channel of Run I & II data separetely.

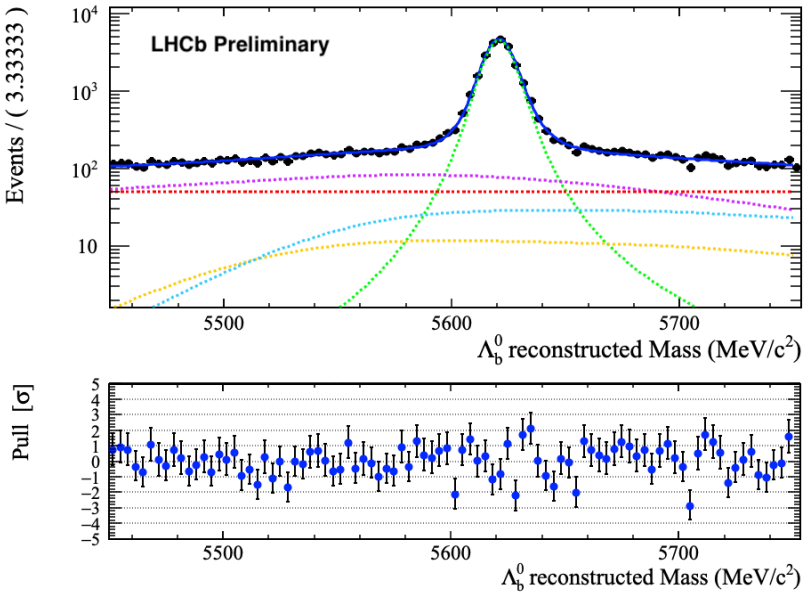

Figure 4.11: Fitted data distribution of the $\Lambda_b^0 \to pKJ/\psi(\mu\mu)$ channel (green) and the contributions from B^0 decays (yellow), B_s^0 decays (light blue), swap of $p-K$ (violet) and an exponential shape modelling combinatorial background(red).

The full R_{pK} measurement uses three more channels not discussed here: the non-

resonant $\Lambda_b^0 \to pK\mu\mu$ and the two electron channels ($\Lambda_b^0 \to pKJ/\psi(e^+e^-)$ and $\Lambda_b^0 \to pKe^+e^-$)). In particular the non-resonant electron channel has never been observed and the analysis is currently blinded while the internal review process happens. A very important check to the results is the measurement of $R_{J/\psi}$, the ratio between yields of the resonant modes corrected by the efficiencies. As discussed earlier, $R_{J/\psi}$ is expected to be 1. In fact this ratio will only be one if all the efficiencies differences between electrons and muons in LHCb are well understood and taken into account, reason why is also kept blind throughout the analysis. The yields obtained through the resonant channel fits will contribute as:

$$R_{J/\psi} = \frac{\mathcal{B}(\Lambda_b \to \Lambda(pK)\ J/\psi(e^+e^-))}{\mathcal{B}(\Lambda_b \to \Lambda(pK)\ J/\psi(\mu^+\mu^-))} = \frac{N_{e-fit}}{N_{\mu-fit}} \times \frac{\epsilon_\mu^{reco}\epsilon_\mu^{trigger}\epsilon_\mu^{sel}}{\epsilon_e^{reco}\epsilon_e^{trigger}\epsilon_e^{sel}} \tag{4.8}$$

Figure 4.12 is an example of the fits for the resonant muon and electron channels in the Run I data. The effort to finalise the systematic checks of the analysis continues and the official results should be released before the end of the year.

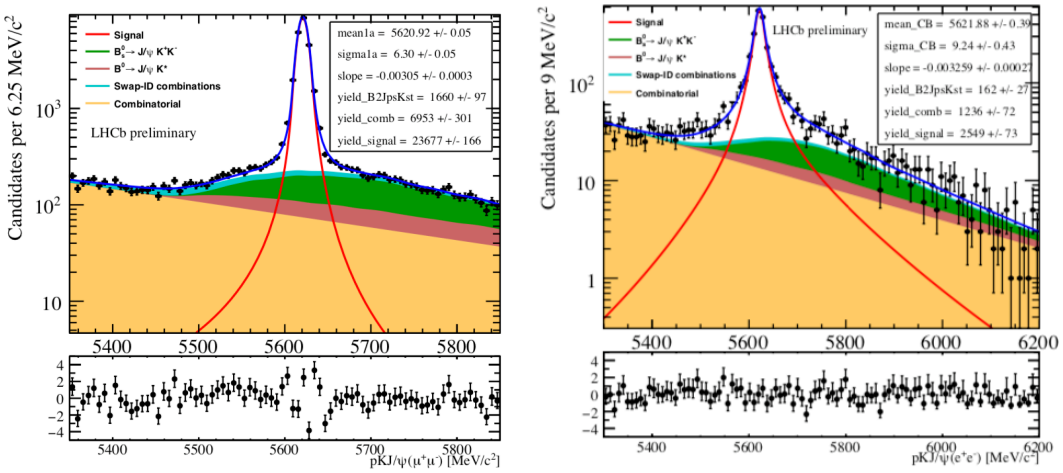

Figure 4.12: Example of the final fits using Run I data for muons (left) and electrons (right). The electrons in this case are coming from just events triggered independently from the tracks in the Λ_b^0 decay. Extracted from [54].

4.2 Evaluation of the $B^+ \to a_1^+(1260)(\pi^+\pi^-\pi^+)\mu^+\mu^-$

The spin structure of the particles produced in a b-hadron decay can shed light on the structure of deviations from the SM. However, the effect of right-handed currents in the measurements of lepton universality can be masked by long distance contributions (such as charm loops). As discussed in [55], there is a symmetry between vector and axial mesons involved in b decays that can be used to extract observables that are sensitive to right handed current contributions while having a better control of the long distance contributions.

One of the pair of mesons involved in the vector axial symmetry is the $a_1(1260)^+$ and the particular decay channel $B^+ \to a_1(1260)^+\mu^+\mu^-$ has never been observed. It is in fact a challenging decay due to the $b \to d$ transition, which is heavily suppressed. LHCb has measured the $b \to d$ in the form of the branching ratio of the $B^\pm \to \pi^\pm\mu^+\mu^-$ decay, which was found to be $\mathcal{B}(B^\pm \to \pi^\pm\mu^+\mu^-) = (1.83 \pm 0.25 \pm 0.05) \times 10^{-8}$ [56]. Therefore, before considering a possible measurement using such decays, one needs to evaluate whether it is possible to observe this decay in the existing LHCb dataset.

The main challenge with identifying this decay channel beside the expected very low branching ratio, is the very broad structure of the $a_1(1260)^+$ resonance, which mostly decays in 3 pions trough the process $a_1(1260)^+ \to \rho(\pi\pi)\pi$ [57]. In a similar way to what was described in Section 4.1, the best way of obtaining this branching ratio would be to measure it as a ratio to the resonant channel $B^+ \to a^+(\pi^+\pi^-\pi^+)J/\psi(\mu^+\mu^-)$, which has a limit set by CLEO [58]. All of these decays are very rare, so it is interesting to make an estimate if they are visible in the LHCb at all. The goal of the next sections is to identify a possible selection using MC samples to judge the feasibility of looking for this decay in LHCb.

4.2.1 Generation and Reconstruction Efficiencies

An MC sample generated tuned to conditions of the 2016 data taking was used with a centre of mass energy of $\sqrt{s}$ = 13 TeV and a mean number of interactions per interactions per bunch crossing 1.6. Of the collisions generated by Pythia, only signal events that have all tracks inside LHCb's efficiency have their passage through the detector simulated. The detector acceptance is $(15.51 \pm 0.05)\%$.

As described in Chapter 2 after generation the simulation data goes through the same

	Basic Selection
μ, π	250 MeV< P_t < 40 GeV hasRich=1 Track χ^2/NDOF < 7 Track Ghost Probability < 0.5
π	Momentum Above Rich Threshold
μ	hasMuon=1 isMuon=1
J/ψ	$2900 < m_{J/\psi} < 3200$

Table 4.4: List of basic selection criteria for the B^+ decay.

steps of trigger and reconstruction as the detector data stream. This process involves reconstruction, triggering and stripping steps. The efficiency for this selection is done by using the matching of truth level MC information with the reconstructed tracks. In the MC dataset with 1009469 events the efficiency after stripping was $(4.73 \pm 0.02)\%$, where the uncertainty is calculated using binomial distribution.

4.2.2 Offline Selection

Prior to performing kinematical or PID selection cuts optimisation, a set o basic criteria is required for both signal and background samples. These cuts are summarised in Table 4.4 and intend to remove poor quality tracks, making sure that they left signals in the detectors responsible for PID.

Particle Identification Selection

With the kinematical selection applied by means of the BDT, one can look at the PID information provided by LHCb. To obtain a pure sample of pions the PID selection has to focus on suppressing the background by removing K and p contributions from the sample (Figure 4.13). Table 4.5 summarises the selection, that has an efficiency of $(27.50 \pm 0.24)\%$.

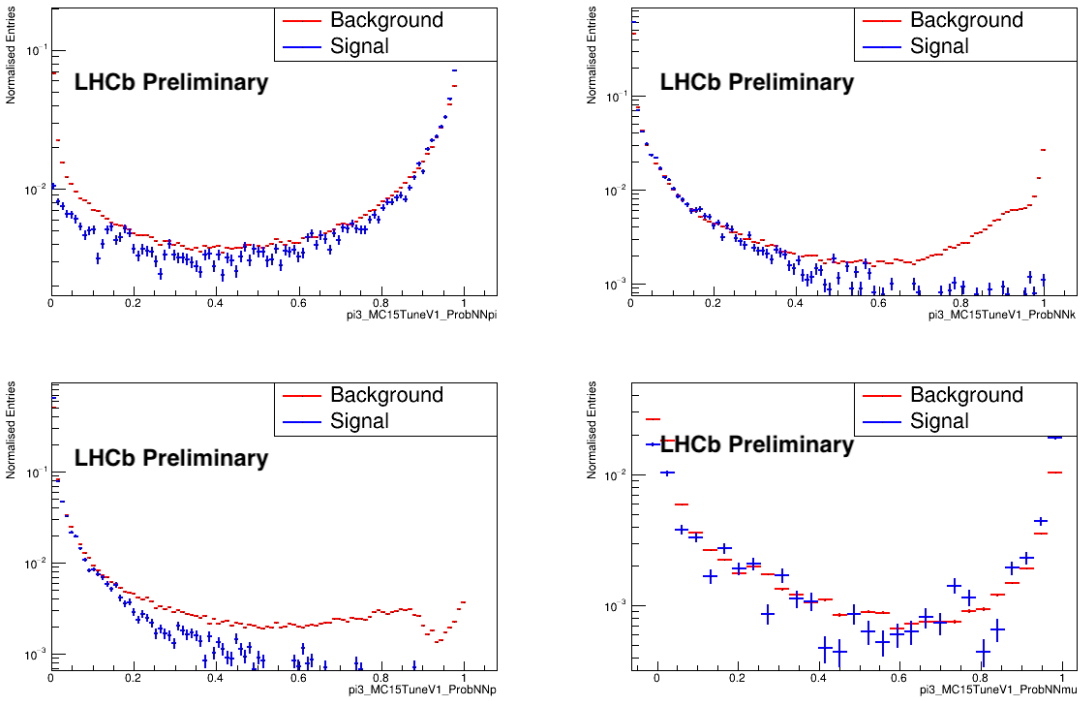

Figure 4.13: Example of variables for particle identification of π tracks. One can notice that the background distribution behaves very similarly to the signal on the π ProbNN. This is the reason why anti-cuts are used to try to remove the contamination from other decays.

	PID Selection
π	MC15TuneV1_ProbNNπ>0.1
	MC15TuneV1_ProbNNp<0.5
	MC15TuneV1_ProbNNghost<0.5
	MC15TuneV1_ProbNNK<0.5
μ	MC15TuneV1_ProbNNμ>0.2

Table 4.5: List of particle identification selection criteria for the final state particles of the B^+ decay. As most particles going through the detector are pions, the biggest challenge is to guarantee the removal of K or p contamination from the π candidates while maintaining good signal efficiency.

BDT input variables
$\log_{10}(B^+$ Flight Distance $\chi^2)$
$\log_{10}(B^+ p_T)$
$\log_{10}$(1-B^+ DIRA)
$\log_{10}(B^+$ IP $\chi^2)$
$\log_{10}(B^+$ Vertex $\chi^2)$
$\log_{10}(\mu$ IP $\chi^2 \times \mu$ IP $\chi^2)$
$\log_{10}(\pi_1$ IP $\chi^2 \times \pi_2$ IP $\chi^2 \times \pi_3$ IP $\chi^2)$

Table 4.6: List of input variables for BDT classifier. Vertex χ^2 stands for the quality of reconstruction of the B^+ vertex, IP is the impact parameter, DIRA stands for the cosine of the angle between momentum and direction of flight, DTF PV χ^2 is the quality improvement of the primary vertex fit by using mass information of the B^+ and p_T is the transverse momentum.

Kinematical Selection

A multivariate selection was employed, using a Boosted Decision Tree (BDT) trained on kinematical variables, in a similar way to what was done in Section 4.1.1. The BDT selection is trained using the truth-matched MC sample as signal and a background sample consisting of a high mass sideband region[5] 2016 LHCb data. The variables used were ranked in level of power of separation between the signal and background. As it was the case in the R_{pk} selection some variables were transformed to make the distributions smoother, which benefits the training phase. Most of these variables are somewhat indicative of the quality of reconstruction of the B^+ meson. As an example, Figure 4.14 shows the signal and background distribution of two variables with the highest discriminatory power. After training the perfomance is evaluated in a slice ($\approx 50\%$) of the MC dataset not used for training, and the efficiency obtained is $(72.60 \pm 0.50)\%$.

4.2.3 Estimation on the Yield

Using the efficiencies obtained with a Monte-Carlo sample on can estimate the possible yield of the decay $B^+ \to a_1^+(1260)(\pi^+\pi^-\pi^+)J/\psi(\mu^+\mu^-)$ in the LHCb Run II dataset.

[5] defined as $M_{B^+} > 5500\,\mathrm{MeV/c^2}$

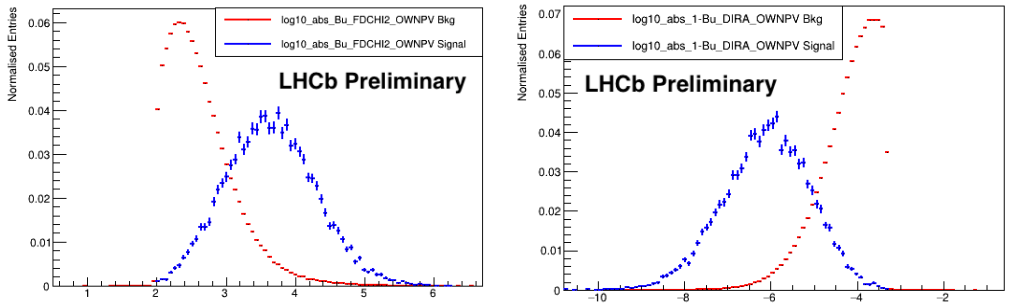

Figure 4.14: Example of variables with high discriminatory power used as input for the BDT. On the left we have $\log_{10}(B^+$ Flight Distance $\chi^2)$ and on the right $\log_{10}$(1-B^+ DIRA) with signal in blue and background in red.

The expected number of events is calculated as:

$$N_{sig} = N(B^+) \times \mathcal{B}(B^+ \to a_1^+(1260)(\pi^+\pi^-\pi^+)\mu^+\mu^-) \times \epsilon_{acc}\epsilon_{Reco}\epsilon_{Sel} \tag{4.9}$$

Combining the efficiencies form acceptance, reconstruction and selection a total efficiency is found to be $\epsilon_{tot} = (0.14 \pm 0.02)\%$.

Although there are not any direct predictions from theory for the amplitude of these channels, one can get an estimate by using the measurement of the decay $B^+ \to J/\psi K(1270)^+$, that has a very similar final state topology. This branching ratio was measured to be $\mathcal{B}(B^+ \to J/\psi K(1270)^+(K\pi\pi)) = (1.80 \pm 0.30 \pm 0.34) \times 10^{-3}$ [59]. Taking into account only the difference in CKM elements, the $a_1^+(1260)$ should have a branching ratio smaller by at least a factor of $(V_{cd}/V_{cs})^2 \times \mathcal{B}(J/\psi \to \mu\mu)$, or around 3.1×10^{-3}. Assuming this value as true for estimating the yield, the value of $\mathcal{B}(B^+ \to a_1^+ J/\psi(\mu\mu))$ is taken as 5.58×10^{-6}.

The total number of B^+ depends on the total luminosity and the production cross-section of the B^+ meson in the LHC. The production cross-section of B^+ mesons has been measured in LHCb to be $38.9 \pm 2.5 \pm 1.3\mu b$ [60]. Using this estimate, the number of expected events in the LHCb dataset per fb^{-1} is:

$$N_{sig}^{exp} = 312 \pm 45 \pm 72, \tag{4.10}$$

where the uncertainties come from statistics of the MC sample and the measurements

input in the calculation, respectively. Considering the already collected 9fb^{-1}, it could be possible to observe the decay $B^+ \to a_1^+(1260)(\pi^+\pi^-\pi^+)J/\psi(\mu^+\mu^-)$, with the caveat that there will be several other decay channels that, through particle misidentification, can contribute to a mass peak. These will need to be controlled properly in order to obtain a significant observation. As for the non-resonant decay $B^+ \to a_1^+(1260)(\pi^+\pi^-\pi^+)\mu^+\mu^-$, its branching ratio is likely to be much lower, so a more accurate assessment of its detection using the upgrade dataset of 50 fb^{-1} could be performed upon observation of the resonant (J/ψ) mode.

5 | Silicon Sensors

Experiments in high energy physics use silicon sensors ubiquitously in their detectors, especially in the closest regions to the interaction points, where very precise position measurements are necessary to achieve good position resolution and efficient pattern recognition. This chapter will briefly review the interaction of ionising particle with silicon, describe the basics of the silicon sensor technology used in the LHCb upgrade and finally discuss the effects that the intense radiation flux in LHC generates in silicon sensors.

5.1 Interaction of Particles with Matter

All LHC experiments, in particular the LHCb Experiment, are interested in reconstructing particles that have been created at the interaction point and go through or decay inside the detector volume. All particles generated in the collisions will ultimately decay in seven particles that are stable enough to leave signals in collider experiments: protons, kaons, pions, neutrons, photons, electrons and muons. Neutrinos are also stable final state particles but the chance of them leaving a signal in a collider experiment is completely negligible. Out of this list, most particles are electrically charge which makes the interaction of relativistic charged particles with matter an important consideration in the design of particles detectors.

Only three years after Schrödinger postulated his non-relativistic quantum mechanics equation, Bethe [61] was able to use it to solve almost completely the way particles loose energy through matter by the means of multiple scattering. This equation was later corrected to take into account the special relativity effects on the shape of the charged particle's electric field[1]. Other corrections take into account higher-order perturbation theory

[1] Due to relativistic effects, the electric field becomes flattened to the plane perpendicular to the direction

and density corrections. The overall behaviour for particles with $m \gg m_e$ is given by:

$$-\left\langle \frac{dE}{dx} \right\rangle = Kz^2 \frac{Z}{A} \frac{1}{\beta^2} \left[\frac{1}{2} \log \frac{2m_e c^2 \beta^2 \gamma^2 T_{\max}}{I^2} - \beta^2 - \frac{\delta(\beta\gamma)}{2} \right], \tag{5.1}$$

where Z and A are the atomic number and mass, c is the speed of light in vacuum, $\beta = \frac{v}{c}$ and γ is the Lorentz Factor. K is a constant: 0.307 MeV mol^{-1}cm^2. I is the medium average ionisation energy and δ describes how much the electric field of a particle is 'squished' in the transverse plane due to Lorentz contraction. $T_{\max}$ is the maximum kinetic energy transferred to a free electron in a single collision, given by:

$$T_{\max} = \frac{2m_e c^2 \beta^2 \gamma^2}{1 + 2\gamma m_e/M + (m_e/M)^2}. \tag{5.2}$$

Bethe's formula gives a precise prediction to the average energy loss per unit of length, which is a function of the particle's mass, momentum and characteristics of the medium being traversed. Figure 5.1 depicts the general shape of the energy loss as a function of the particle's momentum. It is possible to observe that for slower particles ($\beta\gamma < 1$) the energy loss is dominated by a $\beta^{-5/3}$ behaviour. This means that energy loss is attenuated as $\beta\gamma$ increases, until the logarithm term becomes relevant when the incident particle has very high momentum($\beta\gamma \approx 1000$). The region between these two regimen is a broad minimum, with particles in it being referred to as minimum ionising particles (MIP). Particles in this region deposit the lowest possible energy through ionisation and are the general benchmark signal that high energy physics detectors are designed to measure.

5.1.1 Energy Deposition

Equation 5.1 describes the average energy loss of a particle, but gives no information on what the likelihood is for a given energy loss as a function of the distance. In fact, the energy losses will be dominated by hard scatterings, and the probability density function of the deposited energy differs from a Gaussian centred around the Bethe's average energy loss.

In thin absorbers, a considerable fraction of the energy lost by the traversing particle is not deposited inside the material itself. That is due to hard scattered electrons receiving enough energy to escape the energy deposition material. Landau first treated this problem

of motion, increasing the effective cross section.

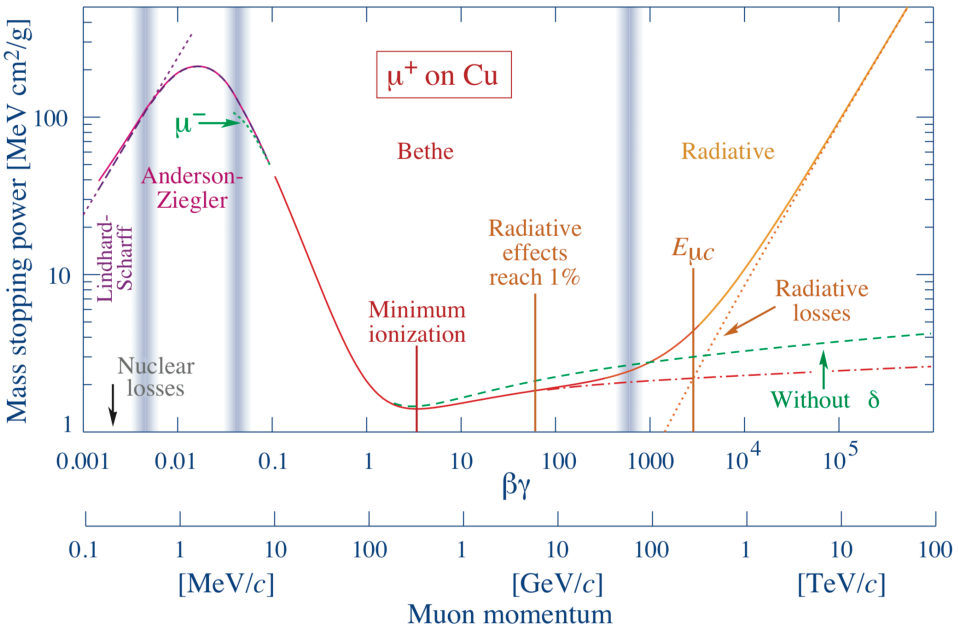

Figure 5.1: Energy loss of a heavy ionising particle as a function of $\beta\gamma$ and momentum for muons passing through solid copper [35].

in 1944 [62]. The probability distribution function that describes the likelihood of a given charge depositions is known as the Landau-Vavilov-Bischel distribution [35], with the most probable value (MPV) given by:

$$\Delta_p = \xi \left[ln\left(\frac{2mc^2\beta^2\gamma^2}{I}\right) + ln\left(\frac{\xi}{I}\right) + j - \beta^2 - \delta(\beta\gamma)\right], \tag{5.3}$$

where β and γ are the relativity factors, δ is the density correction mentioned previously. I is the mean ionisation energy of the material, j has a value of 0.2 and ξ is defined as:

$$\xi = \frac{4\pi N_A r_e^2 m_e c^2}{2}\left\langle\frac{Z}{A}\right\rangle\frac{x}{\beta^2}. \tag{5.4}$$

where N_A is Avogadro's number, r_e the classical electron radius, m_e electron's mass and x is material's thickness. In the limit in which the material thickness is large, the Landau distribution average and MPV should match the average energy loss predicted by Eq. 5.1. Additionally, most detectors will have to deal with sources of noise that adds fluctuations to the energy deposition. For (thin) detectors expecting a Landau signal, the curve that best describes the observed charge deposition is often the convolution of a Landau distribution

with a Gaussian noise distribution.

5.1.2 Scattering in Materials

The movement of charged particles through materials, even in the minimum ionising range, is not completely unperturbed. Their trajectory is composed of a series of Coulomb scatterings with atoms that alter the initial direction of movement by small deviations $\delta\theta$, which compound over the particle's path. After a certain distance x in a material is traversed, with a large number of scatterings taking place, one can approximate the expected angular deviation to a Gaussian distribution centred around zero with standard deviation given by [35]:

$$\theta_0 = \frac{13.6\,\mathrm{MeV}}{\beta cp}\mathrm{Z}\sqrt{x/\mathrm{X}_0}\left[1 + 0.038\ln\left(\frac{x\mathrm{Z}^2}{\mathrm{X}_0\beta^2}\right)\right], \tag{5.5}$$

where p is the particle's momentum and x is the distance traveled in a material with radiation length X_0.

Equation 5.5 is an approximation that is mostly valid for thicker media, i.e. media in which 200 interactions or more happen. For single or plural scattering, a higher number of large angle scatterings are observed, differing from the Gaussian tail. Figure 5.2 exemplifies the transition in behaviour from multiple to single/plural scattering.

5.2 Silicon Sensors in High Energy Physics

Silicon is one of the many semiconductor materials used as a sensitive material for the detection of particles. In fact, the use of semiconductors in high energy physics for high precision tracking is commonplace. They provide a high signal to noise ratio, fast signals and potentially very good spatial resolution.

Silicon detectors used in high-energy physics consist of a charge-free volume, which has an electric field applied within, the same principle that guides almost all detector technologies. Charge deposition by the passage of particles (described in Sec. 5.1) results in the generation of electron-hole pairs in the lattice, that drift towards the electrodes, generating an analogue signal which can then be further manipulated by the readout scheme of choice.

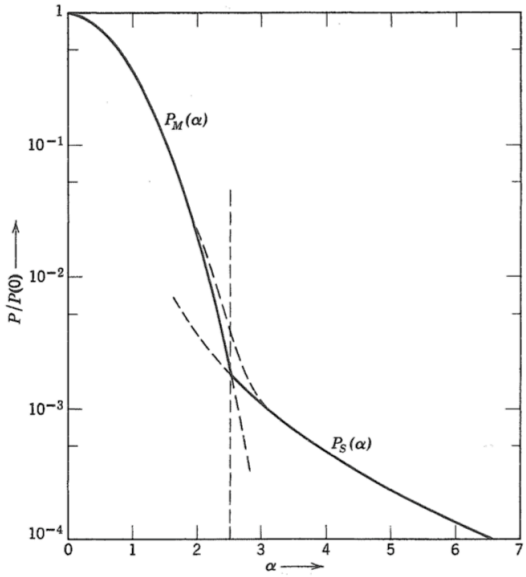

Figure 5.2: Distribution of angular scattering as a function angular spread from initial particle incidence(α). Multiple scattering dominates the region up to $\alpha \approx 2.5$, when the single Rutherford scattering dominates [63].

5.2.1 Silicon and the pn-Junction

A pure silicon lattice organises itself into a diamond structure (Fig. 5.3) with each silicon atom forming covalent bonds with the other four neighbouring atoms. There is a translational periodicity inside the lattice: the potential seen by an electron $U(\vec{x})$ is the same as in any other cell in the lattice $U(\vec{x}+\vec{R})$, where $\vec{R}$ is the lattice period. Therefore, the electron wave-function must be periodic. The result of this periodicity is that not all electron energy states are allowed in the lattice [64], in particular, there will be a forbidden energy band in which no states are allowed. This energy gap (Fig. 5.4) separates the charges in the lattice between the lower energy, valence band and the higher energy, more loosely bound states, dubbed the conduction band. The size of this gap in energy states determines the energy necessary to promote charges to the conduction band. As the name suggests, the harder it is to populate the conduction band states, the less the material is conductive. The value of the energy gap (E_g) varies weakly with temperature:

$$E_g(T) \approx E_g(0) - \frac{\alpha T^2}{T+\beta}, \tag{5.6}$$

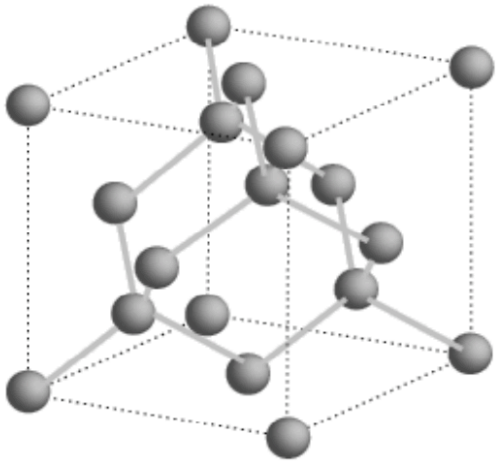

Figure 5.3: Silicon lattice structure, each atom is part of a tetrahedron connected to four other atoms [64].

where α and β are experimentally defined constants. In general E_g decreases with temperature, with values of $E_g(0\,K) = 1.17\,eV$ and $E_g(300\,K) = 1.12\,eV$ for high-purity silicon.

At 0 K all states in the valence band are filled and there are no electrons in the conduction band. As the temperature rises, the equilibrium state has more electrons that can fluctuate to the conduction band. The probability of a given state in the conduction band being occupied is given by the Fermi-Dirac distribution:

$$f(E) = \frac{1}{1 + e^{[(E-E_F)/k_bT]}}, \tag{5.7}$$

where k_b is Boltzmann's constant, T the temperature, E_F the Fermi level, and E the energy of the state. Considering the density of states $N(E)$, the total number of free charge carriers is given by:

$$n = \int_{E_c}^{\infty} f(E)N(E)dE \tag{5.8}$$

and in an intrinsic silicon bulk at 300 K, the number n of free charge carriers present in the silicon is of the order of $\approx 10^{10}\,cm^{-3}$. Taking as an example a $55\,\mu m \times 55\,\mu m$ area, $300\,\mu m$ thick sensor the amount of free charges is of the order of 10^4 while the average charge deposited by a MIP is also $\approx 10^4$ electron-hole pairs. This means that the charges

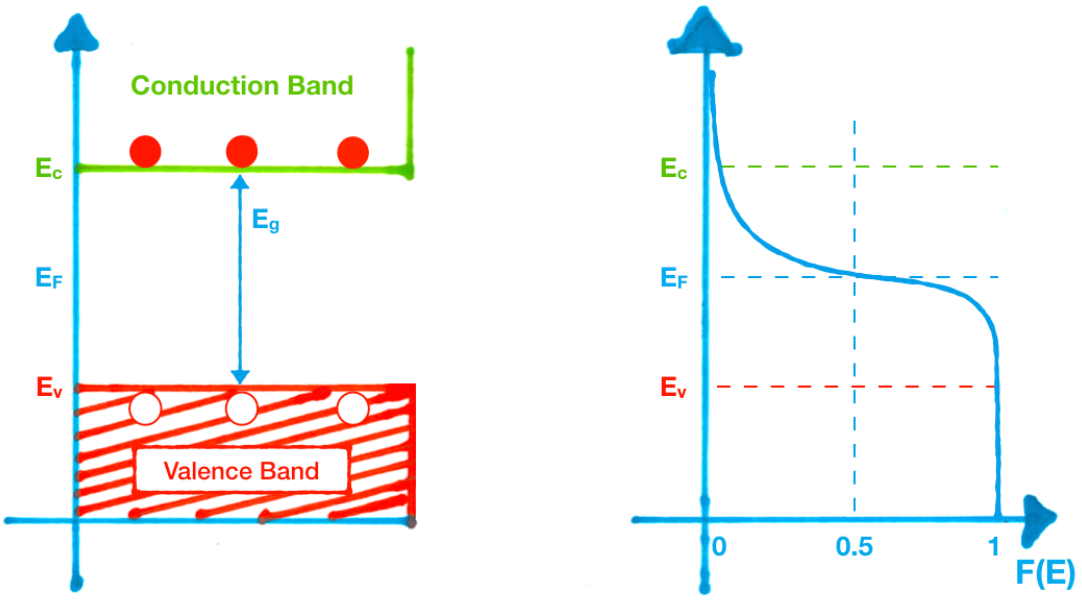

Figure 5.4: Electronic band structure in an intrinsic silicon lattice. The left diagram is a scheme of the band diagram. The right diagram shows the Fermi-Dirac distribution that governs the occupancy of energy levels in the lattice at a given temperature. E_F, E_c and E_v stand for the fermi energy, the conduction band lowest energy state and the valence band highest energy state.

typically deposited in silicon sensors would be completely masked by the free charges in silicon without the establishment of a charge free region.

The charge free region is engineered through the construction of a p-n junction, an interface between two differently doped silicon bulks. The silicon lattice can be doped with donor or acceptor elements[2], which will add electrons or holes[3] in the bulk, respectively. When both p-type/n-type (extra holes/electrons respectively) regions are constructed in the same bulk there will be a charge gradient, which generates a diffusion current until the charges reach thermal equilibrium. Such equilibrium is only reached when concentrations are even throughout the junction. The result is a diffusion current in which extra electrons from n-type will migrate to p-type and holes will migrate in the opposite direction.

The migration of charges in opposite directions in the bulk establishes a built-in potential to the junction caused by the ions in the lattice that are left behind. This potential will counteract the diffusion current, reaching a steady state solution comprised of a volume around the junction with an electric field and no free charge carriers. The main feature of this junction is that it allows current to go through it if it follows the potential drop inside the junction region but it counteracts any current trying to go the other way. Figure 5.5 exemplifies the structure of a simple p-n junction.

This charge free area, desirable for use as an ionising particle detector, is only a few microns thick and needs to be increased in order to be used as a detector effectively. The charge free (depleted) region can be increased by applying a voltage difference between p and n sides. By setting the p-type to a lower voltage than the n-type silicon, the electric filed inside the bulk increases to a new equilibrium with a larger depletion region. The solution for the electric potential inside the silicon bulk is given by solving the Poisson equation [66]:

$$\frac{d^2V}{d\vec{x}^2} = \frac{-\rho(\vec{x})}{\epsilon_0 \epsilon_{\text{Si}}}, \tag{5.9}$$

where $\rho(\vec{x})$ is the charge density, V is the electrostatic potential, ϵ_0 is the vacuum permittivity and ϵ_{Si} is the dielectric constant in silicon. The solution for this equation will depend on the doping profile of the bulk. The total depleted depth for an abrupt pn-junction

[2] Usually, acceptor dopants are from the group III of the Periodic Table, while donors are from group V.

[3] A hole is the lack of an electron in the valence band, and it behaves much like a free charge in the lattice, albeit with different velocity and effective mass than the electron.

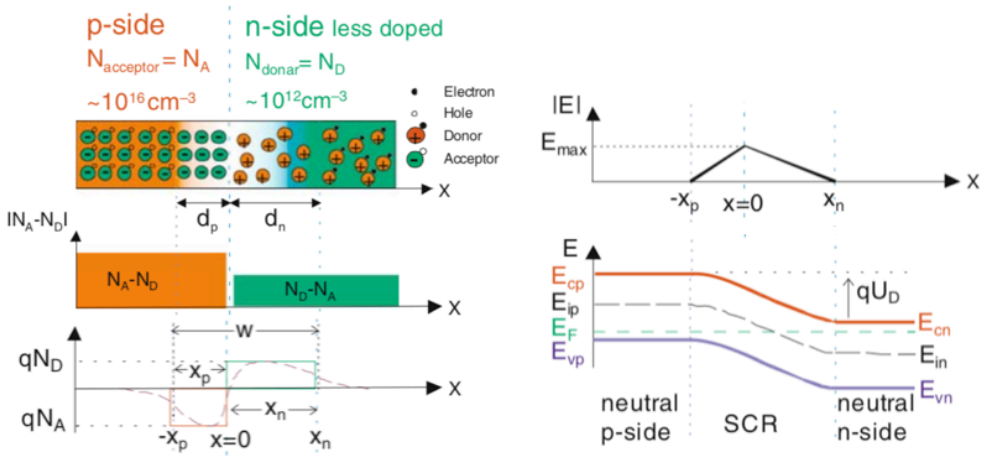

Figure 5.5: Setup of a p-n junction, different concentrations of acceptors and donors lead to a space charge density (qN_d, qN_a) and an internal electric field. Ultimately this leads to a potential drop inside the bulk. Figure adapted from [65].

(ignoring any surface infuence) is given by:

$$D_{\text{depletion}} = \sqrt{\frac{2\epsilon_0\epsilon_{\text{Si}}V_{tot}}{e}\left(\frac{1}{N_a}+\frac{1}{N_d}\right)}, \tag{5.10}$$

where e is the electrical charge, N_a is the number of acceptors, N_d the number of donors and V_{tot} is the sum of the applied bias potential and the built-in junction voltage due to the different dopant and acceptor concentrations. In pixel sensors, we usually encounter a lightly doped bulk and a heavily doped implant in such a way that the depletion region grows mostly into the bulk region. Using the fact that $N_d \gg N_a$, we can approximate the depletion depth as:

$$D_{\text{depletion}} \approx \sqrt{\frac{2\epsilon_0\epsilon_{\text{Si}}V_{tot}}{eN_a}}. \tag{5.11}$$

The pn-junction forms a volume that can be approximated as a parallel plate capacitor, which has a capacitance given by:

$$C = \epsilon\frac{A}{d}, \tag{5.12}$$

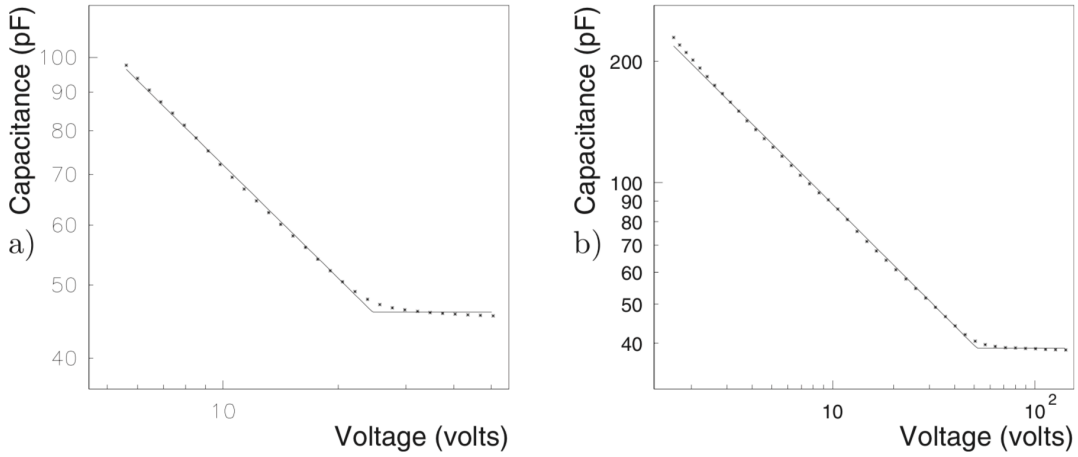

Figure 5.6: Example of capacitance behaviour of p-n junctions in two different 1 cm thick silicon detectors. Capacitance drops as the depletion region increases in the bulk until it reaches the other side of the bulk, when the bulk is fully depleted. Points represent measured data, lines are the fitted behaviour [66].

In this case, A is the total transverse area of the sensor, while d is the depletion depth. It is possible to substitute 5.11 into 5.12, setting $d = D$, and obtain the dependence of the junction capacitance as a function of the bias voltage:

$$\frac{1}{C^2} = \frac{1}{\epsilon A^2}\frac{2}{eN_a}V, \tag{5.13}$$

which is only valid whilst $D_{\text{depletion}}$ is less, or equal to, the sensor thickness (as the depletion region obviously cannot grow past the sensor physical boundaries). The measurement of the point of saturation of the Capacitance-Voltage (CV) curve is in fact used to determine the depletion voltage of sensors as exemplified in Figure 5.6.

When fully depleted the junction will still allow a very small leakage current to flow. This current is created by the thermal excitations in the bulk and so, it scales with the junction volume. The leakage current will also scale with temperature, following the relation:

$$I(T) = I(T_{ref})\left(\frac{T}{T_{ref}}\right)^2 \exp\left(\frac{-E_g}{2k_B}\left[\frac{1}{T} - \frac{1}{T_{ref}}\right]\right), \tag{5.14}$$

where I(T_{ref}) is the leakage current measured at a reference temperature T_{ref} and the other terms were previously defined. This exponential behaviour means that a small increase in

temperature has a big effect on the leakage current in a sensor.

5.2.2 Breakdown Mechanisms

Breakdown is the name given to the phenomena of a reverse-biased diode having an exponential increase in leakage current beyond a certain voltage, known as breakdown voltage (V_{BD}). There are three main mechanisms through which a reverse-biased junction can breakdown: thermal runaway, avalanche multiplication and tunnelling [64] [67].

Thermal runaway[4] is the process through which the power dissipation of the leakage current causes self-heating which further increases the current, activating a positive feedback loop. The temperature of the junction increases the leakage current according to Eq.5.14 and is an important parameter for sensor operation. In silicon Equation 5.14 amounts for an approximate doubling of the current every 8 K, and it can be a very serious issue if not taken into account in the design of the detector. The reverse bias voltage does not alter the temperature behaviour of the current *per se*, but a higher initial power $P(T_0) = V \times I(T_0)$ can push the power consumption beyond the cooling threshold, triggering the thermal runaway.

Avalanche multiplication takes place when the field inside the junction is such that the primary current I_0 generates more free charge carriers by impact ionisation. The minimum energy a free charge carrier has to acquire in order to promote more valence electrons is:

$$E^e_{min} = \frac{3E_g}{2}. \tag{5.15}$$

using the minimum energy for promoting a electron-hole pair to the conduction band and equal effective masses for holes and electrons. The size of the high field region is important, given that the mean free path of an electron in the bulk is approximately 10 µm. As temperature decreases, the mean free path increases, facilitating acceleration and avalanche generation.

Tunnelling breakdown is the process taking place in Zener diodes at high reverse bias voltages. Beyond a certain bias voltage, around $10^5 \sim 10^6$ V/cm, the charge carriers start having a non-negligible probability of tunnelling the bandgap [64]. This is due to valence charges in a p-type bulk seeing only a triangular barrier to the conduction band in the

[4] Alternatively named thermal instability

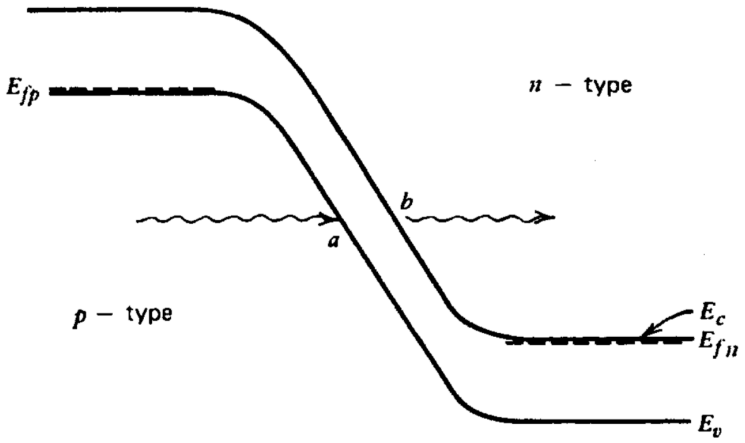

Figure 5.7: Band gap scheme in a heavily reverse biased p-n junction. Electrons in the valence band in the p-type bulk can tunnel through the band gap potential and occupy available states in the conduction band of the n-type silicon [67].

n-type bulk (Fig. 5.7). This barrier will have a length L of [67]:

$$L = \frac{E_g}{q|\vec{E}|}, \tag{5.16}$$

which can be approximately solved using the WKB method [68], obtaining:

$$P_{\text{tunnel}} = \exp\left(-2\int_0^L \sqrt{\frac{2m}{\hbar^2}V(x)}dx\right). \tag{5.17}$$

For a triangular barrier, using Eq. 5.16 this integration can be solved approximately:

$$P_{\text{tunnel}} \approx \exp\left(\frac{-4\sqrt{2m}E_g^{3/2}}{3q\hbar|\vec{E}|}\right). \tag{5.18}$$

Where q is the electron charge, m the electron mass and E the electric field. It is important to note that the probability (P_{tunnel}) is greater with a larger electric field which is the same as having a smaller barrier length. The tunnelling current is going to be proportional to the density N of valence electrons arriving at the junction, the junction cross section A, the velocity of the valence electrons v and the probability of passing the barrier P_{tunnel}:

$$I = qNvAP_{\text{tunnel}}. \tag{5.19}$$

The distinctive feature of this process is the temperature behaviour of the breakdown voltage: as the temperature decreases the breakdown voltage is larger due to the smaller density available for tunnelling. The temperature behaviour of the breakdown is used to identify the effect generating the junction breakdown.

5.2.3 Signal Formation

As a particle passes through the sensor, charge tends to be deposited along its trajectory in the sensor. This charge will immediately move due to two distinct effects. Firstly, movement is caused by the charge drift, due to the presence of an electric field that attracts the charge to the opposite side of the sensor. Secondly, movement is affected by charge diffusion, which will spread the initial charge distribution in all directions. The drift velocity is set by the field and the charge mobility in the silicon (Ohm's Law, Eq. 5.20) while the diffusion velocity is set by the temperature of the substrate, charge mobility (μ) and the charge concentration gradient ($\vec{\nabla} n$) (Eq. 5.21):

$$u_{e^-,h^+} = \mu_{e,h}\vec{E}, \tag{5.20}$$

$$\vec{J} = \frac{kT}{e}\mu_{e,h}\vec{\nabla} n \tag{5.21}$$

The charge deposited will drift towards the electrodes, where it will be collected. The signal itself is not formed by the collection of charge in the electrodes, but by the induction current generated by the charge movement as stated in the Ramo-Shockley theorem [69] [70], and is calculated using the weighting field. The weighting field (E_w) represents how big is the coupling of a charge in a given position and velocity to the readout electrode of interest, and it is not the electric field in the bulk. Equation 5.22 contains the current induced in an electrode (i) from a charge at a time t, increasing with the velocity ($\vec{u}$). Due to electrons having a higher mobility than holes in silicon [64], their contribution to the induced signal always higher than the holes.

$$i_{e^-,h^+}(t) = e\vec{E}_w \cdot \vec{u}_{e^-,h^+}(t) \tag{5.22}$$

Knowledge of both the electric field, responsible for the drift velocity, and the weighting field is necessary to properly predict the signals measured in the readout electrodes.

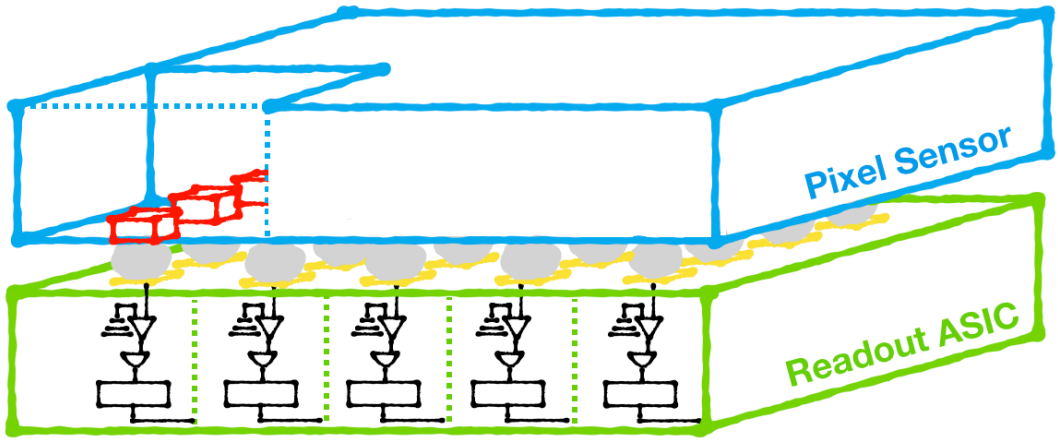

Figure 5.8: Scheme of a Hybrid Pixel Detector assembly. At the top (in blue) the sensor is a semiconductor bulk containing implants (in red) in regular intervals. Bias voltage is applied between both sides to deplete the sensor. Bump bonds connect the sensor pixels to the each independent readout channel in the ASIC.

The total current integrated over the drift time is equal to the total charge deposited originally. As an example, the collection time for sensors in the VELO Upgrade, considering 200 µm thickness and a bias voltage of 140 V is of the order of 2 ns.

5.2.4 Silicon Hybrid Pixel Detectors

It is necessary to readout the charge induced in the sensor electrodes in some manner that allows for posterior use of this information for the event reconstruction. For the purpose of this work, the most relevant readout schemes are the Hybrid Pixel Detectors. Such detectors are composed of two parts: a pixellated silicon sensitive volume which is the sensor, and a readout hybrid composed of independent channels capable of measuring the charge collected and outputting this information in digital form. Both of these elements are joined together by small solder spheres called bump bonds (Fig. 5.8).

In these detectors, the sensitive volume is made of a doped bulk and regularly spaced implants. These implants are placed accordingly to the readout structure that will be connected to it. The readout is done through the implant contact, where the ASIC(Application Specific Integrated Circuit) is attached. The ASICs contain all the readout electronics necessary to take the analog pulse, amplify it and digitise the information before sending it

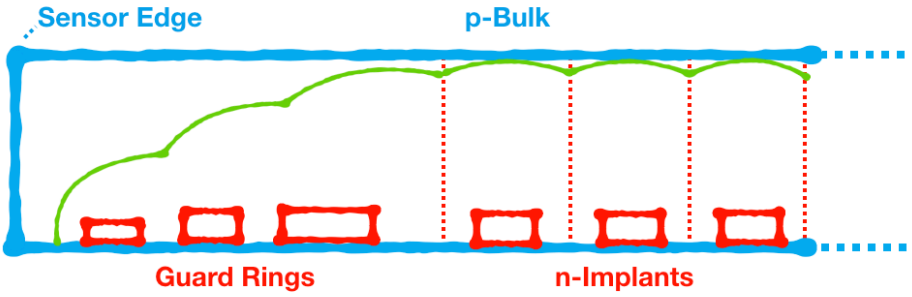

Figure 5.9: Scheme showing the edge region of a sensor, with the guard rings that are responsible for bringing the depletion region (green) in the bulk to zero close to the edge region, avoiding surface charge effects.

out to the connected data acquisition system.

An important feature of pixelated silicon sensors is the guard ring structure. Figure 5.9 shows how the implants at the edge region of the sensor are organised. Guard rings are extra implants places outside the readout implants built in order to guarantee that the potential inside the sensor drops to zero before the physical edge of the sensor. The edge of a sensor is usually composed of a SiO_2 layer formed by the reaction of the silicon bulk with air after the sensors are diced out of the wafer. This SiO_2 layer act as an electron accumulator, creating an area prone to conducting current which leads to sensor breakdown.

The spatial resolution of pixel sensors is related to the size of the pixels, the thickness of the sensor, the bias voltage applied, the amount of charge collected by the readout and the energy resolution of the readout ASIC.

5.3 Radiation Damage Effects

Silicon sensors are exposed to the highest radiation fluxes, due to being the closest to the interaction point. Understanding how different irradiation levels affect their properties is essential to guarantee the appropriate performance throughout an experiment's lifetime.

As discussed previously, the process through which sensors are able to detect the passage of particles is ionising energy loss, where the particles transfer their energy to the electrons present on the silicon crystal lattice. However, it is also possible for particles to undergo Non-Ionising Energy Loss (NIEL) when traversing a material. NIEL happens

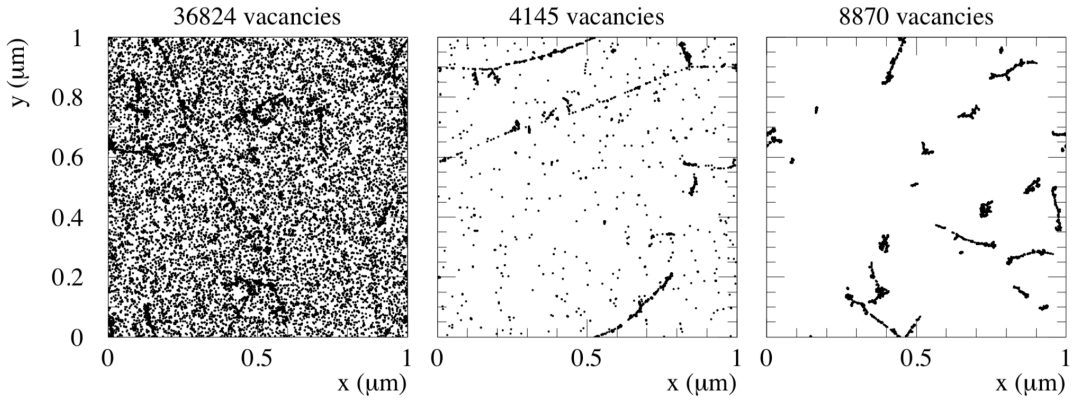

Figure 5.10: Simulation of the vacancies generated in a silicon bulk 1 μm thick when irradiated with 10 MeV protons (left), 24 GeV protons (center) and 1 MeV neutrons (right). All simulations to the same integrated flux of 10^{14} cm^{-2}, taken from [72].

when relativistic particles interact directly with atoms, which might cause a transfer of energy by emission of phonons or a long-lived dislocation of an atom from its original site. When referring to radiation damage, one usually means the compound macroscopic effects of a high number of individual atomic interactions with the crystalline lattice. Macroscopic changes include effects such as changes in free charge mobility and bulk resistivity.

Microscopic damage to the bulk silicon lattice depend on the threshold energy necessary to move one atom. From energies as low as 25 eV the dislocation of a silicon atom is able to generate a interstitial atom and a vacancy [65], which is generally a localised defect [71]. If the atom initially hit acquires an energy greater than 5 keV it might generate more vacancies as it disperses energy through the lattice, which will create a localised cluster defect. The cross section D(E) of the processes that lead to vacancy creation in the lattice depend strongly on the type of particle and energy causing radiation damage. Figure 5.10 exemplifies the different types of damage caused by irradiation with different particles and energies.

Radiation induced defects create a number of allowed states between the valence and conduction bands of the silicon crystal. The energy state of intermediate levels depends on the structural damage to the lattice (Figure 5.11). They are in general formed by individual vacancies/interstitial combining with other vacancies/interstitial. The individual vacancies and intersitial sites can also combine with impurities in the lattice such as Oxygen or Carbon atoms. The new states will alter electric properties of the bulk, with effects

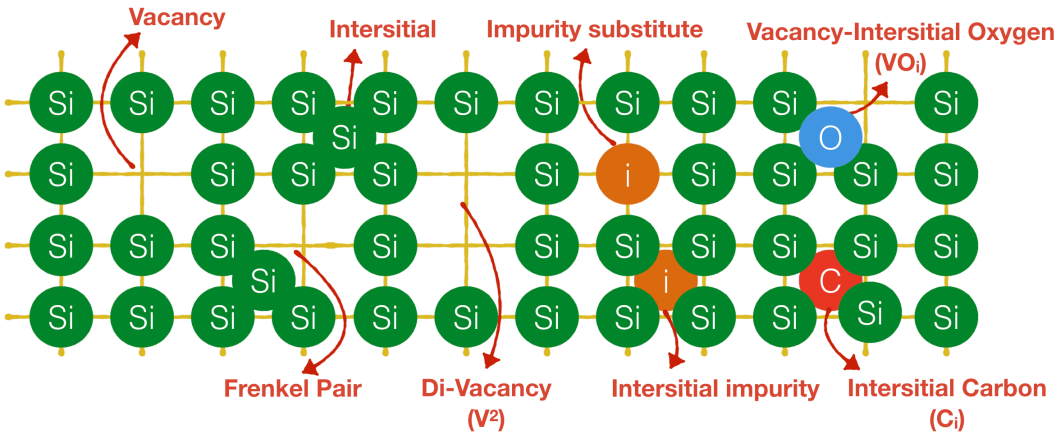

Figure 5.11: Example of common defects introduced in the crystalline structure by irradiation. In the literature they are abbreviated to V or I for Vacancy or Intersitial respectively, or use the impurity element with a v or i subscript [65].

that will be discussed in Sections 5.3.1 through 5.3.5.

In the literature, one refers to NIEL as a shorthand for the assumption that the bulk damage caused by radiation scales proportionally to the displacement damage cross section $D(E)$. Because NIEL is proportional to this cross section, the radiation damage sensitive parameters will be proportional to NIEL. As stated before, both NIEL and $D(E)$ will depend on the energy and type of irradiation. The standard value for the neutron damage cross section is $D_n(1\,\text{MeV}) = 95\,\text{MeV/ mb}$, with the equivalence between $D(E)$ and NIEL being $100\,\text{MeV/mb} = 2.144\,\text{keV cm}^2/\text{g}$ in silicon. With this value, one can rescale the radiation damage from different sources and compare them at the same NIEL level. This rescaling is done by tuning a constant κ, called the hardness factor, to the type of irradiation and energy spectrum. Figure 5.12 contains the $D(E)$ for protons, pions, neutrons and electrons.

It is important to note that, given the different structural differences between damages from different particles, NIEL equivalence is not guaranteed. In fact, non-NIEL equivalence has been seen in different observables such as charge collection at very high fluences ($> 10^{15} 1\,\text{MeV}\,\text{n}_{eq}\text{cm}^{-2}$).

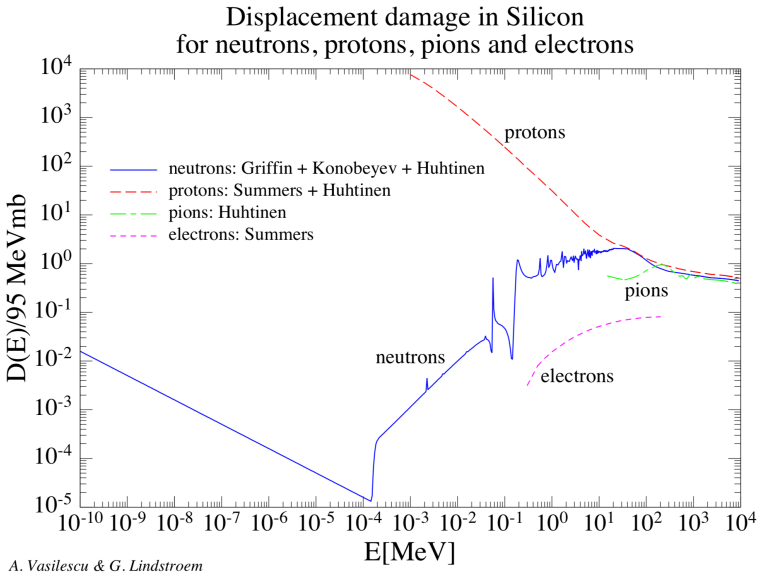

Figure 5.12: Radiation damage cross section as a function of incident particle energy, for different particle types [73].

Defect Annealing

The defects introduced in the crystalline lattice by radiation will not be constrained in their original position in the bulk, being transported by diffusion. At a certain temperature, defects are able to move through the lattice, usually only stopping at ”sinks”, such as the bulk surface. As defects move, more complex defects or clusters can form from the amalgamation of individual ones. If the vibrational energy present in the lattice is larger than the binding energy of a cluster, defects can also dissociate into individual pieces, with at least one of the parts moving away from their original position. The annealing effect in radiation damaged silicon refers to the evolution of the lattice defects reducing the macroscopic effects of radiation damage.

The temperature plays a fundamental role in the movement and dynamics of the defects inside the silicon bulk. The annealing of a specific defect will depend on both the temperature and the time exposed to it. Annealing that has beneficial effects happens rapidly and a slow, performance degrading, annealing effect (”reverse” annealing) takes much longer to occur. The effect of time and temperature on sensors has been studied and parametrised for several different configurations; in Figure 5.13 it is possible to ob-

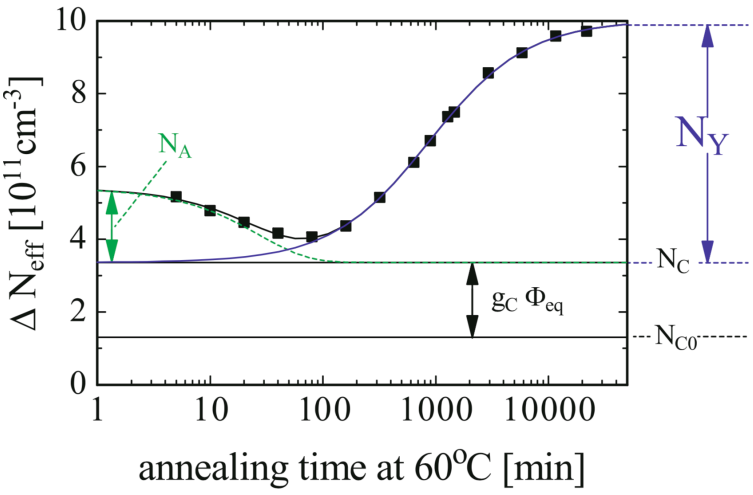

Figure 5.13: Effect of annealing on the effective dopant concentration, discriminated between the initial beneficial annealing (N_A) and the long-setting reverse annealing (N_Y) [65].

serve that the two effects have different timescales.

HEP experiments try to maintain their silicon sensors at sub-zero temperatures at all times. Temperatures around $-5°$C cause the acceptor and donor defects to become inactive by being permanently occupied with free charge carriers. This re-establishes the region that is free of space charges, and defends against reverse annealing, which is important for detector systems expected to run for 10 years. If desired, the sensors can be warmed for short periods of time to profit from the beneficial annealing effect.

5.3.1 Leakage Current Increase

The defects introduced in the lattice create a number of states allowed between the valence and conduction bands of the crystalline structure. Such defects increase the leakage current by acting as generation-recombination centres. The scaling of the current is given by:

$$I_{\text{leak}} = \alpha \Phi_{eq} \text{Vol} \tag{5.23}$$

where I_{leak} is the leakage current at a given bias voltage, Φ_{eq} is the equivalent radiation fluence, Vol is the sensor volume and α is a proportionality constant relating the radiation damage to the leakage current volumetric density. This relation is valid only for bulk current and it does not take into account any effect that might arise from surface currents.

The value of α depends on factors such as the process of silicon fabrication, original dopant concentrations and the annealing history of the silicon sample. Chapter 7 will discuss in detail the current vs voltage results obtained using irradiated VELO Upgrade sensors and how these results were used to tune a model of effective energy levels in silicon at very high fluences.

5.3.2 Charge Collection Loss

The creation of cluster defects in the lattice gives rise to traps that absorb charge generated by the passage of MIPs. These charge traps tend to have a lifetime longer than the shaping time of the electronics, meaning that the trapped charge is released long after the original signal has gone through the pre-amplifier. The trapping then has two practical effects to the detection for particles: it reduces the amount of charge collected for one hit and it increases the average noise level due to the constant out-of-time movement of charges released from traps inside the bulk. Another effect that will play a role in heavily irradiated sensors is the long lifetime of traps deep into the energy gap, that add an additional charge distribution to the bulk. The lifetime of a trap in the lattice (τ_{eff}) is given by:

$$\frac{1}{\tau_{\text{eff}}^{e,h}} = \sum_t N_t(1 - P_t^{e,h})\sigma_t^{e,h} v_t^{e,h} \tag{5.24}$$

where N_t is the trapping defect concentration, P_t the probability that this given defect is already occupied, σ_t is the charge capture cross section and v_t is the thermal velocity of the carriers. The summation runs over all different traps and has different values for electrons and holes [74].

5.3.3 Effective Doping Concentration

Changes in dopant concentration will change the electrical properties of the sensor bulk. The effective dopant concentration N_{eff} is the equivalent dopant concentration a sensor bulk would have in order to reproduce the electrical behaviour of an irradiated sensor and

is parametrised by the Hamburg model:

$$N_{\text{eff}}(\Phi_{eq}) = N_{\text{eff}}(0) - [N_a(\Phi_{eq}, T_a, t) + N_C(\Phi_{eq}) + N_Y(\Phi_{eq}, T_a, t)] \tag{5.25}$$

where Φ_{eq} is the total radiation flux in equivalent 1 MeV $n_{eq}cm^{-2}$, and N_a, N_C and N_Y are, respectively, the annealing, stable damage and reverse annealing components of the concentrations in the bulk. T_a and t are the annealing temperature and the length of time the sensor was at that temperature. Each of this terms has its own functional form, with parameters described by material properties and investigation of silicon diodes at different irradiation levels. They are discussed thoroughly in [71].

The depletion voltage, as stated in Equation 5.11, depends directly on the dopant concentration, which will change with the accumulated bulk damage (N_{eff} substitutes N_a in Eq. 5.11). Each of these terms will impact the bulk, in general acting as a p-doping. This produces a type inversion for n-type bulk sensors, which will become p-type bulk. As the silicon is being damaged the effective depletion voltage initially decreases, reaching a minimum (Fig. 5.14), after which the silicon has type-inverted and is now effectively a p-type sensor. Each of the terms in Eq. 5.25 has its own parameters, determined by measurements of irradiated samples.

As an example, Figure 5.14 shows the effective doping concentration of all of the original VELO sensors as a function of the expected radiation flux superimposed with the Hamburg model predictions, showing an overall good agreement.The inversion point does not go all the way down to zero due to the voltage still needed to drift the charges and fight charge trapping.

5.3.4 Double Junction

As a last note on effects to be considered on irradiated silicon sensors, is the effect of double junction and charge multiplication. As the bulk becomes more and more damaged, particularly with deep energy-level traps, free charges will become spatially bound. This space charge adds to the original dopant distribution changing the configuration of the electric field, potentially departing from a linear or abrupt junction.

In fact, it has been observed that instead of maintaining the electric field uniform, at the

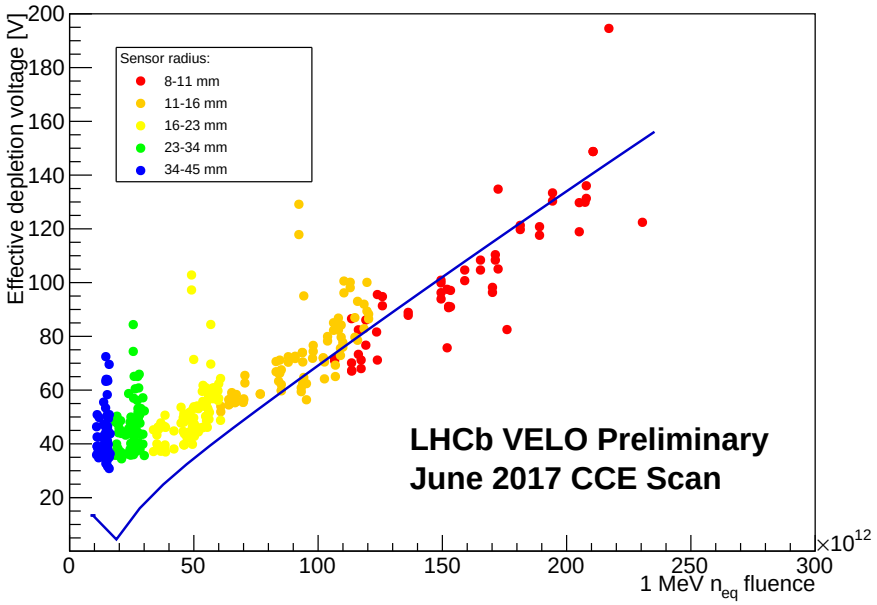

Figure 5.14: Example of the effective depletion voltage as a function of fluence. Effective depletion voltage is plotted as a function of fluence corresponding to their distance to the interaction region. The colours represent a radial region on a sensor, and as expected the depletion voltage is higher on the most irradiated sensors. The line plotted is the depletion voltage value predicted using the Hamburg Model [75].

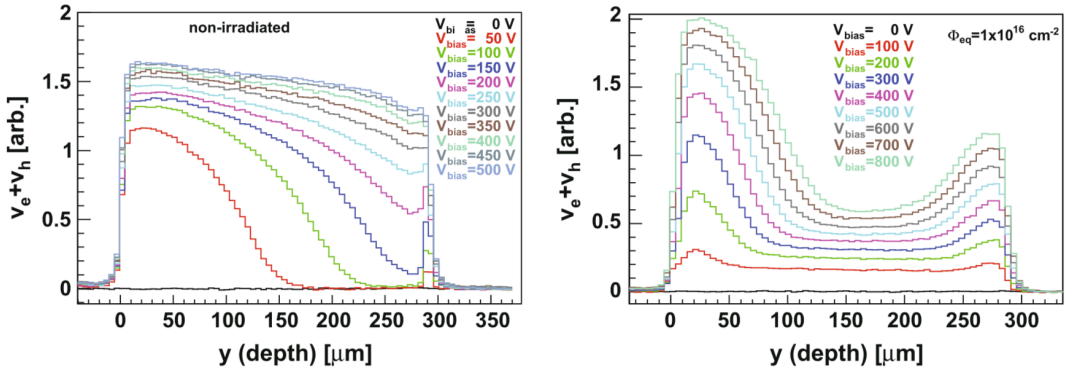

Figure 5.15: Velocity of charges generated in a silicon bulk illuminated by a laser at different depths. The higher the velocity indicates a higher electric field. On the left, is shown the monotonic behaviour of a non-irradiated sensor, and the double peaked structure observed in irradiated sensors on the right [65].

high fluences ($\approx 10^{15}$1 MeV n_{eq} cm^{-2}), the shape of the field changes. It assumes a double peaked shape with high electric fields at each side of the bulk, sandwiching a "undepleted" center. This effect has been observed in irradiated sensors using edge Transient Current Technique(TCT) scans (Fig. 5.15). and grazing angle techniques.

The reason for this effect, even though the damage is fairly uniform within the depth of the bulk, is the previously mentioned deep energy-level traps. Thermally generated electrons and holes drift to opposite sides of the sensor, but instead of travelling through the bulk, they get trapped while drifting, creating an asymmetric space charge distribution. This accumulates electrons mostly on the n-side of the junction and holes on the p-side, adding another space charge contribution to the one present in the original doping profile (and modified according to Eq.5.25). This leads to a parabolic shape in the electric field, with strong electric fields at each end and a non-zero field value inside the bulk [76] (Fig. 5.16). Modelling of the field inside the silicon is obtained through TCAD[5] simulation methods, which have been used to confirm the results obtained experimentaly.

In summary, the effect of a double junction in the silicon sensor is the formation of two regions with high electric field and a non-zero field region in the middle of the bulk, even below the expected depletion voltage.

[5]TCAD is an acronym Technology Computer-Aided Design, a type of simulation software that can model semiconductor behaviours through finite element methods.

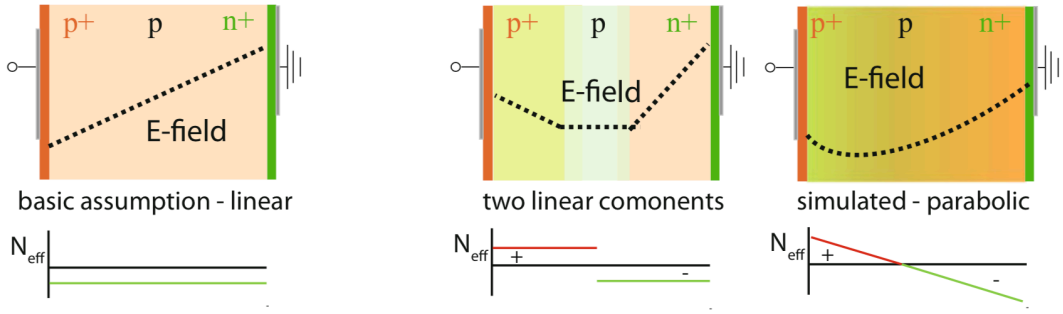

Figure 5.16: Different models for the junction configuration of irradiated sensors. The rightmost image corresponds best to what is observed in experiments [65].

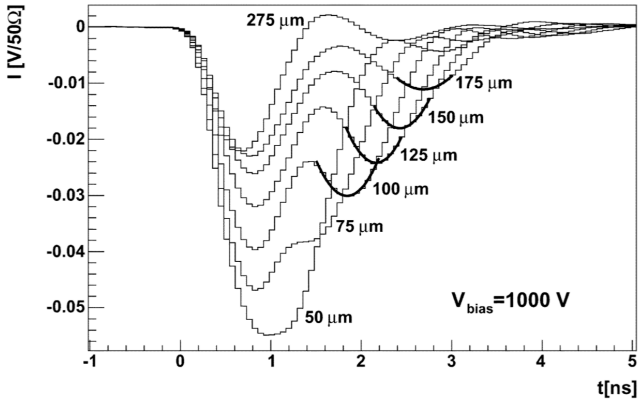

Figure 5.17: Edge TCT scan of a sensor irradiated to 5×10^{15} 1 MeV $n_{eq}cm^{-2}$. It is possible to see the clear formation of a delayed peak associated with the injection of charge, a signal consistent with charge multiplication [77].

5.3.5 Charge Multiplication

In general, as charge collection efficiency degrades, it becomes necessary to increase the operational bias voltage in order to maintain a high signal to noise ratio. The increase in voltage has not so much to do with expanding the depletion region, but ensuring charge collection within the integration time. A collateral effect of increasing the bias voltage is that, at the highest fluences expected for the high luminosity LHC upgrade (approx. 10^{16} 1 MeV $n_{eq}cm^{-2}$) the field in the bulk is large enough to generate charge multiplication by impact ionisation. This is the same mechanism described when discussing avalanche breakdown earlier in Section 5.2.2.

The charge multiplication effect, measured in [77], seems to occur due to a very high

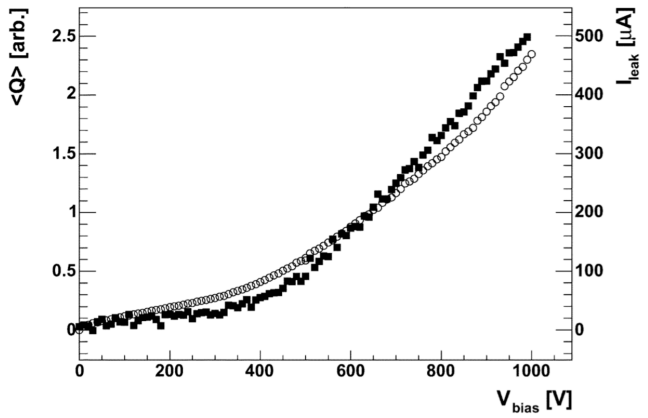

Figure 5.18: Comparison between the observed total charge collected (<Q>, solid markers) and leakage current (open markers). This suggests that the multiplication observed in <Q> also occurs in thermally generated charge [77].

field region formed close to the strip junction (Fig. 5.17). Charge multiplication by itself is not a negative feature, as it can improve the signal yield if it results in a higher signal-to-noise ratio, or time resolution. It has been shown that there is a correlation of the collected charge and the measured leakage current (Fig. 5.18). While it is not clear whether experiments want to use this charge multiplication effect during operation or not, there are new sensor designs implementing a gain layer in the silicon bulk, in order to obtain fast time resolution ($\approx 10\,\mathrm{ps}$) detectors [78].

6 | VELO Upgrade

The upgrade of the Vertex Locator (VELO) is one of the biggest changes in the experiment going from the current LHCb to the version that is being commissioned for Run III. The construction of a new detector is motivated by the change in LHCb's readout rate from 1 to 40 MHz and the necessity of a higher granularity at new operational high luminosity conditions in Run III. The changes in design ensure that the upgrade track and vertex reconstruction performance is at least as good as the original VELO, even with the higher predicted hit density. In this Chapter the new VELO is described in detail along with contributions to the overall project.

6.1 Physics Impact and Requirements

The increased luminosity will lead to a higher particle flux going through the VELO at each bunch crossing: the average number of visible collisions per bunch crossing will jump from 1.7 to 5.2. This will affect the VELO operation in two ways: the higher particle flux means that a higher channel density is needed in order to keep occupancy low and the radiation damage the VELO upgrade will experience is more severe than the original VELO by a factor of 50. The new detector will need to operate in these more stringent conditions whilst maintaining the excellent tracking and vertexing performance.

To reduce occupancy on the readout channels, the change from microstrip to pixel is beneficial, since it removes fake hit association coming from combining hits from strips in stereo angles (Figure 6.1). The change to a pixel readout comes with the price of having far more channels (N^2 vs $2N$) for the same channel pitch, increasing the necessary readout bandwidth.

The VELO is responsible for identifying the positions of both the primary vertices

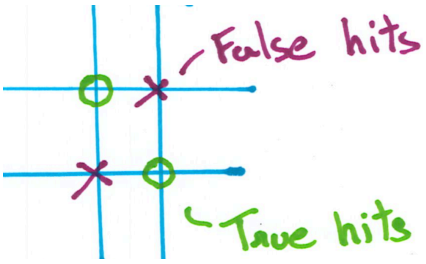

Figure 6.1: In a strip readout configuration, combinations of hits are indistinguishable. This problem increases with the occupancy of a strip detector, ultimately the number of false hit combinations introduces fake tracks in the reconstruction.

e

and secondary vertices generated by particle decays that happen inside of the VELO acceptance. To do so, a good spatial resolution is fundamental. One useful measure of vertexing quality is the the impact parameter resolution (σ_{IP}), which refers to the distance of closest approach between a track and a primary vertex. In one dimension, the IP_x is defined as the distance between the track and the primary vertex in the x-axis at the point of closest approach between the track and vertex. The IP is important to identify displaced secondary vertices, such as decaying b-hadrons. The IP resolution is affected mostly by the relative positions of detected hits, the resolution of such detections and by the Coulomb multiple scattering between the PV and the first measurement point. Considering a model n which there are only two measurement points per track, the 1-dimensional (transversal to the beam direction) impact parameter resolution in LHCb can be approximated to [79]:

$$\sigma^2_{IP_{x,y}} = \frac{\sigma_0^2}{(z_2 - z_1)^2}[(z_1 - z_v)^2 + (z_2 - z_v)^2] + \frac{R^2}{p_T^2}\left(\frac{13.6\,MeV}{\beta c} q\sqrt{x/X_0}[1 + 0.038\ln(x/X_0)]\right)^2 \tag{6.1}$$

where σ_0 is the hit measurement error. The z-axis points in the beam direction such that z_1, z_2 are the z positions of the first and second measurement points respectively and z_v is the the z-axis position of the PV. R is the radial distance from the first measurement point to the PV, x/X_0 is the amount of traversed material in the first measurement plane and p_T the transverse momentum[1]. At high momenta, the dominant effect comes from the resolution of the hits. For lower momenta, the multiple scattering term starts to play a role. This term increases quadratically with the radius of the first measured point, meaning that

[1] for definitions of β, c, x and X_0, see Section 5.1

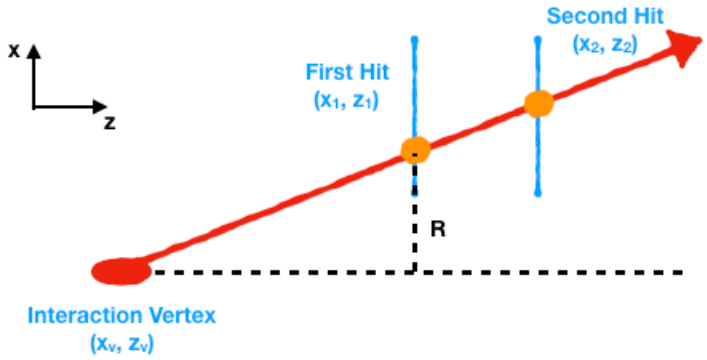

Figure 6.2: The measurement of the impact parameter is impacted by the hit resolution, the distance between measuring planes of the detectors and the multiple scattering.

for low transverse momenta particles it is very beneficial to have the sensors as close to the interaction region as possible.

The IP resolution can be improved by changing the radial distance of the VELO sensors to the interaction region, from 8 mm down to 5.1 mm. The comparison between VELO IP performance compared to what is expected from the VELO Upgrade is shown found in Figure 6.3, where one can observe that the IP_x resolution for the upgrade is similar at high p_t and improved at low p_t values.

However, being so close the interaction region increases the total fluence observed by the VELO during operation. At this radius the sensors are exposed to a very non-uniform flux that decreases approximately 10-fold from the most irradiated corner to the least irradiated corner of one sensor. Monte-Carlo simulations were performed in GEANT4 [81] and FLUKA [82] in order to estimate the radiation profile for the VELO region. Figure 6.4 shows the flux as a function of z and R (notice how the irradiation profile varies with the z-axis inside the VELO).

In order to achieve the best coverage of acceptance and guarantee that particles inside LHCb acceptance will have at least 3 hits detected, the position and number of sensors was optimised using ray-tracing and GEANT4 simulations. Figure 6.5 displays the nominal positions and organisation of the sensor stations in the VELO Upgrade.

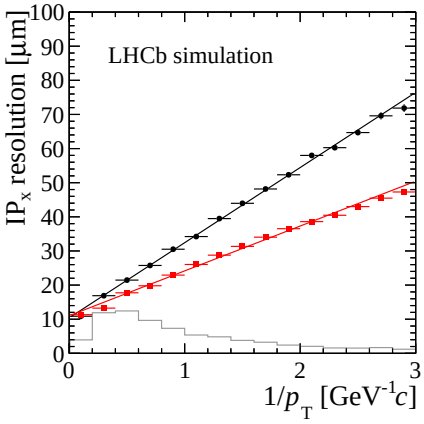

Figure 6.3: Impact parameter resolution as a function of $1/p_T$ on the x axis, comparing the original VELO (black) and the expected performance of the VELO Upgrade (red). The histogram (grey) shows the expected $1/p_T$ distribution of tracks [80].

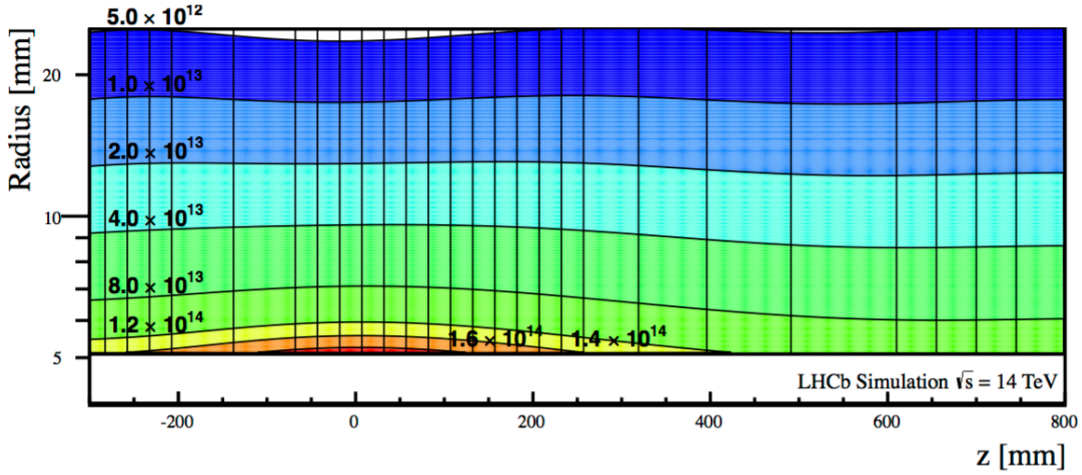

Figure 6.4: Radiation flux per fb^{-1} in units of 1 MeV n_{eq}/cm^2 [80].

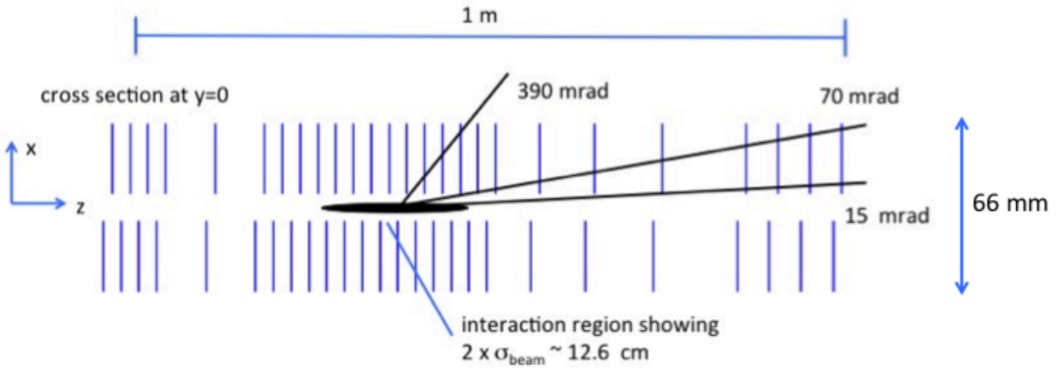

Figure 6.5: Positions of all 26 VELO Upgrade stations and the 52 modules [80]. The axis x denotes the horizontal direction and z the beam direction of travel.

6.2 Mechanics

The VELO Upgrade will use a very similar structure to the one used for the original VELO. The beam-pipe in the interaction region is substituted by the VELO that contains two distinct vacua: the beam volume and the detector volume, separated by a thin foil. The detector modules are held horizontally and mounted on a moving frame that allows for the sensors to be extracted from the beam's path during LHC beam injection. Once the LHC declares stable beams the modules are brought back into position for physics data acquisition. The overall VELO structure can be broken into a few parts: Modules, RF Box and Vacuum Hood. This section will describe each of these parts.

Modules

The modules are the parts inserted in the VELO vacuum, holding sensors, readout electronics and delivering cooling. There will be 52 modules constructed from a silicon substrate containing microchannels for cooling (see next section). Each module will be instrumented with four tiles, with two tiles[2] and GBTx ASIC[3] on each side. Figure 6.6 contains a rendering of what the module will look like once it is completely assembled. The positions of detectors are set such that there is no gap between sensors on either side of the module. The sensors positioned closest to the beam have a 5 mm overhang from the substrate, to

[2] A tile is a sensor bump bonded to three VeloPix readout ASICs, both described later.
[3] ASIC for managing control signals

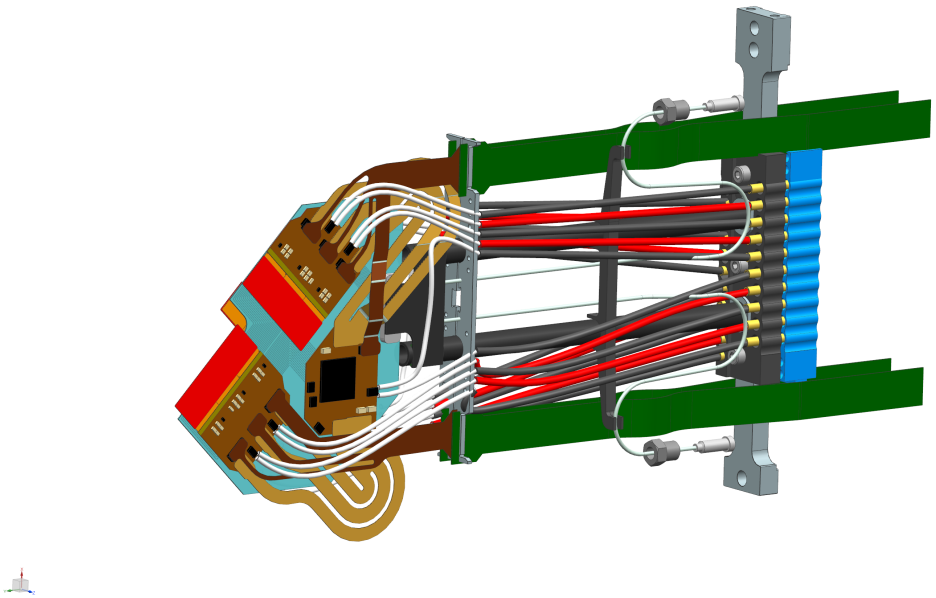

Figure 6.6: Module Fully Assembled. Observe the silicon substrate(teal), soldered to the fluidic connector which is glued to carbon mid-plate(blue), held by the two black carbon fibre legs to connected to the module foot.

minimise material. The ASICs are connected to three Kapton hybrids through wire-bonds that route the signals across the module.

The module will be held by a carbon fibre plate glued directly to the fluidic connector, shown in Fig. 6.7, having also pipes that are the inlet and outlet of coolant. The whole module is secured at the module foot, which is responsible for sustaining the weight of the module and connecting it to the movable frame in a similar way to the original VELO. Figure 6.6 depicts the design of a fully assembled module.

RF Foil and Vacuum Hood

The RF box is responsible for providing the needed continuation of conductive material for the beam image charges. It is also responsible for the separation between the VELO secondary vacuum and the LHC primary vacuum and protecting the electronics from wake-field generated by the beams. The whole box is machined down to 500 µm thickness from a single Aluminium block. The region close to the sensor position is corrugated with a

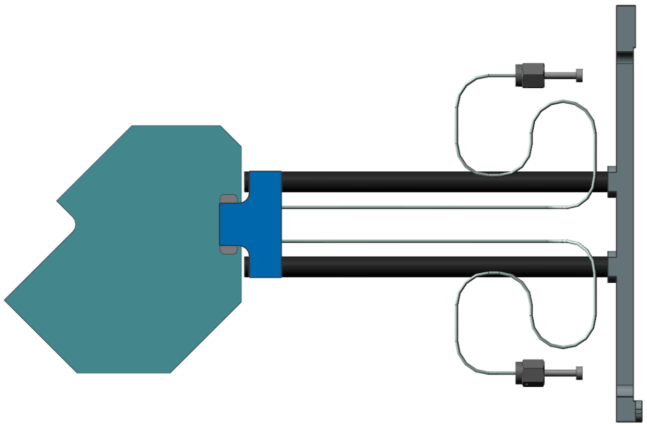

Figure 6.7: Module Mechanical Assembly. Observe the silicon substrate(teal), soldered to the fluidic connector which is glued to carbon mid-plate(blue), held by the two black carbon fibre legs which are connected to the module foot.

shape optimised in simulations in such a way that minimises the average amount of material traversed by particles coming from the interaction point (Fig 6.8). To reduce the material even further this corrugated region is chemically etched down to a thickness of 250 μm, leading to a nominal distance of 890 μm to the edge of the sensors; this distance is important given that any damage to the foil would lead to a leak between LHC and VELO vacuum environments.

The Vacuum Hood is where the RF Foil is attached and serves as housing for the modules, CO_2 pipes, data and power cables and the free space needed to accommodate the motion of the VELO. It is also where the feedthroughs can be found, making the connection between the VELO vacuum and the outside environment. Figure 6.9 contains a design of what the VELO detector will look like when assembled: moving from the beam centre out, there are the modules, which are fixed at the base, there is a space that allows for the bending of cables and pipes when the VELO moves and finally the vacuum feedthrough that takes the signals out of the VELO vacuum. An extra safety feature is the isolation vacuum at the top of the image that prevents ice formation on the CO_2 valves going in and out of the VELO.

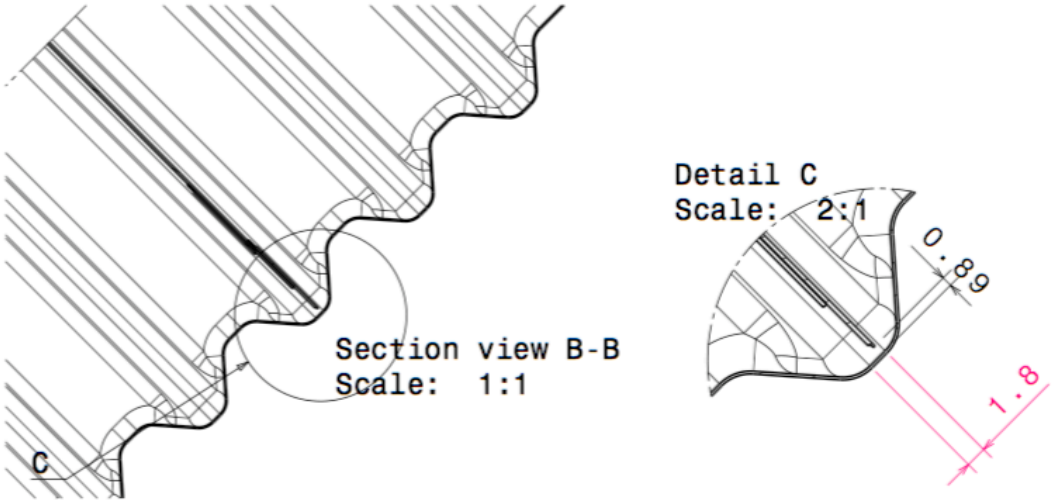

Figure 6.8: VELO nominal module position. The corrugations on the foil allow for a closer approach to the interaction region while minimising material. The distance between the foil and the module is 0.89 mm.

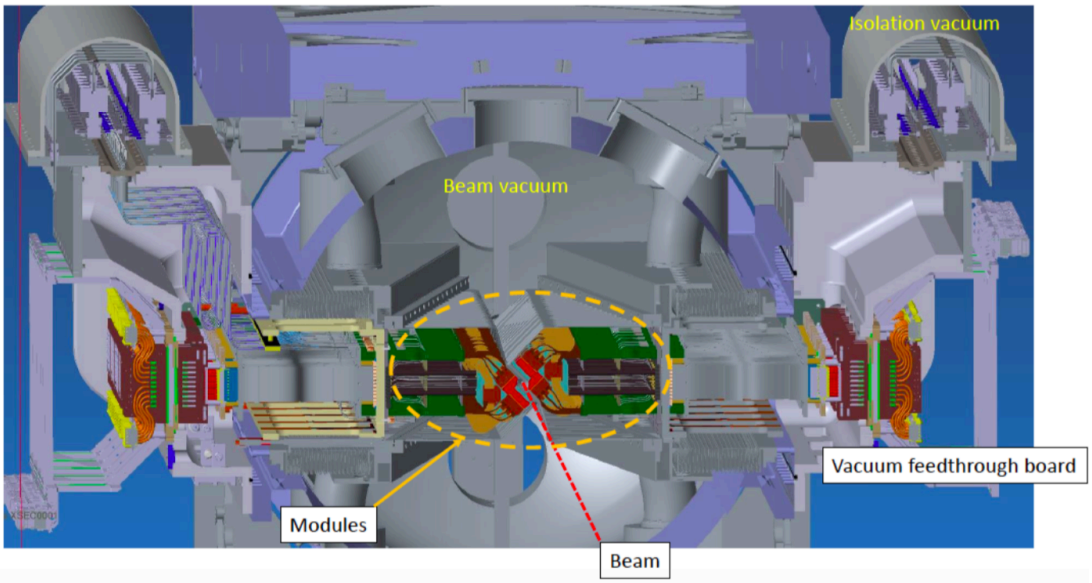

Figure 6.9: Full VELO design, with the most important features outlined.

Module Item	Power [W]	Quantity per Module
Sensor	1	2
VeloPix ASIC	2	12
GBTx ASIC	2	2

Table 6.1: Estimated power consumption of active items on the module. The leakage current after full irradiation in the two outer sensors is much smaller, so they are not included here. This adds up to 30 W power to be dissipated.

6.3 Cooling

The VELO upgrade cooling solution was chosen to be integrated directly into the module structure by the use of a silicon substrate with internal microchannels. They bring evaporative CO_2 cooling to the sensor and readout electronics while minimising the amount of extra material. Due to the chips and sensor all being made of the same material as the substrate (silicon), an extra advantage is the complete match of thermal expansion coefficients between these items. The cooling system must achieve the goal of removing 1.5 kW power from all the modules during operation; the power budgeted for each module element can be found in Table 6.1. This power is mostly coming from the VeloPix hybrids and GBTx, although a contribution from the sensor leakage current is not negligible at the end-of-lifetime irradiation levels.

A CO_2 cooling plant will be built in the LHCb cavern in order to provide liquid CO_2 for both the VELO and the UT[4]. The design of the plant is such that the guaranteed temperature of operation of the system is -30 °C, however this does not include the losses incurring from transport of the CO_2.

6.3.1 Microchannel Cooling

The microchannel design was optimised to deliver the dual phase CO_2 directly to the VeloPix and GBTx readout ASICs. Due to the 5 mm overhang of the sensors, the most irradiated sensors will not be directly attached to the cooling substrate, operating at a slightly higher temperature than the rest of the module.

[4]In fact, two plants will operate separately for the UT and VELO, and either one can support both systems in case one fails.

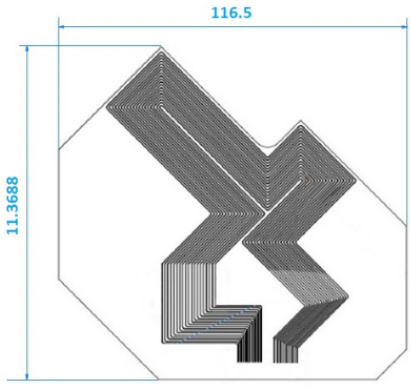

Figure 6.10: Microchannel design, size measured in mm.

The microchannel substrate is formed by photolithographic etching of a silicon wafer with the desired channel pattern, which then is covered by a second, 260 µm thick, silicon wafer that is bonded as a "lid". This is done through the process of hydrophobic bonding, effectively becoming one piece of silicon. The wafer is then thinned down to a total thickness of 500 µm before the in- and outlets connector metallisation is deposited and holes for the connectors are etched.

The nominal cross-section of the 19 channels is 120 µm × 200 µm with lengths that vary from 230 µm to 292 µm depending on the path of the channel through the substrate. They are designed in a racetrack like path along the whole substrate from the inlet to the outlet (Figure 6.10). In the initial 40 µm of the flow, the channels have a restricted cross-section of 60 µm × 60 µm. The change from the restrictions to the nominal cross-section cause a sudden drop in pressure in the liquid, that triggers the change from sub-cooled liquid to dual-phase flow. The restrictions also help decoupling the flow of each channel from all the others.

The pressure resistance of the microchannels was investigated by varying the width and the thickness of the silicon on small samples that used a thick pyrex plate as base. At the nominal temperature the CO_2 liquid and gas saturation pressure is about 20 bar. In case of failure of the cooling system the microchannels should be able to withstand the room temperature pressure of 60 bar. For safety reasons, the microchannels are required to be tested up to 186 bar.

The temperature performance of the microchannels was tested by gluing heating elements on the substrate. They mimicked the power dissipation of ASICs and the sensor.

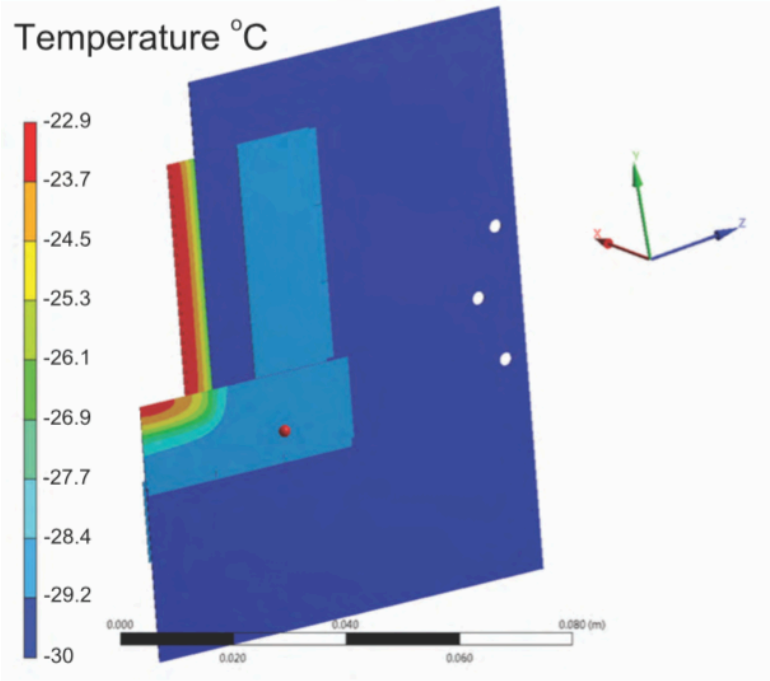

Figure 6.11: Thermal simulation of the substrate temperature with the power dissipation of modules and sensors, using finite element analysis software ANSYS [80].

The difference in temperature of 7 °C with respect to the substrate (at −30 °C) is very similar to what was expected from thermal simulations using finite element analysis [80] (Figure 6.11).

6.4 The VeloPix

The readout ASIC for the VELO Upgrade is called VeloPix, and it is based on the Medipix family of CMOS pixel detector readout chips, more specifically the Timepix3 chip. Figure 6.12 shows a scheme of the VeloPix and the organisation of its pixels [83]. The ASIC was designed using 130 nm CMOS technology; it contains a matrix of 256× 256 pixels, each pixel with a size of 55 µm × 55 µm, grouped in super-pixels of size 4x2 pixels. Each pixel contains a complete analog pre-amplifier, threshold discrimination and test pulse circuitry.

VeloPix was designed to be radiation tolerant up to 400 MRad, including single event upset (SEU) tolerance, achieved by designing all the clock gates, clock multiplexers, finite state machines and registers with triple redundancy [84].

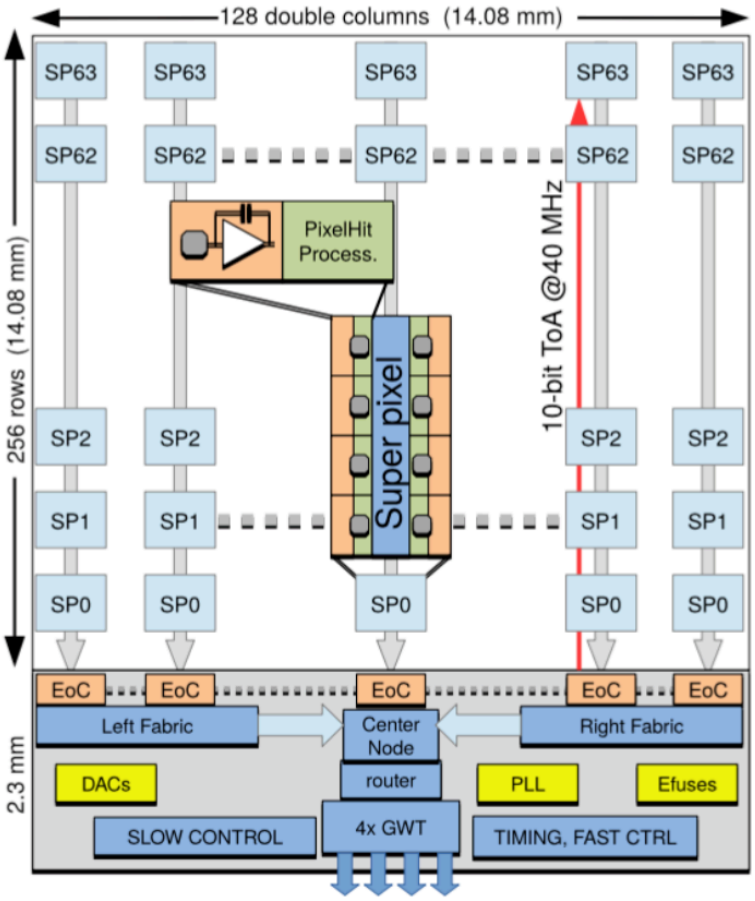

Figure 6.12: VeloPix readout ASIC floor plan. Every pixel is responsible for zero-suppressed binary readout, which then is timestamped in the Super Pixel [83].

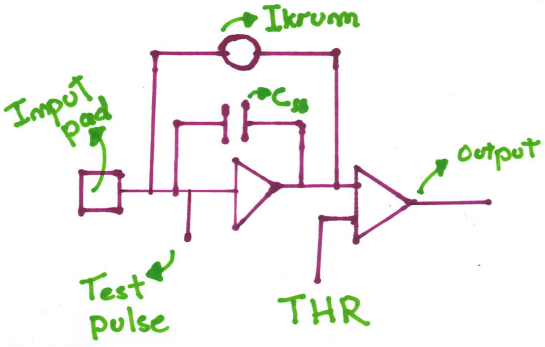

Figure 6.13: Analog pre-amplifier scheme present in each pixel. The signal incoming in the input pad is amplified and goes through a threshold comparison and output a digital signal which is then propagated to the pixel matrix readout.

The output of the readout chips is done through up to 4 high speed GWT[5] links, each operating at 5.12 Gbps. The ASICs can be configured to use 4, 2 or 1 links, depending on the how close that particular chip is to the interaction region.

6.4.1 Signal, Thresholds and Timestamps

As discussed in Chapter 5 a charged particle transversing the sensor will deposit some charge in the sensor, which is picked up by the VeloPix input pad. This signal goes directly into the charge sensitive pre-amplifier. This pre-amplifier is built with a 4 fF feedback capacitor and a Krummenacher [85] leakage current compensation scheme (Fig.6.13). The Krummenacher current (IKrum) can be tuned with a DAC in the ASIC to change the decay time of a signal in the pre-amp back to the baseline level. On the Timepix3, when collecting electrons, the IKrum DAC also sets a limit for the leakage current compensation.

After the preamp, the signal is compared to a voltage threshold, defined by two DAC values: a global 14-bit DAC applied to all pixels and a 4-bit per pixel DAC. The 4-bit DAC is used to make pixels responses uniform over the whole ASIC.

The equalisation procedure is how the values of the 4-bit local DAC are decided, recording how many noise counts are detected using different global threshold values. The global threshold is scanned for all pixels twice, one with the 4-bit local threshold set to 00 (minimum value) and another with it set to 15 (maximum value). As the global threshold

[5]Gigabit Wireline Transceiver

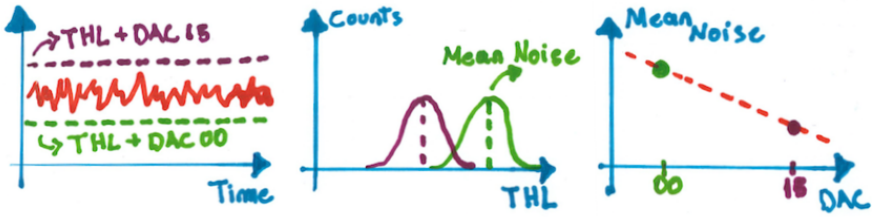

Figure 6.14: Steps taken during the equalisation of a single pixel. On the left a single pixel has a paddrticular noise level, the threshold can be altered by setting a local 4-bit DAC (between 00 and 15). On the centre, if the global threshold is varied with a fixed local threshold, one can find the DAC value with maximum noise counts. By scanning the global threshold with the two extreme value of the local threshold, one can parametrise how the maximum number of noise counts varies with the local DAC. The equalisation then tries to minimise the variance on the position of the noise for all pixels by setting the local threshold accordingly.

is varied, the number of counts in a single pixel will raise, reach a maximum then fall as the threshold goes above the noise. By having the noise curve taken at two extreme local threshold settings, one can model how the noise position varies with the local threshold for each pixel (Figure 6.14). The equalisation step is to use this local parametrisation to tune each pixel in such a way that the variance of the maximum of the noise distribution between all pixels is minimised. The equalisation is a routine procedure before data taking and is present in all chips from the Medipix family.

If the collected signal is higher than the threshold, a hit is recorded. For the VELO operation, the VeloPix will only have binary readout, meaning no information on the amount of charge collected is available. This hit is routed through the super-pixel which performs the Time-of-Arrival measurement with a clock of 40 MHz recorded in 9-bits. For a given 25 ns interval, a packet containing the super-pixel position, and the address of all pixels with a hit in the super-pixel is formed (Figure 6.15). This packet is then propagated down its column to the periphery of the chip where it will be sent to a router. The router is responsible for distributing the packets to all active GWT readout links that will transport the data to the DAQ system. These GWT links output data using the so called GWT protocol. In the VELO only the ASICs closest to the beam will have all 4 links active.

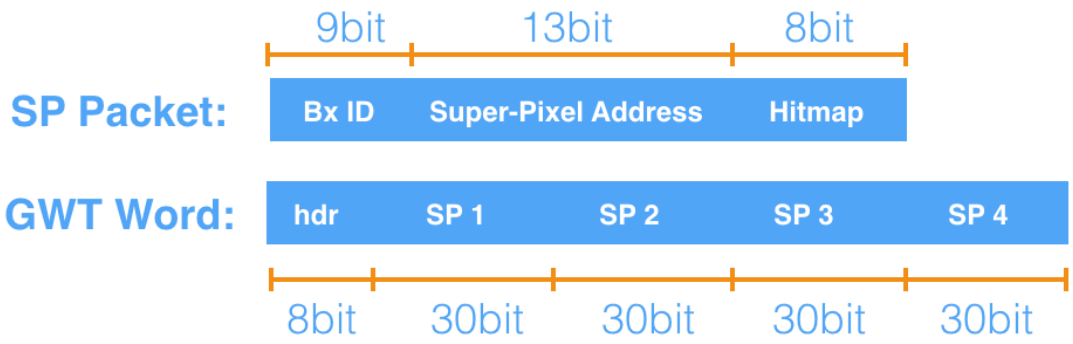

Figure 6.15: Structure of the VeloPix output. The Super-Pixel(SP) packets contains the location of the SP, timestamp and location of pixels with hits on that SP. The Velopix will output 4 SP packets in one GWT word.

Threshold Variation

The first wafers containing VeloPix chips were produced during the second half of 2016. After preliminary tests were done to validate communication and the correct functioning of the ASIC, irradiation tests were performed to guarantee the correct operation under irradiation and that the chip had no lasting effects due to radiation damage. These tests consisted of bringing the VeloPix to an x-ray irradiation facility where the chip was irradiated to 400 MRad. During the irradiation, several equalisations were done, to investigate if any change occurred to the threshold levels due to the irradiation.

Figure 6.16 shows the mean noise value obtained in 32 pixels distributed uniformly throughout the matrix. The noise values were obtained by performing the noise scan step of the equalisation with the local DAC set to 00. This scan was done in 16 irradiation steps from 0 to 400 MRad. There is not any apparent trend of the observed noise levels of the chip as a function of irradiation. Figure 6.17 tracks how the average noise level of individual pixels changes as a function of irradiation dose with respect to the non-irradiated values. Although an increased spread of noise measured seems to appear as a function of irradiation no systematic trend on the average noise is observed. This is desired as it shows that the signal-to-noise ratio will not suffer from further decrease due to irradiation effects to the ASIC.

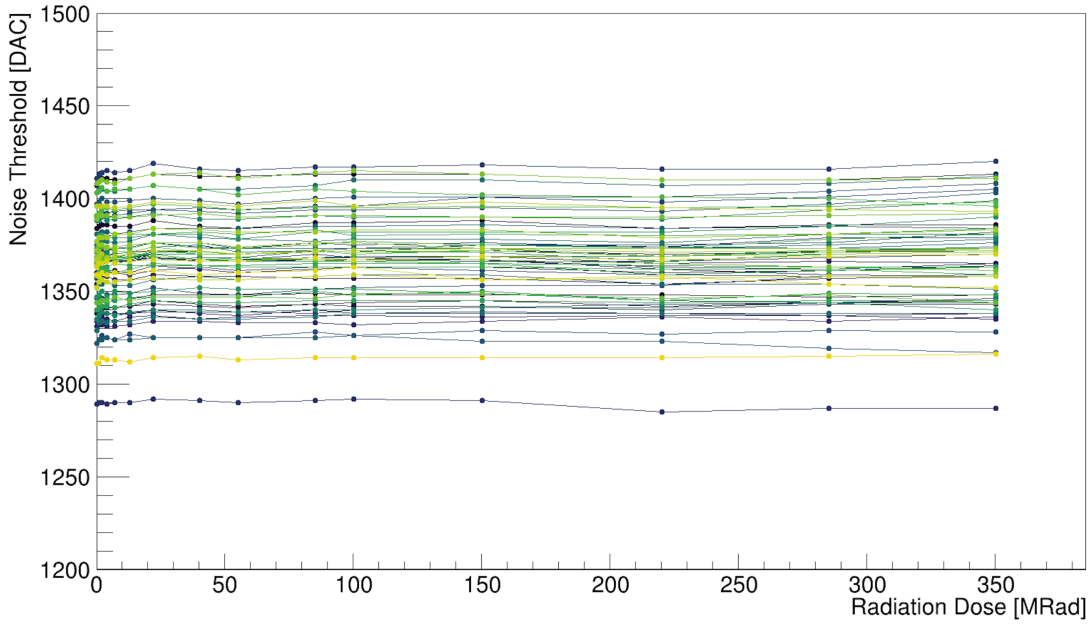

Figure 6.16: Evolution of the base threshold level of 32 individual pixels in the VeloPix matrix as a function of the radiation dose. No trend on the threshold values as a function of irradiation was observed.

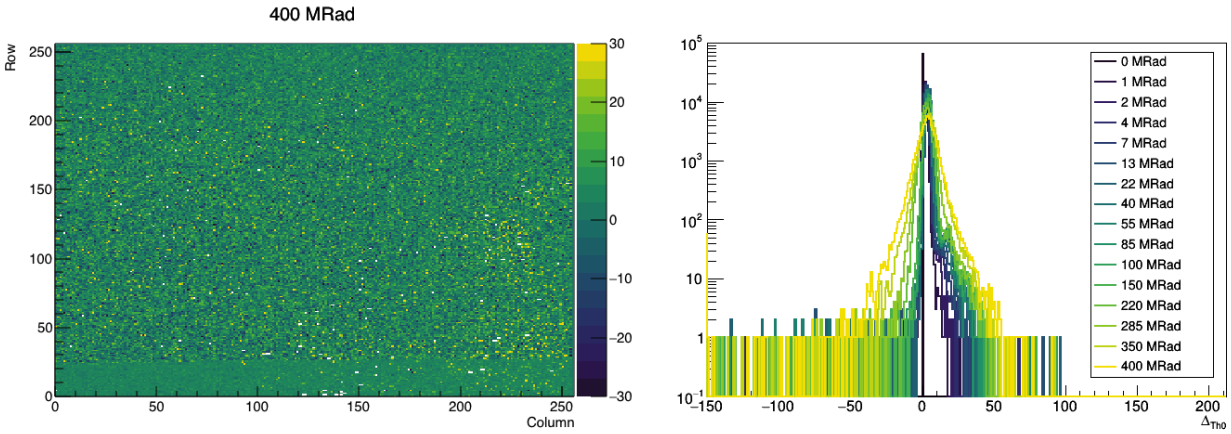

Figure 6.17: Difference in the ASIC noise level observed pixel by pixel when compared to the noise level before irradiation, as measured in an ASIC without a sensor. A 2D map (left) displaying the variation on the pixel matrix and a series of histograms (right) showing that the noise levels do not drift to higher values due to irradiation.

6.5 Readout Electronics and DAQ

Figure 6.18 is a scheme of the data acquisition system from the VeloPix to the MiniDAQ readout, which later sends data to the Event Builder Farm (discussed in Chapter 2). The GWT links are sent through copper data tapes to the vacuum feedthrough, which interfaces the VELO secondary vacuum to the LHCb cavern environment. Immediately after this feedthrough there is the Opto and Power Board (OPB), containing the transducers that receive the signal from the copper tapes and re-transmit them in optical fibres from the LHCb cavern to the mounting racks where the MiniDAQs are located ≈100 m above. The OPB is also responsible for supplying the correct voltages for the ASICs in the module and relaying control signals. The slow control, timing and fast control of the VeloPix ASICs is mediated by the GBTx ASIC present in the module (denoted TFC, ECS and CLK signals in the Figure 6.18).

The MiniDAQ is the general board developed by LHCb for all of its sub-detectors and it consists of an Aria-10 FPGA installed in a PC through a PCIe port. The FPGA is responsible for the data manipulation of the packets before relaying them to the event filter farm. In the VELO, each module will be readout by one MiniDAQ. The software implementation of the MiniDAQ is split in two: the TELL40, responsible for reading out data coming from the ASICs, and the SOL40, responsible for communication of control signals with the electronics in the module. The data output by the VeloPix is naturally asynchronous, due to the trigger-less readout, and so the TELL40 software has to decode the GWT words coming from all data links and sort them in time, and then organise a packet that contains all hits with the same timestamp coming from that module. An additional feature is the addition of an extra bit, the IsoCluFin, responsible for flagging the presence of more than one hit in that particular super-pixel (which might speed up data processing in the trigger farm). Another feature being studied in the TELL40 firmware is the ordering of hits by azimuthal angle, which can improve tracking performance during event reconstruction. Figure 6.19 exemplifies what the data output from a module looks like after MiniDAQ processing.

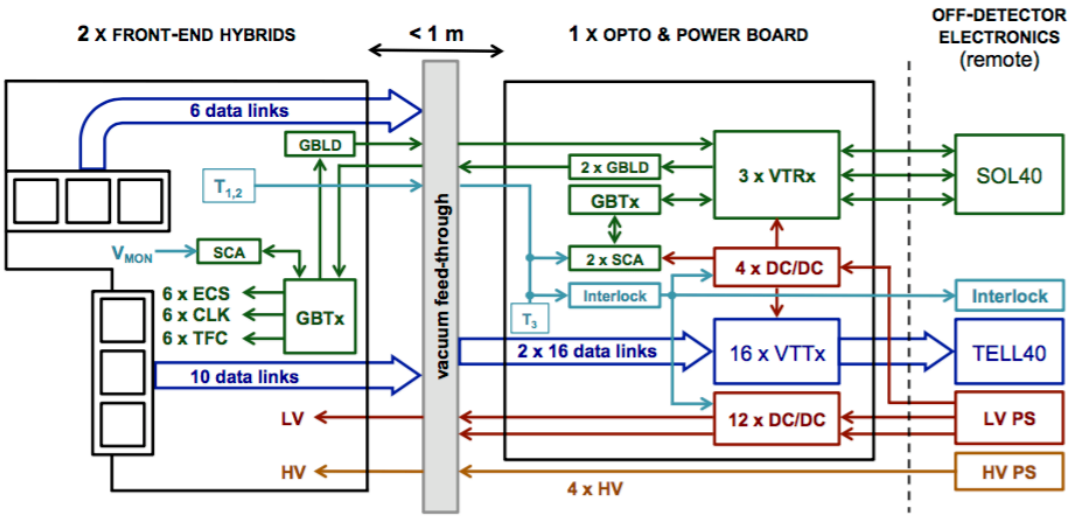

Figure 6.18: Structure of the DAQ chain in the VELO Upgrade. [86]

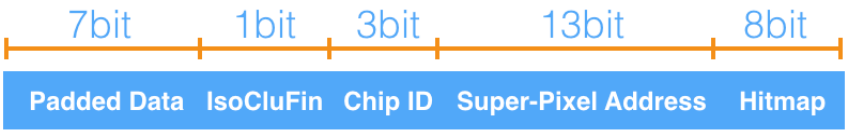

Figure 6.19: MiniDAQ data output packet after data processing. The Bunch Crossing ID (timestamp) is transmitted in the header of the data stream for that particular event.

6.6 Sensors

Sensor performance is critical in the VELO Upgrade, to state the obvious. Differently than other parts of the detector, the radiation flux will cause damages to the sensors, degrading performance during their operational lifetime. The strategy is then to check that the sensor design can meet the set requirements for physics data taking even at "end-of-lifetime" radiation damage conditions. Regarding sensors, the requirements for the VELO described in the technical design report [80] are:

- **Collection of 6000e^- per minimum ionising particle.**
- **Sustained operation at bias voltage of 1000V.**
- **Greater than 99% cluster finding efficiency (CFE).**

All of these are somewhat correlated given that the charge collection efficiency (CCE) can be generally improved by using a higher bias voltage and the cluster finding efficiency will depend on the threshold level, set by how different is the amount of charge coming from a MIP and noise coming from the sensor. Ultimately, during operation, bias voltages will be raised to keep both CCE and CFE above the required levels for physics data taking and, therefore, the sensors high voltage tolerance needs to be probed.

Three different designs were investigated as a possible sensor solution for the VELO. Between these sensors there were also variations on thickness, guard-ring size and implant size.

6.6.1 Sensor Designs

The VELO Upgrade uses a "triple" setup for its sensors, meaning that each sensor is connected to three independent VeloPix chips (Fig. 6.20). The region between the three VeloPix ASICs contains elongated pixels, as some distance between ASICs is needed as clearance during the process of bump-bonding the ASICs to the sensor. The prototype designs were produced by two manufacturers: Hammamatsu (HPK) and Micron. Both of them produced a baseline solution for the sensors which is a n-on-p 200 µm thick silicon with 450 µm guard rings, while also providing variations on the design that might improve the sensor operation.

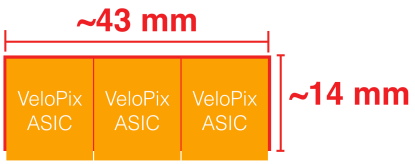

Figure 6.20: Underside of a triple tile bump-bonded to VeloPix ASICs.

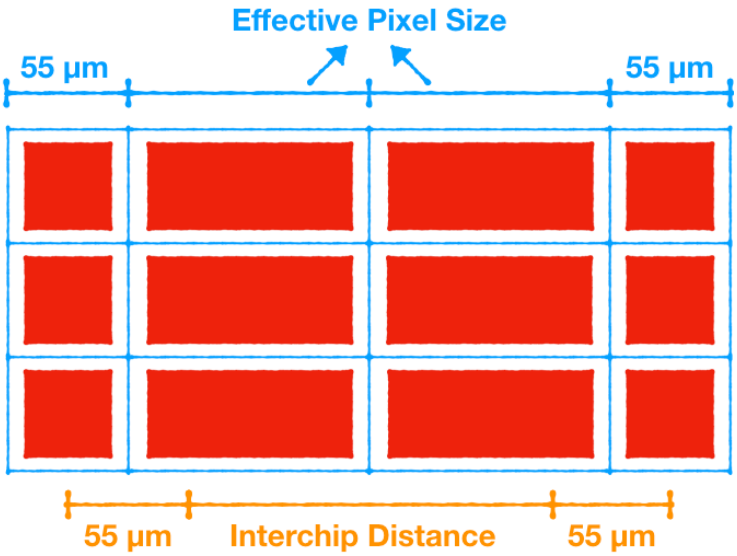

Figure 6.21: Scheme showing the area with elongated pixels in the sensors, which allows for the needed clearance during the flip-chip process. The interchip distance on most of the sensor prototypes was 110 µm but the final design was later modified to have a distance of 165 µm.

During the first round of prototyping the sensor wafers had both "singles" and "triples". Single sensors are pixel matrices of 256× 256 pixels, used to test variation on the sensor design but using only one ASIC per tile. Triples are the format that will be used in the experiment, with a matrix of 768× 256 pixels, and are simultaneously bump-bonded to three ASICs. Triples also include a region with the interchip pixels, designed to "bridge" the area between two chips (Fig. 6.21). This region accounts for 30 µm uncertainty on each ASIC dice line and an extra 50 µm gap requested by the bump-bonding company, totalling 110 µm distance.

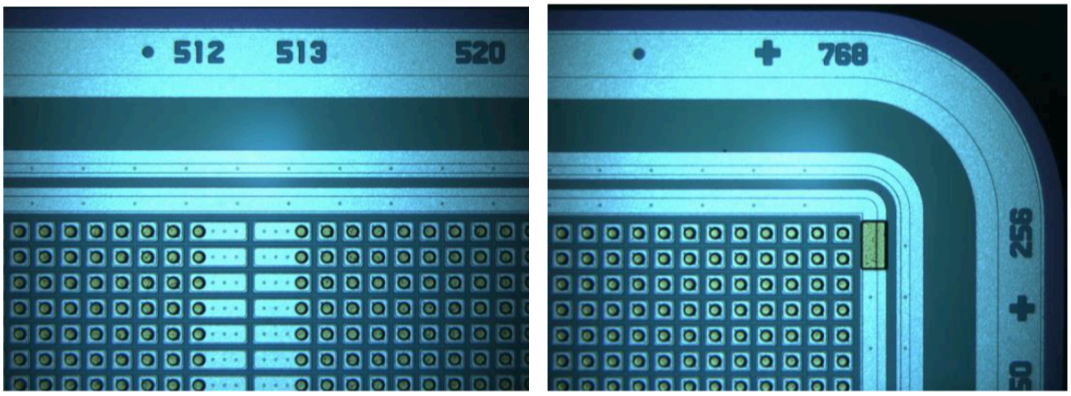

Figure 6.22: Underside of a HPK sensor with UBM in place. The picture on the left region shows the extended pixels present in the region between chips. On the right one can find the curved edge of the sensor, following the guard-ring shape.

HPK Designs

Sensors were produced using a float-zone p-bulk with n-type implants insulated in-between pixels by p-stops. The bulk resistivity quoted is $3 - 8\,\mathrm{k\Omega cm}$ and the nominal thickness for all samples was 200 µm. For even distribution of the bias voltage to the backside, a 1.1 µm Al layer is applied on top of the sensor backside.

Two different sensor wafer types were produced. The first wafer was used for initial test of prototypes and contained sensors with two different guard ring sizes: 450 µm and 600 µm in single and triple sizes. Single sensor samples also added the bigger n-type implant size of 39 µm. The second wafer produced contained mostly triples, all with 450 µm guard ring and the larger 39 µm implant, evaluated to be more efficient than the 35 µm "baseline" option. The interchip distance was increased from 110 µm to 165 µm in width (Fig. 6.21). The last modification with respect to the first wafer was the inclusion of Deep Reactive Ion Etching (DRIE) at the edges of the sensors, making the edges round rather than square. This modification (Figure 6.22) is desired to reduce risk of damaging impacts between sensor corners and the RF foil due to vibrations during VELO closing procedure. The IV and CV characteristics of each sensor are tested by biasing the guard-ring structure once after wafer dicing.

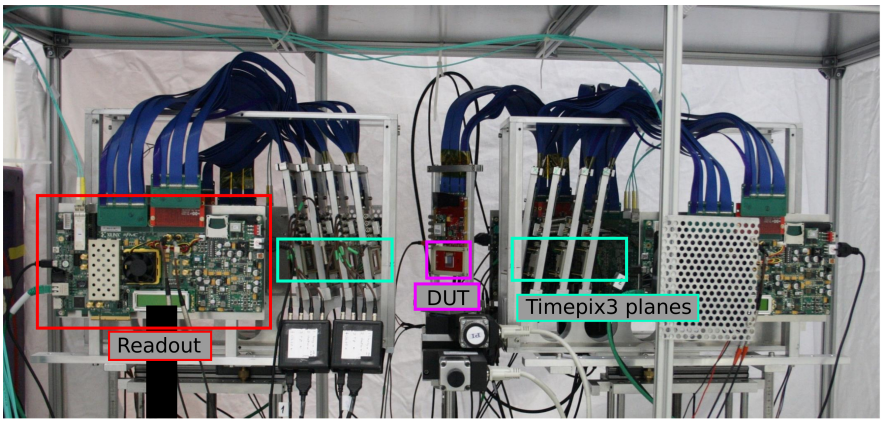

Figure 6.23: Photograph of the Testbeam setup at CERN.

Micron Designs

Micron sensors had a fairly more diverse first batch, design-wise. There were two different wafer types: a p-type bulk, 200 µm thick, and a n-type bulk 150 µm thick. This wafers had a resistivity greater than 5 kΩcm and 1.5 kΩcm, respectively. In both cases pixels are formed by 36 µm n-type implants isolated by p-spray. The sensors had different guard ring sizes: 150 µm, 250 µm, 450 µm.

The n-on-p sensors had a similar Aluminium layer deposited on the backside in order to bias the sensor. On the n-on-n sensors a conductive grid, also made of aluminium was used to distribute the bias, allowing for the possibility of probing sensors with lasers. As it will be discussed in more detail in Chapter 7 the size of the guard-rings heavily affects the HV tolerance of this sensors.

6.7 Sensor Studies using the Timepix3 Telescope

To test charge collection, efficiency and spatial resolution of sensors when measuring MIPs one needs to have a precise knowledge of the trajectory of the particles going through our prototype sensor. The Timepix3 Telescope [87] was built to precisely reconstruct particles in a beamline, in this case the SPS H8 beam. The beam used is mostly composed of pions with a momentum of 180 GeV.

The telescope is composed of 8 planes divided into 2 arms, up- and downstream of the Device Under Test (DUT) (Figure 6.23). In this case the DUT are the VELO upgrade

sensors, bump-bonded to Timepix3 readout ASICs. Each plane is a 300 µm-thick, p-on-n pixel sensor bump-bonded to a Timepix3 ASIC. Using Timepix3 ASICs allows the telescope to have a track time resolution of σ_t =0.35 ns, which in turn means that pattern recognition is simplified for the telescope. In fact, even at high track rates the spatial resolution is unaffected as the telescope mostly sees "one track at a time[6]". The telescope is quoted to have a pointing resolution of 1.68 ± 0.16 µm at the DUT position, allowing for studies with very well defined positions inside a single pixel [87].

As an example of results obtained using VELO upgrade sensors and the Timepix3 Telescope, Figure 6.24 shows the charge collected in associated clusters with track going through the sensor. This measurement can easily be made using the Timepix3 readout due to the ASIC feature of reading the charge deposited in the form of a Time-over-Threshold (ToT) measurement. Associated clusters are the ones identified as the closest to the track within a space (150 µm around intercept point) and time window (10 ns). The non-irradiated samples most probable charge collection is about 16 ke^- and 12 ke^- for 200 µm and 150 µm thick sensor respectively. This value is very close to the expected 80 $e^-/$ µm generated by a MIP. As for the irradiated sensors (Fig. 6.25), one can see that there is barely any change in the charge collected for sensors with different thickness and implant size. All sensors reach a charge collection above the 6 ke^- before 1000 V.

On the next two subsections the results regarding the interchip efficiency and the noise analysis of irradiated n-on-n samples will be described, both of them using information from the Timepix3 Telescope tracks.

6.7.1 n-on-n Edge Noise Analysis

During the 2015 May Testbeam campaign, it was noticed that irradiated n-on-n sensors showed an increased noise only on the pixels close to the sensor edge. Figure 6.26 is a 2D pixel map showing all hits detected during one Telescope run. There is a one pixel layer at the edge that registers thousands more hits than the pixels away from the edge. The few pixels that appear white in this image have been masked previously. I investigated this effect by using telescope data and four different sensor samples (Table 6.2).

In order to correctly identify the nature of these hits, data taken at the testbeam was used, separating the sensor in two areas: an edge area comprising all pixels in the perimeter

[6]The reconstruction software only builds tracks with clusters detected within 10 ns of each other.

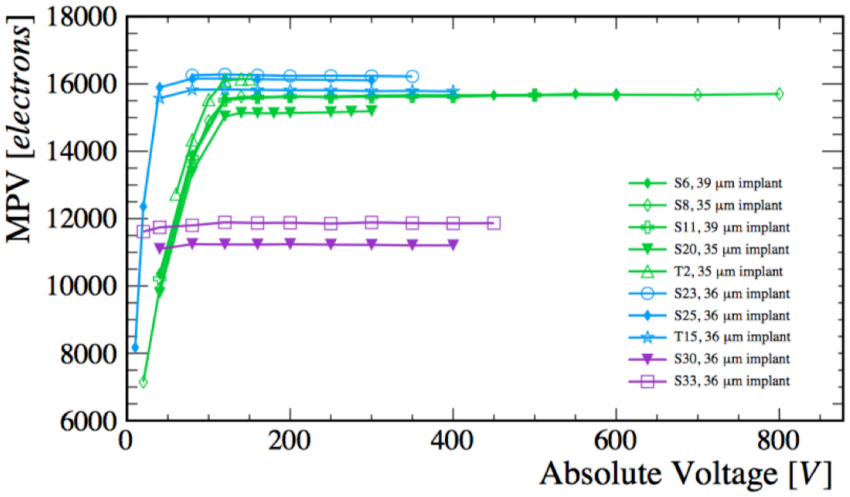

Figure 6.24: Charge Collection Efficiency measurements done using non-irradiated sensor prototypes. One can see the expected difference charge collection for 200 µm thick (blue and green lines) and 150 µm thick sensors (purple lines). The charge collection saturates when the sensors reach depletion voltage [88].

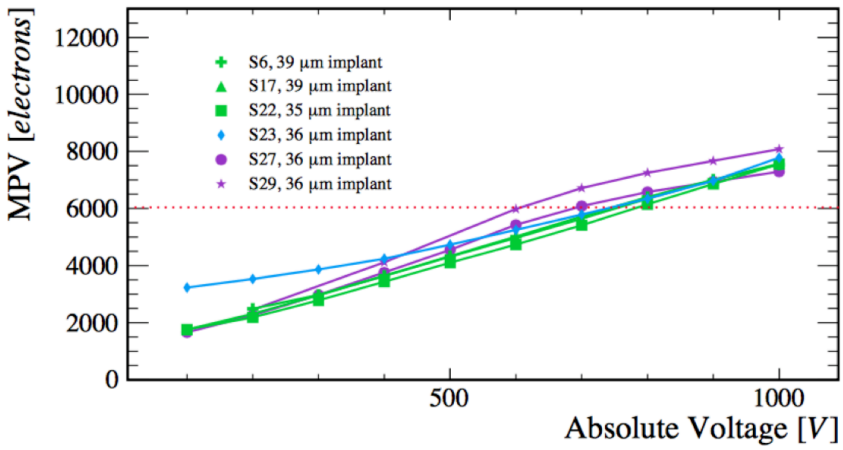

Figure 6.25: Charge Collection Efficiency measurements for irradiated sensors. The sensors have been irradiated and show a much lower collection of charge, as expected, and that the threshold of 6000e is reached before 1000 V [88].

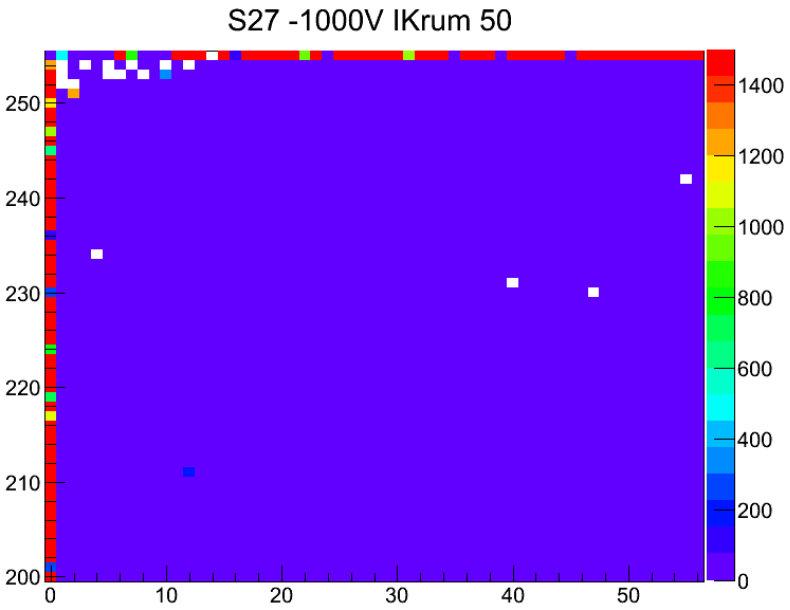

Figure 6.26: Example of edge noise seen in irradiated n-on-n sensors.

Hybrid	Type	Sensor Thickness(μm)	Radiation Dose (1 MeV $n_{eq}cm^{-2}$)
S27	n-on-n	150	8×10^{15}
S29	n-on-n	150	8×10^{15}
S6	n-on-p	200	8×10^{15}
S17	n-on-p	200	8×10^{15}

Table 6.2: Summary of the characteristics for the sensors analysed.

of the sensor, and a central square containing the same number of pixels. Additionally, it is required that only clusters with one hit are considered. Using the telescope information it is possible to ascertain whether hits come from the beam (Track-associated clusters) or are spurious noise hits (Non-associated clusters).

Because the DUTs in the telescope were bump bonded with Timepix3 ASICs, the data contains detailed timestamps of every hit recorded. The event distribution of hits (Fig. 6.27) shows the number of hits as a function time in bins of 150 ms. There is a contribution to the non-associated clusters in the central region from a few individual hot pixels that had not been masked during the run, but that's very different from the time structure observed in the edge. The noise in the edge region is not dependent on the

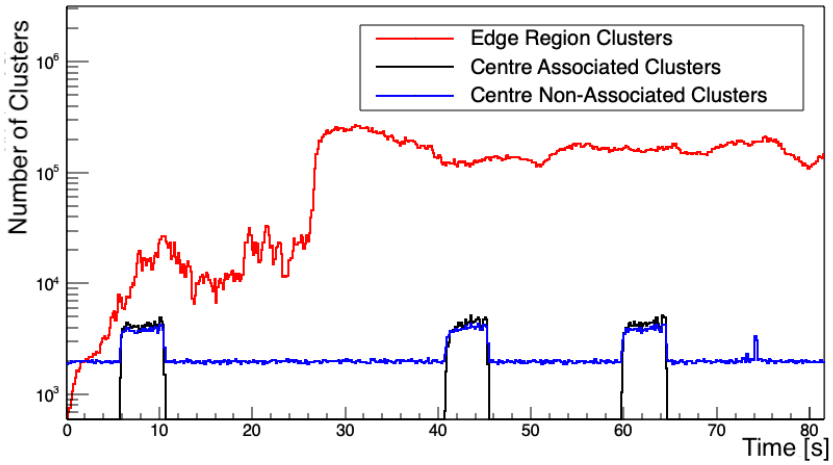

Figure 6.27: Time distribution of hits in the edge (red) and elsewhere in an n-on-n irradiated sensor (S27). One can see that the edge noise (red) is independent of the spills structure coming from the SPS beam (black). One can also observe a continuous distribution of non-associated clusters in the centre region, which comes from radioactive decays in the hybrid and can't be associated to telescope tracks (blue).

beam time structure, and hence is not being triggered by particles activating pixels.

Different IKrum DAC values were used check for any effect on the edge noise. As stated in Section 6.4.1, the Krummenacher current is controlled by the IKrum DAC. The higher the IKrum DAC value in a Timepix3 ASIC, the faster the return to the baseline (which leads to smaller ToT values for the same charge). Due to the analogue readout design, the IKrum DAC in the Timepix3 also tunes the maximum value of leakage current compensation in the pixel. Therefore, the higher the IKrum value, higher the amount of current that can be compensated. Figure 6.28 exemplifies the effect that a larger IKrum has on Time-over-Threshold measurements while Figure 6.29 shows how the ToT profile of edge noise signals is completely different, with very large ToT counts when compared to values observed in Fig. 6.28.

A feature that can be observed in Figure 6.29 is that the noise counts are reduced at higher IKrum values, disappearing at IKrum$=$ 100 DAC, and that a higher bias causes more noise signals. The dependancy on IKrum effect and bias voltage points to the interpretation that the n-on-n design for S27 and S29 have a high local leakage current being pushed through the pixels.

The most likely factor causing this localised effect is the guard-ring structure (Fig. 6.30).

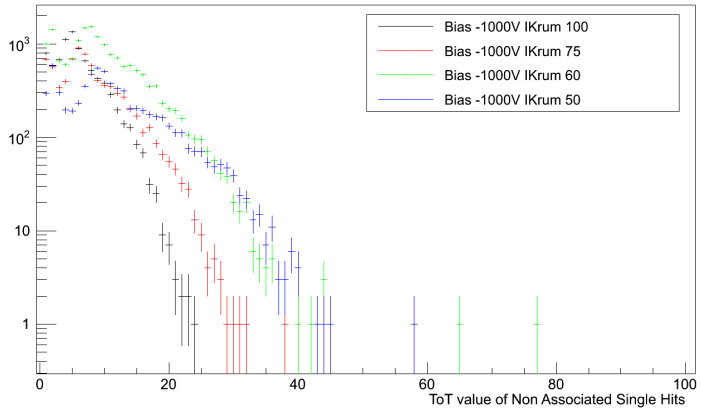

Figure 6.28: Effect of the IKrum setting on sensor S27. The distributions shown here are of hits in the centre region of the sensor that were associated to tracks. The plot shows the expected reduction on the MPV of the Time-over-Threshold measurement with the increase of IKrum DAC.

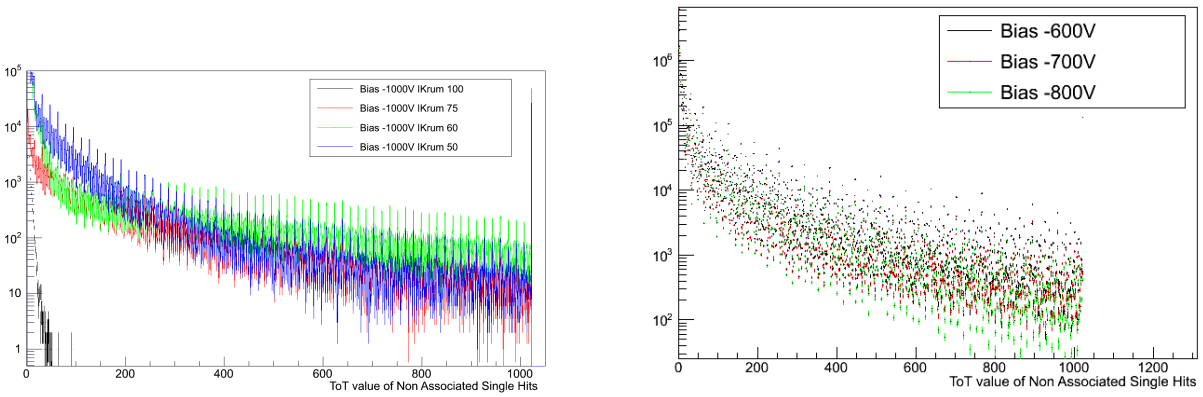

Figure 6.29: The edge region for two sensors: S27(left) and S29(right) shows how ToT measurements of the noise go to very high values when the IKrum setting is low. All S29 measurements were done with the IKrum set to 20, showing that even lowering the bias does not completely remove the noise.

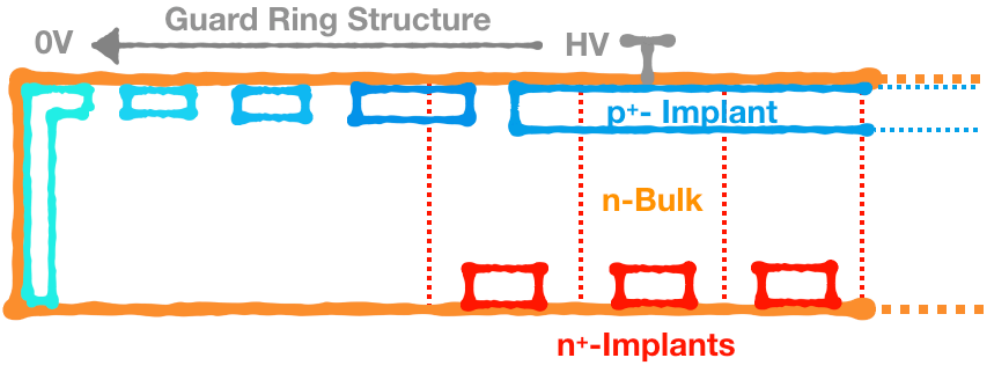

Figure 6.30: Schematic of the n-on-n guard-ring scheme, displaying the overlay between the GR structure and the edge pixels of the sensor.

The n-on-n sensors have guard-ring structures on the opposite side of the substrate. This position allows for the guard-rings to be placed overlapping the last pixel row/column, a design that minimises the inactive silicon edge. However, by putting the guard-ring within the last pixel row/column region, the design creates field non-uniformities that result in large local leakage current. This current flows to the ground through the pixel pre-amplifier, acting as a continuous noise source.

The structure of this noise effect can be compared to the sensors with a different design (HPK n-on-p), irradiated at the same facilities to the same dose (S6 and S17). No edge noise is observed, and an IKrum DAC scan presents only the expected reduction in the ToT measured values (Fig. 6.31). The observation of this edge noise in the n-on-n sensors lead to a second n-on-n design, but ultimately other sensor option was chosen before the irradiated tests could be done.

6.7.2 Interchip Efficiency

The design of the tiple sensors include two interchip regions with extended pixel implants responsible for bridging the region between ASICs. Due to the clearance needed during the bump-bonding/flip-chip process, the distance between the last pixel centre in one ASIC and the first pixel column centre in the next ASIC is 165 µm. The first design of sensors had an interchip distance of 110 µm. This results in the pixels on the inner edges

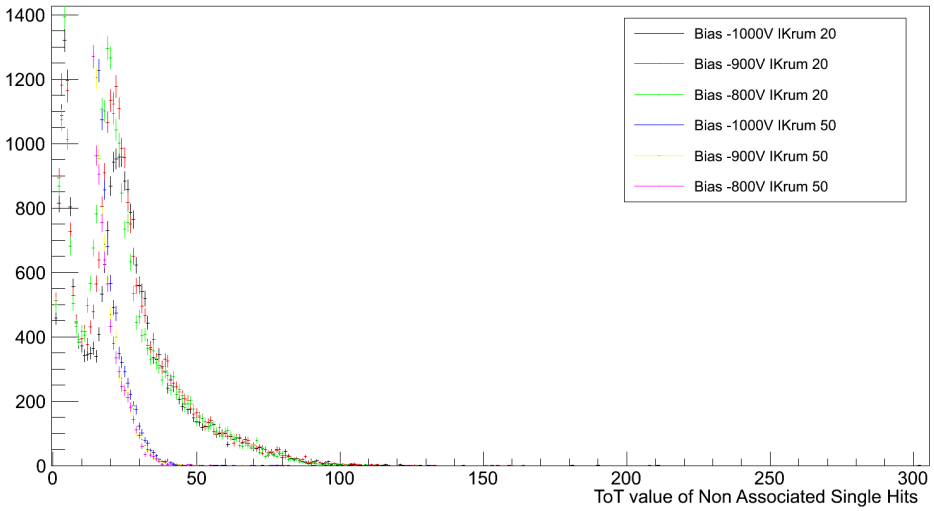

Figure 6.31: Sensor S17 ToT measurements at different bias voltages and IKrum values. No noise was observed either in the ToT or in the hitmaps.

of the ASICs being connected to long pixels of dimensions 55 µm × 137.5 µm or 55 µm × 110 µm, depending on the design (Fig. 6.21).

Using a perpendicular angle of incidence, three irradiated sensors were positioning with the beam directly above the interchip region, and long runs were taken in order to accrue statistics in this very small sensor area. These sensors were non-uniformly irradiated with 23 MeV protons at KIT (see Appendix B) and therefore the irradiation the interchip region has received is small when compared to the most irradiated corner.

The efficiency was measured by selecting very well measured tracks, with clusters within a 10 ns window in all of the telescope planes. The tracks used must have a maximum χ^2 value of 7. All tracks going through the DUT are integrated in the efficiency measurement (Fig. 6.32).

In Figure 6.33 the efficiency of the HPK n-on-p sensor T1 is displayed as a function of the assembly column. The measurement becomes less significant in the regions further away from the beam centre as there are less tracks going through those areas. There is a very small different between the bias voltages, with the 1000 V measurement being slightly higher efficient.

Integrating all the tracks that went through the interchip pixel, one can measure the

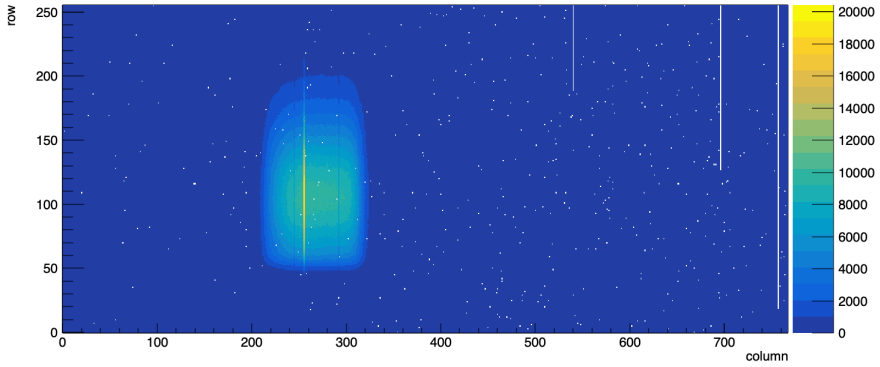

Figure 6.32: Hitmap for a long run with the beam positioned over the interchip region. The beam seems to have straight edges due to the collimators placed upstream of the telescope. There were about 1000 pixels masked in this run, that can be seen as white pixels. Due to the larger area of the interchip pixels, they see a larger rate of signals, approximately twice as much in this case.

efficiency as a function of the position of the track passing inside the pixel. This allows for the possible observation of local inefficiencies inside the pixels. As it can be seen in Figure 6.34, the interchip pixels seem to have a fairly uniform response. As it was mentioned before this region of the irradiated sensors received a much lower dose, and although it is possible to see that the higher bias has a higher efficiency, the improvement is minimal.

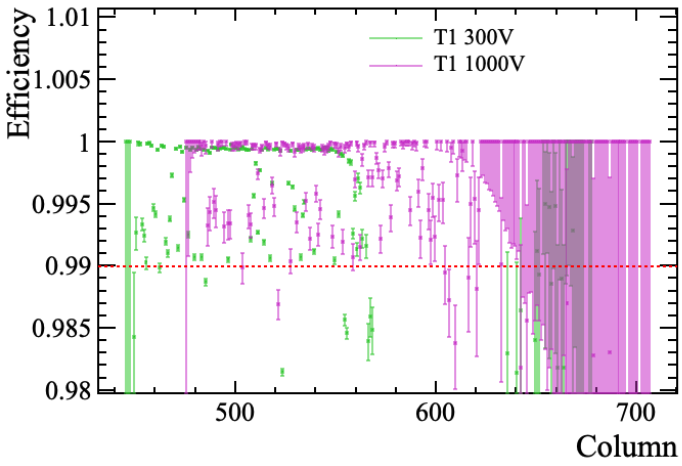

Figure 6.33: Efficiency for the T1 assembly as a function of the column number. The regions on the right have measured very few tracks and so have very large errors on the efficiency value.

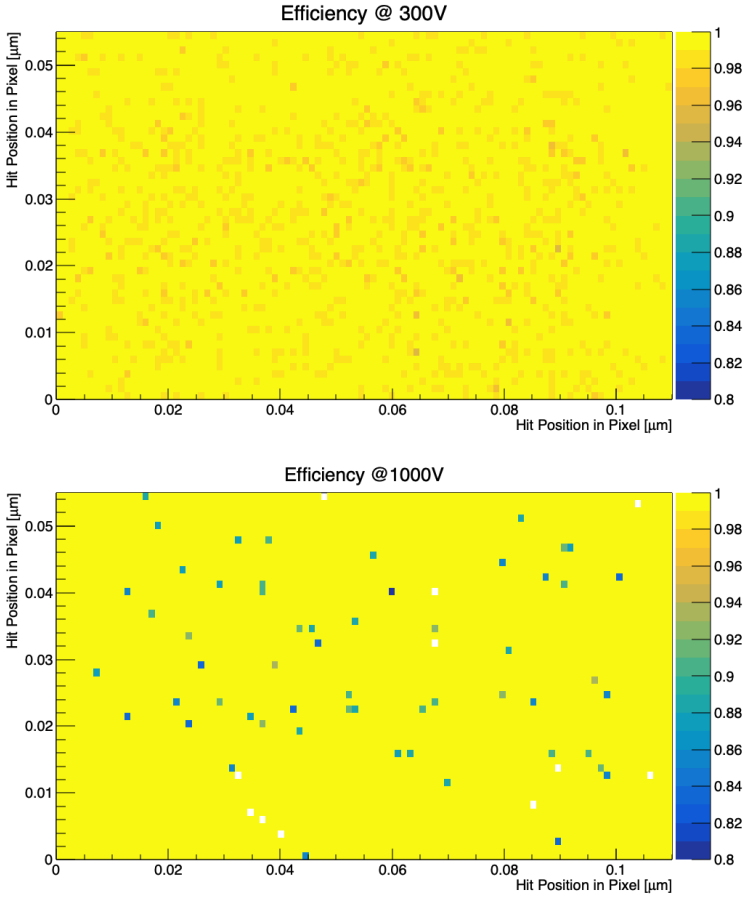

Figure 6.34: Intrapixel efficiency for the T1 assembly, 4×10^{15} 1 MeV $n_{eq}cm^{-2}$, non-uniformily KIT proton irradiated. The efficiency is measured as a function of the tracks position within the interchip pixels in the DUT. This plot is made by using all tracks that hit the DUT in the interchip pixels. The results with 1000 V show a few low efficiency bins due to low statistics in the sample. The results do not show any spatial artefacts and almost all pixels are above the 99% threshold.

7 | High Voltage Tolerance

As part of the R&D for the VELO upgrade, several different sensor design options were proposed. These options were variations on three vendor/technology options: n-on-p sensors produced by Hammamatsu Photonics, and n-on-p or n-on-n sensors produced by Micron Semiconductors. The general goal of the sensor investigations was to check the sensor options that matched the requirements set in Section 6.6, namely high voltage tolerance, efficiency and charge collection. There was also interest in operating sensors in upgrade-like condition so to identify any unpredicted effects. The HV tolerance results obtained were used during the Sensor Engineering Design Review (EDR) and the Production Readiness Review (PRR).

This chapter will be dedicated to results regarding the high voltage tolerance aspect of the sensors. The tests performed included characterisation of designs both before and after irradiation. The irradiation itself, described in Appendix B, was performed in different facilities, to different beam profiles and irradiation types. The tests of high voltage tolerance were performed using three setups, results being contained in Sections 7.2 and 7.3. These results were presented during the Sensor Production Readiness Review and played an important role in deciding the final sensor design as HPK n-on-p sensors. A paper summarising the tests and results obtained is currently in preparation.

During the execution of the tests, interesting features were observed, warranting a more detailed investigation. A discussion on parylene coating and possible interference of this is found in Section 7.4. Finally, the breakdown voltage of sensors and the nature of their temperature dependence is investigated in Section 7.5.

7.1 Testing Setups

Two experimental setups were used to extract the sensor performance results for the VELO Upgrade: the laboratory setup and the testbeam. In the laboratory the IV curves, equalisation procedures and data taking with radioactive sources were done. The testbeam setup was used for testing charge collection efficiency, cluster finding efficiency and resolution of the sensors.

Sensors were tested by bump-bonding them to one or three Timepix3 ASICs, depending on whether the sensors were singles or triples. Singles were used as a way of simplifying the testing procedure, requiring less ASICs per test hybrid, as well as being an easier bump-bond procedure.

A dedicated readout chain was necessary to read the Timepix3 chip: a system called SPIDR [89] was used. The hardware of this readout system consisted in a XlinX VC707 development board[1] and two custom adaptor boards. These boards are used to connect the hybrids to the FPGA and provide all signals and power necessary for the chip operation. The SPIDR readout was connected to a dedicated readout PC were data acquisition was controlled and data was stored. All important data was centrally stored and available to be used for analysis. This system was common to both testbeam and laboratory setups.

Apart from the readout, an extra connection was necessary to provide the high voltage input to bias the sensors. This was done by using a Keithley 2410 Sourcemeter controlled remotely with LabView software.

Laboratory

There were two laboratories equipped to perform Timepix3 characterisation: one at CERN, and one in Liverpool, commissioned in early 2016. Figure 7.1 is a photograph showing all parts of the laboratory setup in Liverpool.

Both of them consist of a vacuum chamber, equipped with scroll and turbo pumps, capable of reaching a typical 10^{-4} to 10^{-5} mbar.The main difference between vacuum tanks in Liverpool and CERN is that the Liverpool tank has an infrared window. The vacuum chamber is equipped inside with a copper block that uses a water and glycol solution, pumped by a chiller outside the chamber, as cooling for the hybrids.

[1] Containing a Virtex7 FPGA chip.

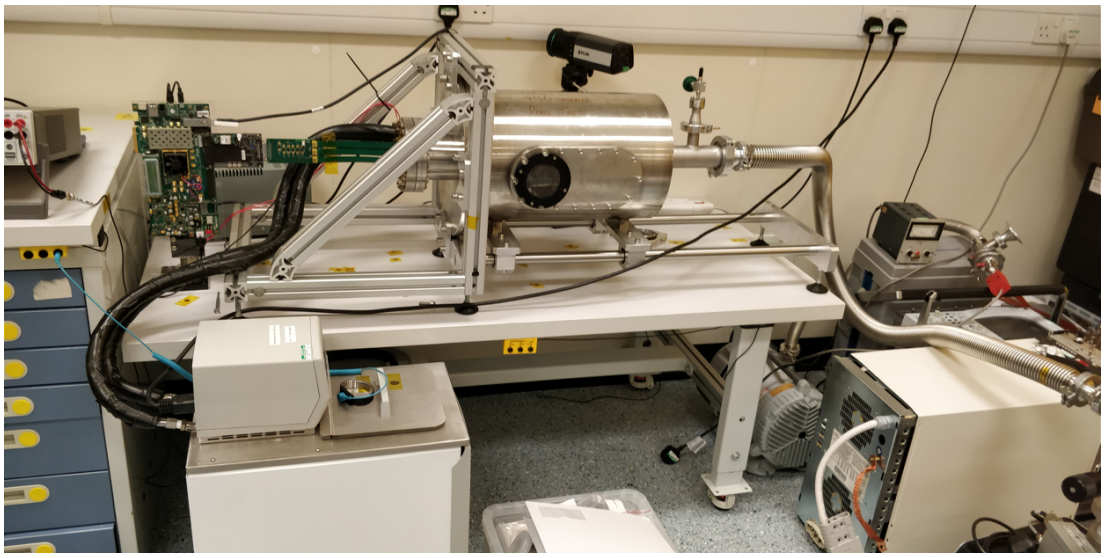

Figure 7.1: Photograph of the laboratory setup assembled at Liverpool. The black window in the vacuum tank is transparent in infrared so thermal imaging can be performed in vacuum.

On top of the copper block, a Peltier element is mounted and on the cooled side of the element is a copper plate, which is where the assemblies were attached. The Peltier element allows the setups to reach temperatures much colder than what would be possible with just the water cooling. Typical running had the cold water set to −15 °C, and the cold side of the Peltier element reaching −30 °C. A better chiller was installed later on in the CERN setup, allowing for the cold side of the Peltier to reach −44 °C. Figure 7.2 details the cooling block in the CERN setup.

This setup was used to perform noise equalisation, test pulse calibration, characterise the IV and source scans using a ^{90}Sr beta radioactive source. When possible, all the equalisation, IV curves and source measurements were done before and after irradiating sensors to the full radiation fluence expected in the VELO lifetime.

Testbeam Telescope

IV Scans and noise equalisations would be ideally done in the Laboratory prior to moving sensors to the testbeam area. However due to the time constraints, sometimes it became necessary to perform such tests while the sensor was mounted in the DUT enclosure. The first Device Under Test (DUT) enclosure, the cylindrical white box in Figure 6.23,

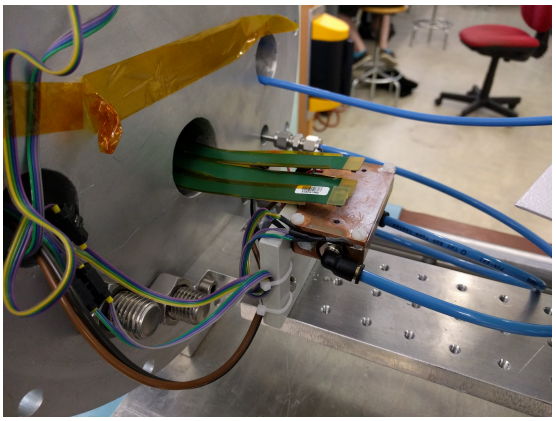

Figure 7.2: Cooling block inside the vacuum chamber at CERN. The blue tubes take cooling water to and from the coper block and back into a chiller running outside the vacuum environment. The temperature of both the copper plate and the copper block are monitored through the use of PT100 temperature sensors.

was sealed but not vacuum tight. The sensors were operated with a constant dry air flow, and only parylene coated sensors were allowed to operate at voltages higher than 300 V. A second DUT enclosure, this time fully capable of holding vacuum, was built and installed during 2016 so tests could be performed on non-parylene coated sensors.

7.2 Non-Irradiated Sensors

During operation the VELO will need to raise operational voltages to mitigate the charge collection efficiency loss caused by radiation damage. This means that during the first years of operation the sensors will be only lightly irradiated, hence requiring a much lower bias. The HV tolerance requirement is a test for irradiated sensors, and other criteria are used for non-irradiated ones. To classify the sensor breakdown for these non-irradiated sensors, it was established that a sensor is not up to standard if it has breakdown when biased below 3 times the full depletion value, as a form guaranteeing there is plenty of operational room through the VELO lifetime. Additionally, it is desirable that sensors can reach stable operation at 800 V, as a higher breakdown voltage is always better.

One of the features that can be tested in the non-irradiated sensors is the impact of the different guard-ring designs. HPK n-on-p sensors had guard-ring size options of 450 µm or 600 µm, while Micron sensors had options of 450 µm/250 µm for n-on-p and

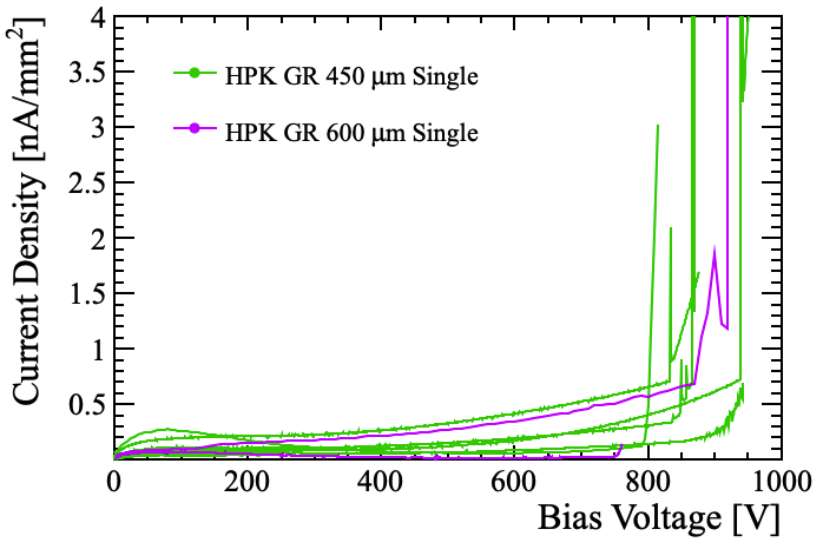

Figure 7.3: Current Density as a function of bias voltage for n-on-p HPK design. Comparison of guard-ring size shows no improvement in high voltage tolerance from samples with 600 µm with respect to the 450 µm guard-ring size.

450 µm/250 µm/150 µm for the n-on-n variant. The idea being that a smaller guard-ring would introduce less dead material in the detector acceptance.

Figure 7.3 compares several single HPK assemblies with 450 µm and 600 µm guard-ring sizes. Both of them show a very similar HV tolerance and leakage current values. The other comparison of guard-ring size comes from the n-on-n and n-on-p Micron assemblies (Fig. 7.4). In both cases, one can see the impact of the smaller guard-ring sizes has on the IV behaviour, leading to earlier breakdown and larger leakage current overall in the n-on-n case.

It is also the opportunity to compare the IV behaviour between singles and triples. Leakage current for sensors of the same doping concentration and bulk resistivity should be the same, scaling with the bulk's volume. In Figure 7.5 there is an example of the current density of single and triple assemblies, rescaled to the same temperature, as a function of voltage. Both IVs are extremely similar, confirming that using single assemblies for testing of HV tolerances is a reliable strategy.

The main purpose of the HV test was to qualify sensor options for operation in the VELO. A total of 45 assemblies, combining all design, were tested for HV tolerance. For the Micron sensors there were 10 n-on-p sensors biased up to breakdown and only one of

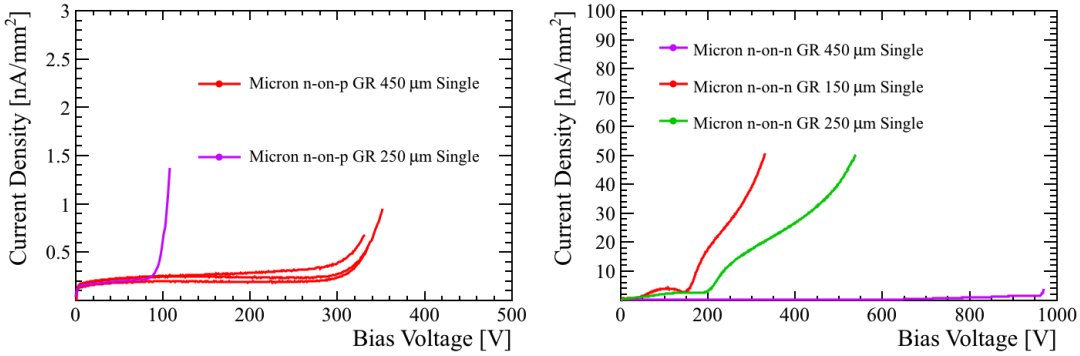

Figure 7.4: Current Density as a function of bias voltage for Micron n-on-p (left) and n-on-n(right) designs. The designs with a smaller guard-ring size show current breakdown at considerably lower voltages.

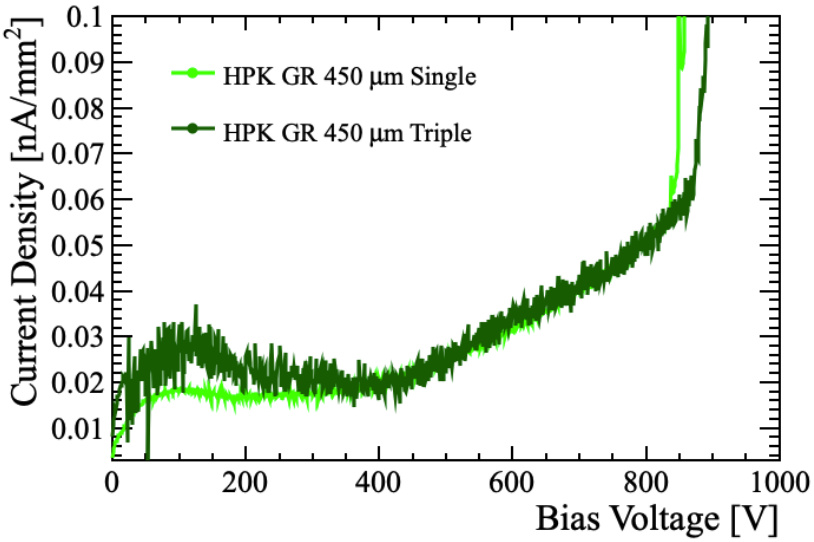

Figure 7.5: Current Density as a function of bias voltage for a single and a triple HPK n-on-p assembly, the single assembly current was rescaled rescaled to the triple temperature, −20 °C.

them having breakdown at a voltage lower than 3 times the depletion voltage. The one assembly with lower breakdown voltage is the one with a 250 µm guard-ring. Observing the Micron n-on-p sensors, there is a clear common trend of the breakdown voltage occurring at around 320 V.

Micron n-on-n sensors have a very low depletion voltage, of around 20 V. As discussed previously, the sensor variants with a more aggressive guard-ring design have very high leakage current values, and early breakdown onset. Focusing on samples with 450 µm guard-ring size (Fig. 7.8) the IV curves show that their breakdown does occur at a higher voltage than the n-on-p Micron variant and all had a breakdown voltage greater than 3 times the depletion voltage. Three n-on-n sensors had a breakdown voltage below the 800 V mark.

Most of the HPK n-on-p tested assemblies had a guard-ring structure of 450 µm and show a consistent behaviour (Fig. 7.6). The depletion voltage was measured to be 140 V, which sets a minimum threshold of 420 V for the breakdown voltage. All sensors have a breakdown at or beyond 800 V.

The characterisation results allows us to rule out the Micron n-on-n/n-on-p 150 µm and 250 µm guard-ring designs, due to their very high leakage current compared to all other sensor variants. All other sensor designs had acceptable, cohesive behaviour between the tested samples. The breakdown voltage of Micron n-on-p sensors, at around 320 V, is much lower than both HPK and Micron n-on-n. This was taken into consideration when choosing the final sensor option.

A final note is on the effects of thinning of the ASIC and bump-bond processes. For most of our test assemblies, a standard 700 µm thick Timepix3 ASIC was used. However, as detailed in Chapter 6, the VeloPix will be thinned down to 200 µm to reduce material in the experiment's acceptance. During testing it was noticed that thinned ASIC samples can have issues, such as a high leakage current, very hot pixels or early breakdown. Figure 7.9 exemplifies the high leakage current observed in the first thinned modules. Further investigation with x-rays and debonding of the assembly by the bump-bonding company identified missing and defective bump bonds. This problem was later on mitigated with a new bump-bonding process developed by the company responsible for the sensor and hybrid bonding.

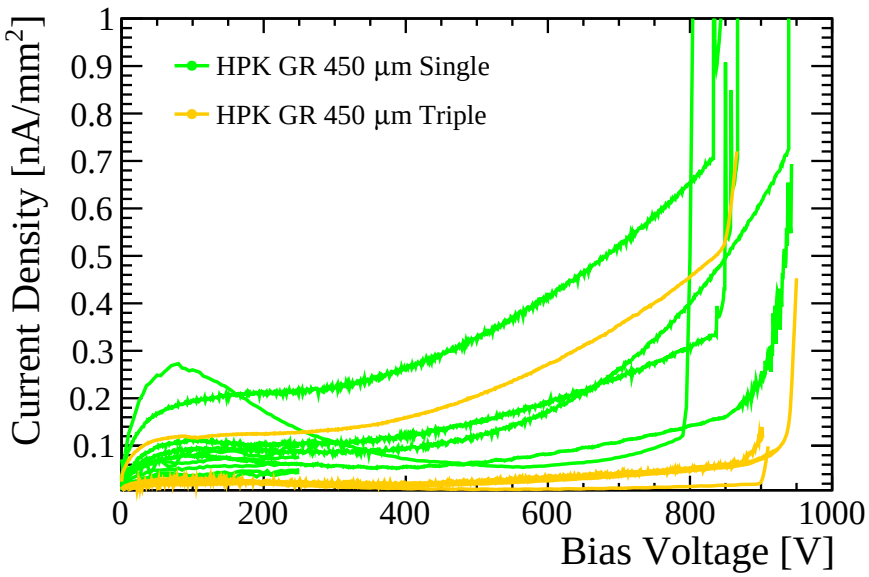

Figure 7.6: HPK sensors with guard-ring size of 450 µm IV scans. There is some spread in the leakage current values, but small variations in the thermal contact and performance of the cooling affect the absolute measured values. Breakdown voltage is consistently above 800 V.

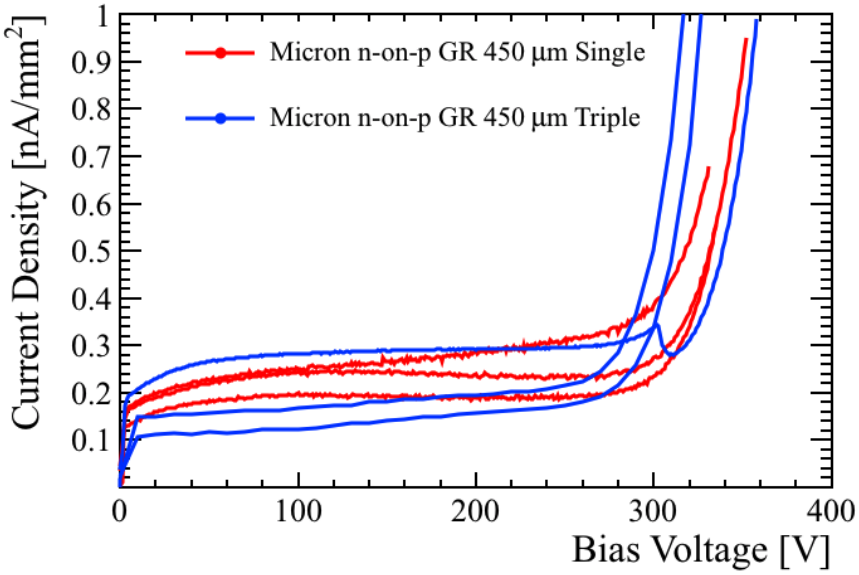

Figure 7.7: IV curves for n-on-p Micron sensors, singles and triples, with a 450 µm guard-ring. All sensors have a very consistent behaviour, with breakdown happening at 320 V.

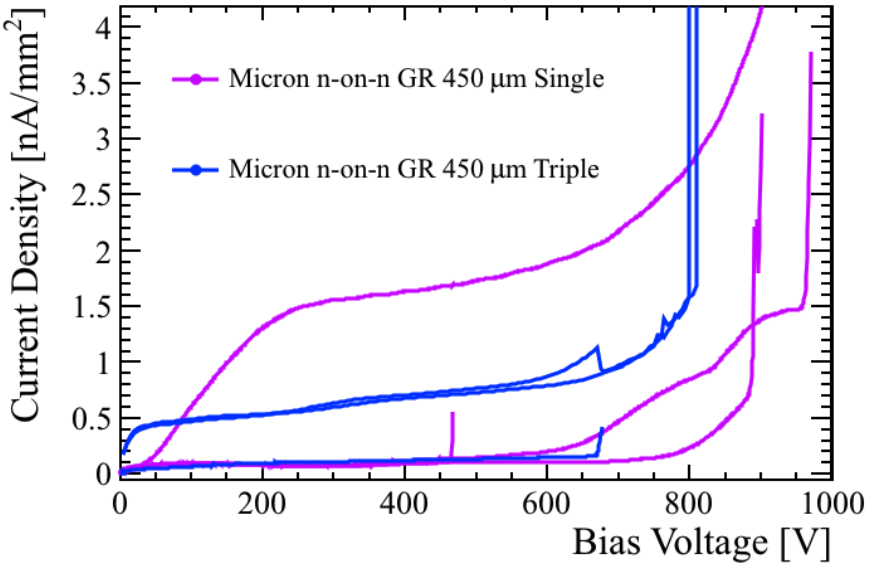

Figure 7.8: IV curves for n-on-n Micron sensors, with 450 µm guard-ring. The leakage current for some of the sensors seems to ramp up before having breakdown. Four pout of the seven sensors had breakdown beyond 800 V.

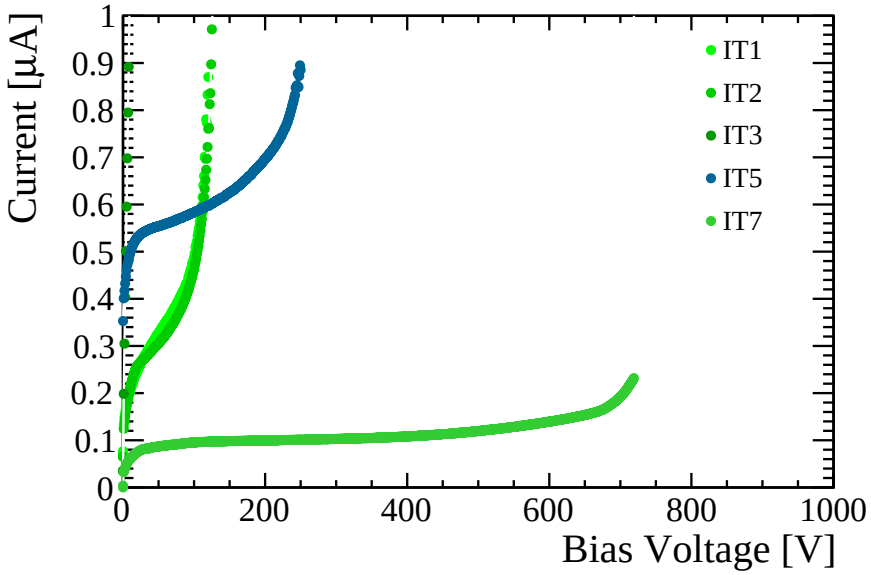

Figure 7.9: First batch of thinned tiple assemblies using HPK (green) and Micron n-on-p (blue) sensors with 200 µm-thick ASICs. The assembly IT7 is the only one that has a leakage current compatible with the behaviour of the other assemblies.

7.3 Irradiated Sensors

Diverse irradiation campaigns were performed to classify sensors after irradiation. The sensors were exposed to half and full irradiation dose (4×10^{15} 1 MeV n_{eq} cm^{-2} and 8×10^{15} 1 MeV n_{eq} cm^{-2}, respectively) in both uniform and non-uniform profiles. The non-uniform profiles were done with a high intensity proton beam in three facilities: KIT[2] and Birmingham, trying to follow the expected profile in LHCb, and IRRAD[3] that has a large, Gaussian beam spot. The average particle composition at LHCb is not perfectly represented by either neutrons or protons, therefore sensors were irradiated in different facilities to improve our knowledge in any possible effects that might appear. More details on the irradiation procedures can be found in Appendix B. In this Section IV curves will be shown in absolute values, rather than the density of leakage current per area due to non-uniformly irradiated sensors having their current completely dominated by one region of the sensor.

Figure 7.10 contains all sensors irradiated at IRRAD, the facility with a hardness factor most similar to the VELO operation conditions; all of the sensors tested there were able to reach 1000 V without breakdown, as required. The two sensors S5 and S21 that show a much lower leakage current are the ones irradiated off the IRRAD beam axis, thus receiving a much lower dose.

Figure 7.11 contains all sensors irradiated with protons in a non-uniform profile at KIT. One can notice that a few sensors present breakdown below 1000 V. Two HPK triplet sensors showed breakdown. These sensors had damaged parylene coating (Section 7.4) which might affect the HV behaviour. The Micron n-on-p IT5 was one of the first thinned assemblies and showed much higher leakage current even before irradiation. The last batch of sensors were uniformly irradiated at JSI-IST (neutrons) and KIT (protons), with the IV curves shown in Figure 7.12; none of them showed breakdown up to 1000 V.

At the time of the sensor PRR, there were in total 22 sensors irradiated, including Micron n-on-p, Micron n-on-n and HPK n-on-p. Within this set, breakdown before 1000 V was observed in four sensors. Of the sensors that had breakdown, one was IT5, discussed previously. Other three T2, T6 and T7 were parylene coated and KIT proton irradiated, showing signs of surface damage. Finally, an additional sensor (T3) proton irradiated, not

[2]KIT - https://www.etp.kit.edu/english/264.php
[3]IRRAD - http://ps-irrad.web.cern.ch

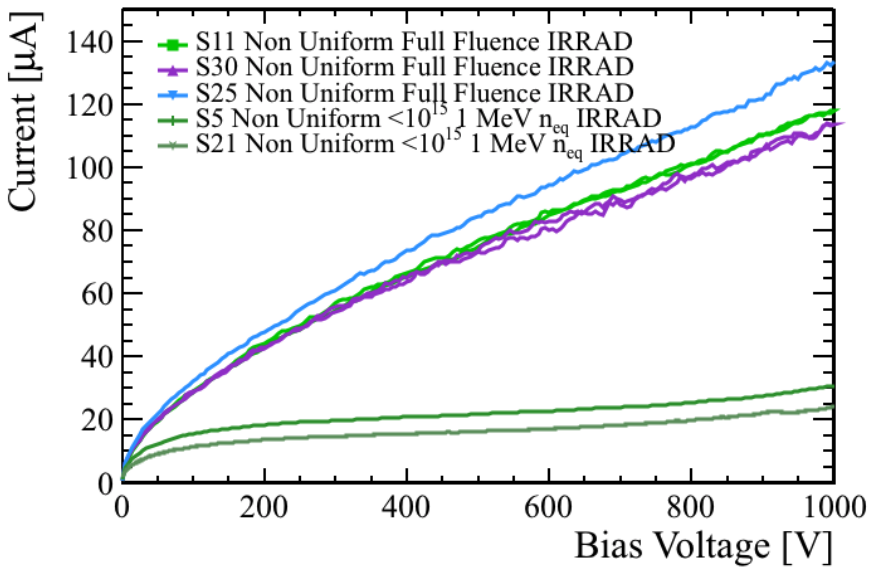

Figure 7.10: IV curves for sensors irradiated at IRRAD.

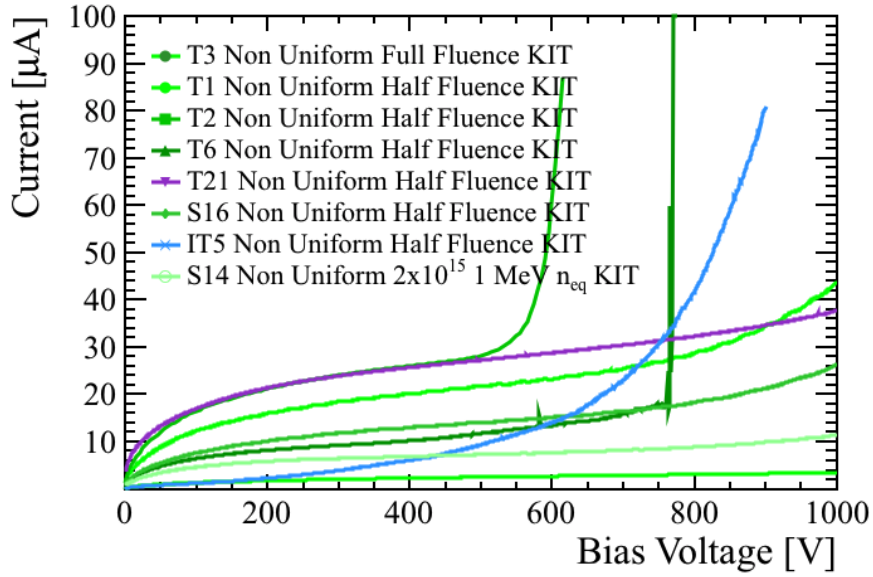

Figure 7.11: IV curves for sensors non-uniformly irradiated at KIT.

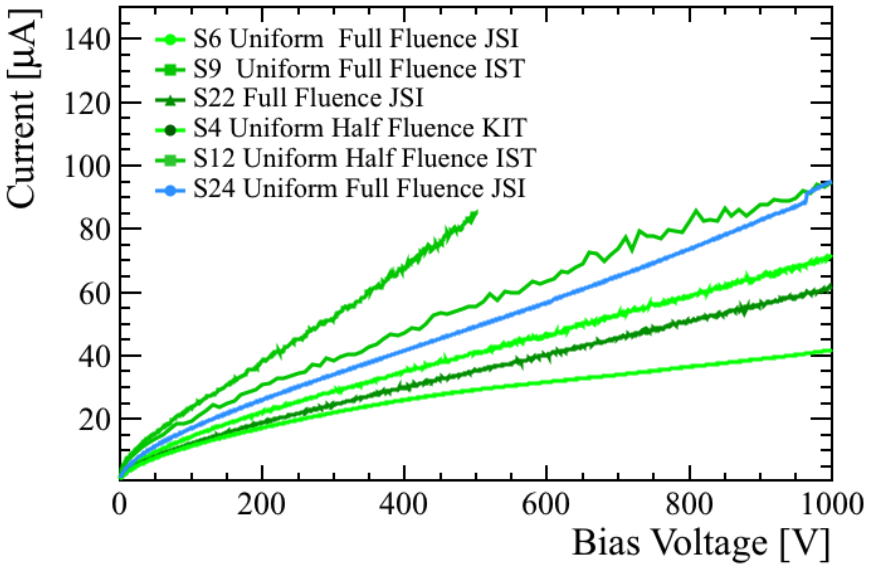

Figure 7.12: IV curves for sensors uniformly irradiated at JSI, IST and KIT.

parylene coated, showed an early breakdown but upon retaking the IV curve it did achieve 1000 V. Later became clear that this was due to a temperature dependance effect investigated in Section 7.5.

Based on these results the final PRR report encouraged the VELO to pursue the HPK n-on-p, 39 μm implant size and 450 μm guard-ring size option, based on the charge collection and high voltage behaviour before and after irradiation.

7.4 Parylene and Irradiation

During the prototype testing phase, the high voltage was maintained while operating the sensors in the laboratory and in the testbeam. When in a normal atmosphere, it has been seen in two assemblies that our n-on-p hybrid assemblies tend to spark above 400 V, destroying the hybrid assembly (Figure 7.13). This is due to the proximity of the sensor backside at the bias voltage and the ground pad of the ASIC, located below the sensor, on the ASIC periphery.

To solve this issue, one can operate the sensors under a vacuum, as they will be in the final detector. However, the necessity of using vacuum increases the time needed to test each sensor enormously. To avoid this time loss, a fraction of the sensors used during the

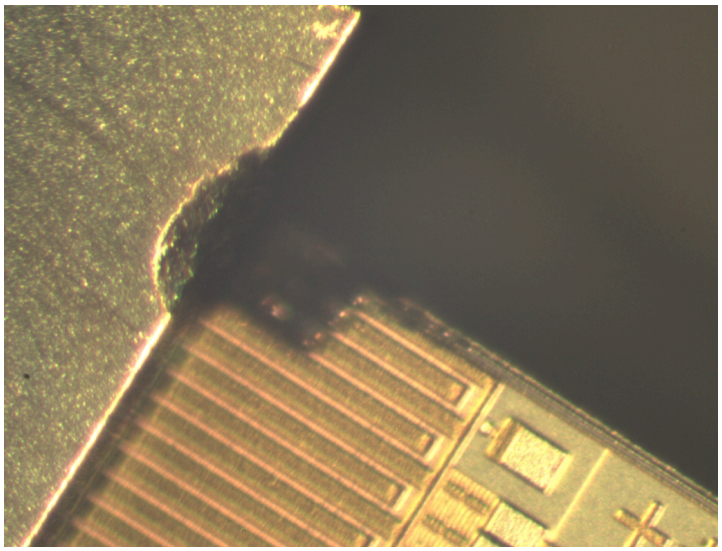

Figure 7.13: Microscope image detailing area of the S15 assembly where the spark happened. As a scale, the pads in this image are 80 µm wide.

R&D have been coated with Parylene coating.

Parylene is a polymer deposited through chemical vapour deposition, forming a conformal thin film on the surface. This film is a powerful dielectric, and is used often to mitigate sparks and shorts such as the ones observed in VELO prototype assemblies [90]. There are a few different Parylene variants, the prototype sensors in this case were coated with Parylene-C. This variant includes a Chlorine atom in the chain, greatly improving the protection from humidity and is also deposited much faster [90].

As it has been noted in the previous Section, the behaviour of irradiated, parylene-coated sensors diverge from non-coated ones. In fact, upon visual inspection (Figure 7.14), one can notice that the Parylene film forms bubbles and seems to detach from the surface. More interesting however is that the higher leakage current effect does not happen in all of the Parylene coated samples. The assemblies shown in Figure 7.14 were all irradiated by protons, while the ones in Figure 7.15 were irradiated with neutrons and seem to maintain their structure with irradiation.

A temperature effect, heating caused by the irradiation beam hitting the sensor, causing the delamination of the coating, was raised as possible reason. Parylene is rated to keep its properties up to a temperature of 290 °C and it is unlikely that the sensors that temperature inside a temperature controlled, cold box. Nevertheless staff at KIT checked

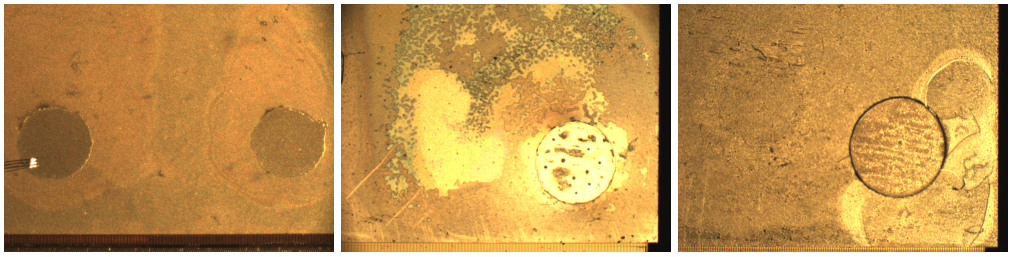

Figure 7.14: Microscope images of proton irradiated sensors S4 90(left), T7 (center) and S11 (right). One can see how the surface looks dirty and delaminated. The circular holes were made in the coating process to allow for wirebonding.

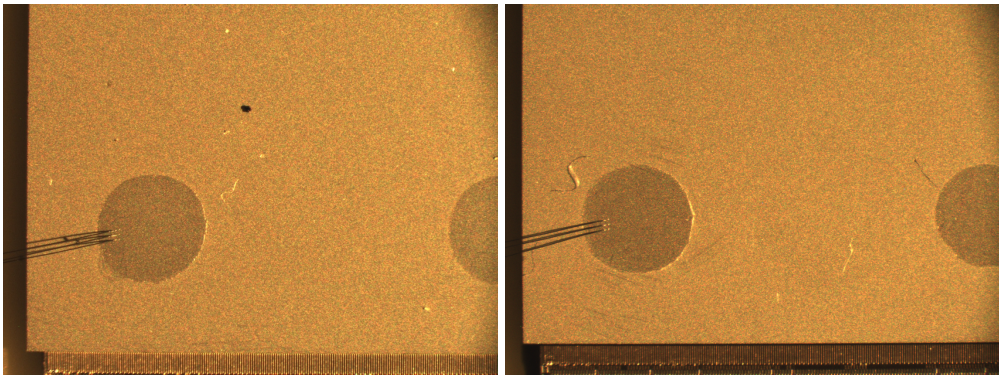

Figure 7.15: Microscope images of neutron irradiated samples sensors: S17(left) and S22(right). No defect on the parylene layer can be observed.

this by placing a PT100 temperature probe on the sensor during irradiation. The temperature was observed to "increase by 3-5 degrees" but never went above −30 °C [91]. Most likely the irradiation itself causes some reaction that destroys the coating. In Figure 7.14 the corners shown are the ones with the highest fluence, coinciding with the region where the damage to the parylene is greater.

Since the observation of this effect, first presented at the sensor engineering design review (EDR), no Parylene coating was used in prototype assemblies and the tests reverted back to measurements in vacuum. Although a complete investigation of the effects of irradiation on Parylene coated devices was out of the scope of this work, the parylene damage has been observed by other groups and it should be avoided in irradiation tests or as solution in experiments.

7.5 Breakdown Voltage Temperature Dependence

It was noticed during the testbeam campaign of early 2017 that non-parylene coated, non-uniformly irradiated sensors were having a breakdown much earlier than what it was expected, sometimes as low as 500 V. This testbeam was also the first in which a new vacuum cold box was installed in the testbeam setup. The goal was then to investigate the cooling system and what was the temperature of the sensor during operation.

It was discovered that operating a cold block at −20 °C with the chip under operation means a sensor temperature of about −3 °C, very different from the expected achieved VELO Upgrade sensor temperature of −25 °C. The setup was improved by the use of a more powerful chiller and optimisation of the Peltier voltages, achieving temperatures lower than −30 °C in the testbeam environment. However, even improvements in the cooling block did not fully prevent the early breakdown issue.

What followed was an attempt to systematically study the effect of temperature changes on the breakdown voltage. Sensors T25/T26 are non-uniformly irradiated, non-parylene coated, n-on-p HPK sensors with rounded edges. IV curves were taken with both sensors at different temperatures using the laboratory vacuum chamber setup, as it can be seen in Figures 7.16.

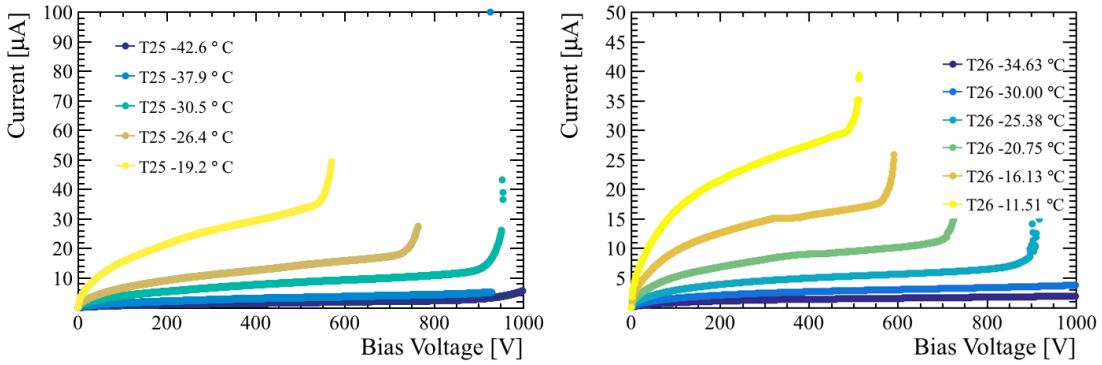

Figure 7.16: IV Curves for sensors T25 (left) and T26 (right) at different temperatures. T25 was non-uniformly irradiated with a maximum fluence of $8 \times 10^{15} \cdot 1\,\text{MeV}\,\text{n}_{\text{eq}}\,\text{cm}^{-2}$ while T26 was non-uniformly irradiated with a maximum fluence of $4 \times 10^{15} \cdot 1\,\text{MeV}\,\text{n}_{\text{eq}}\,\text{cm}^{-2}$.

7.5.1 Temperature and Calibration

In section 7.3 the results for several sensors irradiated with both protons and neutrons did not show early breakdown. At the time temperature probes recorded the temperature both in the cold and warm sides of the Peltier element at the beginning of the IV scan, and were considered to be stable during data taking. As the temperature dependance of the breakdown became evident, the DAQ software for the IV curves was modified so temperatures are recorded while data taking takes place.

An effort to properly calibrate the temperature readout in the cold plate was also made. For calibration, the temperature probe was placed on the surface of the sensor, right at the point that should have received most irradiation. The decision to not place a probe directly on the sensors while performing IV scans was made in order to guarantee the PT100 readout module will not be damaged by the bias voltage on the back side and to not alter the electrical behaviour of the surface. Figure 7.17 shows a calibration curve between the sensor surface temperature and the cold block temperature. The maximum difference between calibrations taken in different days was 0.2 °C in the range between −40 °C and 0 °C. This 0.2 °C difference is taken as the temperature uncertainty.

Figure 7.18 shows the IV scans recorded for a single, neutron irradiated assembly (S22), together with the temperature variation observed while the sensor was being measured. This measurement allows for a point-by-point correction of the measured current to the average temperature recorded during data taking, using Eq. 5.14. One can see

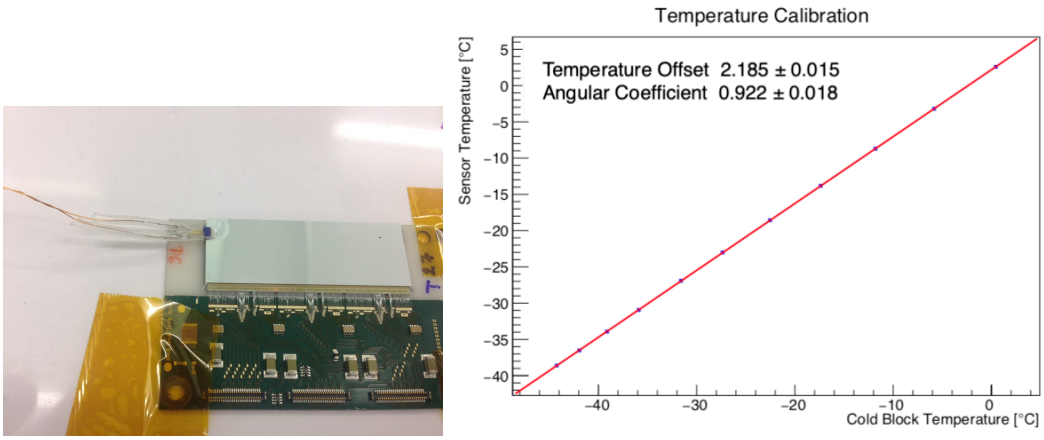

Figure 7.17: Temperature calibration curve (linear function: $ax + b$) between the cold block and the silicon sensor tip. On the left a picture of the temperature sensor positioned in the sensor corner.

that the temperature scaling completely removes the effect caused by the cooling system oscillations around the temperature set point.

A few different sensors had their IV scans taken with varying temperature values, so as to properly identify which of the assemblies showed this breakdown behaviour and if the temperature behaviour was similar and could be identified.

7.5.2 Testing for Thermal Runaway

At first the hypothesis for the breakdown was of a sensor heating causing the leakage current increase. If that was the case, the heat generated in the sensor most irradiated edge would not be conducted away efficiently enough. This would impact greatly the operation and cooling parameters of the upgrade. Figure 7.19 exemplifies the scale of power dissipated in the sensor due to the leakage current, even at high temperatures ($\approx -10\,^{\circ}\mathrm{C}$), is of the order of $\approx 15\,\mathrm{mW}$.

With such a small amount of energy being injected through leakage current, it is hard to argue that the self-heating is actually causing thermal runaway breakdown behaviour. The Timepix3 ASIC when turned on uses of the order of 1.5 W power directly under the sensor. By monitoring the leakage current of an assembly while its ASICs are turned on, one can identify if the breakdown still occurs. If a stable state is achieved, it follows that the thermal runaway power threshold is beyond the 4.5 W being generated by the ASIC and

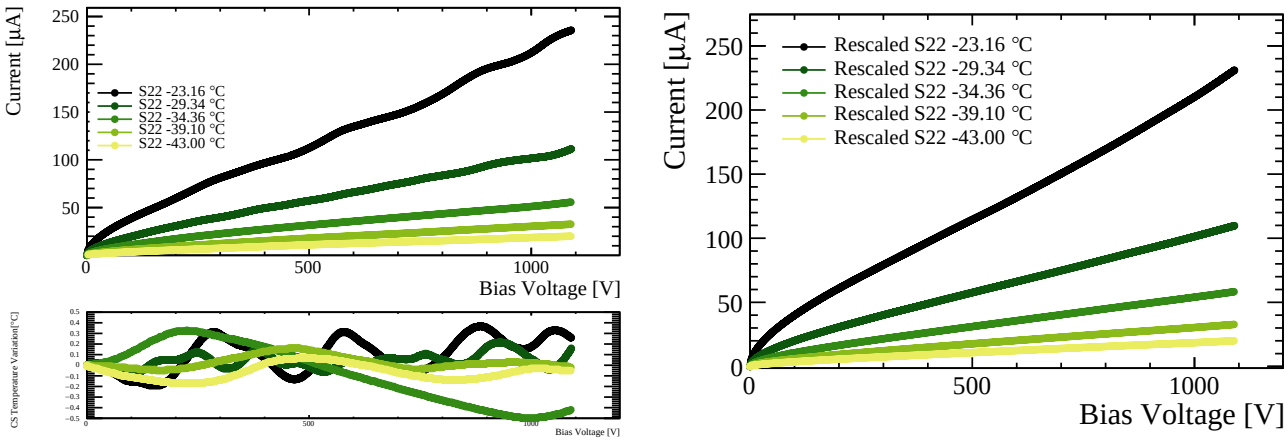

Figure 7.18: Leakage Current and temperature of assembly S22 (uniformly neutron irradiated) as function of bias voltage (left), with the temperature variation recorded as data was taken. The oscillations with respect to the initial temperature are correlated with the current variations. The same curves corrected for the average measured temperature are plotted on the right.

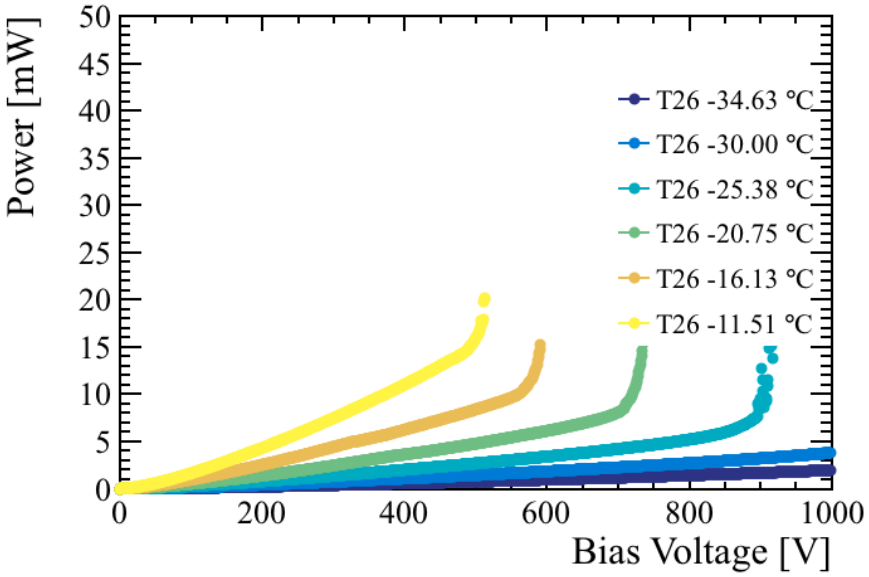

Figure 7.19: Power in the sensor T26 due to leakage current for various temperatures. The breakdown does not seem occur at a threshold power, indicating that the self heating is not responsible for the breakdown.

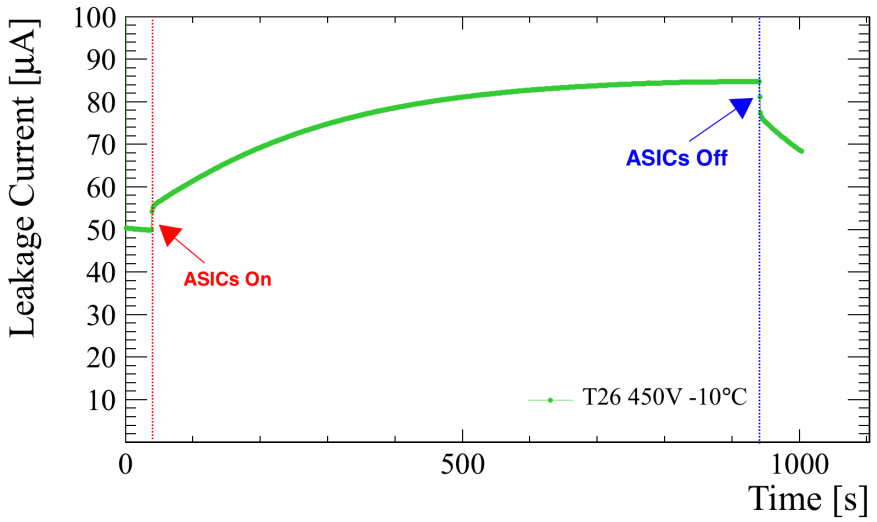

Figure 7.20: Leakage current of assembly T26 in a vacuum tank, cooled by a chiller set to −10 °C having its ASICs turned on. Each one of the 3 ASICs dissipates about 1.5 W of power. The current does increase, but it reaches a new plateau.

the effect observed is not due to thermal runaway cause by leakage current. Figure 7.20, shows that the current increases over a period of about 1000 s after the ASIC is turned on, indicating that the sensor heats up, but a plateau is reached without thermal runaway.

One last possibility is that the current is extremely localised at the most irradiated tip, and the heat generated in that small region is not capable of being distributed in the silicon bulk quickly enough, leading to a localised thermal runaway effect. In order to identify this localised behaviour, a thermal imaging camera that recorded temperatures was used while the sensor was placed in the Liverpool vacuum chamber. Due to the reflective surface of the sensor, it was necessary to cover the sensor with an inert material with no infrared reflectivity. Tests of several tapes showed that a Kapton tape with a very thin layer of thermal compound deposited on top of it was adequate. Both the Kapton and the Kapton with thermal paste did not alter the IV behaviour of the sensor.

The FLIR camera used to monitor the sensor temperature was calibrated using the temperature of the cooling block, in a corner covered with the same Kapton tape used on the sensor. Figure 7.21 shows an example of the temperature imaging of a sensor.

No local temperature increase was observed while the sensor was biased or breaking down. Using this measurements, one can rule out thermal runaway as the cause of the breakdown of these sensors, which is essential information for deciding operational pa-

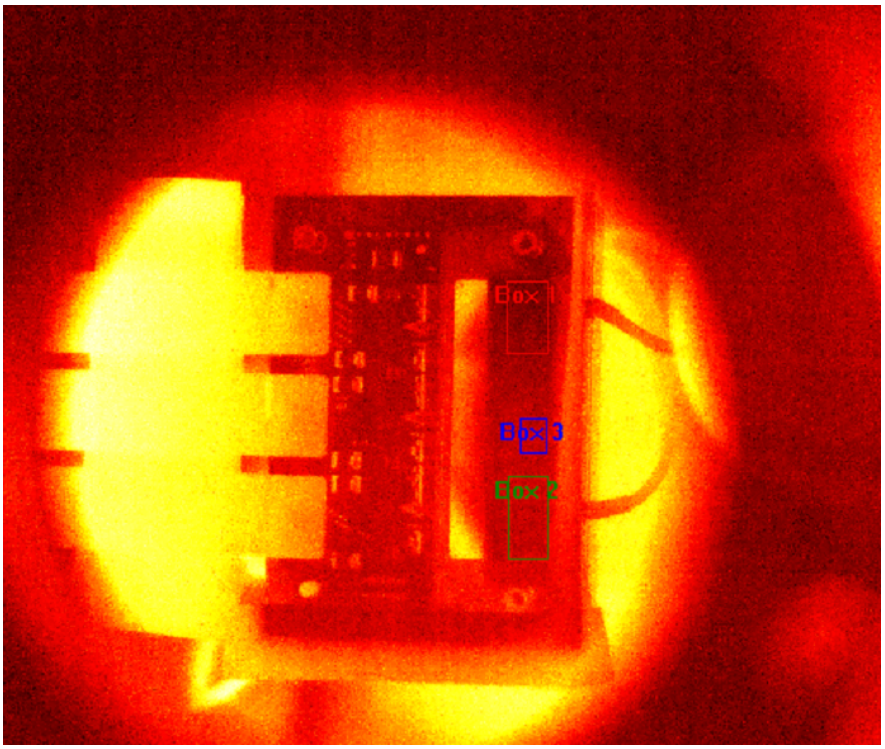

Figure 7.21: Image taken with an infrared camera through the IR window in the Liverpool vacuum tank. The Kapton tape can be seen marked with three regions of interest, while the other half of the sensor backside is uncovered. One can also identify reflections from the outside, marked as the very bright regions in the image.

rameters in the cooling of the VELO.

The objective is to analyse the IV behaviour as a function of the temperature, parametrising the breakdown behaviour. In order to do so a functional form for the IV curve behaviour is used:

$$\mathrm{I}_{\mathrm{leak}}(V) = \mathrm{I}_s(1 - e^{-\alpha V}) + \kappa V + \beta e^{\delta(V - V_{th})}, \tag{7.1}$$

where I_s is the diode saturation current and α is a parameter that controls how fast the diode reaches saturation, composing the Shockley diode equation using the bias voltage. The term κV models the linear increase in current due to irradiation effects, which has been identified as a result of avalanche generation [92] [93]. It is important to note that I_s is also affected by irradiation, increasing linearly with the fluence, and should not be compared with the values of non-irradiated samples. The last term in Eq. 7.1 will model the breakdown, with β initial value set to 10^{-6} guaranteeing that no contributions from this term affect the non-breakdown part of the IV curve, while δ models how fast the breakdown happens and V_{th} is the breakdown threshold voltage.

This model intends to systematically parametrise IV curves of irradiated sensors, in such a way that little tuning of parameters is necessary for performing a fit to the IV curves. For sensors with absolutely no sign of any breakdown behaviour, such as the one in Figure 7.18, the fit can be simplified by removing the breakdown term:

$$\mathrm{I}_{\mathrm{leak}}(V) = \mathrm{I}_s(1 - e^{-\alpha V}) + \kappa V, \tag{7.2}$$

Equations 7.1 and 7.2 allows systematical comparison of the current behaviours between different temperatures and sensors. Figure 7.22 illustrates the behaviour of a sensor IV curve taken at approx. $-35\,^{\circ}$C, fitted with Eq. 7.1.

7.5.3 Effective Band Gap Energy

As discussed in Section 7.5.1, one can use the temperature measurements in order to rescale the leakage current measurements to a stable temperature. The parameter that governs this scaling is the effective band gap energy ($\mathrm{E}_{\mathrm{eff}}$). One can obtain this value by using the

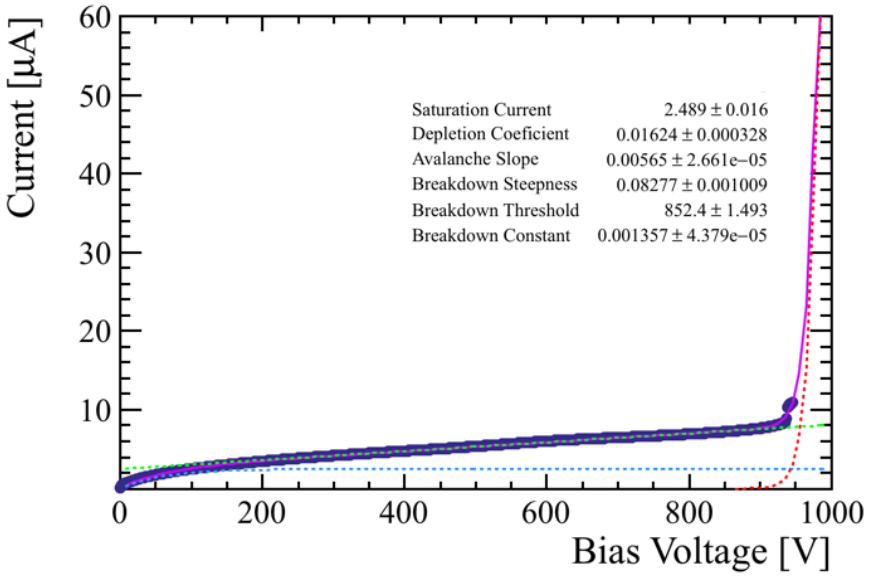

Figure 7.22: T25 at −35 °C IV Curve (black dots) fitted with Eq. 7.1, plotted in violet. The blue dashed line corresponds to the diode saturation current, the green curve is the sum of the first two terms and the breakdown term appears independently in red.

saturation current (I_s) to fit E_{eff} thermal scaling using:

$$I_s(T) = S(T + T_{\text{sys}})^2 \times \exp\left[-\frac{E_{\text{eff}}}{2k_B(T + T_{\text{sys}})}\right], \tag{7.3}$$

where S is a scale factor, T_{sys} is temperature systematic error free parameter and E_{eff} is the effective band gap. Figure 7.23 contains the fit for T25's I_s behaviour as function of temperature. The T_{sys} parameter was originally introduced to account for the difference between measuring the temperature of the sensor itself and of the cold block, however, the calibration applied to the temperature readout in the cold block takes care of this difference, this parameter is not needed to fit the I(T) curves and is fixed to 0.

By trying to use the saturation current parameter from Eq. 7.1 to fit the expected scaling behaviour of Eq. 7.3, one finds poor agreement between model and data. This comes from the parameters I_s and κ being highly correlated, specially at high temperatures, where the I_s term has similar values to κ. One then needs to use the first two terms to properly describe the leakage current voltage behaviour before breakdown. In order to extract an E_{eff} value, the current values obtained from the total fit at a few bias voltages and fit with Eq. 7.3, while maintaining the systematic temperature error fixed.

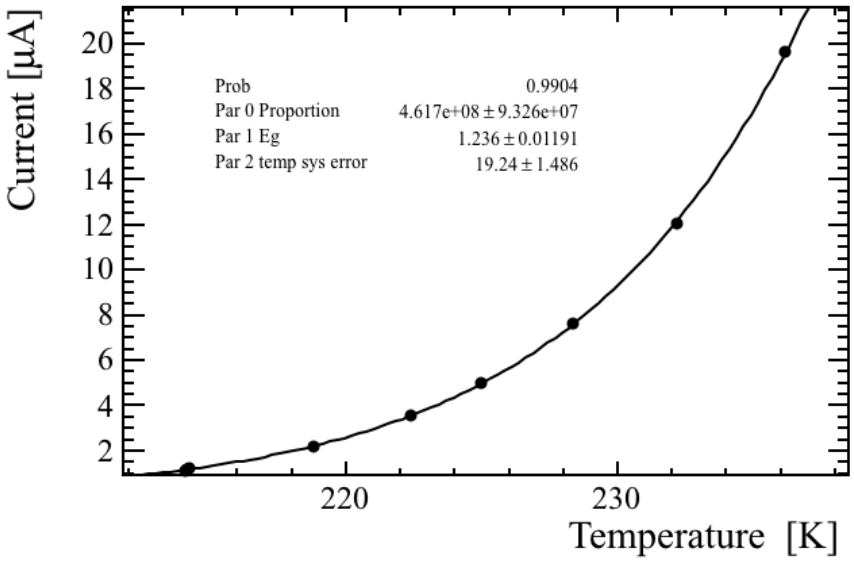

Figure 7.23: T25's saturation current curve fitted as a function of temperature (using Eq. 7.3), using data from the IV curve fits. The effective energy band gap value is compatible with the 1.21 value recommended by literature [94].

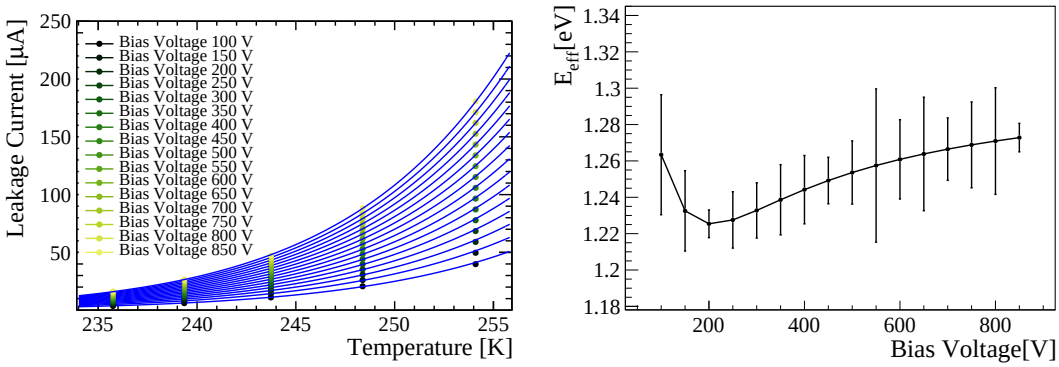

Figure 7.24: Leakage current values scaling with temperature at different voltages for a n-on-p neutron irradiated sensor (S22), uniformly irradiated with neutrons (left). The blue curves show fits of equation 7.3 to each set of points at a given voltage. On the right, the results from the blue curve fits for E_{eff}.

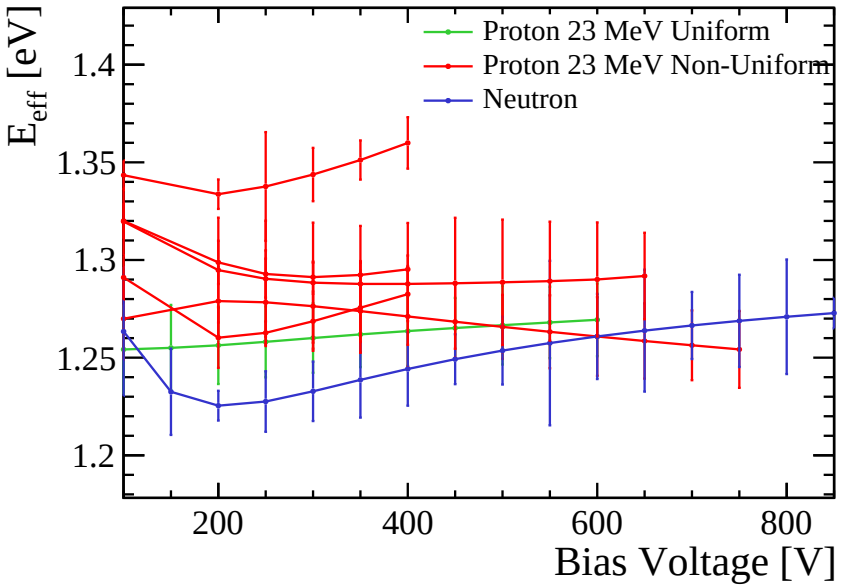

Figure 7.25: E_{eff} measurements as a function of bias voltage.

In Figure 7.24 one example of the leakage current extracted from the IV curve fits at different voltages is shown. The scaling equation fitted to each set of voltages. As this sensor in particular (S22) did not show breakdown behaviour it was possible to probe a wide range of voltages. Figure 7.24 also displays the fitted values for E_{eff} as a function of voltage, with values fluctuating around 1.25 eV.

The same procedure described for sensor S22 consisting of fitting IV and using that to get the temperature scaling was done for 7 other sensors. The E_{eff} result is shown in Figure 7.25. One can observe a consistent behaviour, in which the E_{eff} stabilises at higher voltages. It is quite clear that the average proton irradiated sensors have higher E_{eff} than the neutron-irradiated sensor S22. Considering that the data ultimately comes from the IV fit, the average result between sensors is done by taking the value of E_{eff} measured at 400 V, where all sensors have a "well-behaved" current. The value obtained is:

$$E_{\text{eff}}^{\text{avg}} = 1.28 \pm 0.02\,\text{eV} \tag{7.4}$$

the obtained average result deviates from the literature recommended value of 1.21 eV [94] [95], but fall within measurements performed previously [96] [97]. The qualitative behaviour of a gradual raise in E_{eff} as a function of voltage after the kink seems to be

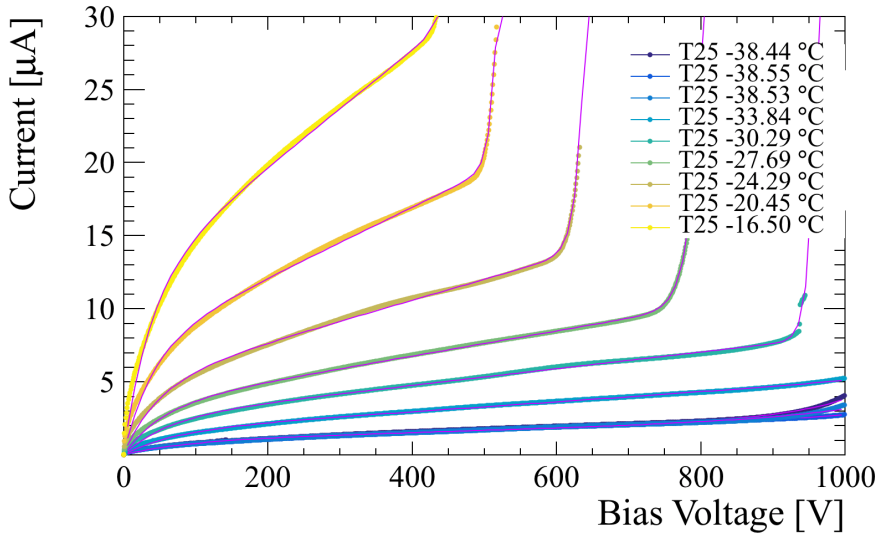

Figure 7.26: IV curves taken with T25 at different temperatures and the fits obtained for the IV behaviour.

present here as well. For all further temperature corrections the 1.21 eV value is used troughout so all IV curves are consistent.

7.5.4 Breakdown Temperature Behaviour

In Figure 7.26 the IV curve mode is shown and how it can fit for IV curves over a range of temperatures. In this case, all IV curves were taken in the same conditions with temperature being altered by changing the power on the Peltier element. At the coldest temperatures the breakdown behaviour is not seen anymore below 1000 V.

Using the information from fits, one can study how the sensors breakdown voltage and leakage current evolve as a function of temperature. Because of the interplay between δ, V_{th} and β, the threshold parameter does not represent a good estimator of the breakdown voltage. Instead, the breakdown voltage (V_{BD}) is defined to be the voltage in which the exponential breakdown component of the IV fit is equal to 10% of the saturation current I_s component. Thus the V_{BD} is calculated from the fit parameters as:

$$V_{BD} = \frac{1}{\delta} \log\left(0.1\frac{I_s}{\beta}\right) + V_{\text{th}} \tag{7.5}$$

To gather more information regarding the sensor breakdown, an additional set of eight

sensors (triples) was irradiated in two facilities: IRRAD and Birmingham. The four sensors at Birmingham were irradiated with 23 MeV protons, with a pencil like beam that scanned the sensor surface in order to create a non-uniform fluence profiles. The additional 4 triple assemblies at IRRAD were irradiated with a (20 GeV/c proton beam, with a gaussian, non-uniform shape. The IRRAD sensors are particularly important as their hardness factor[4] is the most similar to the expected flux in the VELO. Previously, only single assemblies had been irradiated at IRRAD, so it was important to cross-check that the HV tolerance was not dependent on the tile single or triple geometry. Again, details of the irradiations can be found in Appendix B.

Figure 7.27 contains IV curves at approximately the same temperature for each of the eight samples, showing the very different behaviour of the two set of sensors. While sensors irradiated at IRRAD have not shown any sign of breakdown up to 1000 V, sensors irradiated at Birmingham show a very early breakdown (before 500 V). This difference in breakdown behaviour shows how different irradiations, even when scaled to the same neutron equivalent irradiation dose, result in vastly different macroscopic behaviour.

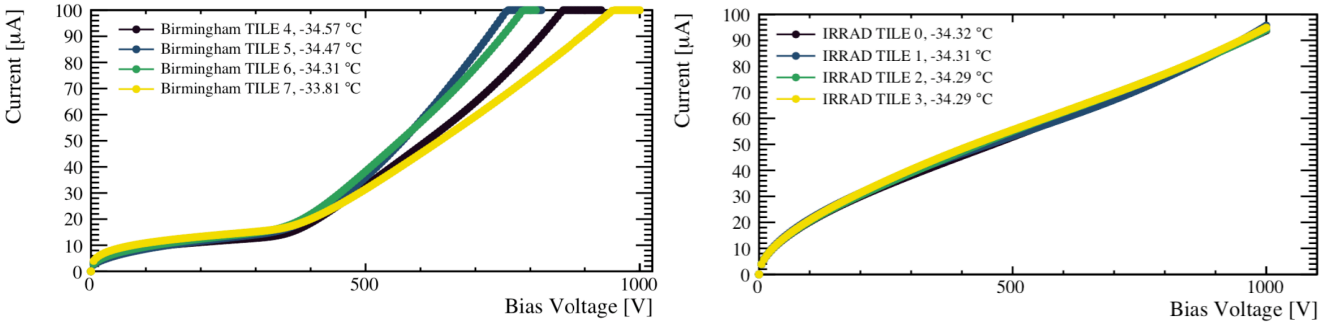

Figure 7.27: IV curves of all eight triple assemblies irradiated at Birmingham and IRRAD for further investigation of the early breakdown. On these plots measurements were taken at the same temperature, but not temperature rescaled. On the left plot a plateau of the current is observed due to a hardware limit to not exceed 100 μA current.

Figure 7.28 contains the V_{BD} for the irradiated sensors that did show breakdown behaviour. To guarantee that differences in the overall current wouldn't affect the breakdown voltage measurement the fits were performed to all IV curves temperature scaled to −20 °C. First of all, one can see that the parylene coated irradiated sensors do not seem to have a systematic temperature effect, but rather just a lower breakdown voltage that is

[4]Equivalence between different irradiations, see Section 5.3.

more or less constant for different temperatures. The irradiated sensors to full fluence have an overall lower breakdown voltage than the half fluence ones. Finally, the sensors irradiated at Birmingham show a very different result, with breakdown voltages much lower than all other samples and a temperature behaviour that seems to be reverse to the KIT irradiated ones. The proton irradiation energy in both facilities is very similar, while the profiles are quite different, which could play a role on the differences observed. Some of the sensors, when cold enough, did not breakdown. This fact that is expressed by the red line in the plot.

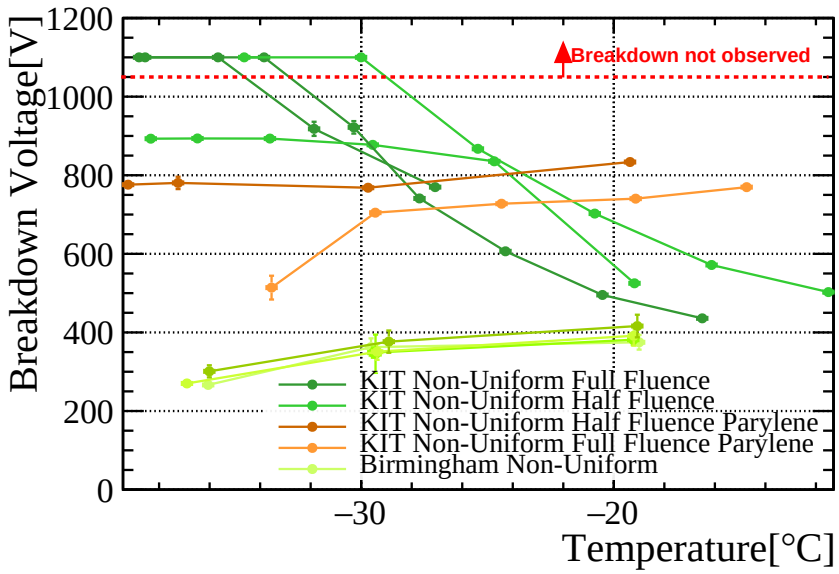

Figure 7.28: Breakdown Voltage of proton irradiated sensors as a function of temperature. If a sensor did not have breakdown before 1000 V the value on this plot is set to above the red line. Sensors irradiated at Birmingham are plotted with slightly different colours to improve visualisation.

Excluded from Figure 7.28 are all sensors that did not show breakdown, namely: S22 (full fluence neutron uniformly irradiated), S4 (23 MeV low fluence proton uniformly irradiated) and S16 (half fluence 23 MeV proton non-uniformly irradiated).

Although the breakdown observed shown here happens before the 1000 V requirement for the upgrade sensors, there are two points to note. Firstly, this behaviour happens only on 23 MeV proton-irradiated sensors, which has a type hardness factor quite different from the expected flux in the VELO (more similar to the IRRAD flux). The second point

follows from the charge collection results, discussed in Chapter 6. The measured charge collection above 6000e$^-$ is around a bias voltage of 800 V. Even if an effect like the one observed in the KIT irradiated samples shows up, the necessary bias voltage for the desired CCE is achievable without breakdown within the cooling constrains of the Upgrade ($\approx -28\,°C$).

Comparison of the κ parameter

The increasing current with bias voltage after the IV curve "knee" has been linked with the presence of avalanche in the bulk through TCAD studies [92]. This increase is accounted for in Eq. 7.1 by the κ parameter. It is interesting to look at the behaviour of κ as a function of temperature, and whether or not it does indeed follow the expected temperature trend of an avalanche behaviour. To better isolate this temperature dependancy, each IV is scaled to a standard temperature of $-20\,°C$[5], which stabilizes the I_s and α parameters across all measurements.

However, the set of sensors that can be used to compare the data has different irradiation profiles. As mentioned in Chapter 5, the leakage current is expected to scale linearly with the NIEL flux. Combining equations 7.1 and 5.23, one gets:

$$I(\Phi_{\text{eq}}, V) = \alpha\Phi_{eq} \times \text{Vol} \times \left(I_s(1 - e^{-\alpha V}) + \kappa V\right) \tag{7.6}$$

due to this linear scaling, the factor $\alpha\Phi_{eq}\times$Vol is built in the parameters fitted (I_s and κ). To compare between sensors, one can sum the flux of the fluence bins of non-uniformly irradiated sensors over the whole assembly area[6]:

$$I(\Phi_{\text{eq}}) = \alpha \left(\sum_{i}^{\text{Area}} \Phi_{\text{eq}}^{i} A^{i} \right) I_0(V) \tag{7.7}$$

The integrated flux can then be used as a scaling parameter between different irradiations. As an example, the IV curves (Fig. 7.29) of all sensors can be scaled to the total flux received by the S4 assembly of $8 \times 10^{15} \cdot 1\,\text{MeV}\,n_{\text{eq}}$.

The same scaling factor can be used to scale the κ parameter, allowing us to compare the slope between neutron and proton irradiations and between different fluences (half

[5] As a remainder, the scale uses $E_{\text{eff}} = 1.21$

[6] The thickness of all assemblies here is the same so one can safely talk about area instead of volume.

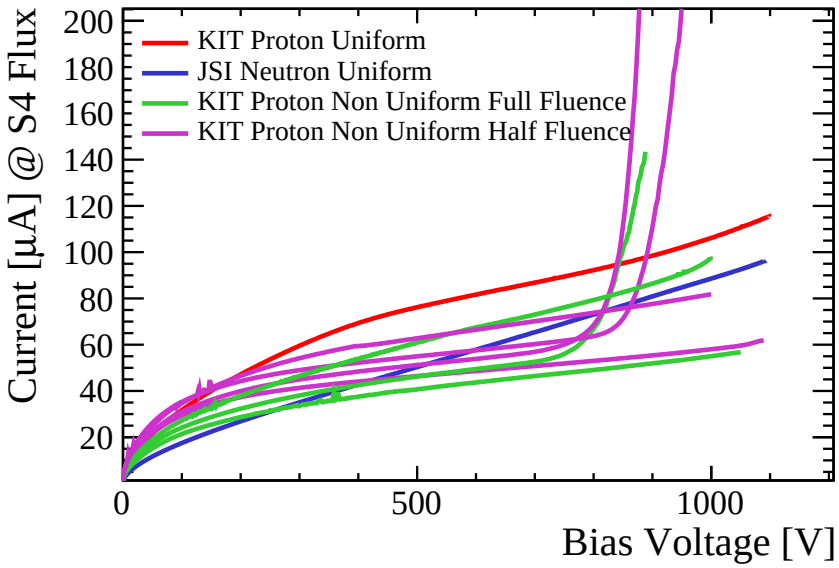

Figure 7.29: Comparison of Leakage current as a function of voltage for different irradiation fluences. All the IV curves in this plot have been rescaled to match the total dose received by assembly S4 (red curve) at the temperature of −20 °C.

and full). The results can be found in Figure 7.30. The biggest contribution to the error comes from the rescaling parameter based on the fluence, in which the fluence uncertainty value quoted by KIT of 20% was used. The sensor with the highest κ parameter is the neutron irradiated (S22), which has also received the most integrated fluence overall. It is clear that one cannot differentiate between non-Uniform KIT samples, as they are all within one margin of error of one another. One can observe, however, that most sensors are grouped quite below the κ value for the neutron irradiated sensors. Perhaps there are effects at this fluences in which the radiation damage leakage current cannot be scaled just assuming NIEL.

It would be extremely useful to obtain predictions of avalanche slopes is obtained TCAD simulations of irradiated sensors based on damages introduced and how does the simulation reproduce the slope and the temperature variation of the silicon lattice. Usually, TCAD simulations models radiation damage by introducing effective energy levels in the band gap. These effective levels reproduce the macroscopic effects caused by irradiation without the complexity of introducing the many possible energy levels introduced by the different damages in the lattice.

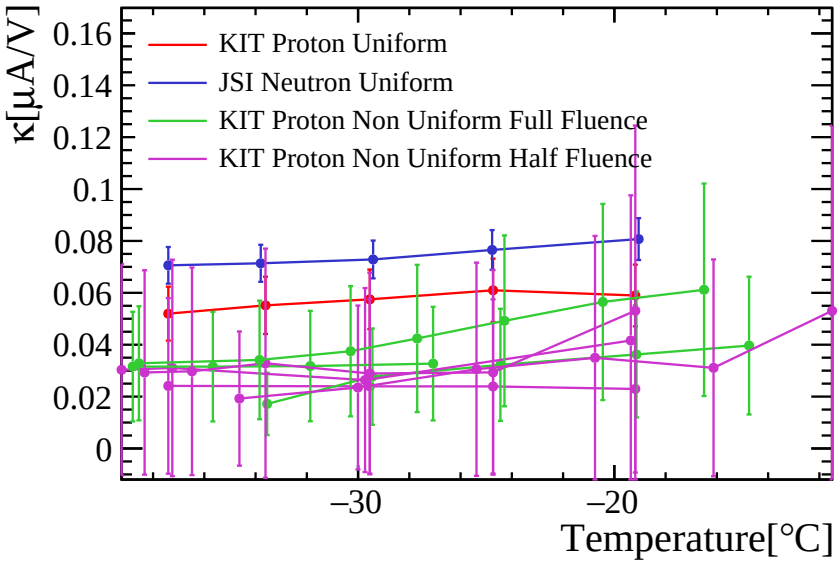

Figure 7.30: Trend of the κ parameter for nine different sensors with four different irradiation profiles. One can see that the values are more or less consistent and stable in temperature. The high error bars come mostly from the dose uncertainty and make the interpretation of half fluence KIT irradiated sensors trends difficult.

8 Bias-through-ASIC Method

As discussed in Chapter 5, silicon sensors for high energy physics work by operating a diode's pn-junction in reverse bias. In the case of the VELO Upgrade the sensors are bump bonded to a readout pixel ASIC, the VeloPix. The process of connecting the sensors to the ASICs through bump bonds needs to be monitored to guarantee the quality of tiles and a high yield of fully functional pixels. This chapter will describe the technique used and the setup built in order to test the bump-bonding and the high-voltage characteristics of tiles after bump-bonding, and before module assembly.

8.1 Tile Probe Card Setup

After the bump-bonding of sensors to the VeloPix ASICs, it will be necessary to test the quality of the connection between the sensor and the pixels in the ASIC before designating them good for module assembly. Usually, tiles are readout by using wire bonds to connect all the necessary data and power channels to readout pads, located in the periphery of the ASIC (Fig. 8.1). Additionally, there is also a bias connection to the sensor backside. Wirebond pads, however, are only reliably usable once, preventing the use of wirebonds for tests before module assembly. The other possibility is to use microscopic needles that gently touch the pads to make contact to the backside and ground pads, delivering the bias without the need for any bonding. Probe cards are Printed Circuit Boards (PCB) cards that hold the many needles needed in a precisely positioned fashion so they can touch each of the readout pads at the same time, powering and reading out an ASIC at the time. The probe station, where the PCB card is mounted, is equipped with microscopes and stages for correctly aligning the ASICs to the needles.

Probe card setups are commonly used to test ASICs before they are diced from the

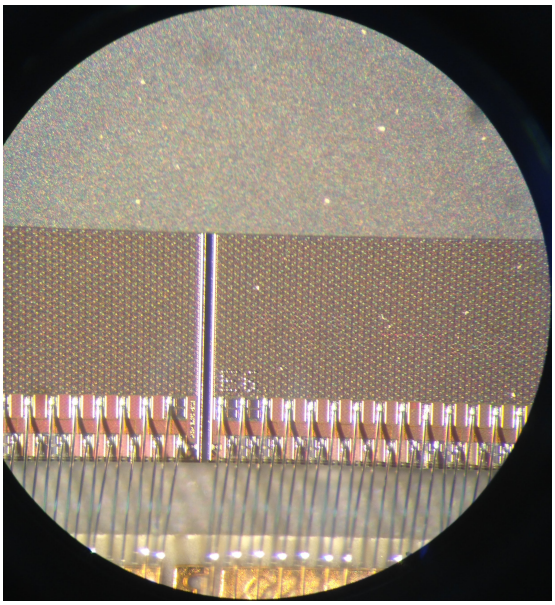

Figure 8.1: Image showing the wirebond connections on a VeloPix ASIC. This high density of connections requires a high precision with wirebonds or probe needle connections. In this image it is possible to see the gap between two ASICs under one sensor.

wafer. This makes it easier to properly readout the ASIC as aligning the wafer globally is sufficient to have the position of each ASIC readout pad in the wafer. The probe station can be programmed to run tests on all of the ASICs automatically. Currently, the process of aligning a VeloPix wafer takes approximately 30 minutes, therefore testing a wafer with roughly 90 chips takes to 9 hours. To test tiles individually, the setup and alignment procedure would have to be done for each tile, which becomes time prohibitive. I designed a setup to position tiles in such a way that a batch of tiles would need to be aligned just once.

Such a setup, to position the bump-bonded tiles precisely, needs to include a very flat and uniform surface using a vacuum chuck to keep the tiles in place during testing and alignment. The probe card setup designed contains five independent vacuum channels, each containing two sets of three 2.5 mm holes, where a set has the space for one tile (Fig. 8.2). Each one of the holes is positioned such that it will be at the centre of the ASIC, trying to reduce any possible warping. The chuck was machined from a single aluminium block in order to achieve a good level of flatness. After machining, the whole chuck surface was treated with a conductive coating to guarantee good electrical conductivity and

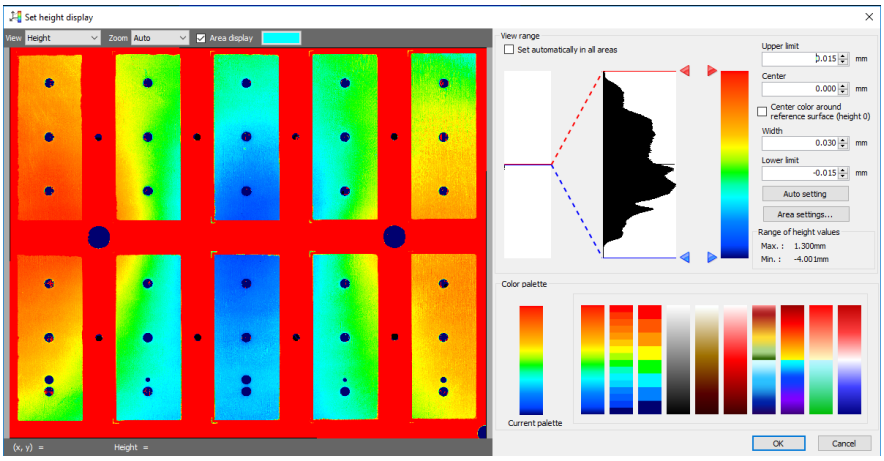

Figure 8.2: Output of the white-light interferometry for surveying flatness of the surface in which the ASICs will be placed. Variation in the z axis is within 15 µm. The red squares correspond to the height of the copper stencil used to place the ASICs accurately in the horizontal directions. The black dots are the vacuum holes, three beneath each tile.

avoid oxidation[1]. Given the constraint of VeloPix readout pads having a size of 80 µm by 200 µm, an alignment copper stencil was designed. This copper stencil is 100 µm thick, and has cutouts so that the tiles can be positioned on the aluminium surface and pressed against the stencil edge. The stencil was designed with alignment marks, to be used to align the tile in the vacuum chuck slot precisely. However, it was found that the tactile feedback of the ASIC sides against the copper stencil proved to be more reliable in aligning the tile with respect to the stencil slot. The stencil was glued to the aluminium chuck and carefully inspected to remove any excessive glue (using an acetone bath) and remains of material that could impact the sensor positioning.

Figure 8.2 shows a white-light interferometry survey of the vacuum chuck surface, detailing the overall flatness of the piece, which was found to be within an acceptable 30 µm range. Figure 8.3 presents measurements made to ensure the precision and repeatability of the positioning of sensors on the jig. The positioning maximal variation from the nominal position was 60 µm (Fig. 8.4). The precise positioning of the probe card needles is done by measuring the left and rightmost corner marks of the VeloPix with the probe station microscope. The positions of the corners are entered into a python script that applies corrections to the nominal position defined by the jig, which improves the agreement of

[1]SURTEC 650 by Nilhaus Suisse

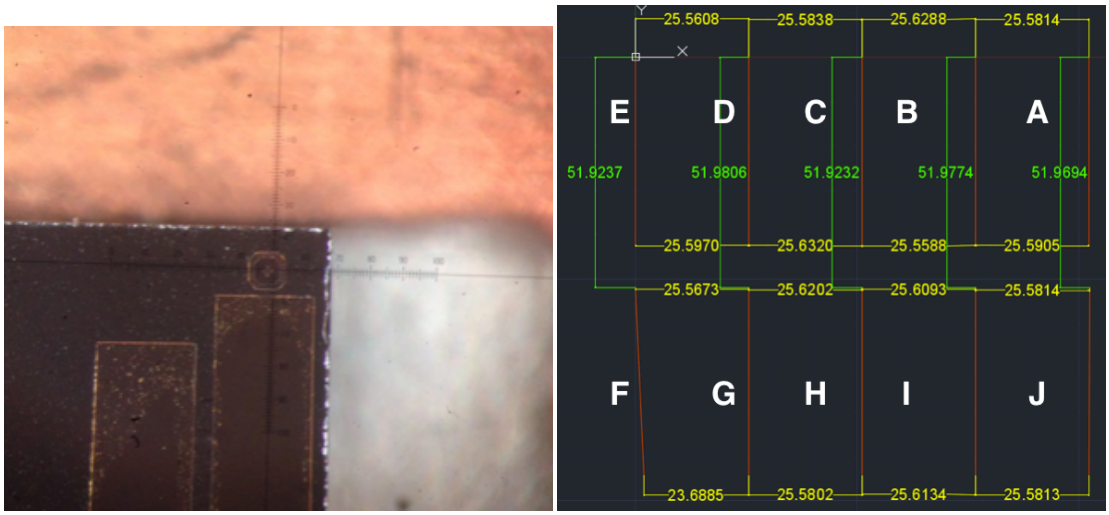

Figure 8.3: Image displaying the reference mark on each mechanical tile used to measure their position with a microscope table (left). Information on the position of each sensor was then loaded to a CAD software (right), globally aligned, and measured to check for deviations larger than 80 µm, that were not found.

the needle–pad positioning to be well within the necessary precision.

8.2 Bias-through-ASIC Method

It is desirable to probe the current-voltage(IV) behaviour of sensors before module assembly, given that the only High Voltage(HV) test the sensors can receive prior to this point is done using the guard ring structures. The sensor design used does not include any biasing structures, known to cause loss of collected charge [98]. An extra constraint is the need for the sensors to perform tests under vacuum, due to the high voltages (up to 1000 V) applied. During the prototyping phase, it was discovered that sparking took place when biasing sensors about 400 V in air. It becomes impracticable to align the probe needles for each ASIC in a hybrid inside a vacuum tank and too time consuming (there are 250 hybrids that need to be tested during the VELO production).

As stated in Chapter 6, the VELO Upgrade sensors are bump-bonded to a readout ASIC, built using CMOS 130 nm technology. In this technology, the pixel electronic elements are embedded in a n-well inside of a p-bulk. In Figure 8.5, one can see that this n-well forms with the p-bulk a diode between the bump-bond pad to the sensor and the

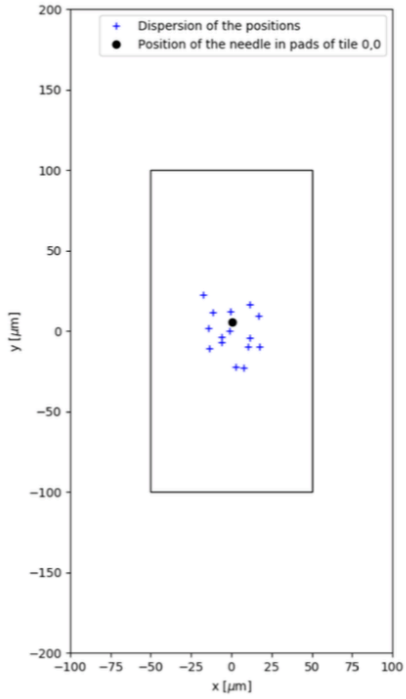

Figure 8.4: Difference in nominal positions and measured pad positions on the probe station.

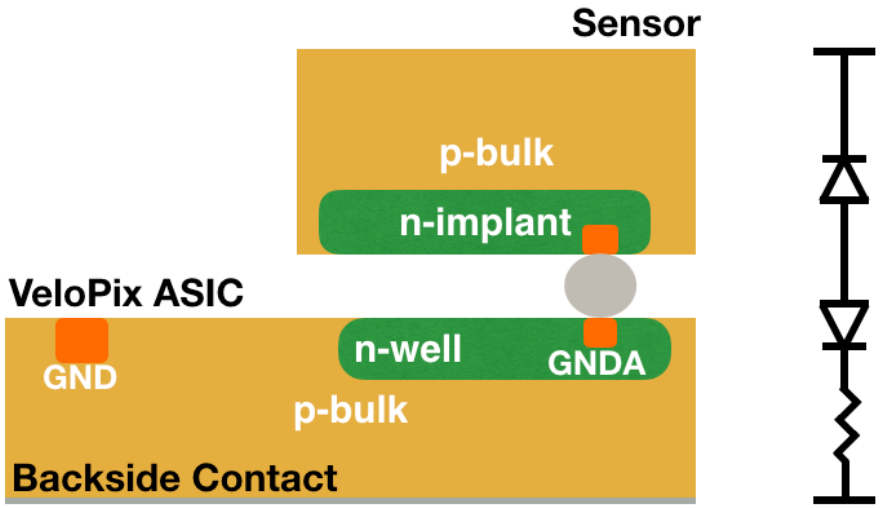

Figure 8.5: Scheme of the orientation of p and n-type implants in both the VELO Upgrade Sensors and the VeloPix and the equivalent diode circuit. The sensor diode is always operated in reverse bias and is composed of a matrix of 256 × 256 n-implants inside the continuous p-type bulk. GND (ground) connection is a readout pad located in the periphery of the ASIC.

ASIC backside, oriented in the opposite direction as the sensor diode. In principle if the sensor diode is being reverse biased, the diode in the VeloPix is forward biased and it should allow conduction of the small leakage current through it.

The VeloPix ASICs used in the VELO will be thinned down from the 750 µm standard wafer thickness to 200 µm, removing passive material that would add radiation length to the experiment. The thinning procedure involves grinding down the wafer's backside, leaving a rough surface on which a layer of SiO_2 grows, which could cause loss of conductivity through the ASIC backside. Hence, to use the VeloPix as a forward-biased diode, to perform a ground connection, it is also necessary to check that the thinned VeloPix has a good conductivity through its backside.

To test this new method of bringing bias to a hybrid pixel detector, a thinned VeloPix

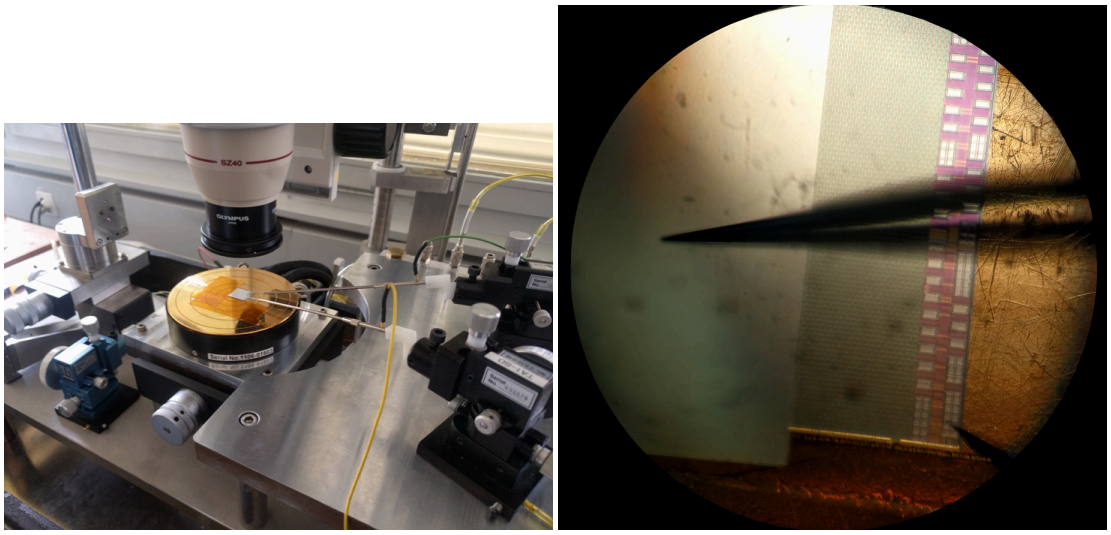

Figure 8.6: Images of needles being positioned on a VeloPix hybrid in order to test the connections between sensor and ASIC backside. Tests were performed using microscopical needles (right) positioned on the correct pads through the use of a microscope (left).

ASIC with no sensor was brought to the DSF lab[2] at CERN so that all connections could be made using probe needles, capable of touching the readout pads in the VeloPix. Figure 8.6 shows pictures of this test setup. To test how effectively the current flows between the analogue ground and the backside, current was injected between the analogue and digital grounds. A diode curve behaviour is expected (Fig. 8.7) with exponentially high current passing through it as the diode becomes forward biased. It is also necessary to test that there was a reliable electric connection between the bulk and the ASIC backside. Figure 8.8 shows that we have a reasonable contact between these two points, with a resistance of approximately 42 kΩ. It is clear, however, that the curve fluctuates a lot. Both tests showed that the backside was conductive and that, in fact, current could pass through the ASIC bulk as a forward biased diode.

Last test performed was to use an ASIC with a sensor bump-bonded to it, apply bias to the sensor and ground it through both the VeloPix readout pads and the ASIC backside, comparing both to make sure the sensor is being properly biased (Fig. 8.9). This new method to bias silicon sensors through the ASIC was proven to function very well and was immediately applied to build a setup that could test VELO production sensors.

[2] http://ssd-rd.web.cern.ch/ssd-rd/

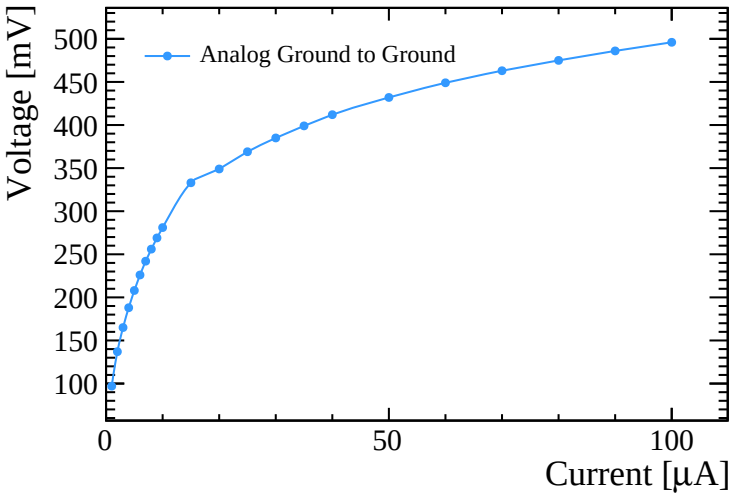

Figure 8.7: Voltage measured across the p-bulk and n-well on the VeloPix by injecting a current forward biasing the diode.

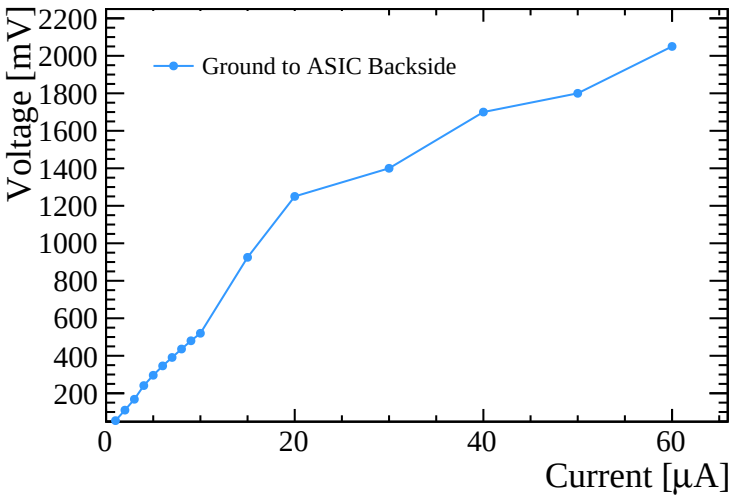

Figure 8.8: Voltage measured across the p-bulk ground contact and the VeloPix backside. This measurement establishes that there is in fact an electrical contact that conducts current.

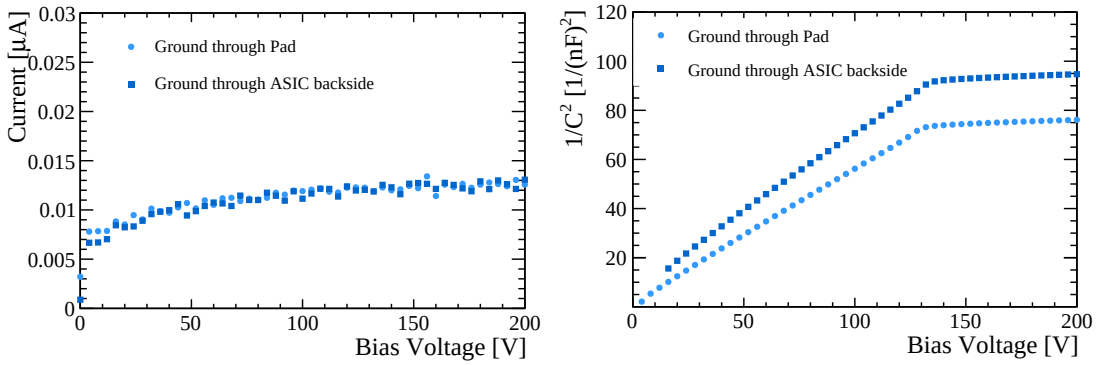

Figure 8.9: Comparison between the regular method of biasing a sensor (through readout pad) and the through the ASIC backside. The IV scans (left) show identical behaviour and overall current. The CV curve shows an added capacitance coming from the extra material between contact points, but the depletion voltage is the same in both cases.

8.3 Vacuum Hood

To probe the high voltage tolerance of the tiles, a vacuum hood was designed to enclose the vacuum chuck, delivering the bias voltage to the backside and using the ground-through-ASIC method to ground the tiles. Figure 8.10 shows the finished hood, with the feedthroughs that connect individual tiles to the HV source. Figure 8.10 also shows the spring-loaded needles that touch the tiles backside. Due to the whole chuck being in a vacuum environment, it is not possible to use the vacuum channels to keep the tiles pressed against the chuck surface. Hence, these needles are used to guarantee good ground contact. The mid-plate carrying the needles is carefully lowered by the use of a screw. The movement of the needles is restrained by brass dowels, such that the needles can only be pressed against the sensor within the limits of the needle spring travel.

Figure 8.11 shows five IV curves taken in vacuum, using the whole jig. Absolute current value and breakdown voltage match those measured in other sensors, and no damage has been observed to the tested tile.

8.4 Conclusion

A new method to bias a CMOS pixel hybrid sensors was developed, tested and implemented in a jig that is capable of precisely positioning the tiles for probe card testing. A

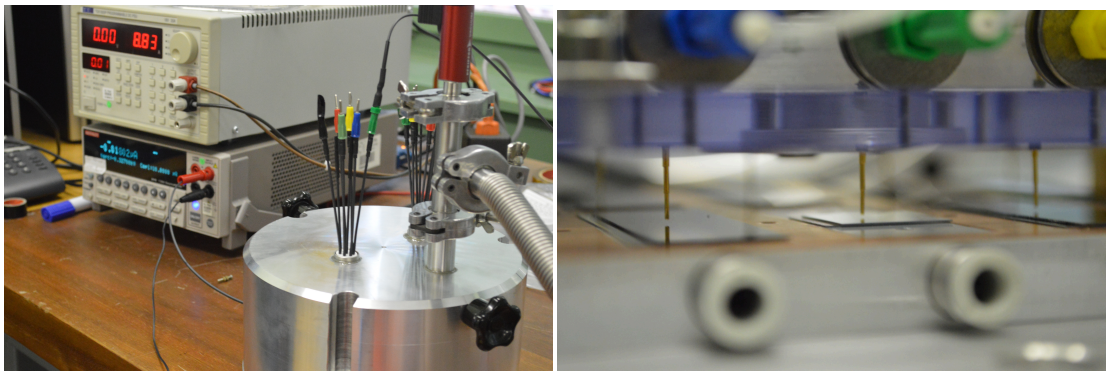

Figure 8.10: Pictures with details of the vacuum hood. The picture on the left has the hood closed. There are 12 independent channels, 10 of them connected to the bias needles. The picture on the right shows the needle mechanism just before touching the sensors backside.

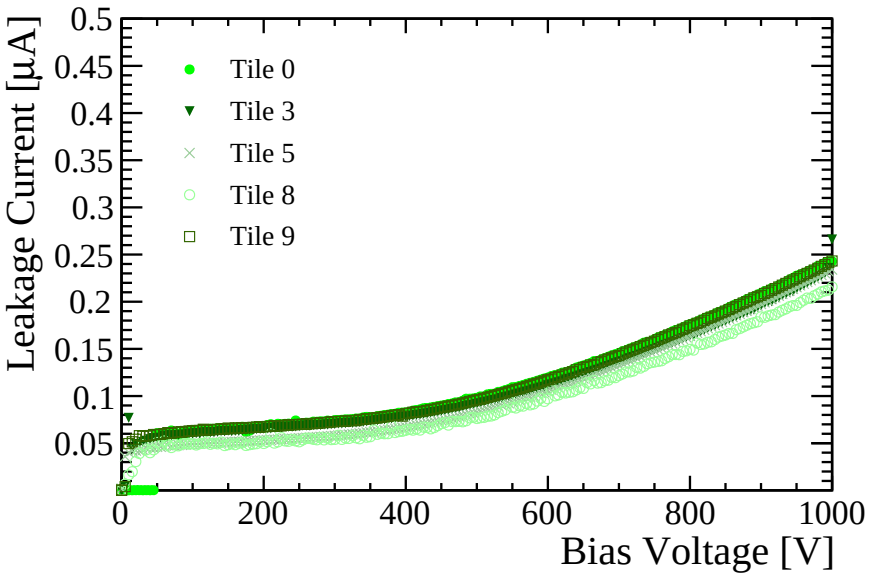

Figure 8.11: IV measurement taken with the vacuum hood, keeping tiles in vacuum. Behaviour of the IV curves and absolute current values are compatible with previously measured IV curves using standard bias delivery with wire bonds.

vacuum tank was also designed and built that encloses the probe card design setup and delivers the bias to the sensor using the new ground-through-ASIC method. Both jigs were carefully constructed and tested, and are being used for pre-production tests. A second setup has been built and will be used in University of Liverpool for tile testing during production.

9 | Conclusion and Outlook

In this last Chapter the main points touched by this thesis will be reiterated, and the context of these results within a larger scale particle physics landscape will be clarified.

There are tensions hinted by the data taken in LHCb during Runs I & II, in particular the lepton universality measurements addressed in **Chapter 3**. It is too soon to say either way, but all deviations seem to point at the same direction, an anomaly that suppresses the muon channel with respect to the electron channel. It will be very interesting to see LHCb's consolidated results using the entire Runs I & II datasets in the future and also other experiments start looking at the same measurements. More than just lepton universality, probing standard model to a very high precision and the measurements to constrain new physics scenarios are fundamental tools on the search for a beyond standard model theory.

The measurement of the R_{pK} ratio, devised as an additional measurement of lepton universality in $b \to sl^+l^-$ transitions, will help clarify the existence of a beyond standard model physics signal in this case. **Chapter 4** describes the methods used in the selection and modelling of the μ signal in Run I data, in particular the PDFs used for signal and background components of the fit that had my direct input. Also included in that chapter is a discussion regarding the very rare decay $B^+ \to a^+(\pi^+\pi^-\pi^+)\mu^+\mu^-$ and its feasibility in LHCb, also motivated as a tool to investigate right handed currents in flavour changing neutral currents. I use a MC sample of the decay of $B^+ \to a^+(\pi^+\pi^-\pi^+)J/\psi(\mu^+\mu^-)$ events to estimate feasibility of the detection of this mode in LHCb.

Ultimately this physics efforts are statically constrained using the final LHCb dataset of just over 9 fb^{-1}. The upgrade of LHCb was devised as a way of overcoming this natural barrier by operating in a luminosity environment 5 times higher with a more efficient trigger. This project however requires the redesign and substitution of many of the original detectors in LHCb, as it was described in **Chapter 2**. A big section of this thesis involved the work on the upgrade for the VELO.

In **Chapter 6**, the fundamental components of the new Vertex Locator were introduced. Aspects of the new detector that had my direct input are discussed. Specifically the radiation effects on the noise levels seen by the VeloPix ASIC and the generation of localised high leakage current on the edge of n-on-n sensors. Also, using the Timepix3 Telescope, I show how the efficiency on the elongated pixels between ASICs maintain high efficiency even after irradiation.

Amongst all the features to be compared between all sensor designs available for the upgrade, the high voltage tolerance is crucial and was discussed in **Chapter 7**. Different parameters such as guard-ring, implant size, shape of the sensor were tested using sensor prototypes bump-bonded to Timepix3 ASICs. The results coming from testing sensor before irradiation pointed out that the best solution would be sensors with a guard-ring of 450 µm and that the "triple" design had no effect on the current × voltage (IV) behaviour of the sensors. A selection of sensors were irradiated at different facilities in order to test which options would perform best after irradiation. Results with proton irradiation (24 GeV/c) and thermal neutrons show that sensors maintain their current behaviour without breakdown up to 1000 V, thus being appropriate to use in the VELO upgrade. Ultimately the final design was chosen to be the HPK n-on-p variant based on meeting the desired criteria consistently and not having any of the negative effects observed in irradiated n-on-n sensors. The IV curves and high voltage tolerance of the sensors were my analysis and were an important input to the selection of sensor design.

Irradiation with lower energy protons (≈13 MeV/c), show signs of interaction with the parylene coating applied to some of the sensors causing unreliable IV behaviour of the sensors. So far, it seems that this effect comes from interaction and damage between the protons and the coating. Another interesting aspect of low energy proton irradiation is the appearance of low-voltage breakdown, independent of parylene coating. I have tried to investigate this effect throughly. The hypothesis of thermal runaway due to a localised source of current can be ruled out after investigating the sensor with a thermal camera.

The behaviour of the breakdown temperature dependence was examined in detail, using a new IV curve model to characterise the breakdown voltage for several sensors measured in a set of temperatures in a systematic manner. The sensors non-uniformly irradiated at KIT show a higher breakdown voltage as their temperature decreases, a characteristic of tunnelling breakdown (as discussed in **Chapter 5**), however the four sensors irradiated at Birmingham show a different trend and a much lower breakdown voltage.

The contrast of different irradiation types on the breakdown of sensors is clear, and is one instance in which neutron-equivalent dose scaling does not hold. The results should be visited in the future with the help of TCAD simulations, to better understand the different damages caused by the irradiation processes and how these affect breakdown characteristics in the bulk. The difference in behaviour according to the type of irradiation is an important factor when developing detectors for experiments.

The development of a new way of testing the IV characteristics of sensors without wire-bonds and under vacuum was discussed in **Chapter 8**. This technique of biasing the sensor by grounding through the ASIC is possible due the combination of n-on-p sensors and the Velopix CMOS process that forms an effective p-on-n diode in the bulk of the ASIC. I confirmed that this arrangement actually worked as a biasing method and then applied it to design a vacuum jig that can serve both as a vacuum chuck for probing the ASICs. This jig is capable of probing tiles (in air) and high voltage test the sensors up to 1000 V in vacuum. This setup has been used to test and grade all 350 tiles for the VELO before they are sent to the production sites to get placed in modules.

In the immediate future, the work present in this thesis is an important part of the production for the Vertex Locator detector for the upgrade of the LHCb experiment. The contributions present here reliable selection of modules would not be possible. While characterising sensor options for the upgrade, an interesting behaviour the sensor high voltage breakdown was found, and it seems to depend heavily on the type of irradiation the sensors have been exposed to. LHCb is safe from this behaviour affecting the operation of the detecto as the type of irradiation to which the VELO is exposed. Even then, with the system running at design cooling specifications, it is still possible to maintain above 6000e of charge collection. The new LHCb detector will allow the observation of very rare transitions, including $b \to d$, as well as allowing for larger precision in flavour changing neutral current phenomena.

Appendices

A | HOP Variable Implementation

The LHCb tracker allows precise reconstruction of four-momenta of charged particles, with a resolution of the order of $\frac{\Delta P}{P} \approx 1\%$. The momentum resolution, combined with the particle identification capabilities yields excellent mass resolution on the reconstruction of decays. As an example, Figure A.1 shows how several different states can be seen individually in LHCb data.

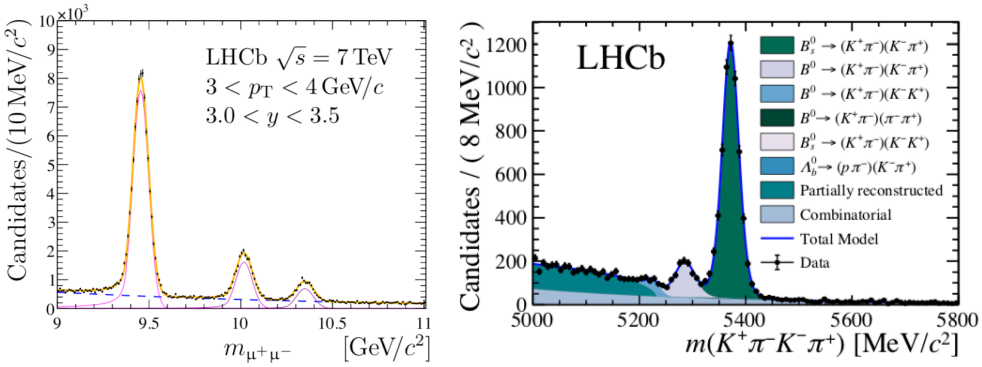

Figure A.1: Example of resonances reconstructed in LHCb. On the left, the Υ bottomnium resonances are reconstructed [99]. On the right, all the contributions to the reconstructed $B \to K\pi K\pi$ can be clearly separated [100].

Decays involving electrons in the final state, however, suffer from a fundamental smearing in their momentum. As electrons are much lighter, their momentum transfer while going through matter is much higher which results in a large amount of energy being irradiated from the electrons in the form of photons emitted through bremsstrahlung process. This emitted radiation significantly reduces the mass resolution for states involving electrons in the final state.

In LHCb electrons that emitted bremsstrahlung photons after the magnet can be reconstructed by identifying clusters in the ECAL that are close to the electron energy

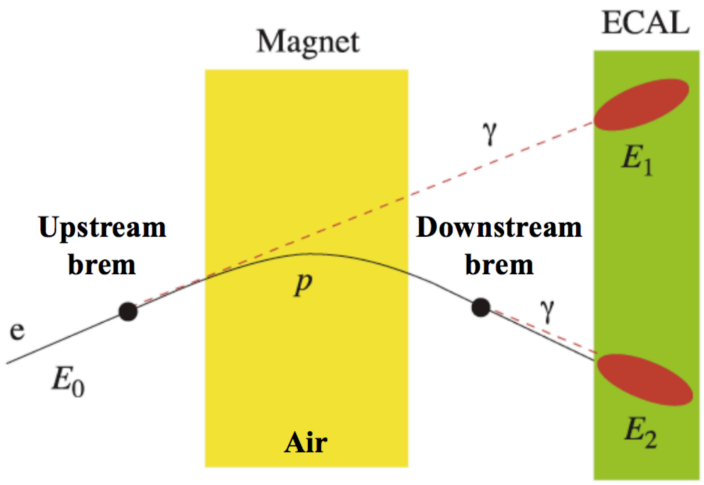

Figure A.2: Different bremsstrahlung emission situations in LHCb [101]. Recovering photons from upstream bremsstrahlung is more complex than downstream brem emissions.

deposit (Fig. A.2). Using this ECAL information it is possible to retrieve some of the bremsstrahlung energy loss. The reconstructed electron four-momenta will however lose resolution due to the energy resolution of the ECAL being lower than what is achieved with the tracker alone.

A second region where the bremsstrahlung photon can be irradiated is before the magnet. For these photons the correlation in positions in the ECAL is mostly lost, and so it becomes very hard to retrieve calorimeter clusters and correctly assign them to the final state electrons. Therefore, electrons that irradiate before the magnet are reconstructed with a smaller momentum than they were produced, which translates to a b-hadron mass distribution that is skewed to lower mass values and broadened. This causes the separation between partially reconstructed decays (in which one misses a final state particle), misidentified decays (in which one assigns the wrong mass hypothesis to a track) and radiative bremsstrahlung difficult.

In order to recover the lost momentum from photons emitted before the magnet one can use the HOP variable. This is a correction applied to the electron momentum based on the momenta of the other charged particles on the decay. Figure A.3 has an illustration of the relevant quantities for calculating this correction.

The HOP correction uses the fact that the b-hadron direction of flight and its momen-

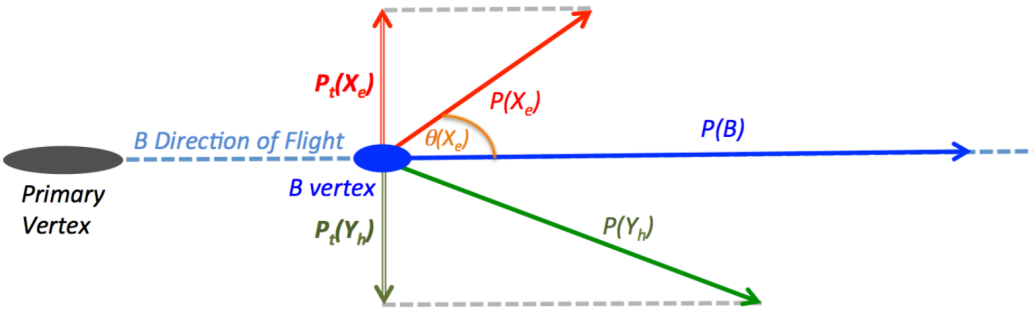

Figure A.3: Schematic detailing relevant variables for the HOP correction. $P(Y_h)$ is the sum of the hadronic momentum while $P(X_e)$ is the sum of electron momentum. The P_ts are transverse with respect to the B direction of flight [102].

tum should be in the same direction. All final state particles created in the decay of this b-hadron should have 0 total transverse momentum with respect to the b-hadron original momentum direction. Considering that the electrons emit bremsstrahlung radiation in a direction close to the their momentum direction, we can recover the missed electron momentum by applying a correction factor based on the ratio of hadron and electron transverse momenta (P_t):

$$\alpha_{HOP} = \frac{P_t^h}{P_t^e}, \tag{A.1}$$

Then α_{HOP} is the ratio between transverse momenta of the hadronic and electronic parts of the decay. If there was no bremsstrahlung the two values would be the same. The then corrected 3-momentum of the electrons in the decay will be:

$$\vec{P}^e_{\text{corr}} = \alpha_{HOP} \times \vec{P}^e, \tag{A.2}$$

From this other kinematical variables can be extracted such as the corrected b-hadron HOP corrected mass. The calculation of the HOP correction for each reconstructed decay uses both the geometric information of the b-hadron direction of flight and the measured momenta of all particles reconstructed.

A.0.1 Implemented Algorithm

Although this HOP correction had already been used in one analysis in LHCb, it was calculated after the reconstruction using code specific for the analysis in question. In order to implement this correction in a general way into the LHCb main software distribution a TupleTool was created. During data processing in LHCb, users can require use certain software tools (called tupletools) to calculate specific variables relevant for a given analysis. The tupletools are all in LHCb main reconstruction/analysis software DaVinci (Chapter 2). These variables will then become available for selection or modelling.

The implementation of the tupletool involved a few distinct steps, namely: finding the electrons, calculating the HOP correction and finally applying the correction to the relevant particle variables.

LHCb reconstruction works by using final state particles and refitting their kinematical properties based on the vertices formed. The information regarding these newly calculated kinematics though are not propagated downwards to the final state particles. The particles that are refitted using vertex information have a much better momentum resolution hence it is desirable to use that instead of only the information on final state particles. For those reasons the tupletool looks up the decay chain for all particles that only have electron decay products and uses the information from those particles when possible.

The HOP correction is then calculated by finding the momenta of the electronic and the non-electronic parts of the decay and taking the transverse component with respect to the b-hadron direction of flight. The momenta are then used to calculate α_{HOP} which then is applied to the momentum of the electronic part of the decay. Finally the HOP corrected mass of the initial decaying particle is calculated.

Due the the fact that the HOP correction depends on the knowledge of the b-hadron direction of flight, the resolution of the corrected mass (HOP mass) will not be as precise as a decay without any bremsstrahlung, however it is still very useful discern between electron decays and partially reconstructed backgrounds.

A.0.2 Results and Comparison

In order to check the performance of the tupletool, results were compared between the existing HOP correction code for the specific decays: $B^0 \to K^{*0}e^+e^-$ and $B^+ \to$

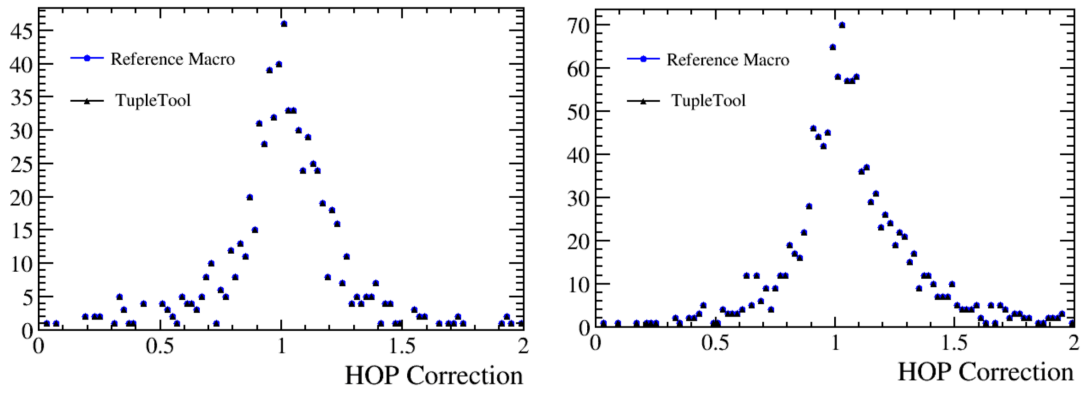

Figure A.4: Comparison between reference macro (blue) HOP correction values and the correction obtained with the tupletool (black) for the $B^0 \rightarrow K^{*0}e^+e^-$ (left) and $B^+ \rightarrow K^+e^+\mu^-$(right) simulation samples. These plots show that the process of selecting particles and transformation to the b-hadron rest frame works.

$K^+e^+\mu^-$. The data samples used come from simulations made for studies of such decays. In Figure A.4 we observe the agreement of the calculated HOP correction between the reference macro and the tupletool for both decays. Figure A.5 displays the HOP mass, calculated using our reference macro, the tupletool and another software tool developed in parallel with the tupletool. They all agree between each other which validated the tool to be added to the LHCb software in 2016.

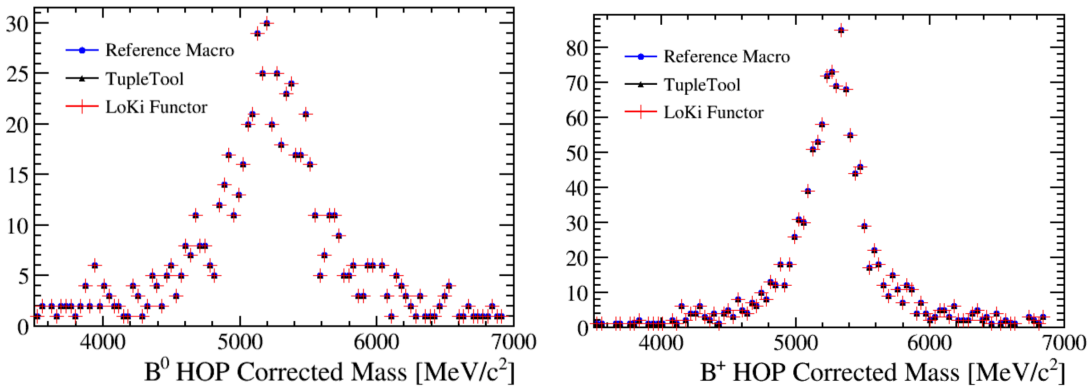

Figure A.5: Comparison between reference macro (blue) HOP b-hadron mass values and the HOP mass obtained with the tupletool (black) for the $B^0 \rightarrow K^{*0}e^+e^-$ (left) and $B^+ \rightarrow K^+e^+\mu^-$(right) simulation samples. These plots show that the process of applying the HOP factor and recalculating the b-hadron mass is applied correctly.

B | Irradiation Campaign

Chapter 6 discussed the VELO Upgrade geometry and how the proximity of the sensors to the interaction region results in a very intense, non-uniform radiation flux. This radioactive flux is expected to amount to a peak 8×10^{15} 1 MeV $n_{eq}\,cm^{-2}$ at the most irradiated corner. As one cannot obtain such high fluences with the particle composition and energy spectrum generated by LHC collisions in an irradiation facility, it is important to diversify in spectrum and irradiation type. This ensures that the effect of radiation damage is known prior to operation.

The irradiation programme consisted of irradiating single tiles in (mostly) uniform profiles while triples were irradiated in a non-uniform manner, trying to mimic the fluence profile present in the VELO Upgrade. In the case of uniform profiles the sensors were irradiated to either 4×10^{15} 1 MeV $n_{eq}\,cm^{-2}$ or 8×10^{15} 1 MeV $n_{eq}\,cm^{-2}$. The specific irradiation dose in each facility was determined by using the hardness factors provided by the facilities themselves. Table B.1 summarises the information of each irradiation facility used.

Facility	Irradiation	Hardness Factor	Flux
KIT	proton	2.0	Uniform and Non-Uniform
Birmingham	proton	2.2	Non-Uniform
IRRAD	proton	0.57	Non-Uniform
JSI	neutron	0.88	Uniform
IST	neutron	N/A	Uniform

Table B.1: Summary of the irradiation facilities used to test VELO Upgrade sensors.

Line (mm)	Single Assembly Fluence	Triple Assembly Fluence
0 - 5	2.00×10^{15}	4.00×10^{15}
5 - 10	7.82×10^{13}	1.57×10^{14}
10 - 15	1.74×10^{13}	3.47×10^{13}
15 - 20	8.68×10^{12}	1.73×10^{13}
20 - 25	6.51×10^{12}	1.30×10^{13}
25 - 30	4.34×10^{12}	8.68×10^{12}
30 - 50	2.17×10^{12}	4.34×10^{12}

Table B.2: KIT irradiation profile for single and triple assemblies in units of 1 MeV n_{eq} cm^{-2}. This profile should be multiplied by a factor that reaches the peak irradiation band quoted.

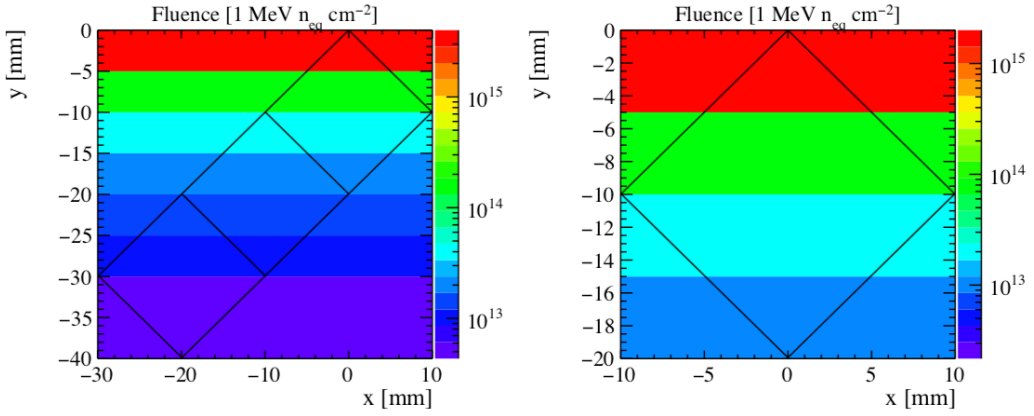

Figure B.1: KIT non-uniform irradiation profile for triple (left) and single (right) assemblies.

KIT

The cyclotron present at KIT is capable of irradiating sensors with low energy protons, of approximately 23 MeV, and a proton current of up to 2 µA. The irradiated material is kept in a box filled with cold nitrogen gas, at a temperature of less than −30 °C. The irradiated tiles are held by Kapton tape on a aluminium frame. Single and triple assemblies were irradiated at KIT non-uniformly, with the expected profile shown in Figure B.1 and Table B.2. A single sensor (named S4) was irradiated uniformly at KIT, and will be used as an important cross-check of the total fluence (which is quoted as having a precision of 20%). Table B.3 summarises all sensors irradiated at KIT.

Hybrid	Type	Implant Size (μm)	Fluence (10^{15} 1 MeV n_{eq} cm^{-2})
S4	HPK n-on-p	39	4
S14	HPK n-on-p	39	2
S16	HPK n-on-p	39	4
T1	HPK n-on-p	39	4
T2	HPK n-on-p	39	4
T3	HPK n-on-p	39	8
T4	HPK n-on-p	39	4
T6	HPK n-on-p	39	4
T7	HPK n-on-p	39	8
T15	Micron n-on-p	39	8
T17	Micron n-on-p	39	8
T21	Micron n-on-n	39	4
IT5	Micron n-on-p	39	4
T24	HPK n-on-p	39	8
T25	HPK n-on-p	39	8
T26	HPK n-on-p	39	4

Table B.3: All sensors irradiated at KIT with protons.

Birmingham

Birmingham also has facilities that allow for proton irradiation coming from the MC40 cyclotron. Protons at Birmingham are at a slightly higher energy than KIT, at 27 MeV [103]. However, the scanning parameters are not the same as in KIT and thus the irradiation profile is slightly different, as represented in Figure B.2. There were only two sensors irradiated at Birmingham previous to the production readiness review (T5 and T19) with four more being irradiated afterwards (Table B.4). Due to time constraints, there were difficulties in reaching full fluence with the sensors irradiated in this facility. This was due to low current beam, which ensured the thermal stability of the sensors. Several dosimetry measurements were done to confirm the fluences achieved [104].

IRRAD

IRRAD is an irradiation facility in the T8 East Hall beam-line at CERN. It uses the high intensity proton beam from the Proton Synchrotron with a momentum of 24 GeV as

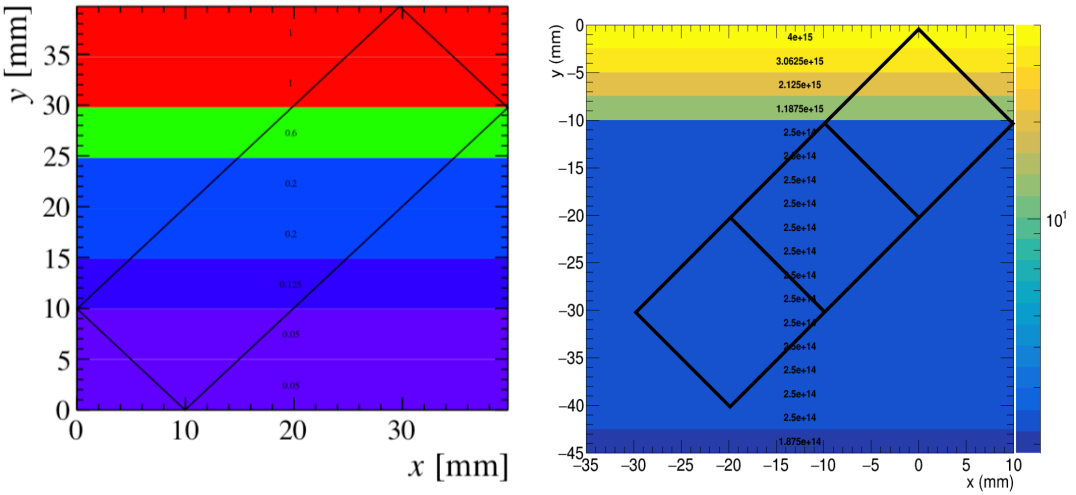

Figure B.2: Birmingham non-uniform irradiation profile for triple assemblies. The profile on the left was the one used with T5 and T19 sensors. The profile on the right was used on the later irradiations.

Hybrid	Type	Implant Size (μm)	Fluence (10^{15} 1 MeV n_{eq} cm^{-2})
T5	HPK n-on-p	35	1.0
T19	Micron n-on-n	36	1.0
TILE4	Micron n-on-n	39	3.1
TILE5	Micron n-on-n	39	5.9
TILE6	Micron n-on-n	39	7.1
TILE7	Micron n-on-n	39	4.0

Table B.4: All sensors irradiated at Birmingham.

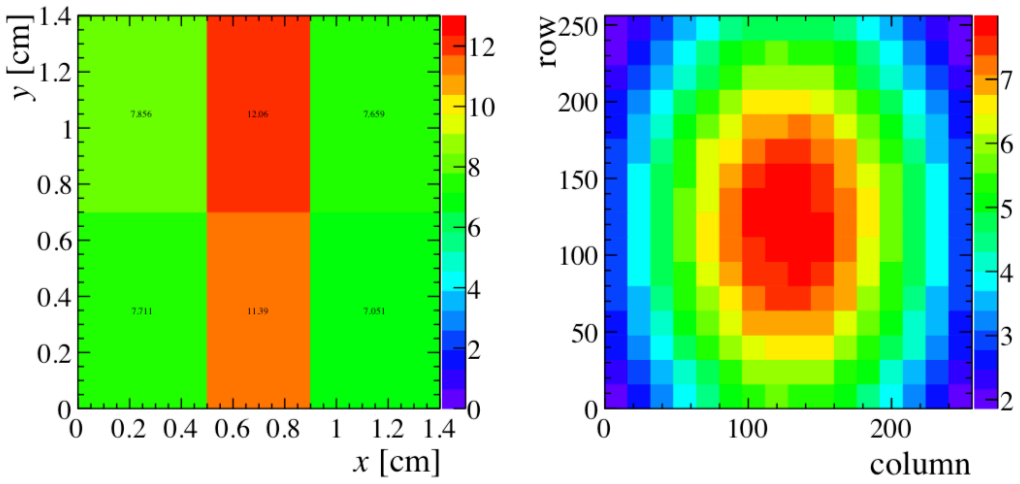

Figure B.3: IRRAD fluence profile for full fluence samples (in units of 10^{15} 1 MeV n_{eq} cm^{-2}). On the left the fluence information from dosimetry measurements made with an aluminium foil. On the right is shown the reconstructed fluence profile obtained by combining dosimetry and sensor activation information.

an irradiation beam. Compared to other proton facilities, IRRAD has a large Gaussian beam, with a transverse full-width half maximum of ≈12 mm. The first irradiation at this facility had the beam away from the sensor center, resulting in a much lower than expected maximum fluence. A later batch of assemblies was irradiated to the full fluence, as it can be seen in Table B.5.

Using a technique consisting of correlating the aluminium foil fluence measurements available in IRRAD and the signals left by activation in the sensor, we can obtain a detailed map of the fluence profile that the IRRAD sensors were exposed to (Fig. B.3) [105].

JSI and IST

The Jozef Stephan Institute (JSI) in Lujbljana and the IST Lisbon are research nuclear reactors that provide special access for irradiation of samples with neutrons. Because the neutrons come from the reactor core, irradiation is uniform and the neutron energy is a broad spectrum on the MeV range. Single assemblies were irradiated to 4×10^{15} 1 MeV n_{eq} cm^{-2} and 8×10^{15} 1 MeV n_{eq} cm^{-2}, referred to as half and full fluence. Table B.6 summarises all sensors irradiated at JSI and IST.

Hybrid	Type	Implant Size (μm)	Fluence (10^{15} 1 MeV n_{eq} cm^{-2})
S5	HPK n-on-p	39	0.4
S8	HPK n-on-p	35	8
S11	HPK n-on-p	39	8
S21	HPK n-on-p	35	0.4
S25	Micron n-on-p	36	8
S30	Micron n-on-n	36	8
TILE0	HPK n-on-p	39	8
TILE1	HPK n-on-p	39	8
TILE2	HPK n-on-p	39	8
TILE3	HPK n-on-p	39	8

Table B.5: All sensors irradiated with protons at IRRAD.

Hybrid	Type	Implant Size (μm)	Fluence (10^{15} 1 MeV n_{eq} cm^{-2})	Facility
S6	HPK n-on-p	39	8	JSI
S7	HPK n-on-p	39	8	IST
S9	HPK n-on-p	39	8	IST
S10	HPK n-on-p	39	8	IST
S12	HPK n-on-p	39	4	IST
S13	HPK n-on-p	39	4	JSI
S15	HPK n-on-p	35	4	JSI
S17	HPK n-on-p	39	8	JSI
S22	HPK n-on-p	35	8	JSI
S23	Micron n-on-p	36	8	JSI
S24	Micron n-on-p	36	8	JSI
S27	Micron n-on-n	36	8	JSI
S29	Micron n-on-n	36	8	JSI

Table B.6: All sensors neutron irradiated at JSI and IST.

Bibliography

[1] S. Chatrchyan *et al.*, "Observation of a New Boson at a Mass of 125 GeV with the CMS Experiment at the LHC," *Phys. Lett.*, vol. B716, pp. 30–61, 2012.

[2] G. Aad *et al.*, "Observation of a new particle in the search for the Standard Model Higgs boson with the ATLAS detector at the LHC," *Phys. Lett.*, vol. B716, pp. 1–29, 2012.

[3] L. Evans and P. Bryant, "LHC Machine," *JINST*, vol. 3, p. S08001, 2008.

[4] CERN. (2018) Proton synchrotron booster web page. [Online]. Available: https://home.cern/about/accelerators/proton-synchrotron-booster

[5] F. Marcastel, "CERN's Accelerator Complex. La chaîne des accélérateurs du CERN," Oct 2013, general Photo. [Online]. Available: https://cds.cern.ch/record/1621583

[6] P. Mouche, "Overall view of the LHC. Vue d'ensemble du LHC," Jun 2014, general Photo. [Online]. Available: https://cds.cern.ch/record/1708847

[7] R. Aaij *et al.*, "LHCb detector performance," *Int. J. Mod. Phys.*, vol. A30, p. 1530022, 2015.

[8] R. Alemany-Fernandez, F. Follin, and R. Jacobsson, "The LHCB Online Luminosity Control and Monitoring," no. CERN-ACC-2013-0028, p. 3 p, May 2013. [Online]. Available: https://cds.cern.ch/record/1567250

[9] A. A. Alves Jr. *et al.*, "The LHCb detector at the LHC," *JINST*, vol. 3, p. S08005, 2008.

[10] LHCb collaboration. (2010) Simulated production of b quark pairs in lhcb. [Online]. Available: https://lhcb.web.cern.ch/lhcb/speakersbureau/html/bb_ProductionAngles.html

[11] LHCb collaboration. (2010) Lhcb magnet website. [Online]. Available: http://lhcb-magnet.web.cern.ch/lhcb-magnet/

[12] R. Aaij *et al.*, "Performance of the LHCb Vertex Locator," *JINST*, vol. 9, p. P09007, 2014.

[13] LHCb collaboration. (2008) Lhcb magnet website. [Online]. Available: https://lhcb-public.web.cern.ch/lhcb-public/en/Detector/Trackers2-en.html

[14] J. D. Jackson, *Classical electrodynamics*, 3rd ed. New York, NY: Wiley, 1999. [Online]. Available: http://cdsweb.cern.ch/record/490457

[15] M. Adinolfi *et al.*, "Performance of the LHCb RICH detector at the LHC," *Eur. Phys. J.*, vol. C73, p. 2431, 2013.

[16] A. A. Alves Jr. *et al.*, "Performance of the LHCb muon system," *JINST*, vol. 8, p. P02022, 2013.

[17] F. Archilli *et al.*, "Performance of the Muon Identification at LHCb," *JINST*, vol. 8, no. CERN-LHCB-DP-2013-001. CERN-LHCB-DP-2013-001. LHCB-DP-2013-001, p. P10020. 20 p, Jun 2013, comments: 17 pages, 10 figures. [Online]. Available: https://cds.cern.ch/record/1553139

[18] S. Löchner and M. Schmelling, "The Beetle Reference Manual - chip version 1.3, 1.4 and 1.5," CERN, Geneva, Tech. Rep. LHCb-2005-105. CERN-LHCb-2005-105, Nov 2006. [Online]. Available: http://cds.cern.ch/record/1000429

[19] LHCb collaboration. Trigger schemes. [Online]. Available: http://lhcb.web.cern.ch/lhcb/speakersbureau/html/TriggerScheme.html

[20] S. Borghi, "Novel real-time alignment and calibration of the lhcb detector and its performance," *Nuclear Instruments and Methods in Physics Research Section A: Accelerators, Spectrometers, Detectors and Associated Equipment*, vol. 845, pp. 560 – 564,

2017, proceedings of the Vienna Conference on Instrumentation 2016. [Online]. Available: http://www.sciencedirect.com/science/article/pii/S0168900216305927

[21] S. Benson, V. Gligorov, M. A. Vesterinen, and J. M. Williams, "The lhcb turbo stream," *Journal of Physics: Conference Series*, vol. 664, no. 8, p. 082004, 2015. [Online]. Available: http://stacks.iop.org/1742-6596/664/i=8/a=082004

[22] "Framework TDR for the LHCb Upgrade: Technical Design Report," no. CERN-LHCC-2012-007, 2012.

[23] "LHCb Tracker Upgrade Technical Design Report," no. CERN-LHCC-2014-001, 2014.

[24] J. M. de Cos *et al.*, "Pacific: Sipm readout asic for lhcb upgrade," *Nuclear Instruments and Methods in Physics Research Section A: Accelerators, Spectrometers, Detectors and Associated Equipment*, vol. 912, pp. 354 – 358, 2018, new Developments In Photodetection 2017. [Online]. Available: http://www.sciencedirect.com/science/article/pii/S0168900217314377

[25] P. J. Garsed *et al.*, "LHCb Upgraded RICH 2 Engineering Design Review Report," CERN, Geneva, Tech. Rep. LHCb-PUB-2016-015. CERN-LHCb-PUB-2016-015, Jun 2016. [Online]. Available: http://cds.cern.ch/record/2158852

[26] M. P. Blago and F. Keizer, "High rate tests of the photon detection system for the LHCb RICH Upgrade," *Nucl. Instrum. Meth.*, vol. A876, pp. 101–103, 2017.

[27] "LHCb Trigger and Online Technical Design Report," no. CERN-LHCC-2014-016, 2014.

[28] B. Odom, D. Hanneke, B. D'Urso, and G. Gabrielse, "New measurement of the electron magnetic moment using a one-electron quantum cyclotron," *Phys. Rev. Lett.*, vol. 97, p. 030801, Jul 2006. [Online]. Available: https://link.aps.org/doi/10.1103/PhysRevLett.97.030801

[29] Y. Akimoto. Particle illustrations. [Online]. Available: http://higgstan.com/particle-image/

[30] F. Halzen and A. D. Martin, *Quarks and Leptons: An Introductory Course on Particle Physics*. New York, USA: Wiley, 1984.

[31] M. Mangano, "Qcd and the physics of hadronic collisions," *CERN Yellow Reports: School Proceedings*, vol. 4, no. 0, p. 27, 2018. [Online]. Available: https://e-publishing.cern.ch/index.php/CYRSP/article/view/833

[32] I. Beiyaev *et al.*, "Handling of the generation of primary events in gauss, the lhcb simulation framework," in *IEEE Nuclear Science Symposuim Medical Imaging Conference*, Oct 2010, pp. 1155–1161.

[33] T. Sjostrand, S. Mrenna, and P. Z. Skands, "PYTHIA 6.4 Physics and Manual," *JHEP*, vol. 05, p. 026, 2006.

[34] D. J. Lange, "The EvtGen particle decay simulation package," *Nucl. Instrum. Meth.*, vol. A462, pp. 152–155, 2001.

[35] M. Tanabashi *et al.*, "Review of particle physics," *Phys. Rev. D*, vol. 98, p. 030001, Aug 2018. [Online]. Available: https://link.aps.org/doi/10.1103/PhysRevD.98.030001

[36] G. W. S. HOU, "Source of cp violation for the baryon asymmetry of the universe," *International Journal of Modern Physics D*, vol. 20, no. 08, pp. 1521–1532, 2011. [Online]. Available: https://doi.org/10.1142/S0218271811019694

[37] K. A. Olive, "TASI lectures on dark matter," in *Particle physics and cosmology: The quest for physics beyond the standard model(s). Proceedings, Theoretical Advanced Study Institute, TASI 2002, Boulder, USA, June 3-28, 2002*, 2003, pp. 797–851.

[38] P. A. R. Ade *et al.*, "Planck 2015 results. XIII. Cosmological parameters," *Astron. Astrophys.*, vol. 594, p. A13, 2016.

[39] K. Abazajian, "Linear cosmological structure limits on warm dark matter," *Phys. Rev.*, vol. D73, p. 063513, 2006.

[40] J. Martin, "Everything You Always Wanted To Know About The Cosmological Constant Problem (But Were Afraid To Ask)," *Comptes Rendus Physique*, vol. 13, pp. 566–665, 2012.

[41] A. J. Buras, J. Girrbach, D. Guadagnoli, and G. Isidori, "On the standard model prediction for $\mathcal{B}(b_{s,d} \to \mu^+\mu^-)$," *The European Physical Journal C*, vol. 72, no. 10, p. 2172, Oct 2012. [Online]. Available: https://doi.org/10.1140/epjc/s10052-012-2172-1

[42] S. Bifani, S. Descotes-Genon, A. Romero Vidal, and M.-H. Schune, "Review of Lepton Universality tests in B decays," *J. Phys.*, vol. G46, no. 2, p. 023001, 2019.

[43] G. Hiller and F. Kruger, "More model-independent analysis of $b \to s$ processes," *Phys. Rev. D*, vol. 69, p. 074020, Apr 2004. [Online]. Available: https://link.aps.org/doi/10.1103/PhysRevD.69.074020

[44] R. Aaij *et al.*, "Test of lepton universality with $B^0 \to K^{*0}\ell^+\ell^-$ decays," *JHEP*, vol. 08, p. 055, 2017.

[45] ——, "Search for lepton-universality violation in $B^+ \to K^+\ell^+\ell^-$ decays," *Phys. Rev. Lett.*, vol. 122, p. 191801, May 2019. [Online]. Available: https://link.aps.org/doi/10.1103/PhysRevLett.122.191801

[46] S. Descotes-Genon, L. Hofer, J. Matias, and J. Virto, "Global analysis of $b \to s\ell\ell$ anomalies," *JHEP*, vol. 06, p. 092, 2016.

[47] S. Bifani. [Online]. Available: https://conference.ippp.dur.ac.uk/event/631/sessions/708/attachments/3020/3284/yeti18.pdf

[48] C. Marin Benito, G. Andreassi, V. Franco Lima, P. Stefko, A. Puig Navarro, and V. Bellee, "Introducing the HOP mass in the LHCb software," CERN, Geneva, Tech. Rep. LHCb-INT-2017-012. CERN-LHCb-INT-2017-012, May 2017. [Online]. Available: https://cds.cern.ch/record/2265969

[49] W. D. Hulsbergen, "Decay chain fitting with a Kalman filter," *Nucl. Instrum. Meth.*, vol. A552, pp. 566–575, 2005.

[50] T. Skwarnicki, "A study of the radiative CASCADE transitions between the Upsilon-Prime and Upsilon resonances," Ph.D. dissertation, Cracow, INP, 1986. [Online]. Available: http://www-library.desy.de/cgi-bin/showprep.pl?DESY-F31-86-02

[51] D. Martínez Santos and F. Dupertuis, "Mass distributions marginalized over per-event errors," *Nucl. Instrum. Meth.*, vol. A764, pp. 150–155, 2014.

[52] R. Aaij *et al.*, "Study of the kinematic dependences of Λ_b^0 production in pp collisions and a measurement of the $\Lambda_b^0 \to \Lambda_c^+ \pi^-$ branching fraction," *JHEP*, vol. 08, p. 143, 2014.

[53] K. S. Cranmer, "Kernel estimation in high-energy physics," *Comput. Phys. Commun.*, vol. 136, pp. 198–207, 2001.

[54] R. Aaij *et al.*, "R_{pK} measurement paper," no. in preparation, Nov 2019.

[55] J. Gratrex and R. Zwicky, "Parity Doubling as a Tool for Right-handed Current Searches," *JHEP*, vol. 08, p. 178, 2018.

[56] R. Aaij *et al.*, "First measurement of the differential branching fraction and *CP* asymmetry of the $B^\pm \to \pi^\pm \mu^+ \mu^-$ decay," *JHEP*, vol. 10, p. 034, 2015.

[57] Aaij, Roel and others, "Studies of the resonance structure in $D^0 \to K^\mp \pi^\pm \pi^\pm \pi^\mp$ decays," *Eur. Phys. J.*, vol. C78, no. 6, p. 443, 2018.

[58] M. Bishai *et al.*, "Study of B —> psi rho," *Phys. Lett.*, vol. B369, pp. 186–192, 1996.

[59] K. Abe *et al.*, "Observation of B —> J / psi K(1)(1270)," *Phys. Rev. Lett.*, vol. 87, p. 161601, 2001.

[60] R. Aaij *et al.*, "Measurement of B meson production cross-sections in proton-proton collisions at $\sqrt{s} = 7$ TeV," *JHEP*, vol. 08, p. 117, 2013.

[61] H. Bethe, "Zur theorie des durchgangs schneller korpuskularstrahlen durch materie," *Annalen der Physik*, vol. 397, pp. 325–400, 1930.

[62] L. Landau, "On the energy loss of fast particles by ionization," *J. Phys. USSR VIII*, vol. 4, pp. 201–205, 1944, cited By 1.

[63] J. D. Jackson, *Classical electrodynamics*, 3rd ed. New York, NY: Wiley, 1999. [Online]. Available: http://cdsweb.cern.ch/record/490457

[64] S. Sze and K. Ng, *Physics of Semiconductor Devices*. Wiley, 2006. [Online]. Available: https://books.google.co.uk/books?id=o4unkmHBHb8C

[65] F. Hartmann, *Evolution of Silicon Sensor Technology in Particle Physics*. Springer-Verlag Berlin Heidelberg, 01 2017. [Online]. Available: https://www.springer.com/br/book/9783642064166

[66] C. Leroy and P.-G. Rancoita, *Silicon solid state devices and radiation detection*, 1st ed. New York, NY: World Scientific, 2012.

[67] G. Lutz, *Semiconductor Radiation Detectors: Device Physics*. Springer, Berlin, Heidelberg, 2007.

[68] J. J. Sakurai and J. Napolitano, *Modern quantum mechanics; 2nd ed.* San Francisco, CA: Addison-Wesley, 2011. [Online]. Available: https://cds.cern.ch/record/1341875

[69] S. Ramo, "Currents induced by electron motion," *Proceedings of the IRE*, vol. 27, no. 9, pp. 584–585, Sept 1939.

[70] W. Shockley, "Currents to conductors induced by a moving point charge," *Journal of Applied Physics*, vol. 9, no. 10, pp. 635–636, 1938, cited By 639. [Online]. Available: https://www.scopus.com/inward/record.uri?eid=2-s2.0-36849131315&doi=10.1063%2f1.1710367&partnerID=40&md5=6213f8aa386011ae58e5e58cf22d7a5a

[71] M. Moll, "Radiation damage in silicon particle detectors:microscopic defects and macroscopic properties," 1999, presented on 30 Nov 1999. [Online]. Available: https://cds.cern.ch/record/425274

[72] M. Huhtinen, "Simulation of non-ionising energy loss and defect formation in silicon," *Nucl. Instrum. Meth.*, vol. A491, pp. 194–215, 2002.

[73] A. Vasilescu and G. Lindstroem, "Displacement damage in silicon, on-line compilation." [Online]. Available: https://rd50.web.cern.ch/rd50/NIEL/default.html

[74] G. Kramberger *et al.*, "Determination of effective trapping times for electrons and holes in irradiated silicon," *Nuclear Instruments and Methods in Physics Research*

Section A: Accelerators, Spectrometers, Detectors and Associated Equipment, vol. 476, no. 3, pp. 645 – 651, 2002, proc. of the 3rd Int. Conf. on Radiation Effects on Semiconductor Materials, Detectors and Devices. [Online]. Available: http://www.sciencedirect.com/science/article/pii/S0168900201016539

[75] E. Buchanan, "The LHCb VELO & ST Operational Performance Run II," 09 2017. [Online]. Available: http://cds.cern.ch/record/2286206

[76] V. Eremin *et al.*, "The origin of double peak electric field distribution in heavily irradiated silicon detectors," *Nucl. Instrum. Meth.*, vol. A476, pp. 556–564, 2002.

[77] G. Kramberger, V. Cindro, I. Mandic, M. Mikuz, M. Milovanovic, M. Zavrtanik, and K. Zagar, "Investigation of irradiated silicon detectors by edge-tct," *IEEE Transactions on Nuclear Science*, vol. 57, no. 4, pp. 2294–2302, Aug 2010.

[78] M. Ferrero *et al.*, "Radiation resistant LGAD design," *Nucl. Instrum. Meth.*, vol. A919, pp. 16–26, 2019.

[79] P. C. Tsopelas, "A Silicon Pixel Detector for LHCb," Ph.D. dissertation, Vrije U.,Amsterdam, 2016. [Online]. Available: https://cds.cern.ch/record/2238509/files/thesis_P_C_Tsopelas_2.pdf

[80] LHCb collaboration, "LHCb VELO Upgrade Technical Design Report," no. CERN-LHCC-2013-021, 2013.

[81] J. Allison *et al.*, "Recent developments in geant4," *Nuclear Instruments and Methods in Physics Research Section A: Accelerators, Spectrometers, Detectors and Associated Equipment*, vol. 835, pp. 186 – 225, 2016. [Online]. Available: http://www.sciencedirect.com/science/article/pii/S0168900216306957

[82] G. Battistoni *et al.*, "Overview of the fluka code," *Annals of Nuclear Energy*, vol. 82, pp. 10 – 18, 2015, joint International Conference on Supercomputing in Nuclear Applications and Monte Carlo 2013, SNA + MC 2013. Pluri- and Trans-disciplinarity, Towards New Modeling and Numerical Simulation Paradigms. [Online]. Available: http://www.sciencedirect.com/science/article/pii/S0306454914005878

[83] T. Poikela *et al.*, "Velopix: the pixel asic for the lhcb upgrade," *JINST*, vol. 10, no. 01, p. C01057, 2015. [Online]. Available: http://stacks.iop.org/1748-0221/10/i=01/a=C01057

[84] M. D. Gaspari, J. Alozy, R. Ballabriga, M. Campbell, E. Fröjdh, J. Idarraga, S. Kulis, X. Llopart, T. Poikela, P. Valerio, and W. Wong, "Design of the analog front-end for the timepix3 and smallpix hybrid pixel detectors in 130 nm cmos technology," *Journal of Instrumentation*, vol. 9, no. 01, p. C01037, 2014. [Online]. Available: http://stacks.iop.org/1748-0221/9/i=01/a=C01037

[85] F. Krummenacher, "Pixel detectors with local intelligence: an ic designer point of view," *Nuclear Instruments and Methods in Physics Research Section A: Accelerators, Spectrometers, Detectors and Associated Equipment*, vol. 305, no. 3, pp. 527 – 532, 1991. [Online]. Available: http://www.sciencedirect.com/science/article/pii/016890029190152G

[86] S. Naik, "On-detector electronics for the LHCb VELO upgrade," *Journal of Instrumentation*, vol. 12, no. 02, pp. C02 031–C02 031, feb 2017. [Online]. Available: https://doi.org/10.1088%2F1748-0221%2F12%2F02%2Fc02031

[87] K. Akiba *et al.*, "LHCb VELO Timepix3 Telescope," *JINST*, vol. 14, no. 05, p. P05026, 2019. [Online]. Available: http://cds.cern.ch/record/2668670

[88] S. E. Richards and J. Velthuis, "Characterisation of silicon detectors for the LHCb Vertex Locator Upgrade," Nov 2017, presented 15 Dec 2017. [Online]. Available: https://cds.cern.ch/record/2626889

[89] B. van der Heijden, J. Visser, M. van Beuzekom, H. Boterenbrood, S. Kulis, B. Munneke, and F. Schreuder, "SPIDR, a general-purpose readout system for pixel ASICs," *Journal of Instrumentation*, vol. 12, no. 02, pp. C02 040–C02 040, feb 2017. [Online]. Available: https://doi.org/10.1088%2F1748-0221%2F12%2F02%2Fc02040

[90] SCS. (2019) Parylene process webpage. [Online]. Available: https://scscoatings.com/parylene-coatings/parylene-expertise/parylene-deposition/

[91] H. Schindler, Personal communication.

[92] A. Folkestad *et al.*, "Development of a silicon bulk radiation damage model for sentaurus tcad," *Nuclear Instruments and Methods in Physics Research Section A: Accelerators, Spectrometers, Detectors and Associated Equipment*, vol. 874, pp. 94 – 102, 2017. [Online]. Available: http://www.sciencedirect.com/science/article/pii/S0168900217309282

[93] M. Benoit, "Pixel detector r&d for the compact linear collider," *Journal of Instrumentation*, vol. 14, no. 06, pp. C06 003–C06 003, jun 2019. [Online]. Available: https://doi.org/10.1088%2F1748-0221%2F14%2F06%2Fc06003

[94] A. Chilingarov, "Temperature dependence of the current generated in si bulk," *Journal of Instrumentation*, vol. 8, no. 10, pp. P10 003–P10 003, oct 2013. [Online]. Available: https://doi.org/10.1088%2F1748-0221%2F8%2F102Fp10003

[95] A. Chilingarov, "Generation current temperature scaling," CERN, Geneva, Tech. Rep. PH-EP-Tech-Note-2013-001, Jan 2013. [Online]. Available: http://cds.cern.ch/record/1511886

[96] M. Nakamura *et al.*, "Radiation damage test of silicon multistrip detectors," *Nuclear Instruments and Methods in Physics Research Section A: Accelerators, Spectrometers, Detectors and Associated Equipment*, vol. 270, no. 1, pp. 42 – 55, 1988. [Online]. Available: http://www.sciencedirect.com/science/article/pii/0168900288900071

[97] K. Gill *et al.*, "Radiation damage by neutrons and protons to silicon detectors," *Nuclear Instruments and Methods in Physics Research Section A: Accelerators, Spectrometers, Detectors and Associated Equipment*, vol. 322, no. 2, pp. 177 – 188, 1992. [Online]. Available: http://www.sciencedirect.com/science/article/pii/0168900292900272

[98] T. Rohe *et al.*, "Position dependence of charge collection in prototype sensors for the cms pixel detector," *IEEE Transactions on Nuclear Science*, vol. 51, no. 3, pp. 1150–1157, June 2004.

[99] R. Aaij *et al.*, "Forward production of Υ mesons in pp collisions at $\sqrt{s} = 7$ and 8TeV," *JHEP*, vol. 11, p. 103, 2015.

[100] Aaij, Roel and others, "First measurement of the CP-violating phase $\phi_s^{d\bar{d}}$ in $B_s^0 \to (K^+\pi^-)(K^-\pi^+)$ decays," *JHEP*, vol. 03, p. 140, 2018.

[101] B. Dey, "Lepton Flavor Universality tests in $b \to s\ell^+\ell^-$ decays at LHCb," Jul 2018. [Online]. Available: http://cds.cern.ch/record/2630554

[102] M.-H. Schune, F. Polci, and M. Borsato, "HOP an additional tool for decays involving electrons," CERN, Geneva, Tech. Rep. LHCb-INT-2015-037. CERN-LHCb-INT-2015-037, Nov 2015. [Online]. Available: https://cds.cern.ch/record/2102345

[103] P. Allport *et al.*, "Recent results and experience with the birmingham MC40 irradiation facility," *Journal of Instrumentation*, vol. 12, no. 03, pp. C03 075–C03 075, mar 2017. [Online]. Available: https://doi.org/10.1088%2F1748-0221%2F12%2F03%2Fc03075

[104] K. Dreimanis, Personal communication.

[105] E. Dall'Occo, "The Timepix3 Telescope andSensor R&D for the LHCb VELO Upgrade," Dec 2018. [Online]. Available: https://cds.cern.ch/record/2651308